BRINGING TRANSITION METAL DICHALCOGENIDES TO THE FOREFRONT: ADVANCEMENTS IN GAS SENSING BEYOND METAL OXIDES

Shuja Bashir Malik

UNIVERSITAT ROVIRA i VIRGILI

Bringing Transition Metal Dichalcogenides to the Forefront: Advancements in Gas Sensing Beyond Metal Oxides

SHUJA BASHIR MALIK

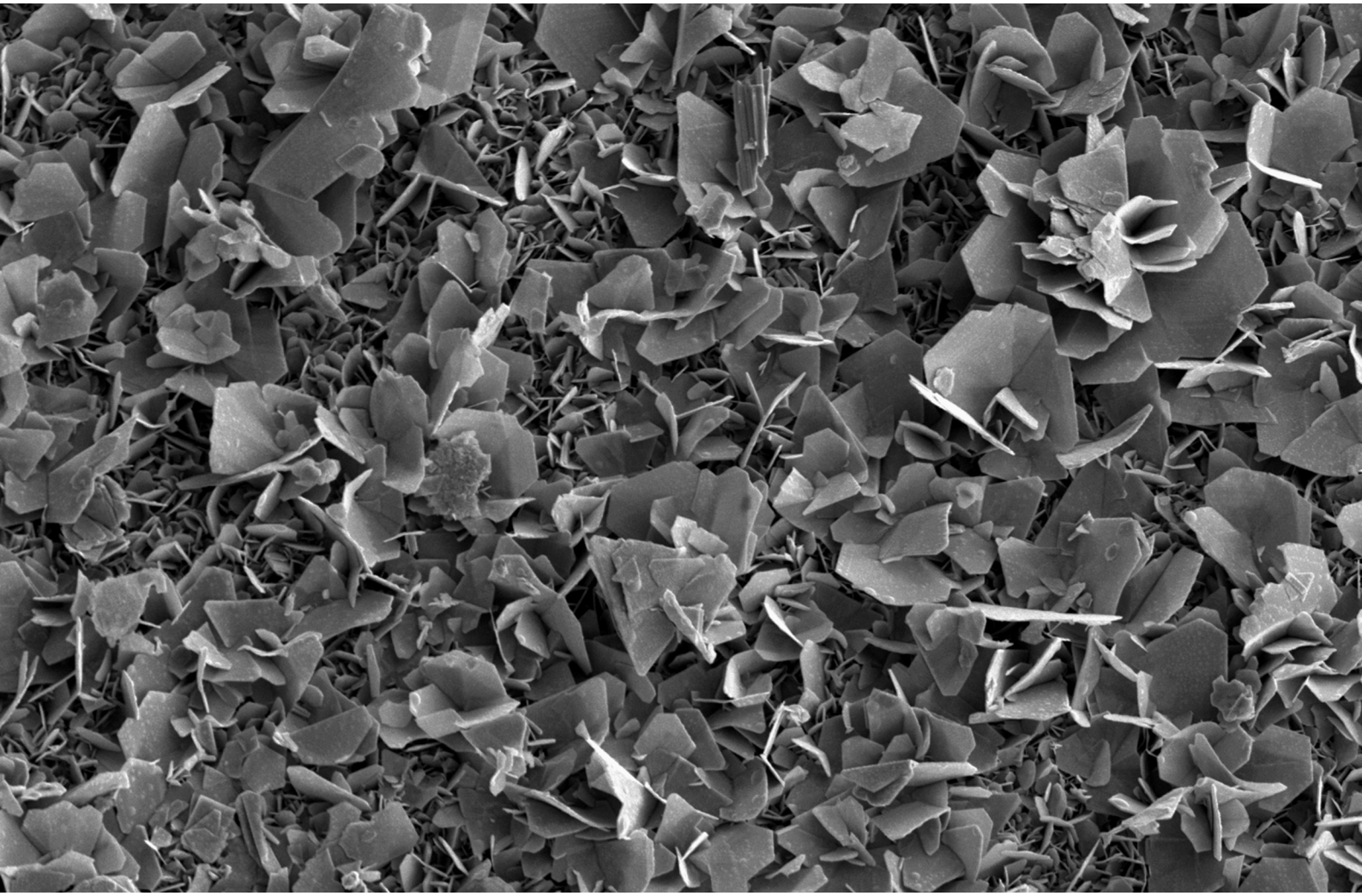

DOCTORAL THESIS
2024

DOCTORAL THESIS

Bringing Transition Metal Dichalcogenides to the Forefront: Advancements in Gas Sensing Beyond Metal Oxides

PhD Thesis

Shuja Bashir Malik

Supervised by:

Dr. Fatima Ezahra Annanouch,

Prof. Frank Güell

and

Prof. Eduard Llobet Valero

Department of Electronic, Electrical and Automation Engineering

UNIVERSITAT ROVIRA i VIRGILI

Tarragona 2024

UNIVERSITAT ROVIRA i VIRGILI

FAIG CONSTAR que aquest treball, titulat “BRINGING TRANSITION METAL DICHALCOGENIDES TO THE FOREFRONT: ADVANCEMENTS IN GAS SENSING BEYOND METAL OXIDES”, que presenta SHUJA BASHIR MALIK per a l’obtenció del títol de Doctor, ha estat realitzat sota la meva direcció al Departament Departament d’Enginyeria Electrònica, Elèctrica i Automàtica d’aquesta universitat.

HAGO CONSTAR que el presente trabajo, titulado “BRINGING TRANSITION METAL DICHALCOGENIDES TO THE FOREFRONT: ADVANCEMENTS IN GAS SENSING BEYOND METAL OXIDES”, que presenta SHUJA BASHIR MALIK para la obtención del título de Doctor, ha sido realizado bajo mi dirección en el Departamento Departament Departament d’Enginyeria Electrònica, Elèctrica i Automàtica de esta universidad.

I STATE that the present study, entitled “BRINGING TRANSITION METAL DICHALCOGENIDES TO THE FOREFRONT: ADVANCEMENTS IN GAS SENSING BEYOND METAL OXIDES”, presented by SHUJA BASHIR MALIK for the award of the degree of Doctor, has been carried out under my supervision at the Department Departament Departament d’Enginyeria Electrònica, Elèctrica i Automàtica of this university.

Tarragona, 14/02/2024

El/s director/s de la tesi doctoral

El/los director/es de la tesis doctoral

Doctoral Thesis Supervisor/s

[Fatima Ezahra Annanouch] [Frank Güell] [Eduard Llobet

Acknowledgements

My doctoral experience has been a remarkable period of personal and intellectual development, filled with profound memories and discoveries. I owe immense gratitude to the exceptional individuals and organizations whose unwavering support and guidance have been indispensable on this journey. Without them, this transformative chapter wouldn't have been possible and achievable.

Firstly, I would like to thank Prof. Eduard Llobet, I am immensely grateful for your mentorship and unwavering guidance throughout my time in the University. Your insights, constructive critiques, and visionary perspective have consistently steered me towards the path of excellence. Your mentorship has been an invaluable asset. Your patient explanations and insightful feedback have been invaluable in helping me navigate through complex challenges.

I am profoundly grateful to Dr. Fatima Ezahra Annanouch. Your influence has been truly transformative. The lessons I have learned from you, both in terms of technique and approach, have played a crucial role in shaping the outcomes of my research. Your resolute belief in my potential has fueled my determination to excel and push the boundaries of my capabilities.

The support of the MINOS group has been the bedrock of my research experience. I am thankful to all the members of MINOS group. Though our challenges might not have been shared directly, the resonance of our determination has woven a knot of unity. The exchange of ideas, while perhaps not in the formal settings of a group, has transcended boundaries, sparking a creative fire that fuels my own reflections. I would also like to thank other Professors from my research group for their valuable scientific discussions during the group meetings, Prof. Xavier Vilanova, Prof. Alfonso Romero, and Prof. Jose Luis. I would also like to thank Prof. Frank Güell for his continuous motivation and support.

I extend my sincere gratitude to my group colleagues whose collaboration and camaraderie have enriched my doctoral journey. I am thankful to Alejandro, Jyayasi, Mubdiul, Ayoub, Eric, Foad, Jose Carlos, and Pineda for their steady support and for fostering a collaborative environment conducive to research excellence. Special mention goes to Xavi, whose technical assistance has been invaluable throughout this endeavor. Your dedication and teamwork have made this journey truly memorable and rewarding.

I would also like to thank Mariana, Merce, Francesc, Eric, Sergi and Rita from Servei de Recursos Científics i Técnics Servei (SRCiT) for their availability and help during material characterization with SEM, FESEM, Raman, XRD and HRTEM.

I would like to extend a special acknowledgment to Prof. André Pereira, Mariana, and Ana at Universidade do Porto. Their guidance, mentorship, and support were invaluable during my secondment period, contributing significantly to my professional development and enriching my learning experience.

This work has been made possible through the financial support of the Martí i Franquès research grant and Marie Skłodowska-Curie Research and Innovation Staff Exchange (RISE)-SENSOFT Project. I extend my gratitude to these agencies for their invaluable contributions to advancing scientific knowledge.

In the realm beyond academia, the support of friends can never be overstated. Akash, Ankur, and Deepanshu, your presence in my life has been a source of immense strength. Your continuous emotional support, uplifting conversations, and moments of shared laughter have kept my spirits high during challenging times. So, here's to the kind of friendships that are as essential to life as oxygen is to breath. I extend my deepest appreciation to Maryam for her steadfast support, understanding, and encouragement throughout this endeavour. Most importantly, I express my deepest gratitude to my family; Huma and Farhan for their unwavering love and boundless support throughout my academic journey and beyond. My parents, Bashir ul Hassan and Mymoona, have served as the cornerstone of my strength always. Finally, I dedicate this thesis to the memory of my late uncle and aunt, Rayees Ahmad and Shameema. Their wisdom, values, and love continue to inspire me. This achievement stands as a tribute to legacy.

With deepest gratitude,
Shuja Bashir Malik

Abstract

Air pollution, originating predominantly from human activities, has become a major global challenge, raising concerns about its widespread impact on both the environment and human health. The World Health Organization (WHO) emphasizes the severity of this issue, linking it to various adverse effects on a global scale, with millions of premature deaths attributed to anthropogenic air pollution. The primary culprits responsible for this pollution are particulate matter (PM), nitrogen dioxide (NO_2), ammonia (NH_3), sulfur dioxide (SO_2), carbon monoxide (CO), ozone (O_3), and various volatile organic compounds (VOCs). These pollutants emerge from diverse sources such as industries, vehicular emissions, agricultural practices, and energy production. The consequences of exposure to these pollutants are severe, leading to respiratory diseases like asthma and chronic obstructive pulmonary disease, cardiovascular diseases, and other health conditions.

Delving into specific pollutants, each plays a unique role in deteriorating both human health and the environment. NO_2 is a red-brown oxidizing gas primarily generated from industrial combustion processes and automobile industries. Its adverse effects include contributing to ground-level ozone formation, acid rain, and inorganic ambient particulate matter. Prolonged exposure to NO_2 can lead to respiratory issues, chronic bronchitis, asthma, and various heart and lung diseases. Regulatory bodies like the Occupational Safety and Health Administration (OSHA) have set safe exposure limits to mitigate its impact. NH_3, another hazardous gas, is emitted from sources like animal and human activities, as well as agricultural practices. NH_3 poses risks to human health, with its pungent odor and potential harm to the skin, eyes, and respiratory system. The National Institute of Occupational Safety and Health (NIOSH) sets indoor concentration limits to safeguard against its detrimental effects. Additionally, NH_3 is flammable and explosive, posing threats to human life in the event of a substantial release into the atmosphere.

SO_2, mainly originating from chemical fertilizers, chemical plants, and mining processes, contributes to adverse health effects such as speech disorders, vomiting, pulmonary edema, and, in extreme cases, asphyxiation or death. Moreover, elevated levels of SO_2 in the environment contribute to the formation of acid rain, causing harm to river and lake ecosystems, soil quality, vegetation, and the corrosion of metals and structures. CO, a colorless, odorless, and tasteless gas primarily derived from the combustion of fossil fuels, is both a contributor to global warming and a significant health risk. Its strong bond with haemoglobin

poses a severe threat to vital organs, including the brain, heart, liver, kidneys, and lungs. Regulatory standards set by organizations like OSHA and the NIOSH aim to limit human exposure to CO.

Volatile organic compounds (VOCs), including ethanol, acetone, toluene, xylene, and formaldehyde, are prominent indoor air pollutants known for their harmful effects on human health, attributed to their poisonous, teratogenic, and cancer-causing properties. Exposure to air containing VOCs has both short and long-term implications on human health and the natural ecosystem. Among these, ethanol serves as a crucial industrial raw material with diverse applications in medical and healthcare, as well as solvents. However, prolonged exposure to ethanol gas poses discomfort, and its flammability introduces potential hazards. Also, the ever-increasing demand for sustainable and clean energy sources has positioned hydrogen (H_2) as a leading contender for the next generation of energy. With its abundance in nature, H_2 holds the potential to replace fossil fuels, offering a pathway to significantly reduce greenhouse gas emissions through water production upon combustion. However, H_2's inherent explosiveness and flammability, particularly in air mixtures above 4%, necessitate cautious storage and handling practices. Even minor hydrogen leakage poses a serious safety threat.

Given the potential risks associated with the mentioned pollutants, threats associated with H_2 leaks, continuous surveillance is crucial for maintaining public health and ecological balance. Timely and accurate detection of these gases is vital for implementing effective mitigation strategies. The obtained data not only aids in formulating targeted interventions but also contributes to the development of comprehensive policies aimed at reducing emissions, improving air quality standards, and also saving lives and property from H_2 leaks related explosions. Taking a proactive approach to monitor gases could lead to creating a healthier and more sustainable living environment for both current and future generations. This has resulted in a notable increase in the demand for gas sensors, propelling substantial growth in the gas sensor industry, and anticipations point towards continued exponential increase in the years to come.

Chemoresistive sensors stand out as the most commonly used gas sensors for monitoring various pollutants and VOCs. However, semiconducting metal oxides, the predominantly used materials in gas sensing applications, exhibit significant drawbacks, including high power consumption, poor long-term stability, limited selectivity, and notably, high sensitivity to humidity. Recent efforts have been concentrated on developing gas sensors that work at lower

temperatures to cater to consumer electronics, wearables, and wireless sensing networks. Two-dimensional (2D) Transition-metal dichalcogenides (TMDs) have emerged as promising candidates for gas sensing applications, offering potential enhancements in sensitivity, selectivity, stability, and response-recovery time. The unique properties of TMDs, such as nanoscale thickness, large specific surface area, abundant active edge sites, and high sensitivity to gas molecules even at lower temperatures, make them valuable for gas sensing.

The focus of this thesis centers on the transition from metal oxide gas sensors to gas sensors based on transition metal dichalcogenides. The aim is to avoid the need for high operating temperatures and address issues related to selectivity and cross-sensitivity in sensing applications. The focus lies on optimizing sensitivity, selectivity, and stability in gas detection while operating under near ambient conditions. The synthesis of 2D layered materials is crucial for gas sensing applications, and this doctoral thesis focuses on developing an edge-enriched morphology to enhance their effectiveness as chemoresistive gas sensors. A facile synthesis route is presented, utilizing aerosol-assisted chemical vapor deposition (AACVD) method to deposit WO_3 films of different morphologies on commercial alumina transducers. Also, a novel atmospheric pressure chemical vapor deposition (APCVD) method is presented to synthesize WS_2 in powder form with yield in hundreds of milligrams.

The **first chapter** of this thesis delves into the current state-of-the-art, providing a comprehensive overview of gas sensors and the traditional gas-sensitive materials. The focus extends to metal oxides and 2D materials, emphasizing on their distinct advantages in the realm of gas sensing applications. A particular emphasis is placed on inorganic analogues of graphene, Transition Metal Dichalcogenides (TMDs), unravelling their unique properties and advantages. Different synthesis methods of the sensing materials are also discussed by carefully studying the methods described in existing literature. Towards the end of the chapter, potential applications of these next-generation materials are explored in the areas like electronics, photovoltaics, and detecting biomolecules.

The **second chapter** discusses the synthesis of WO_3 nanowires with different morphologies using AACVD. The nanowires were drop-casted with CeO_2 nanoparticles to investigate their sensing behavior towards one of the main VOCs, ethanol. The results indicate that the AACVD process, influenced by the flow of carrier gas, results in different morphologies of WO_3 nanowires. Gas sensing studies of the CeO_2-decorated WO_3 nanowires reveal an exponential increase in gas sensing responses. The gas sensing characteristics of pristine and CeO_2-

decorated WO_3 sensors towards oxidizing gas (NO_2) as well as reducing gases (CO, ethanol, H_2) were analyzed, and the sensor responses were calculated accordingly. The sensors exhibited good responses to ethanol under both dry and humid conditions, although the response decreased in humid atmospheres. Specifically, the response of the CeO_2-decorated WO_3 nanowires with floral tops sensor was 10-fold higher than that of pristine WO_3 and 5-fold higher than that of randomly oriented CeO_2-decorated WO_3 nanowires at an operating temperature of 250ºC. The optimal response to ethanol was observed at 250ºC, with no responses detected at temperatures below 100ºC. Stability tests of the sensors were conducted over approximately one year.

Keeping in view the high working temperature, selectivity issues related to the CeO_2 decorated WO_3 nanowires, we transitioned from metal oxides to transition metal disulfide-based sensors.

Chapter 3 discusses the novel APCVD technique developed to synthesize WS_2 sheets/plates in powder form. In this work, we present for the first time the synthesis of large-scale 2D tungsten disulfide (WS_2) sheets through a simple sulfurization process of commercially available tungsten trioxide (WO_3) powder in an APCVD reactor. The resulting powders offer versatile applications, suitable for various printing and coating techniques on substrates like ceramics, silicon, and flexible polymers. Structural and chemical analysis confirms the successful growth of edge enriched WS_2 sheets, which were then deposited as sensing layers on alumina substrates using a home-made airbrushing tool for chemoresistive gas sensors. Gas sensing studies, particularly towards NH_3, exhibited exceptional responses, with reproducible and stable results at 150°C. The sensors demonstrated high selectivity for NH_3 against interfering gases, and the edge-enriched growth contributed to remarkable resilience against high humidity levels (50% RH at 25ºC). Atomistic simulations using density functional theory (DFT) and Bayesian optimization provided insights into the stable adsorption of ammonia on WS_2, revealing a predominantly physisorption-based interaction between gas molecules and WS_2.

Chapter 4 of this thesis introduces an outstanding hybrid sensing material designed for the detection of ultra-low concentrations of NO_2. The methodology involves the fabrication of WS_2-graphene hybrid thin films through a simple airbrushing technique, with WS_2 grown using the APCVD technique. The resulting hybrid films with different WS_2 and graphene ratios are precisely deposited onto the transducer substrate, allowing for controlled thickness. In depth characterization, including morphology, microstructure, phase, and chemical composition, was

conducted on the hybrid sensing films. Gas sensing properties were studied, specifically towards ultra-low concentrations of NO_2, at varying operating temperatures (room temperature, 100°C, and 150°C) in both dry and humid environments. Additionally, the sensors exhibited excellent selectivity against interfering species such as NH_3, CO, H_2, and C_6H_6. Interestingly, the sensors displayed exceptional responses towards ultra-low concentrations of NO_2, with an experimental limit of detection (LoD) of 10 ppb.

Chapter 5 introduces a facile approach to integrating heterojunctions comprising Transition Metal Dichalcogenides (TMDs), specifically WS_2 synthesized through a two-step process involving Aerosol-Assisted Chemical Vapor Deposition (AACVD) and Atmospheric Pressure Chemical Vapor Deposition (APCVD), along with metal oxides (ZnO) grown via AACVD atop WS_2. This combination not only enhances the sensor's sensitivity but also facilitates a significant reduction in the operating temperature. By exploiting the unique properties of both the materials, this study demonstrates gas sensing results towards 500 ppb of NO_2. The influence of WS_2 material on the ZnO gas sensing performances is significant. The operating temperature was shifted towards lower values from 300°C to 150°C. Besides, the ZnO/WS_2 sensor was able to detect such a small concentration of NO_2 at room temperature.

Chapter 6 discusses the Pd decorated multilayered MoS_2 sheets capability to detect hydrogen with high sensitivity. The focus was on the fabrication and characterization of MoS_2-based gas sensors. MoS_2 was airbrushed onto alumina transducers and decorated with Pd nanoparticles using AACVD at 250°C. Detailed characterization using various techniques confirmed the successful decoration of MoS_2 with Pd nanoparticles, showcasing a multilayered crystalline structure. Gas sensing experiments demonstrated a maximum response of 55% for Pd-decorated MoS_2 at 150°C when exposed to 100 ppm of H_2, well below the explosive limit in air. The heigh sensitivity attributed to Pd decoration was attributed to a spillover effect. This study revealed that the sensitivity of the sensors is highly dependent on the amount of Pd decoration. Also, a slight increase in responses was recorded when sensors were exposed to the analyte gas at 50% relative humidity conditions (at 25°C).

Chapter 7 details synthesizing ZnO-piezoelectric polymer composites. This chapter demonstrates developing high-performance flexible piezoelectric nanogenerators (PENGs) for energy harvesting and sensor applications. The research underscores the growing interest in self-powered nanogenerators within the scientific community and charts the progress in piezoelectric nanogenerator research since its inception in 2006. Through the fabrication and

optimization of ZnO-based PENGS, this work contributes to the advancement of efficient and cost-effective energy harvesting technologies, aiming to cater to the increasing demand for flexible and wearable electronics in various fields. The maximum output voltage obtained was 760 mV and 1500 mV for 12 ml NaOH and 30 ml NaOH reaction conditions respectively. The maximum power output recorded was 450μW/m^2 in PENG fabricated using ZnO synthesized using 30 ml NaOH. It was also found that because of the presence of H_3PO_4 in the polymer, around 50% of the ZnO reacts to form hopeite ($Zn_3(PO_4)_2.4H_2O$).

LIST OF ACRONYMS

AACVD	Aerosol Assisted Chemical Vapor Deposition
APCVD	Atmospheric Pressure Chemical Vapor Deposition
CVD	Chemical Vapor Deposition
MOX	Metal Oxide
SMOX	Semiconductor Metal Oxide
MOS	Metal Oxide Sensors
TMDs	Transition Metal Dichalcogenides
SEM	Scanning Electron Microscope
FESEM	Field Emission Scanning Electron Microspcope
TEM	Transmission Electron Microscope
HR-TEM	High Resolution Transmission Electron Microscope
PL	Photoluminescence
NFs	Nanoflowers
NTs	Nanotriangles
2D	Two Dimensional
WHO	World Health Organization
CeO_2	Cerium Oxide
WO_3	Tungsten Trioxide
ZnO	Zin Oxide
WS_2	Tungsten Disulfide
MoS_2	Molybdenum Disulfide
VOC	Volatile Organic Compound
XRD	X-Ray Diffraction
XPS	X-Ray Photoelectron Spectroscopy

DFT	Density Functional Theory
ppm	Parts per million
ppb	Parts per billion
O_2	Oxygen
H_2	Hydrogen
MFC	Mass Flow Controller
LoD	Limit of Detection
TLV	Threshold Limit Value

Table of Contents

List of Figures

List of Tables

CHAPTER 1

Introduction

1.1. State of the art

Anthropogenic air pollution, a prevalent global issue, stems primarily from human activities. According to World Health Organization (WHO), this type of pollution is a significant global health concern contributing to a wide range of adverse effects on environment and human health [1]. As per the alarming data provided by WHO, anthropogenic air pollution is responsible for millions of premature deaths worldwide [2]. These figures highlight the severe impact of human-generated air pollutants on public health and environment. Particulate matter (PM), nitrogen dioxide (NO_2), ammonia (NH_3), sulfur dioxide (SO_2), carbon monoxide (CO), ozone (O_3) and various volatile organic compounds (VOCs) are the main pollutants leading to air pollution [1,2]. The main sources of these pollutants are industries, vehicular emission, agricultural practices, and energy production. Exposure to these pollutants has been linked to a range of health problems, including respiratory diseases (such as asthma and chronic obstructive pulmonary disease), cardiovascular diseases, and other conditions [3]. The impact is particularly pronounced in densely populated urban areas with high levels of industrial and vehicular activities. Efforts to address anthropogenic air pollution involve implementing policies and regulations to reduce emissions from various sources, promoting cleaner technologies, and encouraging sustainable practices [4]. The WHO's emphasis on the significant number of premature deaths underscores the urgency of tackling anthropogenic air pollution to safeguard public health and create a sustainable environment for future generations [5].

When discussing the pollutants, each one plays a distinct role in the degradation of both the human health and the environment. NO_2 is an irritating red-brown oxidizing gas with its main sources being combustion reactions in industrial processes and automobile industries [6]. Naturally, NO_2 is produced from N_2 in air during thunderstorms [7,8]. NO_2 is a direct contributor to the formation of ground level ozone in stratosphere, acid rain and inorganic ambient particulate matter [9–11]. This hazardous pollutant has the potential to induce respiratory issues, chronic bronchitis, asthma, as well as a range of heart and lung diseases, depending on the length of exposure. The Occupational Safety and Health Administration (OSHA) stipulates the safe limit for the human exposure to NO_2 is 5 ppm [12]. As per the U.S. Environmental Protection Agency, the quality standards for NO_2 in ambient air is 53 ppb for the annual average [13].

Also, being a noxious and hazardous gas, ammonia (NH_3) gas presents a significant risk owing to its pungent odor and the potential to cause harm to human skin, eyes, and the respiratory system [14]. NH_3 is emitted from animal and human activities, agricultural activities, waste handling [15]. The National Institute of Occupational Safety and Health specifies that the allowable indoor concentration of NH_3 is limited to only 25 ppm [16,17]. NH_3 is flammable and explosive, posing a substantial threat to human life in the event of a serious release into the open air [18]. In addition, NH_3 is reactive and can generate aerosols upon reaction with nitric or sulfuric acids in the air [15]. One more colourless toxic gas harmful to human health and environment is sulfur dioxide (SO_2). The main sources of SO_2 gas are chemical fertilizers, chemical plants and mining process [19]. Exposure to elevated concentrations of SO_2 can result in various adverse effects on humans, including speech disorders, vomiting, acute pulmonary edema, and the extreme consequences of asphyxiation or death [20]. In the natural environment, elevated levels of SO_2 gas contributes to the formation of acid rain (H_2SO_4), inflicting substantial damage on river and lake ecosystems [20]. This includes detrimental effects on soil quality, vegetation, and the corrosion of metals and structures [19]. Carbon monoxide (CO) is one of the most perilous gases, it not only contributes to global warming but also poses a significant health risk by forming a strong bond with haemoglobin [21–23]. It poses a severe threat to the human body, causing significant toxicity and placing vital organs such as the brain, heart, liver, kidneys, and lungs in serious jeopardy [24]. It is a colorless, odorless and tasteless gas at room temperature and is mainly derived from the combustion of fossil fuels [25]. According to the US Occupational Safety and Health Administration (OSHA), the permissible exposure limit for CO is set at 35 ppm (10-hour ceiling limit), while the US National Institute for Occupational Safety and Health (NIOSH) recommends a limit of 50 ppm (8-hour ceiling limit) [26].

Given the potential risks associated with the pollutant gases such as respiratory issues, damage to vital organs, and environmental degradation, their continuous surveillance is crucial for maintaining public health and ecological balance. Timely and accurate detection of these gases allows for the implementation of effective mitigation strategies, ensuring the protection of human well-being and the sustainability of the environment. The data obtained from gas monitoring will not only aid in formulating targeted interventions, but also contribute to the development of comprehensive policies aimed at reducing emissions and improving air quality standards. The proactive monitoring of gases will serve as a foundational step in fostering a healthier and more sustainable living environment for present and future generations. This has

led to an ever-increasing demand for use of gas sensors and the gas sensor industry has grown tremendously over years with anticipations of exponential growth in the future, Figure 1.1. This necessitates the development of gas sensors that are highly selective, sensitive, and ensure repeatability in detecting gases.

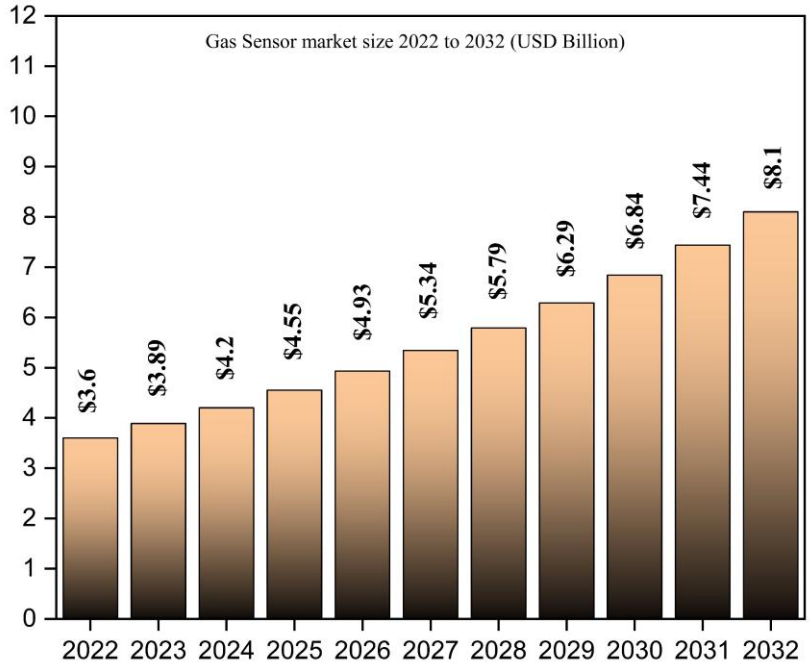

Figure 1.1 Global gas sensor market trends, Source: www.precedenceresearch.com

Table 1.1 shows the threshold limit values (TLV) of some common pollutant species defined by various regulatory bodies.

Table 1.1 Threshold limit values of some common pollutant species.

Pollutant	Threshold Limit Value (TLV)		References
NO_2	5 ppm (OSHA)	100 ppb (EPA)	[27]
NH_3	25 ppm (NIOSH)		[16,17]
SO_2	5 ppm (ACGIH)		[28]
CO	35 ppm (OSHA)	50 ppm (NIOSH)	[26]
CO_2	1000 ppm (ASHRAE)		[29]
O_3	100 ppb (WHO)		[30]
H_2S	20-100 ppb		[31]

***OSHA**: The Occupational Safety and Health Administration, **NIOSH**: National Institute for Occupational Safety and Health, **EPA**: U.S. Environmental Protection Agency, **ACGIH**: American Conference of Governmental Industrial Hygienists, **ASHRAE**: The American Society of Heating, Refrigerating and Air-Conditioning Engineers, **WHO**: World Health Organization*

A significant milestone was achieved in 1962 when Seiyama et al. at Kyushu University in Japan demonstrated that the resistance change of a metal oxide (ZnO) could detect variations in the surrounding atmosphere [32]. Around the same time, an innovator, Naoyoshi Taguchi filed a patent for a tin oxide (SnO_2) based sensor activated with palladium oxide [33,34]. The use of liquefied petroleum gas (LPG) for cooking gained popularity in Japan in 1960s, leading to a surge in domestic gas explosions. Taguchi founded Figaro Engineering Inc. in 1968 and introduced the Taguchi Gas Sensor (TGS) 109, designed for residential gas alarms. These alarms, employing the TGS109 sensor, were cost-effective, approximately one-third of the cost of their catalytic-type sensor predecessors [35]. The widespread adoption of detection systems significantly reduced the occurrence of domestic gas explosions [35]. The resurgence of interest in semiconductor metal oxide (SMOX)-based sensors in 1980s for monitoring air intake in the car passenger cabins. These sensors were used to detect nitrogen oxide (NO_x), carbon monoxide (CO), and various other hydrocarbons [36]. SMOX-based sensors proved highly efficient in monitoring these gases. There has been a tremendous development in SMOX based sensors. Nowadays, all the new constructions including offices, buildings, and industries are installed with gas sensors to detect the presence of toxic and harmful gases. The gas sensor industry has witnessed significant growth over the past few decades and is anticipated to continue evolving in the years ahead as is demonstrated in Figure 1.1.

1.1.1. Gas sensors

A gas sensor employs physical or chemical reactions to transform the concentration of different gases into electrical or optical signals and subsequently provides an output signal [37]. Gas sensors are extensively utilized for detecting toxic gases, harmful substances, and natural gas leaks. The devices serve the purpose of monitoring the presence or levels of gas in stationary environments. They find applications in various industries such as coal mining, petroleum, chemicals, municipalities, healthcare, transportation, and households. Gas sensors are versatile tools capable of measuring the presence and concentration of combustible, flammable, toxic gases, as well as monitoring oxygen consumption. Numerous types of gas sensors are available, and to select the most appropriate one, it is essential to understand the distinct characteristics of each sensor. According to different gas types, sensors can be divided into combustible gas sensors, toxic gas sensors, harmful gas sensors and oxygen sensors. Combustible gas sensors often use catalytic combustion, infrared, thermal conductivity, and semiconductor type sensors. At the same time, toxic gas sensors generally use electrochemical, metal-semiconductor,

photoionization, flame ionization type sensors. Also, harmful gas sensors often involve infrared and ultraviolet sensors.

Moreover, gas sensors are classified based on their different working principles and applications.

a) **Semiconductor gas sensors**: devices that use a semiconductor element as a measuring unit. The operational principle involves the gas undergoing a redox reaction on the semiconductor, resulting in a change in resistance value [38]. As the gas passes the measuring cell, it adsorbs onto its surface and reacts. Gas levels are measured by inducing a change in conductivity or potential, which is characterized by the motion of carriers.
b) **Electrochemical gas sensors:** react with the measured gas and generate an electrical signal proportional to the respective gas concentration [39]. Most electrochemical gas sensors are current sensors, producing a current that is linearly proportional to the gas concentration [40]. The gas diffuses through a diaphragm (membrane) designed to prevent condensation, which also serves as a dust-proof barrier. Subsequently, gas molecules diffuse through a filter, reaching the working electrode. The gas undergoes oxidation or reduction, initiating an electrochemical reaction that leads to a modification in the current flowing through the external circuit.
c) **NDIR (non-dispersive infrared) gas sensors** [41]**:** emit infrared light to make the gas molecules vibrate. The working principle is that different gases can absorb different infrared wavelengths. The more gas there is, the less infrared light can pass through. When infrared rays pass through the gas in the measurement area, the infrared rays resonate with the gas molecules and are absorbed by the gas molecules when the molecules vibrate. This weakens the transmitted infrared rays. Gas molecules vibrate at different frequencies. Some atoms are very small and light, so they vibrate at high frequencies. One of the main advantages of this type of sensor is the non-requirement of oxygen to start the reaction unlike other type of sensors. The most commonly measured gases for NDIR are CH_4 and CO_2.
d) **Catalytic gas sensors:** are actually gas detectors based on a platinum resistance temperature sensors. A high temperature resistant catalyst layer is prepared on the surface of the platinum resistor, and at a certain temperature, the combustible gas is catalytically burned on the surface [42]. Therefore, the platinum resistance temperature increases, resulting in a change in the resistance value. Since the catalytic gas sensor platinum resistance is usually wrapped by porous ceramic beads, this sensor is also called a catalytic bead gas sensor. In theory, this

sensor can detect all combustible gases, but there are many exceptions in practical applications. This sensor can usually be used to detect combustible gases such as methane, LPG, acetone in the air but lacks selectivity.

e) **Magnetic gas sensors:** are mostly magnetic probes with relatively strong measurement capabilities. After the magnetic gas sensor senses heat, light, radiation and pressure in the environment, its magnetic properties will also change accordingly [43]. The working principle of magnetic gas sensors involves detecting changes in the magnetic properties of materials when exposed to gas molecules. This can be achieved through various methods such as the Hall effect, Kerr effect, and ferromagnetic resonance (FMR) [43]. The sensors can exploit phenomena like perpendicular magnetic anisotropy (PMA) induced at the interface between ferromagnetic and non-magnetic layers, as well as the effects of hydrogenation on the magnetic properties of thin films. These changes in magnetic properties upon gas exposure are then used to identify and quantify the presence of specific gases. Commonly used are thermal magnetic convection oxygen analysis sensors and magneto-mechanical oxygen analysis sensors [43].

f) **Photoionization gas sensors (PID):** work by using photo-ionized gas to detect gas [44]. The gas is irradiated with ultraviolet light generated by an ion lamp, and the gas will be ionized after absorbing enough ultraviolet light energy. The measured gas level is calculated by detecting the tiny current generated by the gas ionization. It can detect volatile organic compounds and other toxic gases from 10 ppb to 10000 ppm. Many hazardous substances contain volatile organic compounds, and PID is highly sensitive to volatile organic compounds [45]. It is the most sensitive device for detecting organic volatiles, especially for those gas leaks with very low concentrations, which has incomparable advantages compared to other detectors. However, the problem of selectivity persists in these sensors as well.

g) **Thermal conductivity gas sensors:** are devices that can sense a certain gas in the environment by converting gas concentration information into electrical signals for detection, monitoring, analysis and alarming [46]. Thermally conductive gas-sensitive materials measure their concentration based on the difference in thermal conductivity between different gases and air. Usually, a change in thermal conductivity is translated into a change in resistance through the circuit. The gas type and level are calculated from the change in resistance value. These gas sensors are widely used in chemical, coal, military, environmental only to better optimize the sensor performance.

h) **Gas chromatograph analyzers:** are based on chromatographic separation and detection technology. A certain gas sample is periodically taken from the sampling device. The chromatographic column is carried by a pure carrier gas (mobile phase) with a certain flow rate, and the chromatographic column is filled with a solid or liquid called a stationary phase. The components are repeatedly distributed in the two phases, and flow out of the chromatographic column according to time and enter the detector for quantitative determination. These detectors are bulky, however efforts for miniaturization have been quite successful. These sensors are mostly used for laboratory analysis, and are not suitable for field gas monitoring.

While each sensor type has its unique advantages, they also come with their own set of limitations. Electrochemical sensors are widely preferred for their selectivity, wide operating temperature range, and cost-effectiveness [47]. Nevertheless, they do have drawbacks, including a relatively short life, limited storage period, and humidity dependent sensitivity rendering them unsuitable for numerous applications. Chemoresistive gas sensors have garnered significant attention due to their numerous advantages over alternative sensors, including ease of fabrication, user-friendly simplicity, and cost-effectiveness. Chemoresistors comprise a gas-sensitive material that interacts with the analyte, generating an electrical signal as a response. This signal corresponds to change in the electrical resistance or conductance. The change in resistance occurs because of changes in the concentration of charge carriers prompted by the interaction between the sensing layer and gas molecules [48]. An example of a typical chemoresistive gas sensor employed during this research work is demonstrated in Figure 1.2.

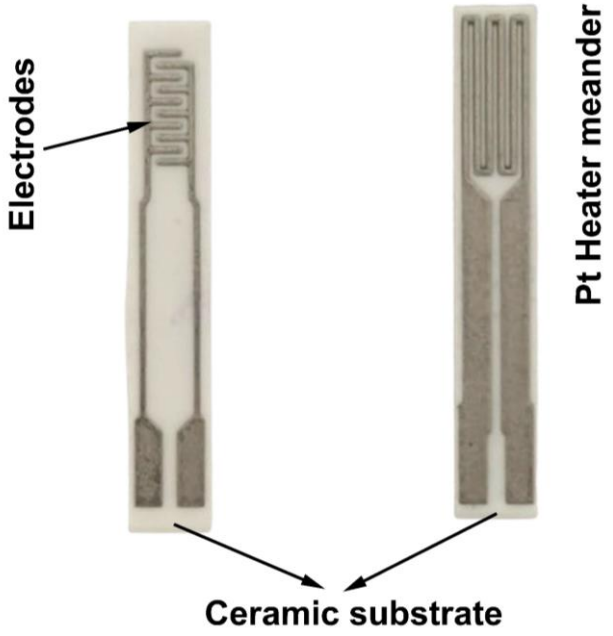

Figure 1.2 Alumina transducer substrate used to deposit different sensing materials.

The performance of a sensor is governed by a number of parameters; selectivity, response, sensitivity, limit of detection (LoD), response and recovery times and long-term stability [49]. Selectivity pertains to the characteristics of a gas sensor that ascertain its ability to differentiate and react to a specific gas within a mixture of various gases [50]. This attribute is crucial for air quality sensors, as multiple gaseous species can induce changes in the sensor's electrical resistance at parts per billion (ppb) or parts per trillion (ppt) levels, much like the desired target gas [49]. The gas sensor response is the percentile change in the baseline resistance of the sensor when exposed to the target gas. Response of a p-type material-based gas sensor towards an oxidizing gas is calculated by using equation (1), while as for a reducing gas, the sensor response is calculated using the equation (2).

$$\text{Response } \% = \frac{R_{air} - R_{gas}}{R_{air}} * 100 \qquad \text{Equation 1}$$

$$\text{Response } \% = \frac{R_{gas} - R_{air}}{R_{air}} * 100 \qquad \text{Equation 2}$$

R_{air} is the sensor resistance in air, while as R_{gas} is the sensor resistance when exposed to analyte gas. Furthermore, the characteristic properties of a sensor to distinguish and respond to a target gas amid a mixture of various gases is referred to as selectivity [51]. Selectivity is one of the most important criteria to determine the performance of a sensor. One of the other crucial parameters defining sensor performance is limit of detection (LoD) [52]. In simple words, it is defined as the lowest concentration of analyte gas a sensor can detect. LoD holds significant

importance for sensor performance in real-world applications, especially considering that environmental agencies establish exposure limits for pollutant gases. The threshold limits of various pollutant gases as mentioned in Table 1.1. Also, response time (t_{res}) is the time it takes for the sensor to achieve 90% of the total resistance change when exposed to the target gas, while the recovery time (t_{rec}) is the time it takes for the sensor to regain 90% of the total resistance change upon the removal of the target gas [53,54]. And finally, a sensor's long-term stability or repeatability, of a sensor is associated with its capability to consistently produce the same signal over time when subjected to identical quantities of a target gas.

1.2. Gas sensing measurements

Throughout this thesis, the gas sensing measurements were conducted using a homemade detection system in a Teflon® chamber with a volume of 35 mL. The chamber is designed to accommodate four sensors simultaneously. The chamber consists of an inlet connected to the gas delivery system and an outlet which is connected to the exhaust. Commercial alumina substrates with interdigitated platinum electrodes (300 µm electrode gap) on the front side and a platinum resistive meander on the back side were used to deposit the sensing material, Figure 1.2 (above schematic). The sensor responses were recorded by monitoring the sensing material resistance using an Agilent-34972A data acquisition system. Calibrated cylinders of NO_2 (total concentration, 1 ppm), H_2 (total concentration, 1000 ppm), NH_3 (total concentration, 100 ppm), CO (total concentration, 100 ppm), and benzene (total concentration, 10 ppm) were mixed with pure synthetic air using Bronkhorst mass-flow controllers. A constant flow rate of 100 mL min^{-1} was maintained during all the experiments. The sensors were exposed to the analyte gas for 10 min and subsequently cleaned in dry air for 60 min. The cleaning time to recover the baseline was adapted according to the sensor operating temperature; 60 min for 50°C, 100°C, and 150°C and 120 min for room temperature operation. The operating temperature of the sensor was controlled by connecting its heater to an external power supply (Agilent U8002A). Prior to gas sensing measurements, sensors were kept under a constant flow of dry air for a minimum of 5 h to completely stabilize their initial baseline resistance. The humidity effect on the sensing performance was evaluated by humidifying (at room temperature) the gas stream through a controller evaporator mixer from Bronkhorst. The schematic of the homemade gas sensing measurement system is shown in Figure 1.3.

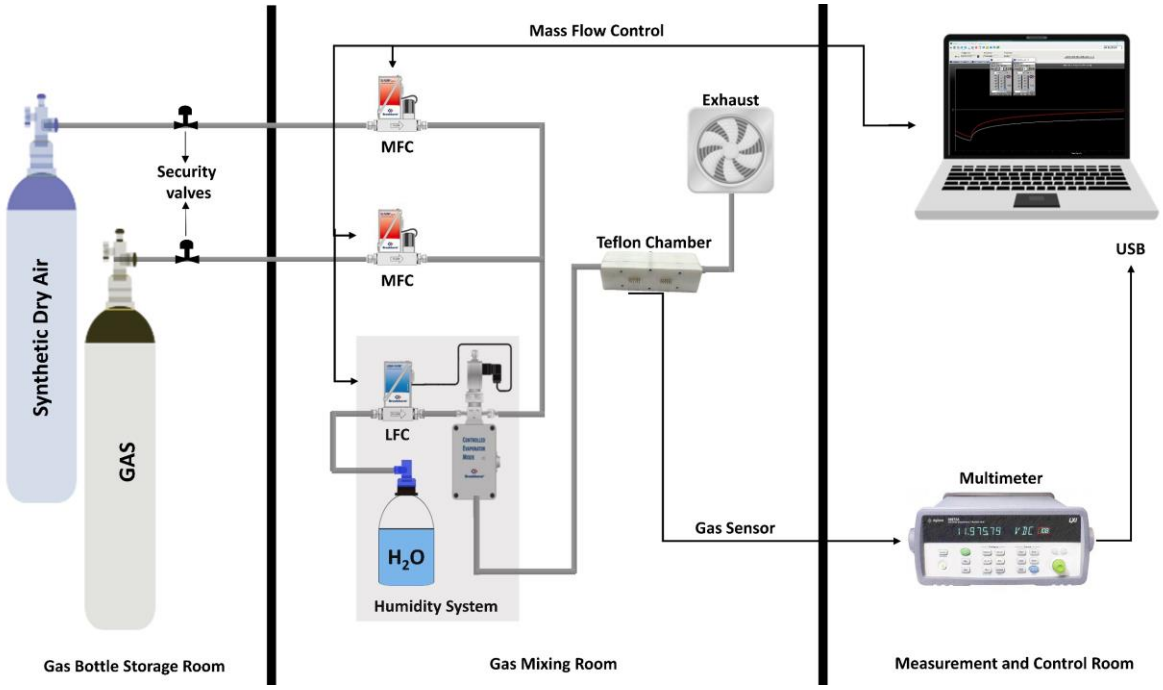

Figure 1.3 Schematic of homemade gas sensing system.

1.3. Semiconductor metal oxide gas sensors

Extensive research efforts have been devoted towards the testing of gas-sensing materials in the development of advanced gas sensors. A diverse range of materials, including semiconductor metal oxides [55,56], carbon nanomaterials [57], conducting polymers [58], and two-dimensional nanostructured materials (2DNMs) [59,60], have been tested for their ability to quantitatively and/or qualitatively detect specific gases. Notably, semiconductor metal-oxide gas sensors have achieved successful commercialization, attributed to their cost-effectiveness, high sensitivity, and easy fabrication processes [61–63]. Semiconducting metal oxide-based sensors are primarily categorized into two types: n-type, where the majority carrier is an electron, and p-type, where the majority carrier is a hole. The operational principle of semiconductor metal oxide (SMOX) gas sensors revolves around inducing an equilibrium shift in surface reactions associated with the targeted analyte, or a change in electrical resistance when the sensor is exposed to the target gas [64]. Typically, reducing gases like NH_3, CO, H_2, result in increased conductivity for n-type semiconductors and decreased conductivity for p-type semiconductors [65,66] Conversely, oxidizing gases like NO_2, O_3, Cl_2 exhibit the opposite effect. Despite n-type SMOX sensors garnering more attention in studies, research indicates that p-type SMOX-based gas sensors have distinct advantages, including lower humidity dependence and high catalytic properties [67]. The fabrication of gas sensors involves intricate

processes involving the selection and preparation of sensing materials, as well as the integration of materials into the sensor. The sensing properties of semiconductor metal oxides towards specific gases depend on the fabrication process, including material types, microstructures of sensing materials, and integration modes for the sensing materials and devices. To address contemporary demands for SMOX-based sensors with enhanced sensitivity, excellent selectivity, and robust stability, researchers are increasingly emphasizing the understanding of sensing mechanisms, morphological structure manipulations, and defect structure manipulations. Figure 1.4 shows different synthesis techniques used to synthesis, properties and sensing mechanism of semiconductor metal oxide sensors. Also, Figure 1.5 illustrates the four different bottom-up approaches for nanomaterial synthesis for gas sensor applications.

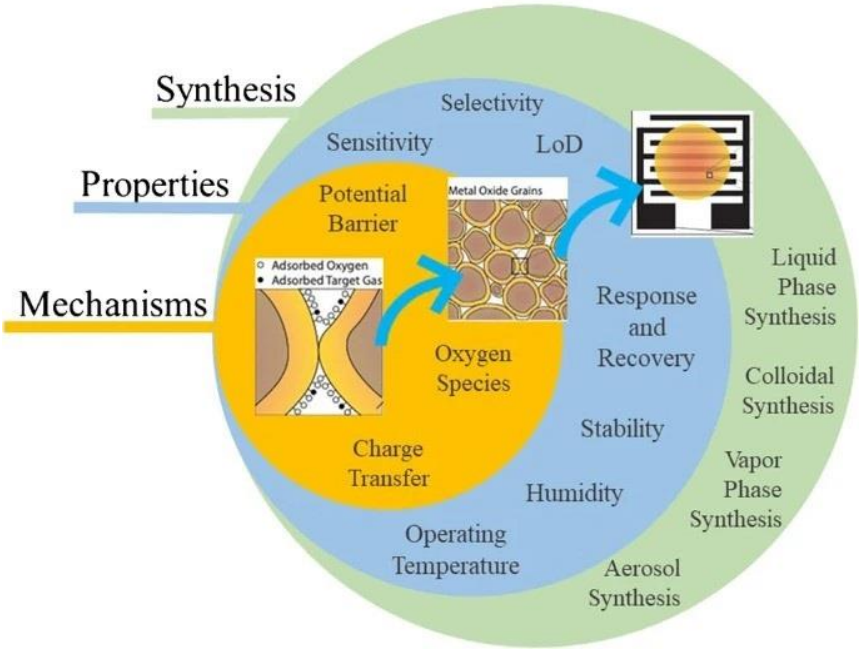

Figure 1.4 Synthesis methods, properties, and sensing mechanism of metal oxide gas sensors in brief [68].

A quick search about “Metal Oxide Gas Sensors” in Scopus yields more than 9800 results as of January 2024. Despite a humongous amount of attention being given to alternative materials, researchers are still reaping the benefit of the excellent gas sensing properties of metal oxides as sensing materials. Agarwal et al. [69] reported hydrothermal synthesis of flower-shaped ZnO nanostructures and their morphology-dependent gas sensing properties. The sensors showed excellent response towards 250 ppb of NO_2 at 200ºC. At 200°C, the flower shaped ZnO showed the highest sensitivity to nitrogen dioxide. In contrast, the ZnO nanorods demonstrated their highest response at 200°C (although it was lower than that of nanoflowers), and their least

responsive state was observed at 250°C. Navarrete et al. [70] reported the direct growth of ZnO nanowires (NWs) on commercially available alumina substrates having screen-printed, platinum interdigitated electrodes and a heating meander. ZnO NWs were synthesized via a catalysed CVD process that results in a vapour-liquid-solid (VLS) growth mechanism. ZnO NWs show high sensitivity of 50 towards 1 ppm of NO_2 when operated at 250°C. Ding and co-workers [71] demonstrated oxygen vacancies defective WO_3 nanosheets with (002) exposed facets for highly sensitive acetone detection. WO_3 nanosheets were obtained by a simple hydrothermal-hydrogenation process. The sensors show a response of 48 towards 100 ppm of acetone at 340ºC.

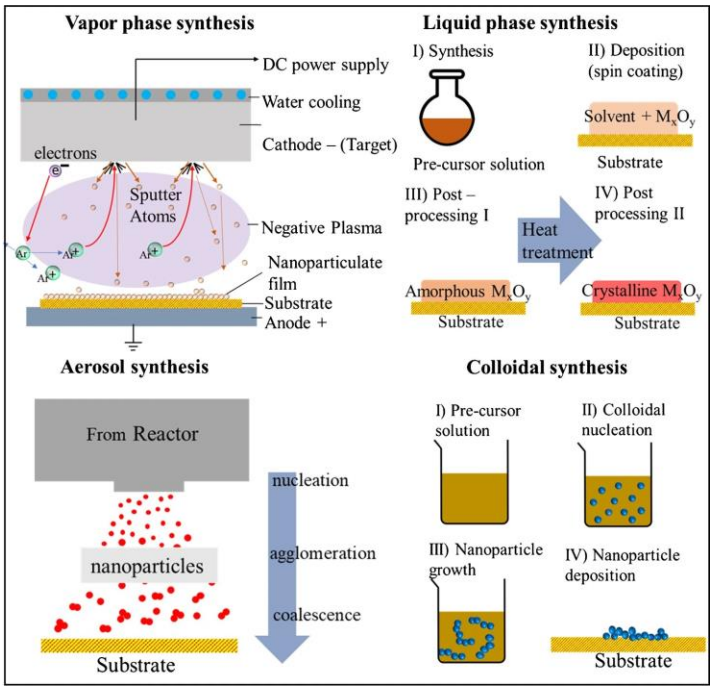

Figure 1.5 Illustration of the four different bottom-up approaches for nanomaterial synthesis [68].

Although, metal oxide gas sensors show high responses towards various pollutant gases. However, the challenges associated with metal oxide gas sensors are evident when considering their high operating temperatures [56], which result in substantial power consumption, rendering them less than ideal for integration into Internet of Things (IoT) devices [72] and other real-world applications. The elevated temperatures not only lead to increased power consumption but also pose a significant obstacle to the efficient and sustainable use of these sensors in various applications [56,72,73]. Additionally, the high operating temperatures lead to a shortened sensor lifespan [73,74], reducing their overall reliability for extended use. Moreover, another notable drawback is the lack of selectivity in metal oxide gas sensors [74],

limiting their ability to differentiate between various gases with precision. These issues underscore the pressing need for further modifications in metal oxide sensor technology to enhance power efficiency, reduce operating temperatures, and improve selectivity, ensuring the viability of metal oxide gas sensors for broader and more diverse applications.

Although chemoresistive metal oxide-based gas sensors require a high operational temperature of approximately 300°C, successful strategies have been devised to mitigate power consumption. These include i) light activation [75], ii) noble metal decoration [76], iii) heterojunction engineering [56], and iv) the incorporation of non-oxide materials. However, it is noteworthy that noble metal decoration and heterojunction engineering prove more effective in enhancing the selectivity of metal oxide gas sensors, enabling robust detection at comparatively lower temperatures [76].

Duan et al. [77] reported WO_3/WS_2 heterostructure for NO_2 detection. The WS2 was synthesized via a simple hydrothermal method. A facile low-temperature in-situ oxidation method was used to fabricate WO_3/WS_2 heterostructure. The heterostructures responded highest at 79ºC towards 5 ppm NO_2. Lee et al. [78] fabricated a SnO_2/NiO nanoparticle based heterostructure for high response formaldehyde sensing. A facile one-step blending process with a low operating temperature of 80ºC was used for the fabrication of SnO_2/NiO heterostructure. The sensors were extremely sensitive towards 10 ppm of formaldehyde with a response of 9121.74. The response time of the sensors was 3 seconds. Cho et al. [79] demonstrated fast responding ethanol gas sensors composed of p-type $SrTi_{1-x}Fe_xO_3$ (STF) with various Fe compositions deposited over vertically aligned SiO_2 nanorods. The fabricated STF on SiO_2 NRs exhibited gas responses ranging from 74 to 528 for 50 ppm ethanol gas depending on the Fe content with fast response and recovery time. The sensors were fabricated via a lift-off process based on photolithography. Malik et al. [56] reported gas sensors based on CeO_2:WO_3 nanowires grown via aerosol assisted chemical vapor deposition (AACVD) and drop casting. The sensors showed an excellent response of ~ 100 towards 20 ppm of ethanol at 250ºC. Kim et al. [80] reported p-n SnO/SnO_2 heterostructure as a promising gas sensing material for NO_2 sensing. The sensors show excellent response towards 100.86 towards 50 ppm of NO_2 at 150ºC. The sensing materials were synthesized via a facile hydrothermal method at 180ºC for 18 hours. Cai and co-workers [81] demonstrated porous Au nanoparticles (NPs) decorated with In_2O_3 NPs embedded in ZnO nanofibers for NO_2 sensing. The sensing material was synthesized using a facile electrospinning method followed by calcination at 400ºC. The sensors showed a high response of 90 towards 5 ppm of NO_2 at room temperature (RT) in

presence of 80% relative humidity (RH). All these reported scientific works are published in 2023-2024. This makes it clear that the zeal of exploring the metal oxides with tremendous gas sensing potential continues. Consequently, there is a need to explore alternative materials that operate selectively and with high sensitivity at room temperature as substitutes for the currently employed metal oxide gas sensing materials.

In this thesis work, metal oxide sensors were fabricated using aerosol assisted chemical vapor deposition (AACVD). Pristine WO_3 NWs were grown directly on a commercial alumina substrate consisting of a pair of screen-printed interdigitated Pt electrodes (with 300 µm electrode gap) on one side and a platinum resistive heater meander on the back side. In a typical synthesis procedure, 50 mg of tungsten hexacarbonyl $W(CO)_6$ (Sigma Aldrich) was dissolved in a solution of acetone (CAS: 67-64-1) and methanol (CAS: 67-56-1) (3:1). The solution was ultrasonicated to ensure full solubilization. The solution was placed in an ultrasonic bath to generate aerosol. N_2 gas with a flow of 0.5 L/min and 1 L/min was used as a carrier to transport the aerosol to the alumina substrate preheated to 400ºC in a hot wall reactor. Different gas flows are used to obtain different morphologies of WO_3 NWs. The growth process takes approximately 40 minutes. The chamber is left to cool down naturally. The substrates with WO_3 NWs are annealed at 500ºC for 2 hours in a Carbolite CWF 1200 muffle furnace within a synthetic air environment. Annealing helps in removing any carbon residues from the solvents and results in fully oxidized WO_3 NWs. Furthermore, our work provides additional insights into nanowires in gas sensing [82].

Moreover, metal nanoparticle decoration on a plethora of materials was carried out using AACVD. Palladium nanoparticles were incorporated onto MoS_2 sensors using aerosol-assisted chemical vapor deposition (AACVD). The reaction was performed at comparatively low temperature of 250°C. To study the effect of Pd concentration on the sensor responses, two amounts of the palladium precursor were used to decorate MoS_2 sensors. In a typical synthesis procedure, 1 mg and 2 mg of Palladium (II) acetylacetonate (Sigma Aldrich, Spain Spain CAS: 14024-61-4) were dissolved in 5 mL methanol (CAS: 67-56-1). The solution was ultrasonicated to ensure full solubilization. The solution was placed in an ultrasonic humidifier to generate aerosol. N_2 gas with a flow of 0.5 L/min was used as a carrier gas to transport the aerosol to the MoS_2 sensors preheated at 250°C in a hot wall reactor. The deposition time was about 5 min; after that, the chamber was left to cool down naturally.

1.4. Transition Metal Dichalcogenides (TMDs)

The discovery of graphene marked a transformative chapter in science. Graphene stands out as the pioneer among two-dimensional (2D) materials that have captivated the interest of researchers and scientists [49,83]. Graphene's remarkable properties, such as exceptional electrical conductivity [84], mechanical strength [85], and flexibility [86], have spurred intensive research efforts toward its integration into various applications, including gas sensors [87]. In comparison to traditional gas sensors based on metal oxide (MOX) nanostructures, graphene offers several advantages, including a large specific surface area in its atomically thin 2D form [88], high conductivity [84], moderate operating temperatures, and minimal electrical noise [49]. Despite the exciting properties, its zero-bandgap nature limits its application in some areas such as in semiconductor electronics. The exploration of advanced two-dimensional (2D) materials has expanded, leading to a focus on transition metal dichalcogenides (TMDs) for gas sensing applications [89].

TMDs are commonly denoted by the formula MX_2. Here, M refers to a transition metal (TM) atom from group IV to V, and X signifies a chalcogen atom (S, Se, or Te) [90]. Figure 1.6 shows the transition metals (highlighted in blue) and chalcogenides (highlighted in green).

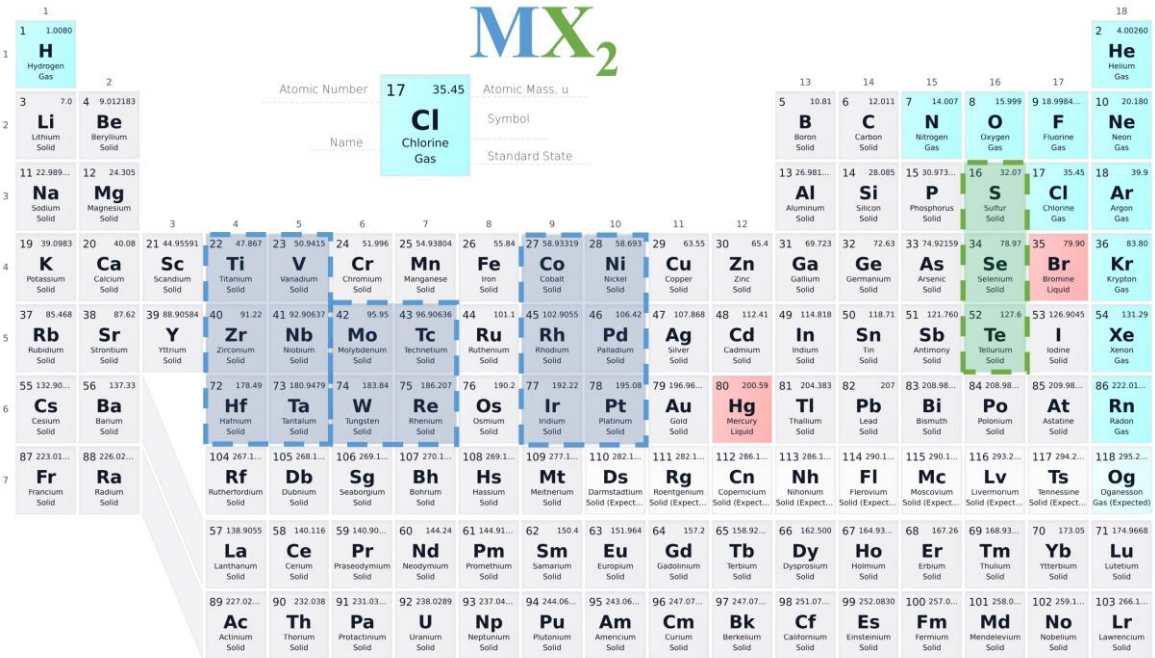

Figure 1.6 In the periodic table, sixteen transition metals and three chalcogen elements (building blocks of the 40 different TMDCs) that form crystalline in 2D layered structures. Partial highlights for Co, Rh, Ir and Ni, because only a few layered structures are observed.

Notable examples of TMDs include molybdenum disulfide (MoS_2) [91–94], molybdenum diselenide ($MoSe_2$) [95–98], tungsten disulfide (WS_2) [66,99,100], and tungsten diselenide (WSe_2) [101,102]. Figure 1.7 illustrates the schematic representation of graphene and typical MX_2 structures.

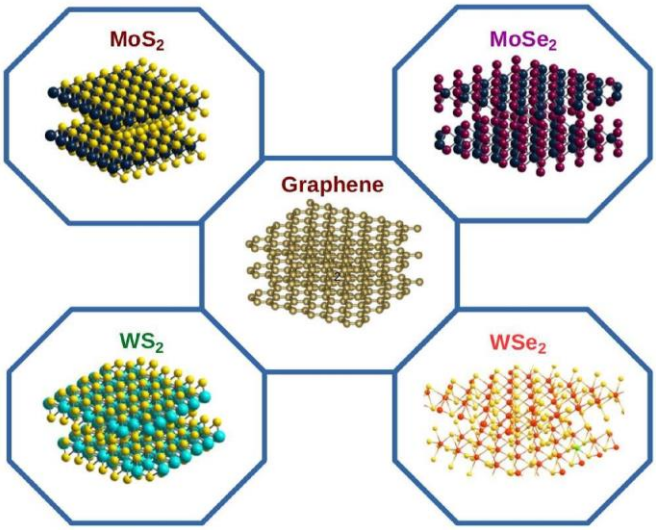

Figure 1.7 The schematic representation of graphene and some TMDs [103].

The layered TMDs adopt the X–M–X configuration, in which the plane of metal atoms separates the two hexagonal planes of chalcogenides [103]. The TMD family comprises over forty different combinations of multi-layered elements, formed through various combinations of transition metals (TMs) and the three chalcogen atoms [103], see Figure 1.6. Due to different coordination spheres of TM atoms, TMDs exhibit different structural phases, commonly defined by trigonal prismatic (2H) or octahedral (1T) TM atom coordination. The diverse electronic behavior of TMDs arises from the gradual filling of the nonbonding d bands by TM electrons, enabling them to exhibit insulating to metallic and semiconducting properties [104,105]. Unlike graphene, single-layered TMDs possess a bandgap. In semiconducting TMDs, transitioning from bulk to monolayer can shift the bandgap from indirect to direct [106]. For example, in the case of MoS_2, a widely studied 2D TMD with the Mo atom sandwiched between two sulfide layers (S–Mo–S) [107,108], the transition from bulk to monolayer changes the indirect band gap (1.9 eV) to a direct one (1.2 eV) [109]. The variable electronic properties, combined with mechanical flexibility and optical sensitivity, make TMDs suitable for diverse applications such as novel semiconductor systems, lightweight wearables, and flexible devices. Hence, these 2D materials offer the potential to overcome selectivity challenges faced by

traditional metal oxide-based sensors, opening new avenues for the development of highly sensitive and specific gas sensing technologies [49,60].

Considering the advantages of TMDs, numerous synthesis techniques have been developed to tailor their properties [110]. Various synthesis methods yield distinct TMDs with diverse properties and applications. These methods fall into two categories: top-down and bottom-up, illustrated in Figure 1.8. The former involves mechanical and chemical exfoliation [111,112], while the latter includes chemical vapor deposition (CVD) [49,66,113] and chemical synthesis [114]. In the top-down approach, MX_2 layers are derived from their bulk form, where intralayer strong covalent bonds and interlayer weak van der Waals (vdW) interactions exist in bulk TMD crystals [115]. This method overcomes vdW forces by applying external energy, such as peeling and ultrasonication, of the bulk crystals, resulting in the development of thin layers. In the Bottom-up method, MX_2 layers are formed on specific substrate materials from elemental precursors. Both techniques have their advantages and disadvantages.

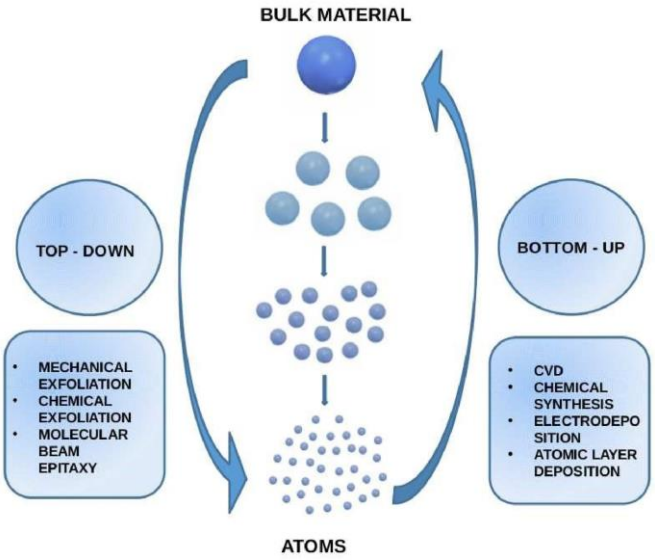

Figure 1.8 Schematic showing the synthesis methods of TMDs, top–down and bottom–up approaches [103].

1.5. Synthesis of TMDs

Mechanical exfoliation

Mechanical exfoliation is a commonly employed technique for creating single or a few layers of nanomaterials from their bulk counterparts. In this method, bulk crystals are either peeled or cleaved using adhesive tape [112]. The "scotch tape method" for thin-layered compounds was initially introduced in 1966 by Frindit, who generated MoS_2 flakes with thickness in the range of a few nanometers [116]. The successful exfoliation of graphene from bulk graphite

opened the door for producing other similar 2D layered materials through the straightforward Scotch tape method [117]. Typically, this method is utilized for synthesizing common monolayer TMDs such as MoS_2 and WS_2 on specific substrates like SiO_2/Si [118,119]. In this process, adhesive tapes peel off the MX_2 layers from their bulk crystals, followed by transferring these layers onto suitable substrates for further device fabrication [120,121]. However, this method is not suitable for massive production because of its poor production yield and its inability to control the thickness, shape, and size of the isolated flakes [115,122].

Chemical exfoliation

Chemical exfoliation (CE) has the potential to overcome the limited production yield associated with mechanical exfoliation. This technique involves ion intercalation and solvent-based techniques [123]. In the CE approach, effective exfoliation of bulk materials is achieved by introducing intercalators into the intermediate layers of the bulk crystal, facilitated by ultrasonication in water [124]. Typically employed intercalators include organometallic compounds such as butyl lithium, naphthyl, and sodium. Jensen et al. used ion intercalation (Morrison method) to exfoliate MoS_2 into monolayers by intercalating with lithium followed by a reaction with water [125]. Also, Zhang et al. proposed a simple yet efficient, rapid, and easily controllable technique for exfoliating semiconductor layers through an electrochemical lithiation discharge process in 2011 [126].

Chemical vapor deposition (CVD)

Chemical Vapor Deposition (CVD) is a highly efficient approach for producing high-quality, thin 2D transition metal dichalcogenides (TMDs) with precise control over morphology, crystallinity, and defects, essential for successful device applications [127]. At elevated temperature and pressure, the substrate is exposed to the reaction precursor. The reaction precursor provides the necessary transition metals (TMs) and chalcogen atoms. After the reaction, the resulting product is deposited onto the substrate material [66,113], yielding atomically thin layered MX_2, such as MoS_2 [128,129], WS_2 [66], $MoSe_2$ [130], and $MoTe_2$ [131]. CVD is a facile and a straightforward synthesis of 2D TMDs. Various CVD-based synthesis techniques have been applied to prepare different 2D TMDs. However, a challenge associated with the CVD method is the need to transfer nanosheets from the deposited substrates for further analysis. Additionally, the higher production cost presents another limitation.

To address the limitations of the Chemical Vapor Deposition (CVD) process in synthesizing Transition Metal Dichalcogenides (TMDs), this thesis introduces an in-house CVD reactor designed to operate at atmospheric conditions without the need for hydrogen. The atmospheric pressure CVD system not only enables the direct growth of TMDs on substrates but also facilitates their synthesis in powder form, which can subsequently be deposited onto any desired substrate. A hydrogen-free Atmospheric Pressure Chemical Vapor Deposition (APCVD) technique was utilized to produce WS2 with a yield in the range of hundreds of milligrams, demonstrating the potential for scalability through an innovative synthesis approach. The process involved use of commercially available tungsten trioxide powder from Sigma Aldrich (CAS: 1314-35-8), which was sulfurized to yield edge enriched WS2 nanostructures in powder form. The sulfurization reaction took place at 900°C for 60 minutes, employing metallic sulfur from Sigma Aldrich (CAS: 7704-34-9) in a custom tube-in-tube setup with a temperature gradient. The schematic of the setup is depicted in Figure 1.9.

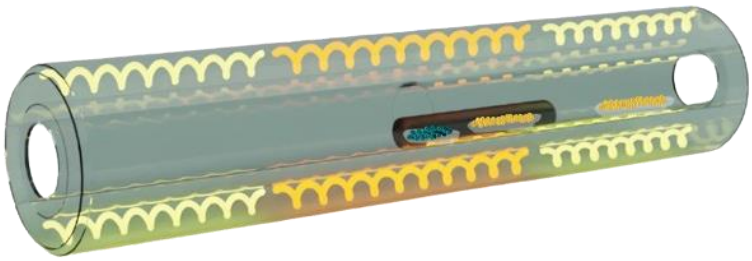

Figure 1.9 Schematic of APCVD furnace.

The furnace, with a bright orange-colored heater coil indicating the set temperature of 900°C in the middle zone, was programmed to heat up from room temperature with a ramp of 40°C/min. Three corundum boats were strategically placed in different temperature zones: one boat contained 100 mg of WO_3 precursor powder, and the other two boats each containing 1 g of sulfur. The boat with WO_3 and a sulfur-containing boat were positioned inside a semi-sealed secondary quartz tube within the 900°C temperature zone. The boat outside the secondary quartz tube was placed upstream of argon flow within the larger quartz tube.

Before the sulfurization process, the quartz tube was flushed with 100 mL/min of Ar to eliminate oxygen. The Ar flow rate during the reaction was maintained at 30 mL/min. Once the furnace reached 900°C, the external quartz tube was carefully positioned so that the sulfur boat, initially located outside the furnace, entered the 400°C temperature zone of the furnace. This strategic arrangement of the boats created a sulfur-rich environment, ensuring the complete

sulfurization of WO_3. The parameters of argon flow rate, ramp-up temperature, reaction time, and sulfur quantity were crucial considerations. After the reaction, the furnace was allowed to cool naturally.

Molecular Beam Epitaxy (MBE)

Molecular Beam Epitaxy (MBE) is used for production of large-area and high quality epilayers of TMDs. This is owed to ultra-high vacuum used during the MBE process [132,133]. MBE stands out for its ability to provide crucial capabilities, allowing for meticulous control over the composition, thickness, structural phases, and other characteristics of TMDs. The precision makes MBE an ideal technique for exploring new investigating technological applications and dig deeper into basic properties of TMDs that hold the potential for intriguing practical uses. The production of epitaxial TMDC films using MBE initiated approximately two decades ago [130]. Despite its precision in controlling material characteristics, molecular beam epitaxy (MBE) has limitations due to slow deposition rates, making it less suitable for large-scale production. Additionally, the ultra-high vacuum requirements and complexity of the MBE system can lead to increased operational and maintenance challenges.

Solution based methods

Solution-phase techniques exhibit potential for the scalable production, functionalization, and hybridization of 2D transition metal dichalcogenides and nanosheets, leading to an extensive exploration of 2D materials for various applications [134,135]. These methods are employed to fabricate large lateral-sized 2D TMDs nanomaterial flakes, such as MoS_2, $MoSe_2$, WS_2, WSe_2, with precise layer-to-layer control [125,136]. Solution-based methods offer several advantages compared to alternative approaches for generating 2D material nanosheets, including the use of cost-effective precursors, scalability for large-scale production, straightforward sorting and separation, easy adjustment of size and thickness, and excellent solubility. This creates a versatile platform for chemical functionalization, enhancing electrical, mechanical, and chemical properties when combined with other materials in solution, and facilitating the convenient transfer of 2D nanosheets in solution [137,138].

1.6. Properties of TMDs

1.6.1. Structural properties

Layered transition metal dichalcogenides share structural similarity with graphite, exhibiting individual monolayers with thicknesses ranging from 0.6 to 0.7 nm. The layers in the TMDs

are held together by an interlayer covalent bond and intralayer weak van der Waals force, forming stacked sandwiched X-M-X layers.

The length of the M-X bond depends on the sizes of both the transition metal and chalcogen ions, ranging approximately from 3.15 Å to 4.03 Å [139]. The TMDs formed can either be layered or non-layered, depending on whether the transition metal belongs to group IV-VII or VIII-X, respectively, in the periodic table [140]. The structural phases of 2D TMDs are classified as tetragonal-1T (octahedral) or hexagonal-2H (trigonal prismatic) based on the arrangement of atoms [140].

The 1T and 2H phases can be further categorized according to the stacking order of each monolayer. In the 2H phase, the top view displays hexagonal symmetry, and the monolayer adopts the X-M-X form, with each transition metal atom covalently bonded to six neighbouring X atoms. In the T phase, the chalcogen atom forms trigonal and triagonal antiprism arrangements at the top and bottom single layers, resulting in a hexagonal arrangement of atoms when viewed from the top. Distortion or dimerization of transition metal atoms in the z direction modifies the displacement of X atoms in the same direction, giving rise to the T' phase.

Thermodynamically stable TMDs formed by the combination of transition metals (from group 4, 5, 6, 7, 9, and 10) with chalcogen atoms (S, Se, and Te) can exist in either 2H or 1T phases, while all others are considered metastable phases. The selection of specific phases by 2D TMDs is determined by the number of electrons in the d-orbital [141,142].

1.6.2. Electronic and optical properties

The most interesting and attractive aspects of 2D TMDs lie in their diverse electronic properties, ranging from semiconductor to superconductor based on their chemical composition. Depending on the material, monolayer TMDs exhibit a broad spectrum of bandgaps extending from the visible to the infrared range [143,144]. Figure 1.10 illustrates the crystal structures and bandgaps of 2D materials [145]. Due to the quantum mechanical confinement of atoms and variations in the hybridization of atomic orbitals of transition metals (TMs) and chalcogenides, reducing the bulk form into a thin monolayer leads to a corresponding change in the electronic band structure from indirect to direct bandgap [146] (e.g., MoS_2, $MoSe_2$, and $MoTe_2$, while some, like GaSe, $ReSe_2$, and a few others, exhibit certain exceptions [147].

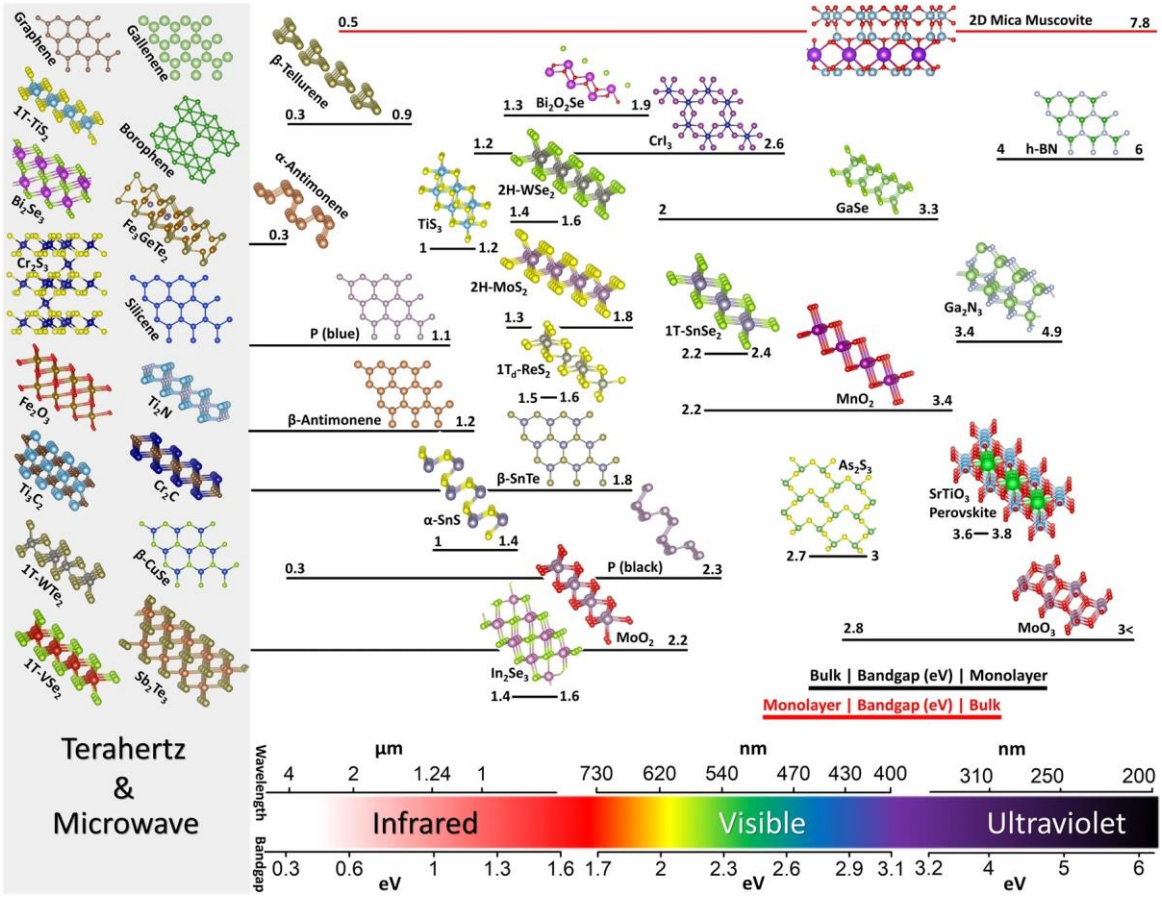

Figure 1.10 Selected family of 2D materials and their bandgaps [145].

2D TMDs such as $MoSe_2$, MoS_2, and WS_2 formed specifically by group 6 TMs are semiconductors in the 2H phase of these monolayers (hexagonal space group: p6m2), possessing hexagonal symmetry in both real and reciprocal space, akin to graphene [148]. Compared to the TMs of 2D TMDs, the influence of the chalcogen atom on the electronic structure is relatively small. Nevertheless, an increase in the atomic number of chalcogens can reduce the broadening of the d band [149]. In 2D materials, electronic properties and applications are defined by the bandgap. Altering thickness [150], doping [151], mechanical deformations [152], and defects engineering [153] are commonly employed methods to modify their bandgap. First principle calculations [154] predict that doping with TMs (such as Ti, Pt, Ni, and Pd) changes the Fermi level of MoS_2. If the shift is towards the positive (or negative) side, the TM + MoS2 transforms into an n-type (or p-type) semiconductor. Similarly, the creation of a metal vacancy in pure 2D $MoSe_2$ changes its semiconducting nature to metallic [155].

The electronic band structure dictates the optical characteristics of TMDs. 2D TMDs possessing direct bandgaps find extensive use in the production of optical components and optoelectronic devices, primarily owing to their band gap falling within the visible region of the electromagnetic spectrum [156]. Techniques such as UV–Vis spectroscopy, Photoluminescence (PL), and Raman spectroscopy are employed to explore the optical attributes of TMDs. The interaction between intermediate layers induces a transition from an indirect bandgap to a direct one. This shift is instrumental in reducing the TMDs from multiple layers to a single layer, rendering them optically active [157]. Notably, TMDs like MoS_2 and $MoTe_2$ exhibit robust PL properties in the visible and near-infrared regions [157]. The optical absorption spectra of TMDs are characterized by strong excitonic peaks due to the Coulomb interaction between electrons and holes [158]. The presence of spin-valley coupling in these materials results in valley-specific optical transitions, offering potential in valleytronics [159]. Additionally, TMDs display remarkable nonlinear optical properties, such as second-harmonic generation and two-photon absorption, enhancing their utility in nonlinear optics and photodetection [160]. The ability to tune their optical properties by varying the thickness and composition further expands the potential applications of TMDs in optoelectronic devices, including photodetectors, light-emitting diodes, and solar cells.

1.6.3. Mechanical properties

Similar to graphene, TMDs exhibit remarkable mechanical strength and flexibility. In the realm of 2D materials, the mechanical properties are significantly influenced by crystal defects and synthesis techniques [161,162]. The strong covalent bond between atoms within the same plane of 2D TMDs imparts robust mechanical characteristics to these materials. Assessing the mechanical properties of 2D materials is challenging due to their non-equivalent deformation. Atomic Force Microscopes (AFM) are crucial tools widely utilized to investigate the mechanical features of 2D materials, including parameters like Young's modulus, pretension, and strain. The pretension of 2D materials depends on both intrinsic mechanical properties and fabrication methods. Semiconducting TMDs, particularly those with metal atoms from group 6, show promise for flexible optoelectronic devices [163]. Studies indicate that increasing the number of layers in MoS_2 reduces the material's Young's modulus due to interlayer stacking errors [161]. Bertolazzi et al. [118] experimentally determined a single-layer's stiffness and breaking strength using AFM, yielding values of 270 ± 100 GPa and 23 GPa, respectively. DFT simulations [163] reveal a linear relationship between mechanical properties and charge transfer, confirming the influence of chemical composition. Chalcogens paired with tungsten

exhibit greater strength than those with molybdenum, attributed to strong hybridization between the vacant p-orbital of chalcogen and the d-orbital of the metal.

1.7. TMDs applications

Given the remarkable electronic, mechanical, and optical properties exhibited by Transition Metal Dichalcogenides (TMDs), their applications extend beyond conventional materials. TMDs have garnered significant attention in various fields, owing to their unique combination of properties. From advanced semiconductor devices to cutting-edge optoelectronic components, the versatility of TMDs is harnessed to push the boundaries of innovation. Their exceptional electronic conductivity, mechanical strength, and optical characteristics pave the way for applications in electronic devices, sensors, and even emerging technologies like quantum computing. As researchers delve deeper into the potential of TMDs, the range of applications continues to expand, showcasing their pivotal role in shaping the landscape of modern materials science and technology.

1.7.1. Optoelectronic devices

TMDs are a promising candidate for optoelectronic applications owing to their broad range of bandgap energy (1.1 to 2.1 eV), and high charge transfer [164]. One of the main domains of TMDs based optoelectronic devices is photodetectors. TMD-based photodetectors take advantage of the strong light-matter interaction in these materials [165]. The direct band gap in monolayer TMDs enhances their sensitivity to light, making them suitable for high-performance photodetectors. Photocurrent is generated when TMDs absorb photons, and this can be utilized in applications such as imaging, communication systems, and light sensing [166]. Hu et al. [167] reported electret/TMD hybridized devices by vertically coupling a MoS_2 channel and the PTFE film, which reveals an optimized photodetection behavior. Utilizing the corona charging method, negative charges were induced in the PTFE layer, mirroring the effect of applying a negative bias to the MoS_2 channel rather than using the conventional voltage-driven back gate. With a charging voltage of −6 kV, PTFE/MoS_2 devices exhibit enhanced photodetection performance and a faster recovery speed compared to their bare MoS_2 counterparts.

1.7.2. Energy storage devices

Monolayered 2D transition metal dichalcogenides (TMDs) are commonly employed in electrochemical energy storage devices such as Li-ion batteries and supercapacitors. However,

certain pristine TMD nanosheets face limitations in supercapacitor applications due to their low conductivity and specific capacitance. In addressing this challenge, heterostructures or hybrids incorporating 2D TMDs emerge as promising candidates for energy storage applications [168,169]. Given that electrochemical reactions are highly reliant on surface and interface properties, the layered structure, substantial surface-to-volume ratio, and numerous active sites make 2D TMDs and their heterostructures preferable materials. A notable example involves the use of a heterostructure consisting of vertically aligned MoS_2 and electrochemically exfoliated graphene, serving as an anode material for Lithium-ion batteries [170]. An electrode composition named EG-MoS_2, comprising 95 wt% MoS_2, demonstrated exceptional performance, achieving an ultrahigh specific capacity of 1250 $mAhg^{-1}$ after 150 stable cycles at 1 Ag^{-1}. It also exhibited remarkable rate performance, delivering 970 $mAhg^{-1}$ at 5 Ag^{-1}.

1.7.3. Photovoltaic applications

Atomically thin two-dimensional materials are favoured for their robust light-matter interactions, adjustable optical bandgaps, and exceptional surface, structural, and electronic characteristics [171]. Moreover, they exhibit high efficiency in solar energy conversion while requiring only a minimal amount of active absorber material. The variable band gap of transition metal dichalcogenides (TMDs), spanning from metallic to insulator in the visible region, facilitates the creation of innovative photovoltaic devices. Semiconducting single-layer TMDs like MoS_2, $MoSe_2$, and WS_2, each with a thickness less than 1 nm, absorb approximately 1–5% of incident sunlight [172], closely aligning with organic-organic solar cell interfaces [173]. Significantly, these materials surpass traditional semiconductors like Ga, As, and Si in sunlight absorption capability. In the context of a typical solar cell, comprising a junction of two materials with opposing charge carriers, the separation of photogenerated electron-hole pairs occurs, leading to the manifestation of the photovoltaic effect [174].

1.7.4. Biosensing applications

Biosensors, crucial for detecting biological elements or biomolecules, find extensive applications in industries, medicine, and agriculture. The growing demand for biomolecule sensing, spanning nitrobenzene, catechol, ammonia, and volatile organic chemicals, has prompted the development of new nanomaterials as sensing substrates. Transition metal dichalcogenides (TMDs), renowned for their exceptional properties, are emerging as prime materials for sensing, particularly in biosensing applications [175,176]. Their high surface area

and interplanar weak van der Waals (vdW) interactions are pivotal characteristics that render them efficient biosensors. Furthermore, the tunability of their surface leads to variations in structural and electronic properties.

In 2017, Yan et al. [176] pioneered the development of highly sensitive MoS_2 nanosheets through ultrasound exfoliation for detecting DNA molecules. Other TMDs, such as $MoSe_2$, WS_2, and TiS_2, have also been employed for the rapid detection of DNA [177]. The sensing capabilities of 2D TMDs can be enhanced through various methods [103], including doping, defect induction, and hybridization. DFT calculations predict that biomolecules like nitrobenzene and catechol exhibit negligible adsorption on the surface of pristine 2D MoS_2 substrates. However, when MoS_2 is doped with transition metals, its sensing ability increases [178]. This can be owed to effective charge transfer between the biomolecule and the decorated metal d-orbitals. Research indicates that Ti-doped MoS_2 holds promise as a potential biosensor. Similarly, Li-doped MoS_2 is well-suited for the detection of nucleobases [103]. TMDs have proven successful as optical, electrochemical, and electronic biosensors, enabling the detection of various biomolecules such as nucleic acids, proteins, and glucose. A recent study focused on four common TMD nanosheets (WS_2, MoS_2, WSe_2, and $MoSe_2$) and devised a sensitive, label-free colorimetric sensing approach for DNA detection based on TMD nanosheet's distinctive affinity for single-strand and double-strand DNA [103].

1.7.5. TMDs based gas sensors

With the continuous expansion of the economy, there is an ever increasing need to develop sensors that are not only energy-efficient, inexpensive, and compact but also possess high reliability and portability. These sensors must exhibit a heigh sensitivity and selectivity to align with the requirements of emerging technologies like the Internet of Things (IoT) and smart devices in the next generation. The increased demand for small, cost-effective gas sensors has instigated a surge in the exploration of innovative materials. Transition metal dichalcogenides (TMDs), with graphene like properties, have emerged as promising candidates for the next wave of gas-sensitive materials. Notably, recent demonstrations of the scalable synthesis of 2D TMDs have revealed the potential to produce low-cost sensors. Moreover, these materials have ignited a research zeal for the advancement of flexible and wearable electronics in the future. For chemoresistive gas sensors, 2D edge-enriched, vertically oriented TMDs exhibit excellent gas sensing properties [49][102]. However, their synthesis in an out-of-plane direction presents a daunting challenge. Indeed, the complex process of growing gas sensitive TMDs materials

demands innovative and precision-based synthesis techniques. One of the main obstacles lies in achieving uniform, reproducible and continuous deposition [49]. To overcome these challenges, Alagh et al. [66] reported hydrogen and alkali halide free direct growth of continuous and vertically oriented WS_2 nanotriangles on standard ceramic transducers. The authors reported a two-step CVD process by combining AACVD and APCVD for the direct growth of WS_2 to be used in chemoresistive sensors. Concurrently, the authors reported the occurrence of WO_3 impurities suggesting an incomplete sulfurization.

Duesberg and team synthesized MoS_2 patterns showcasing a high-sensitivity detection of NH_3 with a limit of detection (LOD) at the parts per million (ppm) level [179]. Zhou and colleagues reported a Schottky-contact MoS_2 chemical sensor responsive to NO_2 and NH_3, demonstrating detection capabilities down to 20 parts per billion (ppb) and 1 ppm, respectively [180]. Zhang and team investigated the performance of MoS_2 gas sensors concerning NO based on their thickness, revealing insights into the sensor's behavior [111]. At room temperature (RT), the MoS_2 p-n junction sensor displayed superior sensitivity and selectivity to NO_2 compared to sensors based on individual n-type or p-type MoS_2 [10]. Zhou et al. [181] explored the impact of the number of WS_2 layers on the ability to detect gases by examining the layer-dependent sensing performance of WS_2-based gas sensors. The fabricated gas sensors were based on WS_2 in both monolayer and multilayer configurations and methodically evaluated their response to various gases, including NO_2, CO, NH_3, and CH_4 at room temperature and 50°C.

However, despite all the above-stated sensing properties, pristine TMDs show poor gas sensing response at room temperature, this is due to the strong adsorption of gas molecules on the TMDs surface which leads to partial desorption of these molecules during the recovery cycle, resulting in much longer response time with low sensing response. Hence, limiting the practical applications of pristine TMDs based gas sensors in the real environment [65]. To overcome the challenges associated with pristine TMDs, researchers have turned to heterostructures of transition metal dichalcogenides (TMDs) for gas sensing applications. The combination of multiple TMD layers or the integration of TMDs with other materials creates a platform that can overcome limitations such as low stability, limited operating temperature range, and reduced selectivity. The utilization of TMD heterostructures presents a promising avenue for advancing the capabilities of gas sensors, paving the way for more efficient and versatile sensing technologies. Alagh et al [65] reported PdO and PtO loaded tungsten disulfide growth on alumina substrates. The sensing material was fabricated through a two-step process.

Initially, metal oxides (PtO, PdO and WO_3) were grown using AACVD, followed by the second step involving APCVD to sulfurize WO_3 into WS_2. The metal oxide loaded sensors showed reproducible, ultrasensitive and enhanced responses towards NO_2 with LoD of 25 ppb. Liang et al. [182] reported the flower-like composites of MoS_2/WS_2 synthesized through a straightforward one-pot hydrothermal method, demonstrating effective NO_2 detection at room temperature. The WS_2 molecules prefer to grow on the edge of as- nucleated MoS_2 to form the MoS_2/WS_2 nanosheets, and then they can grow by layer-by-layer self-assembly to form the MoS_2/WS_2 heterostructure. The optimized MoS_2/WS_2 heterostructure composite displayed remarkably high sensitivity to NO_2 at room temperature, showcasing a combination of elevated response, reliable reproducibility, exceptional selectivity, and long-term stability. Notably, the MoS_2/WS_2 composite exhibited responses ($\Delta R/R_g$) of 6.1% and 23.1% to 5 ppb and 100 ppb NO_2, respectively. Table 1.2 summarizes recent developments and results in transition metal dichalcogenide based gas sensors.

The challenges associated with TMDs synthesis methods as mentioned above, such as direct growth at high temperatures leading to low yields and impracticality for flexible substrates. The techniques are promising for developing gas sensors at the laboratory scale; however, the techniques may not be scaled up to industrial level. This prompted the development of an alternative approach during this thesis: the airbrushing method. The advantage lies in the precision with which the material can be deposited onto various surfaces, including flexible substrates. TMDs sensing films were deposited, via a home-made airbrush system, onto commercial alumina transducer substrates (Ceram Tech GmBH, Germany), which have Pt-interdigitated electrodes with a gap of 300 µm on the front side and Pt-resistive heater meander on the back side. The electrode area was 2.5 mm × 5.1 mm. Prior to their coating with TMDs, substrates were cleaned by sequential sonication in acetone, ethanol, and deionized water followed by blow drying with nitrogen. After that, the cleaned substrates were placed in the hotplate of our home-made airbrushing system, which is composed of a commercial air brush, a hotplate, a multimeter and connectors. Figure 1.11 illustrates our in-house built airbrushing system.

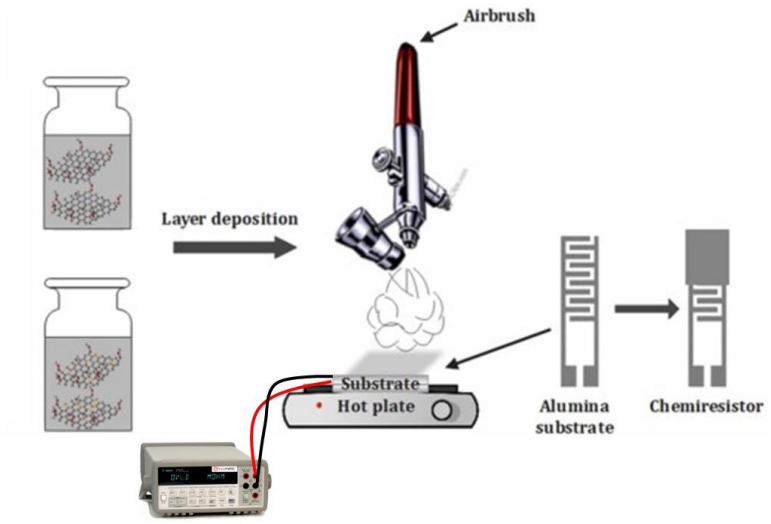

Figure 1.11 In-house built airbrushing system.

Desired TMDs powder was sonicated in absolute ethanol (Scharlab, CAS: 64-17-5) for a particular time to yield a suspension. It is worth noting that the airbrushing technique allows us to use the solvent of choice, during this thesis, absolute ethanol was used to keep the thin film deposition temperature to the minimum possible value, owing to its low boiling point. Next, the obtained solution was transferred to the airbrush container, the electrodes of the substrate transducers were connected to the multimeter, in order to control the resistance of the deposited films and the hotplate was turned on and set at 55 ºC. Finally, the solutions were airbrushed onto the alumina substrates using N_2 gas as a carrier. It is worth mentioning that this technique allows us to deposit thin films of the functional material over virtually any type of application substrate. Airbrushing deposition was tested over polymethyl methacrylate (PMMA), Kapton, silicon and glass substrates. The adhesion and quality of the deposited films on the substrates was found to be excellent.

In order to decorate the sensing films deposited via airbrushing system with palladium nanoparticles, AACVD was used at low temperatures. Palladium nanoparticles were incorporated onto the fabricated MoS_2 sensors using aerosol-assisted chemical vapor deposition (AACVD). The reaction was performed at comparatively low temperature of 250°C. To study the effect of Pd concentration on the sensor responses, two amounts of the palladium precursor were used to decorate MoS_2 sensors. In a typical synthesis procedure, 1 mg and 2 mg of Palladium (II) acetylacetonate (Sigma-Aldrich, Madrid, Spain CAS: 14024-61-4) were dissolved in 5 mL methanol (CAS: 67-56-1). The solution was ultrasonicated to ensure full solubilization. The solution was placed in an ultrasonic humidifier to generate aerosol. N_2 gas

with a flow of 0.5 L/min was used as a carrier gas to transport the aerosol to the MoS_2 sensors preheated at 250°C in a hot wall reactor. The deposition time was about 5 min; after that, the chamber was left to cool down naturally.

Table 1.2 Recent developments in Transition Metal Dichalcogenides based gas sensors.

Material	**Synthesis**	**Transducing scheme**	**Target Gas**	**Range**	**LoD**	**Response intensity**	**Response time**	**Selectivity**	**Stability**	**Humidity**	**Operating Conditions**	**Ref.**
2D WS_2	Liquid phase exfoliation	Cata-luminescence	H_2S	0.3-6 ppm	N/A	10,000 @ 5 ppm	ms	yes	1 week	N/A	187 ºC	[183]
$CNT+WS_2$ or MoS_2	Commercially available	Chemoresistor	NO_2	0.1-10 ppm	0.1 ppm	10% @ 2 ppm	tens of min to hours	yes	N/A	N/A	150 ºC	[184]
Schottky contact +MoS_2	CVD	Chemoresistor	NO_2 (Al) ; $CO+CO_2$ (Ag)	10 ppm	N/A	80% @ 10 ppm	tens of min	No	N/A	20% constant	60 ºC Measured in N_2 background	[185]

WSe_2	Ti_3C_2Tx/WSe_2	WSe_2/WS_2 MoS_2/WSe_2	**Materials**
Liquid phase exfoliation	Liquid phase exfoliation	CVD and ALD	**Synthesis**
Chemoresistor	Chemoresistor	Chemoresistor	**Transducing scheme**
DMMP	EtOH	NO_2 and NH_3	**Target Gas**
10-500 ppm	1-40 ppm	50-500 ppm	**Range**
10 ppm	N/A	N/A	**LoD**
8,91% @10 ppm	9% @40 ppm	150% @ 500 ppm NH_3 300% @ 500 ppm NO_2	**Response intensity**
tens of min	sec	tens of min	**Response time**
yes, VOCs and water, NO_2 or NH_3 not tested.	No (alcohols, aromatics)	yes	**Selectivity**
7 weeks	30 days	N/A	**Stability test**
N/A	Response drops by 50% when moisture changes from dry to 80% RH	N/A	**Humidity**
RT	RT	RT and white light activation N_2 background	**Operating Conditions**
[188]	[187]	[186]	**Ref.**

ZnO NRs/WS_2	VS_2	WS_2–WO_3	MoS_2/rGO	**Materials**
Liquid phase exfoliation and microwave-irradiation-assisted solvothermal	Liqui phase exfoliation	Mechanical exfoliation	Hydrothermal	**Synthesis**
Chemoresistor	Chemoresistor	Chemoresistor	Chemoresistor	**Transducing scheme**
H_2S	NH_3	NO_2	HCHO	**Target Gas**
0.1-5 ppm	1-10 ppm	0.05-5 ppm	1-50 ppm	**Range**
N/A	N/A	N/A	N/A	**LoD**
100% @ 3 ppm	257% @ 10 ppm	16% @ 5 ppm	64% @10 ppm	**Response intensity**
sec to min	tens of min	sec to min	sec to min	**Response time**
yes	N/A	N/A	No (alcohols, ammonia)	**Selectivity**
6 months	2 weeks	6 months	90 days	**Stability test**
Slight drop in response in humid conditions	Response drops with moisture level	Resilient	Response drops with moisture level	**Humidity**
250 ºC	40ºC	RT	RT + visible light	**Operating Conditions**
[192]	[191]	[190]	[189]	**Ref.**

Au-MoS_2	WS_2/WO_3	WS_2/SnO_2	WS_2	Flower WS_2	**Materials**
Hydrothermal	Hydrothermal	Liquid phase exfoliation	Liquid phase exfoliation	Chemical vapour transport	**Synthesis**
Chemoresistor	Chemoresistor	Chemoresistor	Chemoresistor	Chemoresistor	**Transducing scheme**
CO	NO_2	NO_2	NO_2	H_2S	**Target Gas**
N/A	2-50 ppm	0.5-20 ppm	2-10 ppm	10-150 ppm	**Range**
N/A	1 ppm	N/A	N/A	N/A	**LoD**
20% @ 10 ppm	6,600% @ 10 ppm	400% @ 5 ppm	27% @ 10 ppm	153% @ 50 ppm	**Response intensity**
tens of min to hours	tens of min to hours	sec to min	sec to min	sec to min	**Response time**
N/A	not responding to H_2 nor CO	Cross-responsive to EtOH	Cross-responsive to NH_3	No, SOF_2, SO_2, SO_2F_2	**Selectivity**
N/A	N/A	30 days	N/A	N/A	**Stability test**
N/A	N/A	Resilient. 25% drop for 0 to 80%RH	N/A	N/A	**Humidity**
RT	200 ºC	RT, UV light	RT	200 ºC	**Operating Conditions**
[196]	[49]	[195]	[194]	[193]	**Ref.**

Pd-WS_2 or Pt-WS_2	WS_2	WS_2-SnO_2 QDs	Co–Zn doped MoS_2/graphite	**Materials**
CVD	CVD	Liquid phase exfoliation	Wet chemistry synthesis of Zn and Co NPs and impregnation onto commercial MoS_2	**Synthesis**
Chemoresistor	Chemoresistor	Chemoresistor	Chemoresistor	**Transducing scheme**
H_2	NO_2	NH_3	NO_2	**Target Gas**
10-1000 ppm	0.05-0.8 ppm	0.1-10 ppm	0.05-5 ppm	**Range**
5 ppb	5 ppb	10 ppb	6.2 ppb	**LoD**
30% @ 100 ppm	5,500% @ 0,8 ppm	850% @ 10 ppm	60% @ 1 ppm	**Response intensity**
min	min	tens of min to hours	min	**Response time**
cross-responsive to NO_2	cross-responsive to H_2S	ten times lower response to NO_2	cross-sensitive to NH_3	**Selectivity**
6 weeks	8 months	8 weeks	50 days	**Stability test**
Resilient to humidity	50% drop or response at 50% RH	N/A	Affected by humidity for high moisture levels	**Humidity**
150 ºC and RT	150 ºC	RT blue light	RT	**Operating Conditions**
[65]	[66]	[198]	[197]	**Ref.**

MoS_2/ZnO	ReS_2	WSe_2	MoS_2	Cu_2O-WS_2	**Materials**
microwave-hydrothermal	Colloidal synthesis	CVD	CVD	CVD	**Synthesis**
Optical	Electrochemical	Chemoresistor	Chemoresistor	Chemoresistor	**Transducing scheme**
NO_2	NH_3	NO_2 NH_4	NO_2 NH_3	H_2S	**Target Gas**
10-200 ppb	20,000 ppm	0.02-0.8 ppm 2-10 ppm	0.02-0.8 ppm 2-10 ppm	40 ppm	**Range**
0.1 ppb	NA	100 ppb 1 ppm	5 ppb 100 ppb	34 ppb	**LoD**
226% @ 0.2 ppm	3,500% @20,000 ppm	20% @0.8 ppm 16% @ 10 ppm	65% @0.8 ppm 11% @ 10 ppm	138% @ 40 ppm	**Response intensity**
sec to min	sec to min	min	sec to min	min	**Response time**
N/A	No (water, O_2, …)	dually selective via oper temp	dually selective via oper. temp	selective	**Selectivity**
N/A	N/A	4 months	3 months	7 months	**Stability test**
34% decrease in 80% humid air	cross-sensitive	Resilient to humidity	Resilient to humidity	Resilient to humidity	**Humidity**
RT and NIR excitation	RT Measured in N_2	100 ºC 150 ºC	100 ºC RT	RT	**Operating Conditions**
[201]	[200]	[102]	[49]	[199]	**Ref.**

$PdSe_2$	$Re_{0.5}Nb_{0.5}S_2$	WS_2/GeSe/WS_2	1T/2H heterophase MoS_2	WS_2/IGZO	**Materials**
CVD	Chemical vapour transport	Mechanical exfoliation and multiple transfers of flakes using	Li-ion intercalation exfoliation	CVD and PMMA stamp transfer	**Synthesis**
Transistor	Transistor	Transistor	Transistor	Transistor	**Transducing scheme**
NO_2	NO_2	NH_3	NO_2	NO_2	**Target Gas**
0.1-5 ppm	0.05-15 ppm	25-200 ppm	0.025-10 ppm	1-300 ppm	**Range**
100 ppb	N/A	N/A	25 ppb	30 ppb	**LoD**
18% @1 ppm	32% @ 1 ppm	9% @ 25 ppm	25% @2 ppm	30,000% @10 ppm	**Response intensity**
tens of min to hours	tens of min	ms	sec to min	tens of min	**Response time**
yes	yes	No	yes	N/A	**Selectivity**
4 months	N/A	N/A	N/A	N/A	**Stability test**
N/A	40% high response increase to NO_2	N/A	N/A	N/A	**Humidity**
RT	RT	RT and red light. Measured in vacuum	RT	RT	**Operating Conditions**
[206]	[205]	[204]	[203]	[202]	**Ref.**

References

[1] H. Yang, X. Huang, D.M. Westervelt, L. Horowitz, W. Peng, Socio-demographic factors shaping the future global health burden from air pollution, Nat. Sustain. 6 (2023) 58–68. https://doi.org/10.1038/s41893-022-00976-8.

[2] K. Nansai, S. Tohno, S. Chatani, K. Kanemoto, S. Kagawa, Y. Kondo, W. Takayanagi, M. Lenzen, Consumption in the G20 nations causes particulate air pollution resulting in two million premature deaths annually, Nat. Commun. 12 (2021) 6286. https://doi.org/10.1038/s41467-021-26348-y.

[3] G.-P. Bălă, R.-M. Râjnoveanu, E. Tudorache, R. Motișan, C. Oancea, Air pollution exposure—the (in)visible risk factor for respiratory diseases, Environ. Sci. Pollut. Res. 28 (2021) 19615–19628. https://doi.org/10.1007/s11356-021-13208-x.

[4] H. Khreis, K.A. Sanchez, M. Foster, J. Burns, M.J. Nieuwenhuijsen, R. Jaikumar, T. Ramani, J. Zietsman, Urban policy interventions to reduce traffic-related emissions and air pollution: A systematic evidence map, Environ. Int. 172 (2023) 107805. https://doi.org/10.1016/j.envint.2023.107805.

[5] H.M. Tran, F.-J. Tsai, Y.-L. Lee, J.-H. Chang, L.-T. Chang, T.-Y. Chang, K.F. Chung, H.-P. Kuo, K.-Y. Lee, K.-J. Chuang, H.-C. Chuang, The impact of air pollution on respiratory diseases in an era of climate change: A review of the current evidence, Sci. Total Environ. 898 (2023) 166340. https://doi.org/10.1016/j.scitotenv.2023.166340.

[6] K. Sun, G. Zhan, L. Zhang, Z. Wang, S. Lin, Highly sensitive NO2 gas sensor based on ZnO nanoarray modulated by oxygen vacancy with Ce doping, Sensors Actuators B Chem. 379 (2023) 133294. https://doi.org/10.1016/j.snb.2023.133294.

[7] M.M.M.F. Jion, J.N. Jannat, M.Y. Mia, M.A. Ali, M.S. Islam, S.M. Ibrahim, S.C. Pal, A. Islam, A. Sarker, G. Malafaia, M. Bilal, A.R.M.T. Islam, A critical review and prospect of NO2 and SO2 pollution over Asia: Hotspots, trends, and sources, Sci. Total Environ. 876 (2023) 162851. https://doi.org/10.1016/j.scitotenv.2023.162851.

[8] P. Chawala, S. Priyan R, S.N. SM, Climatology and landscape determinants of AOD, SO2 and NO2 over Indo-Gangetic Plain, Environ. Res. 220 (2023) 115125. https://doi.org/10.1016/j.envres.2022.115125.

[9] D. Zhang, Z. Liu, C. Li, T. Tang, X. Liu, S. Han, B. Lei, C. Zhou, Detection of NO 2 down to ppb Levels Using Individual and Multiple In 2 O 3 Nanowire Devices, Nano Lett. 4 (2004) 1919–1924. https://doi.org/10.1021/nl0489283.

[10] W. Zheng, Y. Xu, L. Zheng, C. Yang, N. Pinna, X. Liu, J. Zhang, MoS 2 Van der Waals p–n Junctions Enabling Highly Selective Room-Temperature NO 2 Sensor, Adv. Funct. Mater. 30 (2020). https://doi.org/10.1002/adfm.202000435.

[11] N. Sun, Q. Tian, W. Bian, X. Wang, H. Dou, C. Li, Y. Zhang, C. Gong, X. You, X. Du, P. Yin, X. Zhao, Y. Yang, X. Liu, Q. Jing, B. Liu, Highly sensitive and lower detection-limit NO2 gas sensor based on Rh-doped ZnO nanofibers prepared by electrospinning, Appl. Surf. Sci. 614 (2023) 156213. https://doi.org/10.1016/j.apsusc.2022.156213.

[12] S. Jain, A. Paliwal, V. Gupta, M. Tomar, Long Range Surface Plasmons assisted highly sensitive and room temperature operated NO2 gas sensor, Sensors Actuators B Chem. 311 (2020) 127897. https://doi.org/10.1016/j.snb.2020.127897.

[13] A. Andringa, J.R. Meijboom, E.C.P. Smits, S.G.J. Mathijssen, P.W.M. Blom, D.M. de Leeuw, Gate-Bias Controlled Charge Trapping as a Mechanism for NO 2 Detection with Field-Effect Transistors, Adv. Funct. Mater. 21 (2011) 100–107. https://doi.org/10.1002/adfm.201001560.

[14] S. Abdulla, T.L. Mathew, B. Pullithadathil, Highly sensitive, room temperature gas sensor based on polyaniline-multiwalled carbon nanotubes (PANI/MWCNTs) nanocomposite for trace-level ammonia detection, Sensors Actuators B Chem. 221 (2015) 1523–1534. https://doi.org/10.1016/j.snb.2015.08.002.

[15] M.S. Nam, J.-Y. Kim, A. Mirzaei, M.H. Lee, H.W. Kim, S.S. Kim, Au- and Pt-decorated Ti3C2Tx MXenes for preparing self-heated and flexible NH3 gas sensors, Sensors Actuators B Chem. 403 (2024) 135112. https://doi.org/10.1016/j.snb.2023.135112.

[16] Q. Hu, Z. Wang, J. Chang, P. Wan, J. Huang, L. Feng, Design and preparation of hollow NiO sphere- polyaniline composite for NH3 gas sensing at room temperature, Sensors Actuators B Chem. 344 (2021) 130179. https://doi.org/10.1016/j.snb.2021.130179.

[17] S. Gai, B. Wang, X. Wang, R. Zhang, S. Miao, Y. Wu, Ultrafast NH3 gas sensor based on phthalocyanine-optimized non-covalent hybrid of carbon nanotubes with pyrrole,

Sensors Actuators B Chem. 357 (2022) 131352. https://doi.org/10.1016/j.snb.2021.131352.

[18] Y. Fu, T. Wang, X. Wang, X. Li, Y. Zhao, F. Li, G. Zhao, X. Xu, Investigation of p-n sensing transition and related highly sensitive NH3 gas sensing behavior of SnPx/rGO composites, Chem. Eng. J. 471 (2023) 144499. https://doi.org/10.1016/j.cej.2023.144499.

[19] X.-Y. Liu, J.-M. Zhang, K.-W. Xu, V. Ji, Improving SO2 gas sensing properties of graphene by introducing dopant and defect: A first-principles study, Appl. Surf. Sci. 313 (2014) 405–410. https://doi.org/10.1016/j.apsusc.2014.05.223.

[20] K.D. Pham, T.-D. Hoang, Q.-T. Nguyen, D.-Q. Hoang, Fe-doped SnSe monolayer: A promising 2D material for reusable SO2 gas sensor with high sensitivity, J. Alloys Compd. 940 (2023) 168919. https://doi.org/10.1016/j.jallcom.2023.168919.

[21] V.R. Naganaboina, S.G. Singh, Graphene-CeO2 based flexible gas sensor: Monitoring of low ppm CO gas with high selectivity at room temperature, Appl. Surf. Sci. 563 (2021) 150272. https://doi.org/10.1016/j.apsusc.2021.150272.

[22] N. Roy, R. Sinha, T.T. Daniel, H.B. Nemade, T.K. Mandal, Highly Sensitive Room Temperature CO Gas Sensor Based on MWCNT-PDDA Composite, IEEE Sens. J. 20 (2020) 13245–13252. https://doi.org/10.1109/JSEN.2020.3004994.

[23] S. Li, X. Wei, S. Zhu, Q. Zhou, Y. Gui, Low temperature carbon monoxide gas sensor based on Co3O4@TiO2 nanocomposites: Theoretical and experimental analysis, J. Alloys Compd. 882 (2021) 160710. https://doi.org/10.1016/j.jallcom.2021.160710.

[24] M.U. Ali, Y. Yu, B. Yousaf, M.A.M. Munir, S. Ullah, C. Zheng, X. Kuang, M.H. Wong, Health impacts of indoor air pollution from household solid fuel on children and women, J. Hazard. Mater. 416 (2021) 126127. https://doi.org/10.1016/j.jhazmat.2021.126127.

[25] J. Zhang, Y. Liu, L. Jiang, S. Lu, F. Wang, X. Chen, A chemiluminescent probe for highly sensitive detection of carbon monoxide in aqueous solution and air, Sensors Actuators B Chem. 351 (2022) 130936. https://doi.org/10.1016/j.snb.2021.130936.

[26] D. Zhang, J. Wu, Y. Cao, Cobalt-doped indium oxide/molybdenum disulfide ternary

nanocomposite toward carbon monoxide gas sensing, J. Alloys Compd. 777 (2019) 443–453. https://doi.org/10.1016/j.jallcom.2018.10.365.

[27] Y.-X. Zhen, B.-Y. Song, W.-X. Liu, J.-X. Ye, X.-F. Zhang, Z.-P. Deng, L.-H. Huo, S. Gao, Ultra-high response and low temperature NO2 sensor based on mesoporous SnO2 hierarchical microtubes synthesized by biotemplating process, Sensors Actuators B Chem. 363 (2022) 131852. https://doi.org/10.1016/j.snb.2022.131852.

[28] K. Wetchakun, T. Samerjai, N. Tamaekong, C. Liewhiran, C. Siriwong, V. Kruefu, A. Wisitsoraat, A. Tuantranont, S. Phanichphant, Semiconducting metal oxides as sensors for environmentally hazardous gases, Sensors Actuators B Chem. 160 (2011) 580–591. https://doi.org/10.1016/j.snb.2011.08.032.

[29] A. Singh, S. Singh, B.C. Yadav, Gigantic enhancement in response of heterostructured CeO2/CdS nanospheres based self-powered CO2 gas sensor: A comparative study, Sensors Actuators B Chem. 377 (2023) 133085. https://doi.org/10.1016/j.snb.2022.133085.

[30] B.S. de Lima, A.A. Komorizono, W.A.S. Silva, A.L. Ndiaye, J. Brunet, M.I.B. Bernardi, V.R. Mastelaro, Ozone detection in the ppt-level with rGO-ZnO based sensor, Sensors Actuators, B Chem. 338 (2021) 129779. https://doi.org/10.1016/j.snb.2021.129779.

[31] Y. Wang, S. Zhang, D. Xiao, S. Wang, T. Zhang, X. Yang, S. Heng, M. Sun, CuO/WO3 hollow microsphere P-N heterojunction sensor for continuous cycle detection of H2S gas, Sensors Actuators B Chem. 374 (2023) 132823. https://doi.org/10.1016/j.snb.2022.132823.

[32] T. Seiyama, K. Fujiishi, M. Nagatani, A. Kato, A New Detector for Gaseous Components Using Zinc Oxide Thin Films, J. Soc. Chem. Ind. Japan. 66 (1963) 652–655. https://doi.org/10.1246/nikkashi1898.66.5_652.

[33] N. Taguchi, Gas-Detecting Device, US3695848, 1972.

[34] G. Neri, The Stannic Oxide Gas SensorPrinciples and Applications, CRC Press, 2017. https://doi.org/10.1201/9780203735893.

[35] K. Ihokura, J. Watson, The Stannic Oxide Gas SensorPrinciples and Applications, CRC

Press, 2017. https://doi.org/10.1201/9780203735893.

[36] G. Wiegleb, J. Heitbaum, Semiconductor gas sensor for detecting NO and CO traces in ambient air of road traffic, Sensors Actuators B Chem. 17 (1994) 93–99. https://doi.org/10.1016/0925-4005(94)87035-7.

[37] G. Wiegleb, Physical-Chemical Gas Sensors, in: Gas Meas. Technol. Theory Pract., Springer Fachmedien Wiesbaden, Wiesbaden, 2023: pp. 215–285. https://doi.org/10.1007/978-3-658-37232-3_4.

[38] M.V. Nikolic, V. Milovanovic, Z.Z. Vasiljevic, Z. Stamenkovic, Semiconductor Gas Sensors: Materials, Technology, Design, and Application, Sensors. 20 (2020) 6694. https://doi.org/10.3390/s20226694.

[39] S. Dhall, B.R. Mehta, A.K. Tyagi, K. Sood, A review on environmental gas sensors: Materials and technologies, Sensors Int. 2 (2021) 100116. https://doi.org/10.1016/j.sintl.2021.100116.

[40] E. Gorbova, F. Tzorbatzoglou, C. Molochas, D. Chloros, A. Demin, P. Tsiakaras, Fundamentals and Principles of Solid-State Electrochemical Sensors for High Temperature Gas Detection, Catalysts. 12 (2021) 1. https://doi.org/10.3390/catal12010001.

[41] M. Xu, B. Peng, X. Zhu, Y. Guo, Multi-Gas Detection System Based on Non-Dispersive Infrared (NDIR) Spectral Technology, Sensors. 22 (2022) 836. https://doi.org/10.3390/s22030836.

[42] I.I. Ivanov, A.M. Baranov, V.A. Talipov, S.M. Mironov, S. Akbari, I. V. Kolesnik, E.D. Orlova, K.S. Napolskii, Investigation of catalytic hydrogen sensors with platinum group catalysts, Sensors Actuators B Chem. 346 (2021) 130515. https://doi.org/10.1016/j.snb.2021.130515.

[43] P. V. Shinde, C.S. Rout, Magnetic gas sensing: working principles and recent developments, Nanoscale Adv. 3 (2021) 1551–1568. https://doi.org/10.1039/D0NA00826E.

[44] G. Coelho Rezende, S. Le Calvé, J.J. Brandner, D. Newport, Micro photoionization

detectors, Sensors Actuators B Chem. 287 (2019) 86–94. https://doi.org/10.1016/j.snb.2019.01.072.

[45] S. Pyo, K. Lee, T. Noh, E. Jo, J. Kim, Sensitivity enhancement in photoionization detector using microelectrodes with integrated 1D nanostructures, Sensors Actuators B Chem. 288 (2019) 618–624. https://doi.org/10.1016/j.snb.2019.03.045.

[46] E.L.W. Gardner, J.W. Gardner, F. Udrea, Micromachined Thermal Gas Sensors—A Review, Sensors. 23 (2023). https://doi.org/10.3390/s23020681.

[47] J. Baranwal, B. Barse, G. Gatto, G. Broncova, A. Kumar, Electrochemical Sensors and Their Applications: A Review, Chemosensors. 10 (2022) 363. https://doi.org/10.3390/chemosensors10090363.

[48] K. Potje-Kamloth, Semiconductor Junction Gas Sensors, Chem. Rev. 108 (2008) 367–399. https://doi.org/10.1021/cr0681086.

[49] F.E. Annanouch, A. Alagh, P. Umek, J. Casanova-Chafer, C. Bittencourt, E. Llobet, Controlled growth of 3D assemblies of edge enriched multilayer MoS 2 nanosheets for dually selective NH 3 and NO 2 gas sensors, J. Mater. Chem. C. 10 (2022) 11027–11039. https://doi.org/10.1039/D2TC00759B.

[50] M. Wusiman, F. Taghipour, Methods and mechanisms of gas sensor selectivity, Crit. Rev. Solid State Mater. Sci. 47 (2022) 416–435. https://doi.org/10.1080/10408436.2021.1941752.

[51] P. Barik, M. Pradhan, Selectivity in trace gas sensing: recent developments, challenges, and future perspectives, Analyst. 147 (2022) 1024–1054. https://doi.org/10.1039/D1AN02070F.

[52] J. Burgués, J.M. Jiménez-Soto, S. Marco, Estimation of the limit of detection in semiconductor gas sensors through linearized calibration models, Anal. Chim. Acta. 1013 (2018) 13–25. https://doi.org/10.1016/j.aca.2018.01.062.

[53] X. Li, X. Li, Z. Li, J. Wang, J. Zhang, WS2 nanoflakes based selective ammonia sensors at room temperature, Sensors Actuators B Chem. 240 (2017) 273–277. https://doi.org/10.1016/j.snb.2016.08.163.

[54] S. Sharma, R. Saini, G. Gupta, D.J. Late, Room-temperature highly sensitive and selective NH 3 gas sensor using vertically aligned WS 2 nanosheets, Nanotechnology. 34 (2023) 045704. https://doi.org/10.1088/1361-6528/ac9c0c.

[55] A. Dey, Semiconductor metal oxide gas sensors: A review, Mater. Sci. Eng. B. 229 (2018) 206–217. https://doi.org/10.1016/j.mseb.2017.12.036.

[56] S.B. Malik, K. V. Mejia-Centeno, P.R. Martínez-Alanis, A. Cabot, F. Güell, F.E. Annanouch, E. Llobet, Synergistic effect of CeO2 nanoparticles and WO3 nanowires in gas sensing applications, Sensors Actuators B Chem. 400 (2024) 134879. https://doi.org/10.1016/j.snb.2023.134879.

[57] E. Llobet, Gas sensors using carbon nanomaterials: A review, Sensors Actuators B Chem. 179 (2013) 32–45. https://doi.org/10.1016/j.snb.2012.11.014.

[58] J. Janata, M. Josowicz, Conducting polymers in electronic chemical sensors, Nat. Mater. 2 (2003) 19–24. https://doi.org/10.1038/nmat768.

[59] X. Liu, T. Ma, N. Pinna, J. Zhang, Two-Dimensional Nanostructured Materials for Gas Sensing, Adv. Funct. Mater. 27 (2017) 1–30. https://doi.org/10.1002/adfm.201702168.

[60] S.B. Malik, F.E. Annanouch, E. Llobet, Pd-Nanoparticle-Decorated Multilayered MoS2 Sheets for Highly Sensitive Hydrogen Sensing, Chemosensors. 11 (2023) 550. https://doi.org/10.3390/chemosensors11110550.

[61] E. Comini, Metal oxides nanowires chemical/gas sensors: recent advances, Mater. Today Adv. 7 (2020) 100099. https://doi.org/10.1016/j.mtadv.2020.100099.

[62] A. Singh, S. Sikarwar, A. Verma, B. Chandra Yadav, The recent development of metal oxide heterostructures based gas sensor, their future opportunities and challenges: A review, Sensors Actuators A Phys. 332 (2021) 113127. https://doi.org/10.1016/j.sna.2021.113127.

[63] Gas Sensors Based on Conducting Metal Oxides, Elsevier, 2019. https://doi.org/10.1016/C2016-0-00984-1.

[64] A. Oprea, D. Degler, N. Barsan, A. Hemeryck, J. Rebholz, Basics of semiconducting metal oxide–based gas sensors, in: Gas Sensors Based Conduct. Met. Oxides, Elsevier,

2019: pp. 61–165. https://doi.org/10.1016/B978-0-12-811224-3.00003-2.

[65] A. Alagh, F.E. Annanouch, K. Al Youssef, C. Bittencourt, F. Güell, P.R. Martínez-Alanis, M. Reguant, E. Llobet, PdO and PtO loaded WS2 boosts NO2 gas sensing characteristics at room temperature, Sensors Actuators B Chem. 364 (2022) 131905. https://doi.org/10.1016/j.snb.2022.131905.

[66] A. Alagh, F.E. Annanouch, P. Umek, C. Bittencourt, A. Sierra-Castillo, E. Haye, J.F. Colomer, E. Llobet, CVD growth of self-assembled 2D and 1D WS2 nanomaterials for the ultrasensitive detection of NO2, Sensors Actuators B Chem. 326 (2021) 128813. https://doi.org/10.1016/j.snb.2020.128813.

[67] T. Russ, M. Zhang, T. Zhou, U. Weimar, T. Zhang, N. Barsan, Fabrication of metal oxide heterostructures for the application in chemoresistive gas sensors, in: Met. Oxide-Based Heterostruct., Elsevier, 2023: pp. 247–295. https://doi.org/10.1016/B978-0-323-85241-8.00005-0.

[68] N.A. Isaac, I. Pikaar, G. Biskos, Metal oxide semiconducting nanomaterials for air quality gas sensors: operating principles, performance, and synthesis techniques, Microchim. Acta. 189 (2022) 196. https://doi.org/10.1007/s00604-022-05254-0.

[69] S. Agarwal, P. Rai, E.N. Gatell, E. Llobet, F. Güell, M. Kumar, K. Awasthi, Gas sensing properties of ZnO nanostructures (flowers/rods) synthesized by hydrothermal method, Sensors Actuators B Chem. 292 (2019) 24–31. https://doi.org/10.1016/j.snb.2019.04.083.

[70] E. Navarrete, F. Güell, P.R. Martínez-Alanis, E. Llobet, Chemical vapour deposited ZnO nanowires for detecting ethanol and NO2, J. Alloys Compd. 890 (2022) 161923. https://doi.org/10.1016/j.jallcom.2021.161923.

[71] J. Ding, S. Chen, M. Xie, Y. Shen, F. Li, J. Li, Z. Li, Y. Wang, Defective WO 3 Nanosheets with (002)-Exposed Facet for Highly Sensitive Acetone Detection, ACS Appl. Nano Mater. 6 (2023) 12211–12218. https://doi.org/10.1021/acsanm.3c01928.

[72] R. Paul, B. Das, R. Ghosh, Novel approaches towards design of metal oxide based hetero-structures for room temperature gas sensor and its sensing mechanism: A recent progress, J. Alloys Compd. 941 (2023) 168943.

https://doi.org/10.1016/j.jallcom.2023.168943.

[73] J. Zhang, X. Liu, G. Neri, N. Pinna, Nanostructured Materials for Room-Temperature Gas Sensors, Adv. Mater. 28 (2016) 795–831. https://doi.org/10.1002/adma.201503825.

[74] S. Aftab, M. Zahir Iqbal, S. Hussain, H.H. Hegazy, F. Kabir, S. Hassan Abbas Jaffery, G. Koyyada, New developments in gas sensing using various two-dimensional architectural designs, Chem. Eng. J. 469 (2023) 144039. https://doi.org/10.1016/j.cej.2023.144039.

[75] M. Li, J. Chang, Z. Deng, L. Mi, M. Kumar, S. Wang, Y. He, G. Meng, Discriminating gas molecules at room temperature by UV light modulation (ULM) of nonselective metal oxide sensors, Sensors Actuators B Chem. 378 (2023) 133115. https://doi.org/10.1016/j.snb.2022.133115.

[76] X. Yang, Y. Deng, H. Yang, Y. Liao, X. Cheng, Y. Zou, L. Wu, Y. Deng, Functionalization of Mesoporous Semiconductor Metal Oxides for Gas Sensing: Recent Advances and Emerging Challenges, Adv. Sci. 10 (2023) 1–24. https://doi.org/10.1002/advs.202204810.

[77] X. Duan, D. Xu, W. Jia, R. Li, B. Sun, R. Yan, W. Zhao, WO3/WS2 nanoflowers fabricated by low-temperature in-situ oxidation for rapid detection of nitrogen dioxide, Sensors Actuators A Phys. 365 (2024) 114854. https://doi.org/10.1016/j.sna.2023.114854.

[78] J. Lee, Y.J. Kim, W. Lee, Synergetic crystal phases of SnO2/NiO heterostructure in an interconnected morphology for chemiresistive formaldehyde sensors, Sensors Actuators B Chem. 404 (2024) 135257. https://doi.org/10.1016/j.snb.2023.135257.

[79] S.H. Cho, M.-J. Choi, B. Koo, J. Kim, T.H. Lee, J.M. Suh, T.H. Eom, S.Y. Park, T. Kim, W. Jung, H.W. Jang, Rapid and ultrahighly sensitive ethanol sensing in p-type SrTi1-xFexO3, Sensors Actuators B Chem. 403 (2024) 135137. https://doi.org/10.1016/j.snb.2023.135137.

[80] J. Kim, M. Nazarian-Samani, J. Lee, S. kil Lee, J.H. Pi, K.H. Lee, Y.J. Kim, S. Lee, W. Lee, Extrinsic oxygen defects in SnO/SnO2 heterostructure for efficient NO2 gas detection, Sensors Actuators B Chem. 399 (2024) 134751.

https://doi.org/10.1016/j.snb.2023.134751.

[81] Z. Cai, J. Park, S. Park, Room temperature selective detection of NO2 using Au-decorated In2O3 nanoparticles embedded in porous ZnO nanofibers, J. Alloys Compd. 965 (2023) 171352. https://doi.org/10.1016/j.jallcom.2023.171352.

[82] R.K. Gupta, Nanowires, CRC Press, Boca Raton, 2023. https://doi.org/10.1201/9781003296621.

[83] Y.C. Lin, R. Torsi, R. Younas, C.L. Hinkle, A.F. Rigosi, H.M. Hill, K. Zhang, S. Huang, C.E. Shuck, C. Chen, Y.H. Lin, D. Maldonado-Lopez, J.L. Mendoza-Cortes, J. Ferrier, S. Kar, N. Nayir, S. Rajabpour, A.C.T. Van Duin, X. Liu, D. Jariwala, J. Jiang, J. Shi, W. Mortelmans, R. Jaramillo, J.M.J. Lopes, R. Engel-Herbert, A. Trofe, T. Ignatova, S.H. Lee, Z. Mao, L. Damian, Y. Wang, M.A. Steves, K.L. Knappenberger, Z. Wang, S. Law, G. Bepete, D. Zhou, J.X. Lin, M.S. Scheurer, J. Li, P. Wang, G. Yu, S. Wu, D. Akinwande, J.M. Redwing, M. Terrones, J.A. Robinson, Recent Advances in 2D Material Theory, Synthesis, Properties, and Applications, ACS Nano. 17 (2023) 9694–9747. https://doi.org/10.1021/acsnano.2c12759.

[84] Z. Wang, Y. Zhang, P. Tang, Z. Deng, P. He, M.-J. Chen, Z.-Z. Yu, H.-B. Zhang, Silk fibroin reinforced graphene fibers with outstanding electrical conductivity and mechanical strength, Carbon N. Y. 203 (2023) 886–894. https://doi.org/10.1016/j.carbon.2022.12.002.

[85] R.C. Andrew, R.E. Mapasha, A.M. Ukpong, N. Chetty, Mechanical properties of graphene and boronitrene, Phys. Rev. B. 85 (2012) 125428. https://doi.org/10.1103/PhysRevB.85.125428.

[86] M. Kong, M. Yang, R. Li, Y.-Z. Long, J. Zhang, X. Huang, X. Cui, Y. Zhang, Z. Said, C. Li, Graphene-based flexible wearable sensors: mechanisms, challenges, and future directions, Int. J. Adv. Manuf. Technol. (2023). https://doi.org/10.1007/s00170-023-12007-7.

[87] P. Recum, T. Hirsch, Graphene-based chemiresistive gas sensors, Nanoscale Adv. 6 (2023) 11–31. https://doi.org/10.1039/d3na00423f.

[88] G. Neri, Thin 2D: The New Dimensionality in Gas Sensing, Chemosensors. 5 (2017)

21. https://doi.org/10.3390/chemosensors5030021.

[89] J.A. Wilson, F.J. Di Salvo, S. Mahajan, Charge-density waves and superlattices in the metallic layered transition metal dichalcogenides, Adv. Phys. 24 (1975) 117–201. https://doi.org/10.1080/00018737500101391.

[90] J.A. Wilson, F.J. Di Salvo, S. Mahajan, Charge-density waves and superlattices in the metallic layered transition metal dichalcogenides, Adv. Phys. 24 (1975) 117–201. https://doi.org/10.1080/00018737500101391.

[91] J. Xie, H. Zhang, S. Li, R. Wang, X. Sun, M. Zhou, J. Zhou, X.W. (David) Lou, Y. Xie, Defect-Rich MoS 2 Ultrathin Nanosheets with Additional Active Edge Sites for Enhanced Electrocatalytic Hydrogen Evolution, Adv. Mater. 25 (2013) 5807–5813. https://doi.org/10.1002/adma.201302685.

[92] Y. Zhan, Z. Liu, S. Najmaei, P.M. Ajayan, J. Lou, Large-Area Vapor-Phase Growth and Characterization of MoS 2 Atomic Layers on a SiO 2 Substrate, Small. 8 (2012) 966–971. https://doi.org/10.1002/smll.201102654.

[93] X. Ma, M. Shi, Thermal Evaporation Deposition of Few-layer MoS2 Films, Nano-Micro Lett. 5 (2013) 135–139. https://doi.org/10.1007/BF03353741.

[94] Y. Li, H. Wang, L. Xie, Y. Liang, G. Hong, H. Dai, MoS 2 Nanoparticles Grown on Graphene: An Advanced Catalyst for the Hydrogen Evolution Reaction, J. Am. Chem. Soc. 133 (2011) 7296–7299. https://doi.org/10.1021/ja201269b.

[95] Y. Zhao, H. Lee, W. Choi, W. Fei, C.J. Lee, Large-area synthesis of monolayer MoSe 2 films on SiO 2 /Si substrates by atmospheric pressure chemical vapor deposition, RSC Adv. 7 (2017) 27969–27973. https://doi.org/10.1039/C7RA03642F.

[96] Y. Zhang, T.-R. Chang, B. Zhou, Y.-T. Cui, H. Yan, Z. Liu, F. Schmitt, J. Lee, R. Moore, Y. Chen, H. Lin, H.-T. Jeng, S.-K. Mo, Z. Hussain, A. Bansil, Z.-X. Shen, Direct observation of the transition from indirect to direct bandgap in atomically thin epitaxial MoSe2, Nat. Nanotechnol. 9 (2014) 111–115. https://doi.org/10.1038/nnano.2013.277.

[97] Y. Shi, C. Hua, B. Li, X. Fang, C. Yao, Y. Zhang, Y. Hu, Z. Wang, L. Chen, D. Zhao, G.D. Stucky, Highly Ordered Mesoporous Crystalline MoSe 2 Material with Efficient

Visible-Light-Driven Photocatalytic Activity and Enhanced Lithium Storage Performance, Adv. Funct. Mater. 23 (2013) 1832–1838. https://doi.org/10.1002/adfm.201202144.

[98] O. Lehtinen, H.-P. Komsa, A. Pulkin, M.B. Whitwick, M.-W. Chen, T. Lehnert, M.J. Mohn, O. V. Yazyev, A. Kis, U. Kaiser, A. V. Krasheninnikov, Atomic Scale Microstructure and Properties of Se-Deficient Two-Dimensional MoSe 2, ACS Nano. 9 (2015) 3274–3283. https://doi.org/10.1021/acsnano.5b00410.

[99] Z. Jia, J. Xiang, C. Mu, F. Wen, R. Yang, C. Hao, Z. Liu, Improved photoresponse and stable photoswitching of tungsten disulfide single-layer phototransistor decorated with black phosphorus nanosheets, J. Mater. Sci. 52 (2017) 11506–11512. https://doi.org/10.1007/s10853-017-1318-9.

[100] L. Cheng, W. Huang, Q. Gong, C. Liu, Z. Liu, Y. Li, H. Dai, Ultrathin WS 2 Nanoflakes as a High-Performance Electrocatalyst for the Hydrogen Evolution Reaction, Angew. Chemie Int. Ed. 53 (2014) 7860–7863. https://doi.org/10.1002/anie.201402315.

[101] J.-K. Huang, J. Pu, C.-L. Hsu, M.-H. Chiu, Z.-Y. Juang, Y.-H. Chang, W.-H. Chang, Y. Iwasa, T. Takenobu, L.-J. Li, Large-Area Synthesis of Highly Crystalline WSe 2 Monolayers and Device Applications, ACS Nano. 8 (2014) 923–930. https://doi.org/10.1021/nn405719x.

[102] A. Alagh, F.E. Annanouch, A. Sierra-Castillo, E. Haye, J.F. Colomer, E. Llobet, Three-Dimensional Assemblies of Edge-Enriched WSe2Nanoflowers for Selectively Detecting Ammonia or Nitrogen Dioxide, ACS Appl. Mater. Interfaces. 14 (2022) 54946–54960. https://doi.org/10.1021/acsami.2c16299.

[103] S. Joseph, J. Mohan, S. Lakshmy, S. Thomas, B. Chakraborty, S. Thomas, N. Kalarikkal, A review of the synthesis, properties, and applications of 2D transition metal dichalcogenides and their heterostructures, Mater. Chem. Phys. 297 (2023) 127332. https://doi.org/10.1016/j.matchemphys.2023.127332.

[104] A.K. Geim, I. V. Grigorieva, Van der Waals heterostructures, Nature. 499 (2013) 419–425. https://doi.org/10.1038/nature12385.

[105] V.K. Sangwan, M.C. Hersam, Electronic Transport in Two-Dimensional Materials,

Annu. Rev. Phys. Chem. 69 (2018) 299–325. https://doi.org/10.1146/annurev-physchem-050317-021353.

[106] E. Blundo, M. Felici, T. Yildirim, G. Pettinari, D. Tedeschi, A. Miriametro, B. Liu, W. Ma, Y. Lu, A. Polimeni, Evidence of the direct-to-indirect band gap transition in strained two-dimensional WS2, MoS2, abd WSe2, Phys. Rev. Res. 2 (2020) 012024. https://doi.org/10.1103/PhysRevResearch.2.012024.

[107] T.F. Jaramillo, K.P. Jørgensen, J. Bonde, J.H. Nielsen, S. Horch, I. Chorkendorff, Identification of Active Edge Sites for Electrochemical H 2 Evolution from MoS 2 Nanocatalysts, Science (80-.). 317 (2007) 100–102. https://doi.org/10.1126/science.1141483.

[108] T. Eknapakul, P.D.C. King, M. Asakawa, P. Buaphet, R.-H. He, S.-K. Mo, H. Takagi, K.M. Shen, F. Baumberger, T. Sasagawa, S. Jungthawan, W. Meevasana, Electronic Structure of a Quasi-Freestanding MoS 2 Monolayer, Nano Lett. 14 (2014) 1312–1316. https://doi.org/10.1021/nl4042824.

[109] X. Li, H. Zhu, Two-dimensional MoS2: Properties, preparation, and applications, J. Mater. 1 (2015) 33–44. https://doi.org/10.1016/j.jmat.2015.03.003.

[110] S.A. Han, R. Bhatia, S.-W. Kim, Synthesis, properties and potential applications of two-dimensional transition metal dichalcogenides, Nano Converg. 2 (2015) 17. https://doi.org/10.1186/s40580-015-0048-4.

[111] H. Li, Z. Yin, Q. He, H. Li, X. Huang, G. Lu, D.W.H. Fam, A.I.Y. Tok, Q. Zhang, H. Zhang, Fabrication of Single- and Multilayer MoS 2 Film-Based Field-Effect Transistors for Sensing NO at Room Temperature, Small. 8 (2012) 63–67. https://doi.org/10.1002/smll.201101016.

[112] K.S. Novoselov, D. Jiang, F. Schedin, T.J. Booth, V. V. Khotkevich, S. V. Morozov, A.K. Geim, Two-dimensional atomic crystals, Proc. Natl. Acad. Sci. 102 (2005) 10451–10453. https://doi.org/10.1073/pnas.0502848102.

[113] X. Wang, H. Feng, Y. Wu, L. Jiao, Controlled Synthesis of Highly Crystalline MoS 2 Flakes by Chemical Vapor Deposition, J. Am. Chem. Soc. 135 (2013) 5304–5307. https://doi.org/10.1021/ja4013485.

[114] Q. Li, J.T. Newberg, E.C. Walter, J.C. Hemminger, R.M. Penner, Polycrystalline Molybdenum Disulfide (2H−MoS 2) Nano- and Microribbons by Electrochemical/Chemical Synthesis, Nano Lett. 4 (2004) 277–281. https://doi.org/10.1021/nl035011f.

[115] P. Wang, Y. Huan, P. Yang, M. Cheng, J. Shi, Y. Zhang, Controlled Syntheses and Multifunctional Applications of Two-Dimensional Metallic Transition Metal Dichalcogenides, Accounts Mater. Res. 2 (2021) 751–763. https://doi.org/10.1021/accountsmr.1c00092.

[116] R.F. Frindt, Single Crystals of MoS2 Several Molecular Layers Thick, J. Appl. Phys. 37 (1966) 1928–1929. https://doi.org/10.1063/1.1708627.

[117] H. Li, J. Wu, Z. Yin, H. Zhang, Preparation and Applications of Mechanically Exfoliated Single-Layer and Multilayer MoS 2 and WSe 2 Nanosheets, Acc. Chem. Res. 47 (2014) 1067–1075. https://doi.org/10.1021/ar4002312.

[118] S. Bertolazzi, J. Brivio, A. Kis, Stretching and Breaking of Ultrathin MoS 2, ACS Nano. 5 (2011) 9703–9709. https://doi.org/10.1021/nn203879f.

[119] N. Huo, Z. Wei, X. Meng, J. Kang, F. Wu, S.-S. Li, S.-H. Wei, J. Li, Interlayer coupling and optoelectronic properties of ultrathin two-dimensional heterostructures based on graphene, MoS 2 and WS 2, J. Mater. Chem. C. 3 (2015) 5467–5473. https://doi.org/10.1039/C5TC00698H.

[120] J. Brivio, D.T.L. Alexander, A. Kis, Ripples and Layers in Ultrathin MoS 2 Membranes, Nano Lett. 11 (2011) 5148–5153. https://doi.org/10.1021/nl2022288.

[121] B. Radisavljevic, M.B. Whitwick, A. Kis, Integrated Circuits and Logic Operations Based on Single-Layer MoS 2, ACS Nano. 5 (2011) 9934–9938. https://doi.org/10.1021/nn203715c.

[122] P. Joensen, R.F. Frindt, S.R. Morrison, Single-layer MoS2, Mater. Res. Bull. 21 (1986) 457–461. https://doi.org/10.1016/0025-5408(86)90011-5.

[123] P. Joensen, R.F. Frindt, S.R. Morrison, Single-layer MoS2, Mater. Res. Bull. 21 (1986) 457–461. https://doi.org/https://doi.org/10.1016/0025-5408(86)90011-5.

[124] M.A. Lukowski, A.S. Daniel, F. Meng, A. Forticaux, L. Li, S. Jin, Enhanced Hydrogen Evolution Catalysis from Chemically Exfoliated Metallic MoS 2 Nanosheets, J. Am. Chem. Soc. 135 (2013) 10274–10277. https://doi.org/10.1021/ja404523s.

[125] Z. Zeng, Z. Yin, X. Huang, H. Li, Q. He, G. Lu, F. Boey, H. Zhang, Single-Layer Semiconducting Nanosheets: High-Yield Preparation and Device Fabrication, Angew. Chemie Int. Ed. 50 (2011) 11093–11097. https://doi.org/10.1002/anie.201106004.

[126] J.N. Coleman, M. Lotya, A. O'Neill, S.D. Bergin, P.J. King, U. Khan, K. Young, A. Gaucher, S. De, R.J. Smith, I. V. Shvets, S.K. Arora, G. Stanton, H.-Y. Kim, K. Lee, G.T. Kim, G.S. Duesberg, T. Hallam, J.J. Boland, J.J. Wang, J.F. Donegan, J.C. Grunlan, G. Moriarty, A. Shmeliov, R.J. Nicholls, J.M. Perkins, E.M. Grieveson, K. Theuwissen, D.W. McComb, P.D. Nellist, V. Nicolosi, Two-Dimensional Nanosheets Produced by Liquid Exfoliation of Layered Materials, Science (80-.). 331 (2011) 568–571. https://doi.org/10.1126/science.1194975.

[127] Y. Lee, X. Zhang, W. Zhang, M. Chang, C. Lin, K. Chang, Y. Yu, J.T. Wang, C. Chang, L. Li, T. Lin, Synthesis of Large-Area MoS 2 Atomic Layers with Chemical Vapor Deposition, Adv. Mater. 24 (2012) 2320–2325. https://doi.org/10.1002/adma.201104798.

[128] Y. Kobayashi, S. Sasaki, S. Mori, H. Hibino, Z. Liu, K. Watanabe, T. Taniguchi, K. Suenaga, Y. Maniwa, Y. Miyata, Growth and Optical Properties of High-Quality Monolayer WS 2 on Graphite, ACS Nano. 9 (2015) 4056–4063. https://doi.org/10.1021/acsnano.5b00103.

[129] X. Ling, Y.-H. Lee, Y. Lin, W. Fang, L. Yu, M.S. Dresselhaus, J. Kong, Role of the Seeding Promoter in MoS 2 Growth by Chemical Vapor Deposition, Nano Lett. 14 (2014) 464–472. https://doi.org/10.1021/nl4033704.

[130] J. Rhyee, J. Kwon, P. Dak, J.H. Kim, S.M. Kim, J. Park, Y.K. Hong, W.G. Song, I. Omkaram, M.A. Alam, S. Kim, High-Mobility Transistors Based on Large-Area and Highly Crystalline CVD-Grown MoSe 2 Films on Insulating Substrates, Adv. Mater. 28 (2016) 2316–2321. https://doi.org/10.1002/adma.201504789.

[131] L. Zhou, A. Zubair, Z. Wang, X. Zhang, F. Ouyang, K. Xu, W. Fang, K. Ueno, J. Li, T.

Palacios, J. Kong, M.S. Dresselhaus, Synthesis of High-Quality Large-Area Homogenous 1T′ MoTe 2 from Chemical Vapor Deposition, Adv. Mater. 28 (2016) 9526–9531. https://doi.org/10.1002/adma.201602687.

[132] M. Nakano, Y. Wang, Y. Kashiwabara, H. Matsuoka, Y. Iwasa, Layer-by-Layer Epitaxial Growth of Scalable WSe 2 on Sapphire by Molecular Beam Epitaxy, Nano Lett. 17 (2017) 5595–5599. https://doi.org/10.1021/acs.nanolett.7b02420.

[133] J.H. Park, S. Vishwanath, X. Liu, H. Zhou, S.M. Eichfeld, S.K. Fullerton-Shirey, J.A. Robinson, R.M. Feenstra, J. Furdyna, D. Jena, H.G. Xing, A.C. Kummel, Scanning Tunneling Microscopy and Spectroscopy of Air Exposure Effects on Molecular Beam Epitaxy Grown WSe 2 Monolayers and Bilayers, ACS Nano. 10 (2016) 4258–4267. https://doi.org/10.1021/acsnano.5b07698.

[134] C. Tan, H. Zhang, Two-dimensional transition metal dichalcogenide nanosheet-based composites, Chem. Soc. Rev. 44 (2015) 2713–2731. https://doi.org/10.1039/C4CS00182F.

[135] D. Hanlon, C. Backes, E. Doherty, C.S. Cucinotta, N.C. Berner, C. Boland, K. Lee, A. Harvey, P. Lynch, Z. Gholamvand, S. Zhang, K. Wang, G. Moynihan, A. Pokle, Q.M. Ramasse, N. McEvoy, W.J. Blau, J. Wang, G. Abellan, F. Hauke, A. Hirsch, S. Sanvito, D.D. O'Regan, G.S. Duesberg, V. Nicolosi, J.N. Coleman, Liquid exfoliation of solvent-stabilized few-layer black phosphorus for applications beyond electronics, Nat. Commun. 6 (2015) 8563. https://doi.org/10.1038/ncomms9563.

[136] J.R. Brent, N. Savjani, P. O'Brien, Synthetic approaches to two-dimensional transition metal dichalcogenide nanosheets, Prog. Mater. Sci. 89 (2017) 411–478. https://doi.org/10.1016/j.pmatsci.2017.06.002.

[137] X. Zhang, Z. Lai, C. Tan, H. Zhang, Solution-Processed Two-Dimensional MoS 2 Nanosheets: Preparation, Hybridization, and Applications, Angew. Chemie Int. Ed. 55 (2016) 8816–8838. https://doi.org/10.1002/anie.201509933.

[138] S. Ippolito, P. Samorì, Defect Engineering Strategies Toward Controlled Functionalization of Solution-Processed Transition Metal Dichalcogenides, Small Sci. 2 (2022). https://doi.org/10.1002/smsc.202100122.

[139] X. Chen, C. Liu, S. Mao, Environmental Analysis with 2D Transition-Metal Dichalcogenide-Based Field-Effect Transistors, Nano-Micro Lett. 12 (2020) 1–24. https://doi.org/10.1007/s40820-020-00438-w.

[140] J.H. Kim, H. Sung, G.-H. Lee, Phase Engineering of Two-Dimensional Transition Metal Dichalcogenides, Small Sci. 4 (2024). https://doi.org/10.1002/smsc.202300093.

[141] S. Manzeli, D. Ovchinnikov, D. Pasquier, O. V. Yazyev, A. Kis, 2D transition metal dichalcogenides, Nat. Rev. Mater. 2 (2017) 17033. https://doi.org/10.1038/natrevmats.2017.33.

[142] A. V. Kolobov, J. Tominaga, Two-Dimensional Transition-Metal Dichalcogenides, Springer International Publishing, Cham, 2016. https://doi.org/10.1007/978-3-319-31450-1.

[143] W. Choi, N. Choudhary, G.H. Han, J. Park, D. Akinwande, Y.H. Lee, Recent development of two-dimensional transition metal dichalcogenides and their applications, Mater. Today. 20 (2017) 116–130. https://doi.org/10.1016/j.mattod.2016.10.002.

[144] F. Xia, H. Wang, D. Xiao, M. Dubey, A. Ramasubramaniam, Two-dimensional material nanophotonics, Nat. Photonics. 8 (2014) 899–907. https://doi.org/10.1038/nphoton.2014.271.

[145] A. Chaves, J.G. Azadani, H. Alsalman, D.R. da Costa, R. Frisenda, A.J. Chaves, S.H. Song, Y.D. Kim, D. He, J. Zhou, A. Castellanos-Gomez, F.M. Peeters, Z. Liu, C.L. Hinkle, S.-H. Oh, P.D. Ye, S.J. Koester, Y.H. Lee, P. Avouris, X. Wang, T. Low, Bandgap engineering of two-dimensional semiconductor materials, Npj 2D Mater. Appl. 4 (2020) 29. https://doi.org/10.1038/s41699-020-00162-4.

[146] A. Kuc, N. Zibouche, T. Heine, Influence of quantum confinement on the electronic structure of the transition metal sulfide TS2, Phys. Rev. B. 83 (2011) 245213. https://doi.org/10.1103/PhysRevB.83.245213.

[147] O. Del Pozo-Zamudio, S. Schwarz, M. Sich, I.A. Akimov, M. Bayer, R.C. Schofield, E.A. Chekhovich, B.J. Robinson, N.D. Kay, O. V. Kolosov, A I Dmitriev, G. V. Lashkarev, D.N. Borisenko, N.N. Kolesnikov, A.I. Tartakovskii, Photoluminescence of

two-dimensional GaTe and GaSe films, 2D Mater. 2 (2015) 035010. https://doi.org/10.1088/2053-1583/2/3/035010.

[148] G.G. Naumis, Electronic properties of two-dimensional materials, in: Synth. Model. Charact. 2D Mater. Their Heterostruct., Elsevier, 2020: pp. 77–109. https://doi.org/10.1016/B978-0-12-818475-2.00005-2.

[149] M. Chhowalla, H.S. Shin, G. Eda, L.-J. Li, K.P. Loh, H. Zhang, The chemistry of two-dimensional layered transition metal dichalcogenide nanosheets, Nat. Chem. 5 (2013) 263–275. https://doi.org/10.1038/nchem.1589.

[150] Q.H. Wang, K. Kalantar-Zadeh, A. Kis, J.N. Coleman, M.S. Strano, Electronics and optoelectronics of two-dimensional transition metal dichalcogenides, Nat. Nanotechnol. 7 (2012) 699–712. https://doi.org/10.1038/nnano.2012.193.

[151] M. Terrones, A. Voshell, M.M. Rana, Review of optical properties of two-dimensional transition metal dichalcogenides, in: M. Matin, A.K. Dutta, S. Chowdhury (Eds.), Wide Bandgap Power Energy Devices Appl. III, SPIE, 2018: p. 21. https://doi.org/10.1117/12.2323132.

[152] M. Ghorbani-Asl, S. Borini, A. Kuc, T. Heine, Strain-dependent modulation of conductivity in single-layer transition-metal dichalcogenides, Phys. Rev. B. 87 (2013) 235434. https://doi.org/10.1103/PhysRevB.87.235434.

[153] S. KC, R.C. Longo, R. Addou, R.M. Wallace, K. Cho, Impact of intrinsic atomic defects on the electronic structure of MoS 2 monolayers, Nanotechnology. 25 (2014) 375703. https://doi.org/10.1088/0957-4484/25/37/375703.

[154] X. Deng, X. Liang, S.-P. Ng, C.-M.L. Wu, Adsorption of formaldehyde on transition metal doped monolayer MoS2: A DFT study, Appl. Surf. Sci. 484 (2019) 1244–1252. https://doi.org/10.1016/j.apsusc.2019.04.175.

[155] A. Shafqat, T. Iqbal, A. Majid, A DFT study of intrinsic point defects in monolayer MoSe2, AIP Adv. 7 (2017). https://doi.org/10.1063/1.4999524.

[156] W. Tang, S.S. Rassay, N.M. Ravindra, Electronic & Optical properties of Transition-Metal Dichalcogenides, Madridge J. Nanotechnol. Nanosci. 2 (2017) 58–64.

https://doi.org/10.18689/mjnn-1000111.

[157] M. Terrones, A. Voshell, M.M. Rana, Review of optical properties of two-dimensional transition metal dichalcogenides, in: M. Matin, A.K. Dutta, S. Chowdhury (Eds.), Wide Bandgap Power Energy Devices Appl. III, SPIE, 2018: p. 21. https://doi.org/10.1117/12.2323132.

[158] M. Koperski, M.R. Molas, A. Arora, K. Nogajewski, A.O. Slobodeniuk, C. Faugeras, M. Potemski, Optical properties of atomically thin transition metal dichalcogenides: observations and puzzles, Nanophotonics. 6 (2017) 1289–1308. https://doi.org/10.1515/nanoph-2016-0165.

[159] H. Ai, D. Liu, J. Geng, S. Wang, K.H. Lo, H. Pan, Theoretical evidence of the spin–valley coupling and valley polarization in two-dimensional MoSi 2 X 4 (X = N, P, and As), Phys. Chem. Chem. Phys. 23 (2021) 3144–3151. https://doi.org/10.1039/D0CP05926A.

[160] J.H. Kim, J.H. Jeong, N. Kim, R. Joshi, G.-H. Lee, Mechanical properties of two-dimensional materials and their applications, J. Phys. D. Appl. Phys. 52 (2019) 083001. https://doi.org/10.1088/1361-6463/aaf465.

[161] J.H. Kim, J.H. Jeong, N. Kim, R. Joshi, G.-H. Lee, Mechanical properties of two-dimensional materials and their applications, J. Phys. D. Appl. Phys. 52 (2019) 083001. https://doi.org/10.1088/1361-6463/aaf465.

[162] K. Liu, J. Wu, Mechanical properties of two-dimensional materials and heterostructures, J. Mater. Res. 31 (2016) 832–844. https://doi.org/10.1557/jmr.2015.324.

[163] J. Li, N. V. Medhekar, V.B. Shenoy, Bonding Charge Density and Ultimate Strength of Monolayer Transition Metal Dichalcogenides, J. Phys. Chem. C. 117 (2013) 15842–15848. https://doi.org/10.1021/jp403986v.

[164] H. Yuan, L. Kong, T. Li, Q. Zhang, A review of transition metal chalcogenide/graphene nanocomposites for energy storage and conversion, Chinese Chem. Lett. 28 (2017) 2180–2194. https://doi.org/10.1016/j.cclet.2017.11.038.

[165] S. Aftab, S. Hussain, F. Kabir, Y. Kuznetsova, A.G. Al-Sehemi, Progress in

Photodetector Devices Utilizing Transition Metal Dichalcogenides, J. Mater. Chem. C. (2024) 1211–1232. https://doi.org/10.1039/d3tc04253g.

[166] N. Huo, G. Konstantatos, Recent Progress and Future Prospects of 2D-Based Photodetectors, Adv. Mater. 30 (2018) 1–27. https://doi.org/10.1002/adma.201801164.

[167] L. Hu, X. Li, X. Guo, M. Xu, Y. Shi, N.B. Herve, R. Xiang, Q. Zhang, Electret Modulation Strategy to Enhance the Photosensitivity Performance of Two-Dimensional Molybdenum Sulfide, ACS Appl. Mater. Interfaces. 15 (2023) 59704–59713. https://doi.org/10.1021/acsami.3c14836.

[168] B. Chen, D. Chao, E. Liu, M. Jaroniec, N. Zhao, S.-Z. Qiao, Transition metal dichalcogenides for alkali metal ion batteries: engineering strategies at the atomic level, Energy Environ. Sci. 13 (2020) 1096–1131. https://doi.org/10.1039/C9EE03549D.

[169] H. Yuan, L. Kong, T. Li, Q. Zhang, A review of transition metal chalcogenide/graphene nanocomposites for energy storage and conversion, Chinese Chem. Lett. 28 (2017) 2180–2194. https://doi.org/10.1016/j.cclet.2017.11.038.

[170] G. Wang, J. Zhang, S. Yang, F. Wang, X. Zhuang, K. Müllen, X. Feng, Vertically Aligned MoS 2 Nanosheets Patterned on Electrochemically Exfoliated Graphene for High-Performance Lithium and Sodium Storage, Adv. Energy Mater. 8 (2018) 1–8. https://doi.org/10.1002/aenm.201702254.

[171] C. Li, Q. Cao, F. Wang, Y. Xiao, Y. Li, J.-J. Delaunay, H. Zhu, Engineering graphene and TMDs based van der Waals heterostructures for photovoltaic and photoelectrochemical solar energy conversion, Chem. Soc. Rev. 47 (2018) 4981–5037. https://doi.org/10.1039/C8CS00067K.

[172] M. Bernardi, M. Palummo, J.C. Grossman, Extraordinary Sunlight Absorption and One Nanometer Thick Photovoltaics Using Two-Dimensional Monolayer Materials, Nano Lett. 13 (2013) 3664–3670. https://doi.org/10.1021/nl401544y.

[173] S. Joseph, M.K. Ravva, B.A. Davis, S. Thomas, N. Kalarikkal, Theoretical Study on Understanding the Effects of Core Structure and Energy Level Tuning on Efficiency of Nonfullerene Acceptors in Organic Solar Cells, Adv. Theory Simulations. 4 (2021) 1–8. https://doi.org/10.1002/adts.202100019.

[174] M.-Y. Li, C.-H. Chen, Y. Shi, L.-J. Li, Heterostructures based on two-dimensional layered materials and their potential applications, Mater. Today. 19 (2016) 322–335. https://doi.org/10.1016/j.mattod.2015.11.003.

[175] C. Zhu, Z. Zeng, H. Li, F. Li, C. Fan, H. Zhang, Single-Layer MoS 2 -Based Nanoprobes for Homogeneous Detection of Biomolecules, J. Am. Chem. Soc. 135 (2013) 5998–6001. https://doi.org/10.1021/ja4019572.

[176] L. Yan, H. Shi, X. Sui, Z. Deng, L. Gao, MoS 2 -DNA and MoS 2 based sensors, RSC Adv. 7 (2017) 23573–23582. https://doi.org/10.1039/C7RA02649H.

[177] T. Wang, R. Zhu, J. Zhuo, Z. Zhu, Y. Shao, M. Li, Direct Detection of DNA below ppb Level Based on Thionin-Functionalized Layered MoS 2 Electrochemical Sensors, Anal. Chem. 86 (2014) 12064–12069. https://doi.org/10.1021/ac5027786.

[178] A. Vaidyanathan, S. Lakshmy, G. Sanyal, S. Joseph, N. Kalarikkal, B. Chakraborty, Nitrobenzene sensing in pristine and metal doped 2D dichalcogenide MoS2: Insights from density functional theory investigations, Appl. Surf. Sci. 550 (2021) 149395. https://doi.org/10.1016/j.apsusc.2021.149395.

[179] K. Lee, R. Gatensby, N. McEvoy, T. Hallam, G.S. Duesberg, High-Performance Sensors Based on Molybdenum Disulfide Thin Films, Adv. Mater. 25 (2013) 6699–6702. https://doi.org/10.1002/adma.201303230.

[180] B. Liu, L. Chen, G. Liu, A.N. Abbas, M. Fathi, C. Zhou, High-Performance Chemical Sensing Using Schottky-Contacted Chemical Vapor Deposition Grown Monolayer MoS 2 Transistors, ACS Nano. 8 (2014) 5304–5314. https://doi.org/10.1021/nn5015215.

[181] Y. Zhou, S. Wang, S. Xin, S. Sayin, Z. Yi, Z. Li, M. Zaghloul, Layer-Dependent Sensing Performance of WS2-Based Gas Sensors, Nanomaterials. 14 (2024). https://doi.org/10.3390/nano14020235.

[182] Z. Liang, M. Wang, S. Liu, M. Hassan, X. Zhang, S. Lei, G. Qiao, G. Liu, One-pot hydrothermal synthesis of self-assembled MoS2/WS2 nanoflowers for chemiresistive room-temperature NO2 sensors, Sensors Actuators B Chem. 403 (2024) 135215. https://doi.org/10.1016/j.snb.2023.135215.

[183] Q. Zhou, H. Song, T. Sun, L. Zhang, Y. Lv, Cataluminescence on 2D WS2 nanosheets surface for H2S sensing, Sensors Actuators B Chem. 353 (2022). https://doi.org/10.1016/j.snb.2021.131111.

[184] W.S. Lee, J. Choi, Hybrid Integration of Carbon Nanotubes and Transition Metal Dichalcogenides on Cellulose Paper for Highly Sensitive and Extremely Deformable Chemical Sensors, ACS Appl. Mater. Interfaces. 11 (2019) 19363–19371. https://doi.org/10.1021/acsami.9b03296.

[185] Y. Kim, S.-K. Kang, N.-C. Oh, H.-D. Lee, S.-M. Lee, J. Park, H. Kim, Improved Sensitivity in Schottky Contacted Two-Dimensional MoS 2 Gas Sensor, ACS Appl. Mater. Interfaces. 11 (2019) 38902–38909. https://doi.org/10.1021/acsami.9b10861.

[186] Y. Kim, S. Lee, J.G. Song, K.Y. Ko, W.J. Woo, S.W. Lee, M. Park, H. Lee, Z. Lee, H. Choi, W.H. Kim, J. Park, H. Kim, 2D Transition Metal Dichalcogenide Heterostructures for p- and n-Type Photovoltaic Self-Powered Gas Sensor, Adv. Funct. Mater. 30 (2020) 1–11. https://doi.org/10.1002/adfm.202003360.

[187] W.Y. Chen, X. Jiang, S.N. Lai, D. Peroulis, L. Stanciu, Nanohybrids of a MXene and transition metal dichalcogenide for selective detection of volatile organic compounds, Nat. Commun. 11 (2020) 1–10. https://doi.org/10.1038/s41467-020-15092-4.

[188] B. Li, X. Chen, C. Su, Y. Han, H. Wang, M. Zeng, Y. Wang, T. Liang, Z. Yang, L. Xu, Enhanced dimethyl methylphosphonate detection based on two-dimensional WSe2nanosheets at room temperature, Analyst. 145 (2020) 8059–8067. https://doi.org/10.1039/d0an01671c.

[189] J. Wang, H. Deng, X. Li, C. Yang, Y. Xia, Visible-light photocatalysis enhanced room-temperature formaldehyde gas sensing by MoS2/rGO hybrids, Sensors Actuators, B Chem. 304 (2020) 127317. https://doi.org/10.1016/j.snb.2019.127317.

[190] Y. Han, Y. Liu, C. Su, X. Chen, B. Li, W. Jiang, M. Zeng, N. Hu, Y. Su, Z. Zhou, Z.G. Zhu, Z. Yang, Hierarchical WS2-WO3Nanohybrids with P-N Heterojunctions for NO2Detection, ACS Appl. Nano Mater. 4 (2021) 1626–1634. https://doi.org/10.1021/acsanm.0c03094.

[191] J. Kang, F. Xu, C. Zhang, F. Li, O.A. Al-Hartomy, A. Al-Ghamdi, S. Wageh, G. Zhao,

T. Yang, H. Zhang, Vanadium Disulfide Nanosheets Synthesized by Facile Liquid-Phase Exfoliation for Ammonia Detection with High Selectivity, Adv. Electron. Mater. 8 (2022) 1–8. https://doi.org/10.1002/aelm.202100567.

[192] N. Sakhuja, R.K. Jha, R. Sai, N. Bhat, ZnO Nanorods Grown on WS2Nanosheets for Chemiresistive H2S Sensing, ACS Appl. Nano Mater. 5 (2022) 9241–9251. https://doi.org/10.1021/acsanm.2c01580.

[193] D. Chen, J. Tang, X. Zhang, P. Wu, Y. Li, B. Xiao, Q. Miao, K. Liu, WS Nanostructure-Based Gas Sensor for SF Decomposition Products: Experimental and First-Principles Study, IEEE Sens. J. 22 (2022) 20171–20176. https://doi.org/10.1109/JSEN.2022.3201672.

[194] D. Simon Patrick, P. Bharathi, M. Krishna Mohan, C. Muthamizchelvan, S. Harish, M. Navaneethan, Liquid phase exfoliated WS2 nanosheet-based gas sensor for room temperature NO2 detection, J. Mater. Sci. Mater. Electron. 33 (2022) 9235–9245. https://doi.org/10.1007/s10854-021-07246-x.

[195] Y. Xia, L. Xu, S. He, L. Zhou, M. Wang, J. Wang, S. Komarneni, UV-activated WS2/SnO2 2D/0D heterostructures for fast and reversible NO2 gas sensing at room temperature, Sensors Actuators B Chem. 364 (2022) 131903. https://doi.org/10.1016/j.snb.2022.131903.

[196] S. Rawat, P. Bamola, S. Chandel, H. Kala, C. Dwivedi, H. Sharma, Environmental gas sensing studies using flower-like MoS2hybrid structure, Mater. Today Proc. 83 (2023) 39–42. https://doi.org/10.1016/j.matpr.2023.01.142.

[197] J.-L. Fan, X.-F. Hu, W.-W. Qin, M. Zhou, Y.-S. Liu, S. Cheng, S.-J. Gao, L.-P. Tan, G.-Q. Wang, W. Zhang, Room-temperature sensing performance of binary Co–Zn doped MoS 2 /graphite composites toward ppb-level NO 2, J. Mater. Chem. C. 11 (2023) 2364–2374. https://doi.org/10.1039/D2TC04680F.

[198] I. Sharma, K.N. Kumar, J. Choi, Highly sensitive chemiresistive detection of NH3 by formation of WS2 nanosheets and SnO2 quantum dot heterostructures, Sensors Actuators B Chem. 375 (2023) 132899. https://doi.org/10.1016/j.snb.2022.132899.

[199] A. Alagh, F.E. Annanouch, P. Umek, C. Bittencourt, J.F. Colomer, E. Llobet, An

Ultrasensitive Room-Temperature HS Gas Sensor Based on 3D Assembly of CuO Decorated WS Nanomaterial, IEEE Sens. J. 21 (2021) 21212–21220. https://doi.org/10.1109/JSEN.2021.3103925.

[200] B. Martín-García, D. Spirito, S. Bellani, M. Prato, V. Romano, A. Polovitsyn, R. Brescia, R. Oropesa-Nuñez, L. Najafi, A. Ansaldo, G. D'Angelo, V. Pellegrini, R. Krahne, I. Moreels, F. Bonaccorso, Extending the Colloidal Transition Metal Dichalcogenide Library to ReS 2 Nanosheets for Application in Gas Sensing and Electrocatalysis, Small. 15 (2019). https://doi.org/10.1002/smll.201904670.

[201] Y. Xia, C. Hu, S. Guo, L. Zhang, M. Wang, J. Peng, L. Xu, J. Wang, Sulfur-Vacancy-Enriched MoS2 Nanosheets Based Heterostructures for Near-Infrared Optoelectronic NO2 Sensing, ACS Appl. Nano Mater. 3 (2020) 665–673. https://doi.org/10.1021/acsanm.9b02180.

[202] H. Tang, Y. Li, R. Sokolovskij, L. Sacco, H. Zheng, H. Ye, H. Yu, X. Fan, H. Tian, T.L. Ren, G. Zhang, Ultra-High Sensitive NO2 Gas Sensor Based on Tunable Polarity Transport in CVD-WS2/IGZO p-N Heterojunction, ACS Appl. Mater. Interfaces. 11 (2019) 40850–40859. https://doi.org/10.1021/acsami.9b13773.

[203] B. Zong, Q. Li, X. Chen, C. Liu, L. Li, J. Ruan, S. Mao, Highly Enhanced Gas Sensing Performance Using a 1T/2H Heterophase MoS 2 Field-Effect Transistor at Room Temperature, ACS Appl. Mater. Interfaces. 12 (2020) 50610–50618. https://doi.org/10.1021/acsami.0c15162.

[204] A.M. Afzal, M.Z. Iqbal, G. Dastgeer, G. Nazir, S. Mumtaz, M. Usman, J. Eom, WS 2 /GeSe/WS 2 Bipolar Transistor-Based Chemical Sensor with Fast Response and Recovery Times, ACS Appl. Mater. Interfaces. 12 (2020) 39524–39532. https://doi.org/10.1021/acsami.0c05114.

[205] A. Azizi, M. Dogan, H. Long, J.D. Cain, K. Lee, R. Eskandari, A. Varieschi, E.C. Glazer, M.L. Cohen, A. Zettl, High-Performance Atomically-Thin Room-Temperature NO 2 Sensor, Nano Lett. 20 (2020) 6120–6127. https://doi.org/10.1021/acs.nanolett.0c02221.

[206] J.-L. Fan, X.-F. Hu, C. Fu, W.-W. Qin, X.-J. Min, J.-W. Zhao, L.-B. Luo, W. Zhang,

Few-Layer PdSe 2 Nanofilm/Si Heterojunction for Sensing NO 2 at Room Temperature, ACS Appl. Nano Mater. 4 (2021) 7358–7370. https://doi.org/10.1021/acsanm.1c01339.

CHAPTER 2

Synergistic effect of CeO_2 nanoparticles and WO_3 nanowires in gas sensing applications

Synergistic effect of CeO_2 nanoparticles and WO_3 nanowires in gas sensing applications

Shuja Bashir Malik[1], Karol V. Mejia-Centeno[2], Paulina R. Martínez-Alanis[2], Andreu Cabot[2,3], Frank Güell*[1,4], Fatima Ezahra Annanouch[1] and Eduard Llobet*[1]

[1] Universitat Rovira i Virgili, MINOS, Països Catalans 26, 43007 Tarragona, Catalunya, Spain.
[2] Catalonia Energy Research Institute – IREC, Jardins de les Dones de Negre 1, Sant Adrià de Besós, 08930, Barcelona, Catalunya, Spain.
[3] ICREA, Pg. Lluis Companys, 08010, Barcelona, Catalunya, Spain.
[4] ENFOCAT, Universitat de Barcelona, Martí i Franquès 1, 08028 Barcelona, Catalunya, Spain.
*Corresponding authors: eduard.llobet@urv,cat, frank.guell@ub.edu

Abstract

The search for a highly selective ethanol sensor is still an open challenge. Metal oxides still face selectivity issues when it comes to gas sensing especially in case of ethanol. Keeping this in sight, in this work we explore the sensing properties of WO_3 nanowires grown via the aerosol assisted chemical vapour deposition and decorated with CeO_2 nanoparticles by drop casting. The nanocomposites were characterized by X-ray diffraction, field emission scanning electron microscopy, energy dispersive X-ray, photoluminescence, Raman and X-ray photoelectron spectroscopies. Upon exposure to different gas analytes, the electrical characterization showed that sensors responded well to ethanol both under dry and humid conditions (RH= 50%, 25ºC), though the response towards ethanol decreased in humid atmospheres. The long-term stability was studied, and a gas sensing mechanism is introduced and discussed.

Keywords: metal oxide nanowires, gas sensors, nanoparticle decoration, AACVD, WO_3, CeO_2

2.1. Introduction

Air pollution as a result of rapid population boom and industrialization is a leading contributor to heart and lung diseases and premature deaths[1]. NO_2 is one of the main air pollutants among others like sulfur dioxide (SO_2), and ozone (O_3). The prime sources of NO_2 being burning of fossil fuels in automobiles, and industries. Volcanic eruptions and lightening are the natural sources of NO_2. On the other hand, carbon monoxide (CO) is a highly toxic, odourless, tasteless, and colourless gas. CO is a leading ecological pollutant in developing and developed nations[2]. Exposure to CO over extended periods leads to decreased oxygen-carrying capacity of blood as the affinity of the human blood to CO is 250 to 300 times higher than oxygen[3]. Moreover, the discharge of chemical contaminants from industries has received considerable attention as it is associated with the release of volatile organic compounds (VOCs)[4]. The presence of VOCs in our environment adversely effects human's health[5]. Even though ethanol is not among the most dangerous VOCs, it has received a wide attention for its multifarious applications. Ethanol is colourless and transparent at room temperature and pressure and highly volatile. It is widely used in the chemical industry, for example as a solvent in the synthesis of other organic chemicals or in paints, produced from agricultural products, ethanol is used as an additive to automotive gasoline, present in alcoholic beverages, food industry products and pharmaceuticals [6,7]. While ethanol consumption can lead to driving accidents, the exposure to ethanol vapours can lead, in the long term, to vomiting, eye irritation and drowsiness[8]. Furthermore, ethanol is also an inhibitor of central nervous system[9]. Additionally, ethanol vapours can form an explosive mixture in the air, thus making it potentially dangerous among other VOCs[4]. All these aspects make it mandatory for the development of sensitive and cost-effective ethanol sensors that can be widely used. Chemoresistive sensors, especially metal oxide gas sensors (MOS) have been reported for monitoring pollutant gases and VOCs[10]. MOS have been commercially available for over

60 years[11]. Owing to their robustness, cost-effectiveness, sensitivity and small size, MOS sensors are attractive for a wide range of applications[12]. However, it is difficult to apply a single MOS in practical applications as they need high operating temperatures and are poorly selective.

To overcome these challenges, heterojunctions of metal oxides have been explored as a way to improve sensing performance, particularly selectivity [13–15] The heterojunctions are found to be enhancing the sensor performance[16,17]. Noteworthily, a variety of methods have been devised to fabricate different heterojunctions to enhance the ethanol gas sensing properties of MOS for example, InO_2 nanoparticles (NPs) modified GaN composites have been reported for detecting nitrogen dioxide [18], CeO_2 modified WO_3 for detecting n-Butanol [19] or $ZnWO_4/WO_3$ composites for the trace detection of H_2S[20]. Zhang et al. [21] reported bimetal-organic framework (BMOF)-derived porous Co_3O_4-ZnO heterojunction nanofibers. The sensors recorded a response of R_a/R_g of 101.5 at 275ºC for 100 ppm of ethanol. Similarly, Li et al. [22] reported CeO_2-TiO_2 porous heterojunction nanosheets derived from BMOFs. The porous nanosheets exhibited response of 41.72 towards 50 ppm of ethanol at 250ºC. On the other hand, Doan et al. [23] reported heterojunctions of n-ZnO/p-Co_3O_4. The sensors showed high response, outstanding selectivity, and good repeatability for low concentrations of ethanol (1 ppm) at 300ºC. Fang et al. [24] used indium containing MOFs as sacrificial templates for preparing hollow structured metal oxides (In_2O_3 hollow microtubes). The In_2O_3 microtubes were decorated by the Pr-doped SnO_2 NPs. The heterojunctions showed a response of 75 towards 50 ppm ethanol at the optimum temperature, 240ºC. Cao et al. [25] reported double-layer nanofilm by sputtering SnO_2 and co-sputtering $SnO_2/ZnSnO_3$ porous top layer with SnO_2 and ZnO targets. The sensors showed a response of 11.5 towards 50 ppm ethanol at 290ºC. Wang et al. [26] reported ethanol gas sensors based on p-Bi_2O_3 and n-ZnO heterostructures. The sensors exhibited a response of 21.6 towards 100 ppm ethanol at 175ºC. Moreover, the

sensors were able to detect ethanol concentration ranging from 1 to 500 ppm. Li et al. [27] reported 3D SnO_2-ZnO aerogels by two step reactions and annealing process. UV irradiation in coordination with SnO_2-ZnO was used to detect very low concentration of ethanol, 10 ppb at 300ºC.

N-type semiconducting metal oxides (ZnO, WO_3, SnO_2, CeO_2) show stable physicochemical properties and response towards targeted gases, thus have been investigated in gas sensing applications[28–30]. Owing to its wide band gap, CeO_2 films exhibit a large baseline resistance at room temperature, thus requiring high operating temperatures[31]. CeO_2 shows excellent stability and quick response and recovery times, which are essential for enhancing the gas-sensing behaviour of CeO_2-based nano and microstructures[32]. Making efficient heterostructures with an efficient surface/interface charge transport mechanism for achieving good gas-sensing qualities at low operating temperatures is the most challenging problem for developing novel CeO_2-based sensors. Moreover, CeO_2 exhibits the oxidation-reduction (Ce^{4+}/Ce^{3+}) capabilities making it one of the desired materials for gas sensors, photocatalysis and electrochemical sensors. Owing to its unique electronic structure and lower tendency to form a hydrogen bond with interfacial water molecules, resulting in humidity independent gas sensing performances. Also, decorating WO_3 nanowires with CeO_2 significantly improves the ethanol sensing performance and excellent selectivity [33]. Employing CeO_2 nanoparticles with a size below 10 nm with WO_3 nanowires synergistically enhances the overall sensing performance of the sensors.Herein, WO_3 NWs were first synthesized via aerosol assisted chemical vapour deposition (AACVD) and then CeO_2 NPs were decorated onto the NWs by drop casting method. The sensing nanocomposites were characterized by field emission scanning electron microscopy (FESEM), X-ray diffraction (XRD), Raman spectroscopy, photoluminescence (PL) and X-ray photoelectron spectroscopy (XPS). The gas sensing properties of the pristine WO_3 NWs and CeO_2 decorated WO_3 NWs were analysed towards the

detection of ethanol vapours under dry and humid conditions. To check their selectivity, sensors were exposed towards different analytes such as CO, NO_2, and H_2.

2.2. Experimental section

2.2.1. WO_3 NWs synthesis

Pristine WO_3 NWs were grown directly on a commercial alumina substrate consisting of a pair of screen-printed interdigitated Pt electrodes (with 300 µm electrode gap) on one side and a platinum resistive heater meander on the back side. In a typical synthesis procedure, 50 mg of tungsten hexacarbonyl $W(CO)_6$ (Sigma Aldrich) was dissolved in a solution of acetone (CAS: 67-64-1) and methanol (CAS: 67-56-1) (3:1). The solution was ultrasonicated to ensure full solubilization. The solution was placed in an ultrasonic bath to generate aerosol. N_2 gas with a flow of 0.5 L/min and 1 L/min was used as a carrier to transport the aerosol to the alumina substrate preheated to 400ºC in a hot wall reactor. Different gas flows are used to obtain different morphologies of WO_3 NWs. Randomly oriented WO_3 NWs with pointed tips are obtained with high carrier gas flow of 1 L/min. On the other hand, WO_3 NWs with floral tops are obtained with low carrier gas flow of 0.5 L/min. The growth process takes approximately 40 minutes. The chamber is left to cool down naturally. Keeping in view our previous studies with WO_3 nanowires of similar morphology [34–36], we decided to proceed with the morphology studied in the manuscript, because our previous results have shown that this one leads to better sensing performance. The substrates with WO_3 NWs are annealed at 500ºC for 2 hours in a Carbolite CWF 1200 muffle furnace within a synthetic air environment. Annealing helps in removing any carbon residues from the solvents and results in fully oxidized WO_3 NWs.

2.2.2. CeO_2 NPs synthesis.

The CeO_2 NPs were synthetized according with the reported method by Berestok et al.[37]. In a 3-necked flask connected in a Schlenk line, 1 mmol of cerium (III) nitrate hexahydrate ($Ce(NO_3)_3{\cdot}6H_2O$, 99%, Sigma -Aldrich), 6 mmol of Oleylamine (OAm, 90%, Sigma -Aldrich) and 4 ml of 1- octadecene(ODE, 90% Sigma-Aldrich) were added. The reaction mixture was degassed at 80°C for 30 min with an argon flux. After degassing, the mixture was heated at 300°C for one hour and then cooled to 160°C. Once at 160°C, 2 ml of toluene (analytical grade, Panreac) were added. The reaction mixture was dried under vacuum at 60°C. In order to eliminate the organic residues, the dried solid obtained was washed with 25 ml of acetone and subsequently centrifuged at 6500 rpm for 6 minutes. The solid was then washed three more times with 25 mL of chloroform followed by a final wash with acetone. All the washing steps were followed by a centrifugation step at 6500 rpm for six minutes. The final product was dried in vacuum for 40 minutes at room temperature. Finally, the product was placed in an oven under air flux with a ramp of 5ºC /min at 400°C for 4 hours.

2.2.3. CeO_2 NPs deposition on WO_3 NWs

The homogeneous suspension of 10 mg of CeO_2 NPs in 15 ml of chloroform was prepared by mixing in a 20 mL glass. 20 µl of the suspension was drop casted onto the WO_3 NWs substrates over a hot plate at 40ºC. Finally, the substrate was heated in an oven under air flux with a ramp of 5ºC /min at 400°C for 4 hours.

2.2.4. Characterization techniques

The morphology of the WO_3 NWs decorated with CeO_2 NPs was examined using FESEM from Thermo Scientific Scios 2. Energy-dispersive X-ray (EDX) was performed in the same FESEM equipment. XRD measurements were made using a Bruker-AXS D8-Discover diffractometer equipped with parallel incident beam (Göbel mirror), vertical θ-θ goniometer, XYZ motorized stage and with a GADDS (General Area Diffraction System). Samples were placed directly on

the sample holder for reflection analysis. An X-ray collimator system allows to analyze areas of 500 μm. The X-ray diffractometer was operated at 40 kV and 40 mA to generate Cukα radiation. The GADDS detector was a VÅNTEC-500 (silicon strip technology) placed at 15cm from the sample. Three frames were collected (2D XRD pattern) that covered at such distance a range from 18 up to 80º 2θ. The exposition time was 300 s per frame. The resulting images were 2θ integrated to obtain a 2θ conventional diffractogram. The elemental and chemical composition was studied via XPS with a PHI 5500 Multitechnique System equipped with a monochromatic X-ray radiation source of Al Kα (1486.6 eV) at 350 W. The sample was placed perpendicular to the analyser axis and calibrated using the 3d5/2 line of Ag with a full width at half maximum (FWHM) of 0.8 eV. The diameter circle of the analysed area was 0.8 mm. The resolution for the general and depth profile spectra were 187.5 eV of pass energy at 0.8 eV/step, and 23.5 eV of pass energy at 0.1 eV/step, respectively. All measurements were made in an ultra-high vacuum (UHV) chamber with pressure (5·10-9 and 2·10-8 torr). The binding energies (BE) values are referred to the 1s BE at 284.8 eV. Component analysis has been performed by constructive curve joint Shirley and Tougaard functions to determine the peak background, and the line shape of the curves was fitted with mixed Lorentzian-Gaussian. The Raman spectroscopy measurements were obtained using a Renishaw laser 514 nm, ion argon-Novatech, 25 mW. The PL measurements at room temperature were made using a chopped Kimmon IK Series He-Cd laser (325 nm and 40 mW). Fluorescence was dispersed with an Oriel Corner Stone 1/8 74000 monochromator, detected using a Hamamatsu H8259-02 with a socket assembly E717-500 photomultiplier, and amplified through a Stanford Research Systems SR830 DSP. A filter of 360 nm was used against stray light. All spectra were corrected for the response function of the setups.

2.2.5. Gas sensing tests

The gas sensing characteristics of pristine and CeO_2 loaded WO_3 sensors were measured using a homemade detection system. Figure S1 shows the schematic of the homemade measurement setup. The sensors were placed inside an inert, airtight Teflon® chamber (35 mL in volume) under a continuous gas flow of 100 sccm. The chamber can accommodate up to 4 sensors simultaneously. Calibrated gas bottles of hydrogen, ethanol, nitrogen dioxide and carbon monoxide balanced in dry air were employed. The carrier gas was zero-grade dry air. The gas analysis was set as pulses consisting of target gas concentrations with intercalated steps of dry air to recover to the baseline at a 100 ml min^{-1} constant flow. Reproducible concentrations of different gases were delivered into the chamber with the help of a computer-driven automated mass-flow control system. 5, 10, 15, and 20 ppm of ethanol, 1, 5, 7.5, 10, 15, and 20 ppm of carbon monoxide, 50 and 100 ppm of hydrogen and 100, 250, 500 and 1000 ppb of nitrogen dioxide concentrations were tested. After exposing the sensors to different gases, the baseline was recovered under dry air. The electrical resistance of the sensors was measured using an Agilent-34972A multimeter data acquisition system. The sensors were exposed to a particular analyte for 10 minutes and in order to recover the initial baseline, the chamber was purged with dry air for 60 minutes. The sensors were tested at various operating temperatures from 100ºC to 250ºC in intervals of 50ºC to understand the effect of the temperature on the sensor responses. Prior to the deposition of the sensing layer on the transducer, the sensor heater was electrically characterized by applying a bias voltage to the heater and the corresponding current was analysed. The respective voltage and current values were plotted in a graph depicting relationship between

temperature and heater power consumption as a function of voltage. To analyse the effect of humidity and moisture cross-sensitivity on the sensing performance of the sensors, a liquid mass flow was employed for specific measurements in humidified backgrounds.

2.3. Results and discussion

2.3.1. Structural and morphological characteristics

Bare tungsten trioxide (WO_3) nanowires were successfully grown and directly integrated onto MEMS-based gas sensor substrates. Bare WO_3 nanowires were decorated with CeO_2 nanoparticles via drop casting technique. The colour of as deposited films was dark blue, which is an indication of having partially reduced tungsten oxide (WO_{3-x})[38], and also amorphous carbon from burnt organic solvents. The as-grown samples were annealed for 2 hours at 500°C in a muffle furnace under synthetic air. This annealing treatment at 500°C changes the thin film colour to pale yellow greenish, indicating the removal of most of the carbon impurities and that a nearly stoichiometric tungsten trioxide is achieved. Field emission scanning electron microscopy (FESEM) images give a good impression of the size and morphology of the CeO_2 decorated WO_3 nanostructures and are displayed in Figure 2.1. WO_3 nanowires with floral tops are obtained with low carrier gas flow of 0.5 L/min. The average diameter of the flowers is calculated as 798 nm. On the other hand, randomly oriented nanowires with pointed tips are obtained with high carrier gas flow of 1 L/min. The average length of the nanowires is higher than 1 µm. Nanowires show a tendency to grow vertically aligned to the substrate and are homogeneously dispersed across the entire electrode area of the commercial alumina substrates. Owing to the low loading of the CeO_2 nanoparticles, the CeO_2 nanoparticles were not seen in FESEM. However, EDX analysis of the thin films reveals the presence of CeO_2 decorations, Figure S2(b and c). Peaks attributed to Al in the EDX diffractogram comes from the commercial alumina substrate Figure S2 (c). More details about morphology of the

nanowires are detailed in Table S1 and TEM details of CeO_2 nanoparticles are illustrated in Figure S3.

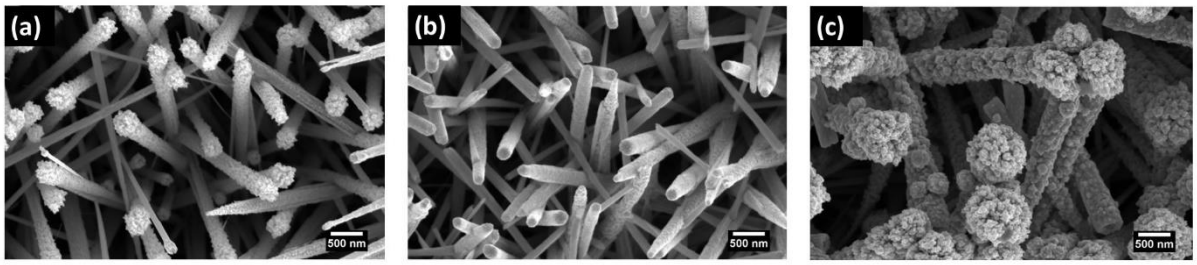

Figure 2.1 FESEM images (a) pristine WO_3 nanowires, (b) CeO_2 decorated WO_3 nanowires, and (c) CeO_2 decorated WO_3 floral tops nanowires.

The nanowires were analysed by XRD to investigate the crystallographic structures of pure and CeO_2 decorated WO_3 as depicted in Figure 2.2. The diffraction patterns of WO_3 in all the samples were indexed to ICDD card number 83-0951. It can be concluded from characteristic peaks that WO_3 has a monoclinic crystal structure and matches the space group of P21/n with lattice parameters, a= 7.301 Å, b= 7.538 Å, and c= 7.689 Å. WO_3 shows an intense diffraction peak at $2\theta = 24.36^{o}$ with preferred orientation in the (200) direction. The WO_3 nanowires synthesized are single crystalline. The diffraction patterns of CeO_2 were indexed to ICDD card number 89-8436. From the diffraction pattern of CeO_2, it can be concluded that CeO_2 has a cubic crystal structure matching the space group Fm-3m with the lattice parameters a= 5.41120 Å. At 2θ=28.54, the peaks of WO_3 and CeO_2 almost coincide, hence in Figure 2.2 (b) and (c), the peak is intense than Figure 2.2 (a), pristine WO_3.

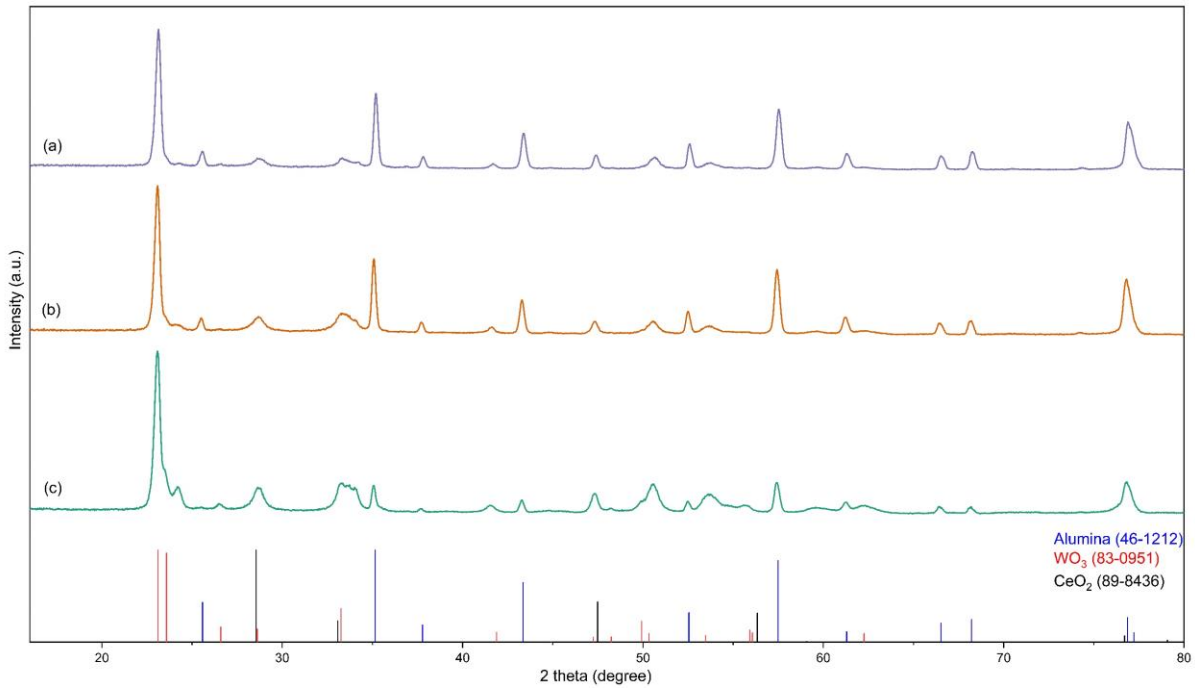

Figure 2.2 XRD diffractograms recorded of (a) WO_3, (b) CeO_2 decorated WO_3 randomly oriented and (c) CeO_2 decorated WO_3 with floral tops.

The PL spectra measured at room temperature are presented in Figure 2.3. The intensity of each spectrum was normalized to the maximum emission intensity for relative comparison. By pumping at 325 nm, we observed an emission peak of the WO_3 nanowires at around 450 nm (2.75 eV) with a FWHM of 370 meV. When decorating the WO_3 nanowires with the CeO_2 NPs, the emission peak is shifted to 490 nm (2.53 eV) and 530 nm (2.34 eV) and the FWHM are around 1150 and 950 meV, respectively. This broadening observed on the FWHM indicates that the quantity of intrinsic defects is higher when decorating the WO_3 nanowires with the CeO_2 nanoparticles [39].

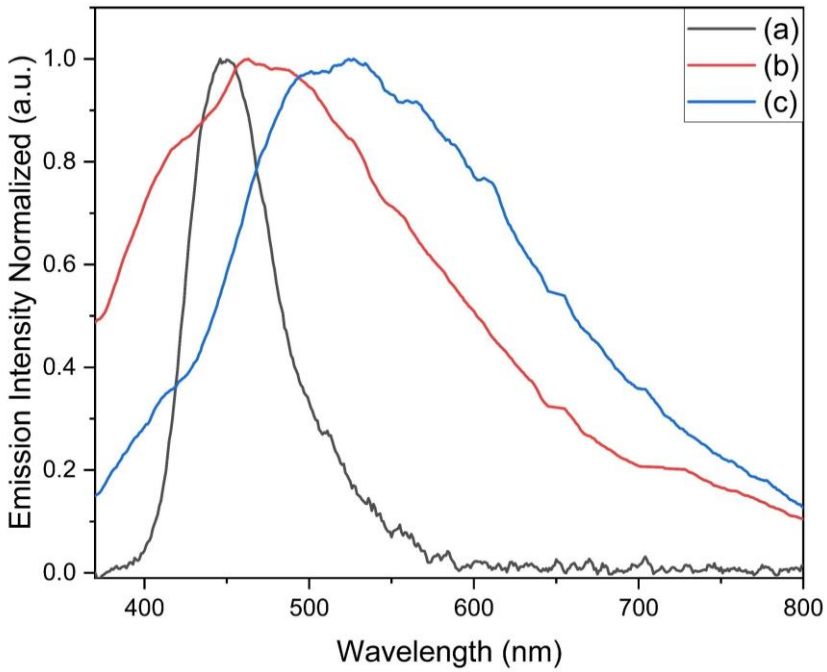

Figure 2.3 PL spectra of (a) WO_3, (b) CeO_2 decorated WO_3 randomly oriented nanowires, and (c) CeO_2 decorated WO_3 nanowires with floral tops.

Figure 2.4 shows the survey XPS spectra of the CeO_2/WO_3 NWs and CeO_2/WO_3 floral tops NWs. The analysis by XPS of the samples were performed using internal charge reference to C 1s at binding energy (BE) of 284.8 eV. Besides the C 1s peak corresponding to adventitious carbon, a low intensity peak at BE of 287-290 eV region was assigned to the presence of carbonate species. These carbonate species could be formed from CO_2 when the samples are exposed to ambient conditions. Figure 2.4(b) shows the spectra corresponding to the O1*s* core level, which can be deconvoluted into two components. The main contribution is by the band centred at around 530.3 eV BE, which could be related to lattice oxygen (O_L). The broad band centred at around 531.9 eV binding energy indicates the presence of hydroxyl groups (OH). Hydroxyl contribution in the CeO_2/WO_3 NWs sample is higher than in the CeO_2/WO_3 floral tops NWs sample. The W4f BE shows two main peaks assigned to W^{6+} at 35.9 and 38.2 eV corresponding to $W4f_{7/2}$ and $W4f_{5/2}$, respectively. There are two minority peaks assigned to W^{5+} species at 34.9 and 36.5 eV corresponding to $W4f_{7/2}$ and $W4f_{5/2}$, respectively. The Ce 3d BE shows a complicated spectrum due the mixture of $Ce3d_{5/2}$ and $Ce3d_{3/2}$ species at 882.3 eV

and 900.7 eV in the samples and their satellites. As per the spectra, the atomic concentration of the exposed Ce is increased, and the W atoms reduced in CeO_2/WO_3 NWs sample (Ce 15%, W 55%, O 37%) with respect to the CeO_2/WO_3 floral tops NWs sample (Ce 8%, W 48%, O 37%). These results suggest that CeO_2/WO_3 ratio could be responsible for the different sensing behaviour of the samples. The XPS results are in line with the XRD results.

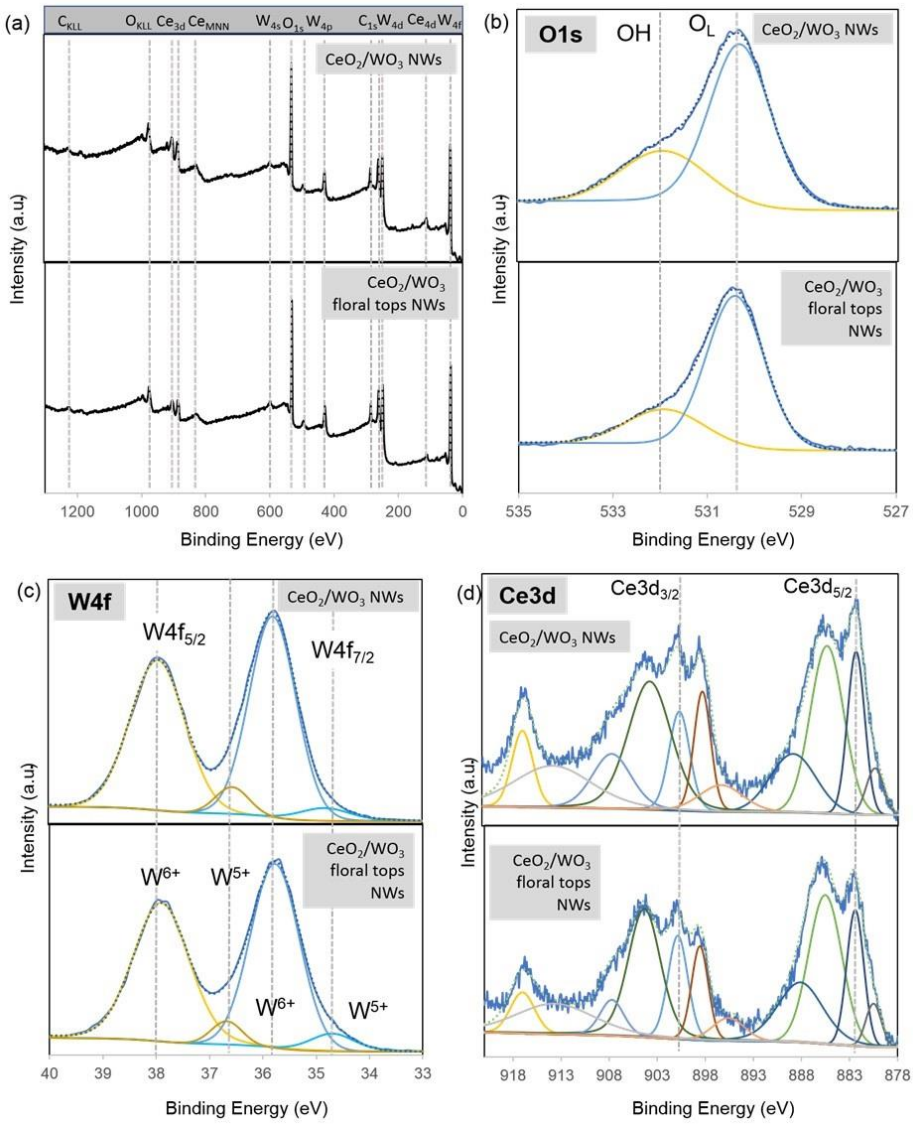

Figure 2.4 XPS spectra of the CeO_2/WO_3 floral tops NWs and the CeO_2/WO_3 NWs (a) full spectra, (b) O1s, (c) W4f and (d) Ce3d BE.

Raman spectra of as prepared samples is presented in Figure 2.5. The spectrum indicates that all the samples have similar spectra. As can be seen from the Raman spectrum, three main regions appear at 600-900, 200-400 and below 200 cm^{-1} for WO_3 vibrations. The regions

respectively correspond to stretching, deformation and lattice modes [40]. The WO_3 nanowire films exhibited well-defined Raman bands at 272, 326, 715 and 805 cm^{-1}. These bands are characteristic of the four intense vibrational modes of monoclinic WO_3 [41] confirming the XRD results that the WO_3 deposited by AACVD belongs to monoclinic phases. Also, the peak at 133 cm^{-1} is attributed to the relative translational or rotational motions of WO_6 octahedral units in the same unit cell (lattice models) [42]. The intense bands at 272 and 326 cm^{-1} are due to the bending modes of the bridging oxygen (W-O-W), whereas the bands at 715 and 805 cm^{-1} are assigned to the stretching modes (W + 6-O) [41]. There are no visible peaks directly corresponding to CeO_2 which is because of the low quantity of the CeO_2.

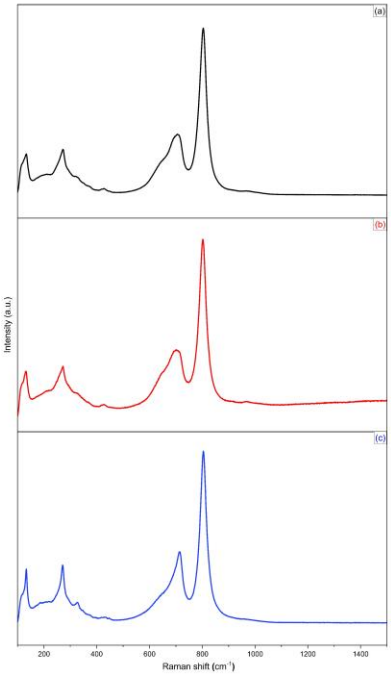

Figure 2.5 Raman spectra, (a) WO_3, (b) randomly oriented CeO_2 decorated WO_3 nanowires and (c) CeO_2 decorated WO_3 nanowires with floral tops.

2.3.2. Gas sensing response analysis

Gas sensing tests were carried out at different concentrations of ethanol by using direct-current resistance measurements. The gas sensing characteristics of pristine and CeO_2 decorated WO_3 sensors towards oxidising gas (NO_2) as well as reducing gases (CO, ethanol, H_2) has been analysed and the sensor responses are calculated for oxidising gases as $R = \frac{R_{gas}}{R_{air}}$ and $R = \frac{R_{air}}{R_{gas}}$

for reducing gases. Pristine and CeO_2-decorated WO_3 nanowires were tested at temperatures ranging from room temperature up to 250°C in order to understand the effect of the temperature on the sensor responses. More than three replicates of the measurements were performed to assess the reproducibility of the results. Figure 2.6 displays the response of the different sensors tested towards 20 ppm of ethanol as a function of the operating temperature. None of the sensors responded to any concentrations of ethanol when operated below 100°C, especially at RT or at 50°C. Also, the response suddenly dropped beyond 250°C and became unreproducible. This is because at too high temperatures the gas molecules start to desorb from the surface of the metal oxides[43]. Furthermore, at high temperatures, the oxidation of the surface of WO_3 proceeds faster than the reduction caused by the ethanol[44,45]. Therefore, 250°C is the optimal working temperature for the pristine and CeO_2 decorated WO_3 nanowires and is adopted for all the investigations in case of ethanol sensing hereinafter.

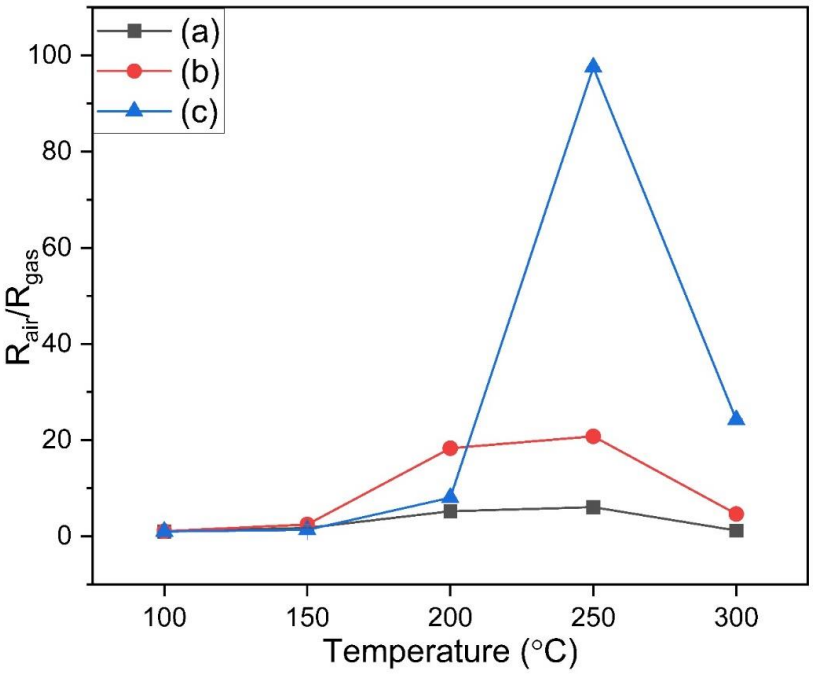

Figure 2.6 Sensor response to 20 ppm of ethanol as a function of operating temperature (a) WO_3, (b) randomly oriented CeO_2 decorated WO_3 nanowires and (c) CeO_2 decorated WO_3 nanowires with floral tops.

Figure 2.7 illustrates the resistance changes of pristine and CeO_2 decorated WO_3 nanowires towards ethanol pulses with concentrations ranging from 5 to 20 ppm at the working optimum

temperature (250ºC). When exposed to the reducing gas ethanol, the sensors displayed an n-type semiconducting behaviour, which is characterized by a decrease in the electrical resistance when exposed to ethanol vapours. The response of the sensors was stable as was demonstrated by full baseline resistance recovery. To check the reproducibility of the sensor responses, the sensors were re-exposed to 5 ppm of ethanol as is shown in Figure S4. The sensors showed reproducible behaviour. The corresponding gas-sensing responses calculated from the change in resistance of pristine WO_3 and CeO_2 decorated WO_3 nanowires are plotted as a function of the ethanol concentration as shown in Figure 2.8. The results of the pristine WO_3 are similar to the ones reported in our previous works [35]. As is evident from the results, the decoration of WO_3 nanowires with CeO_2 has greatly enhanced the sensitivity towards ethanol. At the lowest concentration of ethanol used (5 ppm), the response of CeO_2 decorated floral top WO_3 nanowires is 72 times higher than the pristine WO_3. The sensitivity of the pure WO_3 sensor towards ethanol was very small as compared to the CeO_2 decorated WO_3 sensors especially the ones with floral top nanowires. The response and concentration follow the power law. The details are illustrated in Figure S5. The sensor's corresponding resistance changes towards the lowest concentration of ethanol (5ppm) at 250ºC are shown in Figure S4. The variation of baseline resistance as a function of temperature in is shown in Figure S6.

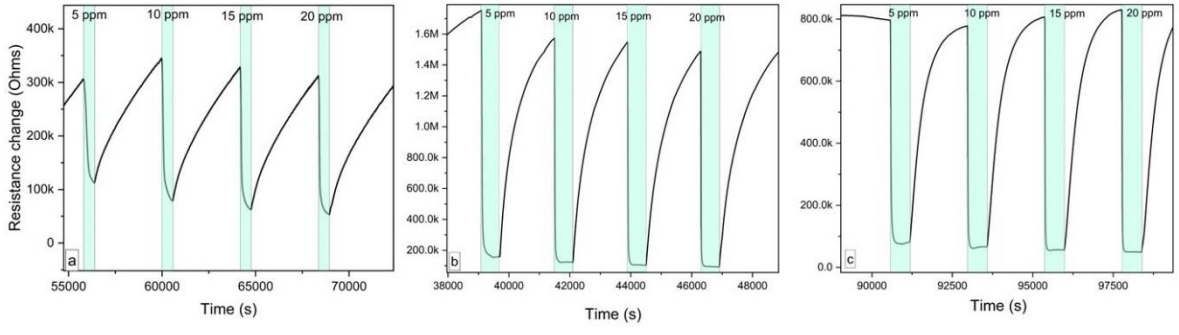

Figure 2.7 Film resistance changes (a) WO_3, (b) randomly oriented CeO_2 decorated WO_3 nanowires (c) CeO_2 decorated WO_3 nanowires with floral tops towards various ethanol concentrations at 250ºC.

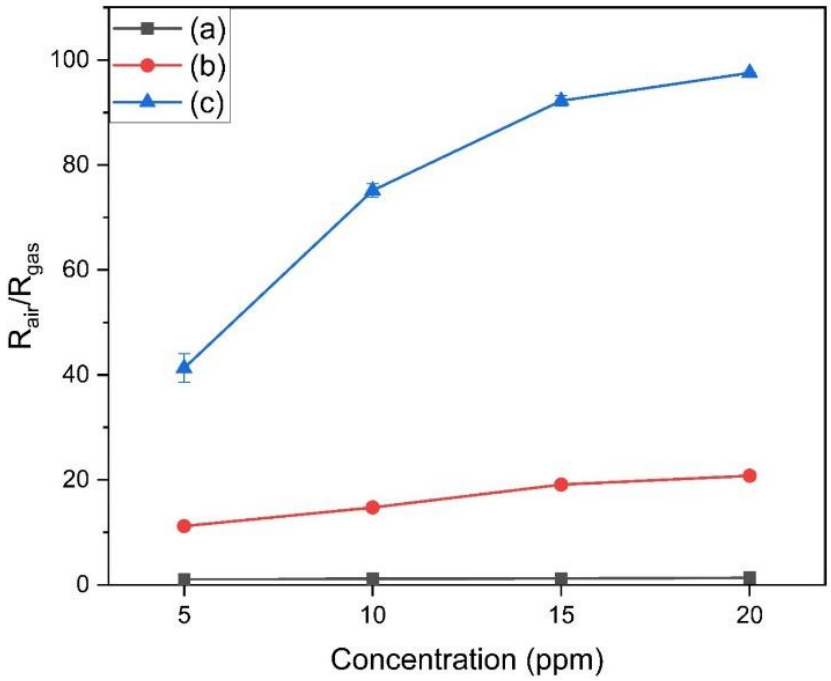

Figure 2.8 Sensor responses towards various ethanol concentrations at 250ºC (a) WO_3, (b) CeO_2 decorated WO_3 randomly oriented nanowires, and (c) CeO_2 decorated WO_3 nanowires with floral tops.

2.3.2.1. Nitrogen dioxide (NO_2)

The gas sensors were exposed towards different concentrations of NO_2 ranging from 100 ppb to 1 ppm. In our previous research[35], it was found that the response of WO_3 nanowires towards NO_2 decreases beyond 200ºC. We found the same trend in case of CeO_2 decorated WO_3 nanowires as well. Figure S7 shows the resistance change of the CeO_2 decorated WO_3 nanowires towards 500 ppb of NO_2 at 150ºC for pristine WO_3 and at 200ºC for CeO_2 decorated WO_3 nanowires. The response of the sensors towards various NO_2 concentrations is shown in Figure 2.9.

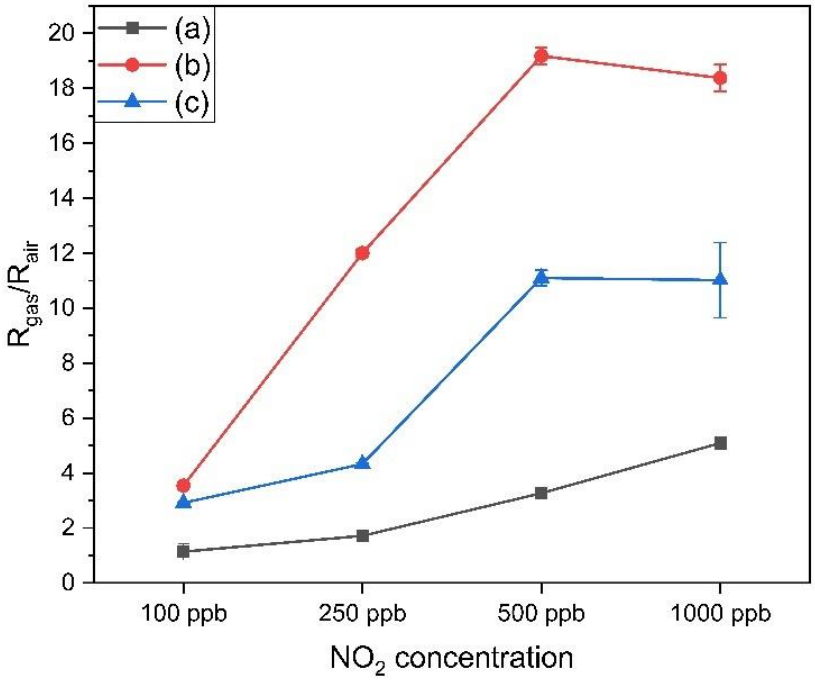

Figure 2.9 Sensor responses towards various NO_2 concentrations at 150ºC (a) WO_3, and at 200ºC for (b) CeO_2 decorated WO_3 randomly oriented nanowires, and (c) CeO_2 decorated WO_3 nanowires with floral tops.

Loading of tungsten trioxide with CeO_2 results in an increased responsiveness towards NO_2. In case of CeO_2 decorated WO_3, the maximum response was recorded at 200ºC while as the response of pristine WO_3 is maximum at 150ºC and starts to decrease with the increase of the temperature as is shown in Figure 2.10. The same trend was recorded in our previous research[36] for pristine WO_3 nanowires. Gas sensing results towards CO and H_2 are in presented in the supporting file.

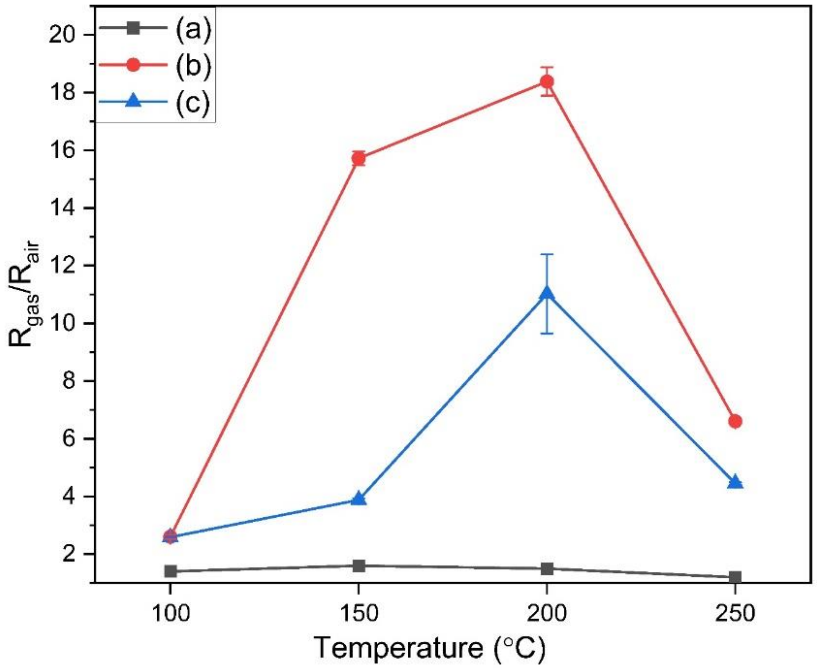

Figure 2.10 NO_2 sensing results for 1 ppm (a) WO_3, (b) CeO_2 decorated WO_3 randomly oriented nanowires, and (c) CeO_2 decorated WO_3 nanowires with floral tops.

2.3.3. Selectivity test

Selectivity is an important parameter to be considered in gas detection, since it demonstrates the ability of the sensor to discriminate the target gas from interfering gases. Herein, we chose H_2, NO_2 and CO as interfering gases; their concentrations were equal or higher than that of ethanol, except for NO_2, where its concentration was 1 ppm, which is actually a very high concentration (e.g., the EPA has set the annual average NO_2 standard of 53 ppb), OSHA PEL recommendations for CO (25 ppm) and NO_2 (1 ppm) for eight-hour average exposure. Figure 2.11 illustrates the obtained results. It is clear that incorporating CeO_2 in the WO_3 host matrix, enhances the responses towards ethanol especially in case of CeO_2 decorated WO_3 nanowires with floral tops. Indeed, at an operating temperature of 250ºC, the response of this sensor was 10-fold higher than that of pristine WO_3 and 5-fold higher than that of CeO_2 decorated WO_3 randomly oriented nanowires. Moreover, its responses towards the interfering gases, at the 250ºC, were negligible and very weak compared to the one of ethanol. Therefore, CeO_2

decorated WO_3 nanowires with floral tops exhibit excellent sensitivity and selectivity towards ethanol.

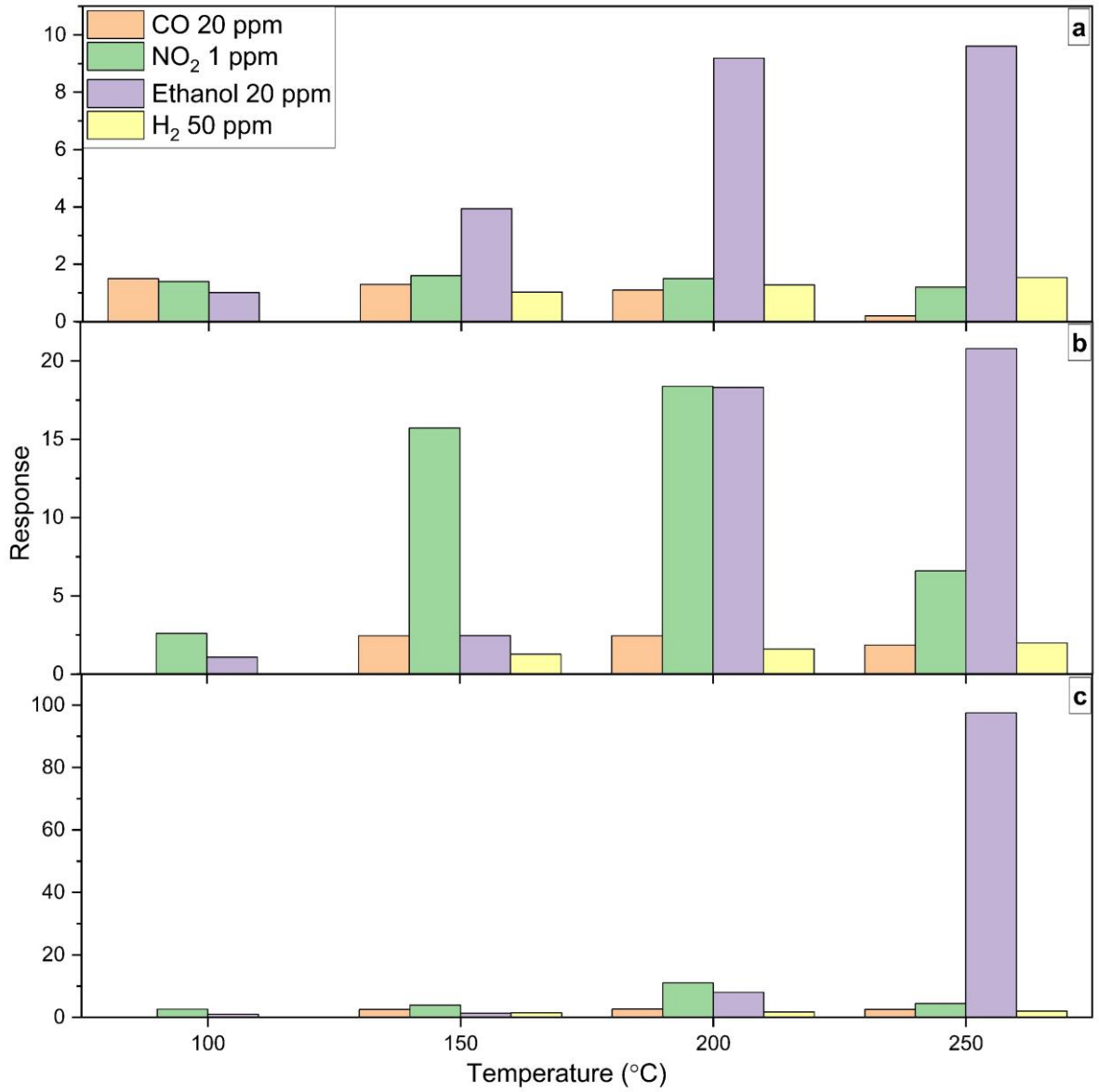

Figure 2.11 Selectivity histogram of (a) WO_3, (b) CeO_2 decorated WO_3 randomly oriented nanowires, and (c) CeO_2 decorated WO_3 nanowires with floral tops.

2.3.4. Humidity measurements

The impact of water vapour on the sensing performance is one of the most crucial aspects to consider while developing chemoresistive metal oxide gas sensors. The electrical properties and sensitivity of the metal oxide sensors is dramatically influenced by the presence of moisture. To study the effect of humidity on the sensor responses, the influence of 50% relative

humidity (RH) at RT on the sensor performance was also analysed. There is a 69% decrease in the sensing response in case of pristine WO_3 nanowires, 73% drop in the sensing response in case of CeO_2 decorated WO_3 floral nanowires and 76% decrease in case of CeO_2 decorated randomly oriented WO_3 nanowires under humid atmosphere. However, the baseline recovery in humid environment is more promising than in the dry conditions in case of CeO_2 decorated WO_3 nanowires as can be seen in Figure S12. There is comparatively less noise in the measured values under humid conditions than under dry conditions. The decrease in the response can be owed to the competition between the water molecules (formation of hydroxyl groups) and ethanol active sites[46]. Upon removal of the humidity, the sensors baseline resistances are recovered and so are the responses towards ethanol.

Table 2.1 summarizes the comparison of sensing properties of CeO_2 decorated WO_3 and previously published works. Compared to the majority of the works shown in the table, our sensors exhibit great sensitivity to the target gases at lower working temperatures. Also, our sensors can detect ethanol at low concentrations. Some studies do not report the humidity cross-sensitivity effects, despite ambient moisture significantly influences the electrical characteristics of gas sensors and impacts their sensitivity. Most reported results lack of data about the long-term stability of sensors. In our work, sensor responses have been gathered for more than 40 weeks, which has enabled assessing this aspect.

Table 2.1 Comparison of ethanol gas sensing performance of various sensors based on WO_3 and/or CeO_2 reported in literature.

Structure	**Host Matrix**	**Nps[$]**	**T_{op} (^oC)**	**Conc. (ppm)**	**Response**	**Selectivity test**	**Humidity effect studied**	**Reference**
CeO_2-WO_3	WO_3	CeO_2	250	20	97.6	Yes	Yes	This work
CeO_2-ZnO	ZnO	CeO_2	310	100	90	Yes	No	[47]
CeO_2-TiO_2	TiO_2	CeO_2	270	500	3.5	Yes	No	[48]
CeO_2-$ZnSnO_3$	$ZnSnO_3$	CeO_2	200	100	219.2	No	Yes	[49]
MoS_2/CeO_2	MoS_2	CeO_2	RT	50	7.5	Yes	Yes	[50]
CeO_2/ZnO	ZnO	CeO_2	310	100	90	Yes	No	[51]
WO_3	WO_3	-	250	50	20.5*	Yes	Yes	[12]
WO_3	WO_3	-	320	100	7.6	Yes	No	[52]

$ Nps: nanoparticles, T_{op} = operating temperature, * $R = \frac{G_{gas}-G_{air}}{G_{air}}$

2.3.5. Gas sensing mechanism

The interaction of the gas molecules with the semiconductor surface includes adsorption onto the surface, electronic charge transfer and reduction/oxidation process of the semiconductor [53,54]. The atmospheric molecular oxygen reacts with the oxygen vacancies in the film chemisorbing oxygen in the form of O_2^-, O^-, O^{2-} depending on the sensor's operating temperature [55,56]. The reactions are depicted in equation 1, 2 and 3. The interactions create oxygen adsorbates and deplete electrons from the conduction band of the *n*-type semiconductor. The chemisorbed oxygen species on the metal oxide semiconductor surface generate extrinsic surface acceptor states immobilizing conduction band electrons leading to the formation of a

depletion layer. When ethanol gas interacts, these chemisorbed oxygen species serve as charge carriers and are then extracted from the surface when the chemisorbed oxygen is consumed.

$$O_{2\,(gas)} + e^- \rightarrow O^-_{2\,(ads)}\ (80\ ℃ - 150\ ℃) \qquad \text{Equation 1}$$

$$O^-_{2\,(ads)} + e^- \rightarrow 2O^-_{(ads)}\ (150\ ℃ - 260\ ℃), \qquad \text{Equation 2}$$

$$O^-_{(ads)} + e^- \rightarrow O^{2-}_{(ads)}\ (300\ ℃ - 500℃) \qquad \text{Equation 3}$$

With the exposure of sensors to ethanol, reaction takes place between ethanol and the oxygen ions releasing the electrons back to the heterojunction. This leads to the generation of more electrons in the material leading to the narrowing of the electron depletion layer and the potential barrier between CeO_2 and WO_3 gets reduced significantly [57]. The thickness of the depletion layer gets reduced due to the release of more electrons into the conduction band of the nanowires as described in equation 4.

$$C_2H_5OH + 6O^- \rightarrow 2CO_2 + 3H_2O + 6e^- \qquad \text{Equation 4}$$

This leads to the decrease in the resistance of the sensing layers in the ethanol environment. Moreover, when exposed to a reducing gas like ethanol at a temperature (optimum working temperature) providing sufficient thermal energy for surface reactions, the reactive gas oxidizes due to oxygen ions, releasing trapped electrons to the conduction band in turn leading to the decrease in the sensor resistance. There is a possibility of intermediate reaction products like ethylene and water [58,59] due to the dehydration of WO_3 [12] as described in equation 5. The gas sensing mechanism is illustrated in Figure 2.12.

$$C_2H_5OH \rightarrow C_2H_4 + H_2O \qquad \text{Equation 5}$$

Upon being exposed to synthetic air, oxygen molecules adsorb onto the active sites of the CeO_2 decorated WO_3. This leads to the extraction of electrons from the nanowire's conduction band, leading to the formation of O^- species as dictated by the operating temperature (250ºC). An electron depletion layer is generated on the nanowires reducing the conduction band channel and increasing the resistance of the sensors. This also alters the depletion layer thickness and

improves the material conductivity. The potential barrier of the CeO_2-WO_3 heterojunction gets is increased due to the generation of thicker electron depletion layer when the sensors are exposed to air [57]. During the ethanol free environment (recovery cycle), the removed oxygen species are replenished, immobilizing the surface conduction electrons leading to the increase of the sensor resistance back to the original values. The CeO_2 is known to possess high-mobility oxygen vacancies, contributing to increasing the number of ionosorbed oxygen species at the surface, thus trapping electrons injected via the conduction band of the WO_3. This leads to an increase in the baseline resistance of the sensitive film. Also, CeO_2 acts as a sensitizer material while as the WO_3 provides a high work function. The work function of WO_3 (4.8 eV) surpasses that of CeO_2 (4.69 eV) [33] leading to an electron transfer from conduction band of CeO_2 to that of WO_3. This results in a higher resistance of CeO_2-WO_3 hybrid compared to pristine WO_3 nanowires. Due to the small size of the CeO_2 nanoparticles (average size 3 nm), the electron accumulation layer beneath the surface of WO_3 present at the CeO_2-WO_3 interface would easily be occupied by O_2 molecules. This leads to an increase in the number of electrons trapped by O_2 and in turn leads to generation of more chemisorbed oxygen species on the nanowire surfaces [29]. Increased number of oxygen species react with more ethanol molecules, leading to release of more electrons back to the conduction band of the WO_3. Also, at the interface of CeO_2-WO_3 hybrid, the hole accumulation layer of CeO_2 would further increase the number of electrons releasing from the oxygen species when the hybrid is exposed to ethanol vapours. These combined effects enhance the release of more electrons back to CeO_2-WO_3 hybrid than pristine WO_3 nanowires, ultimately responding strongly to ethanol.

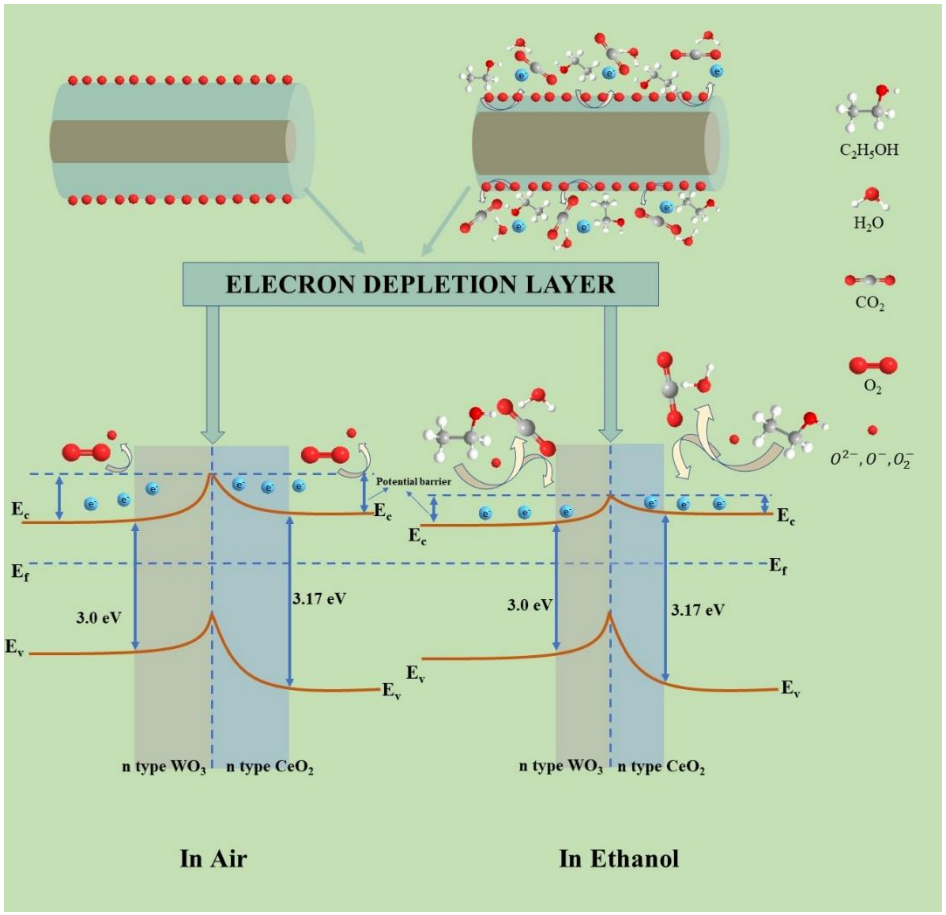

Figure 2.12 Proposed sensing mechanism of ethanol detection by CeO_2 decorated WO_3 nanowires.

2.3.6. Stability results

The sensor responses were checked over a period of 40 weeks. During this period sensors were regularly exposed to ethanol and to changing humidity backgrounds. Figure 2.13 shows the long-term stability of responses towards 5 ppm ethanol at 250ºC. There is a 47.28% decrease in the response from week 1 to week 19 in case of pristine WO_3 nanowires. This decrease is 56.04% and 57.69% for CeO_2 decorated WO_3 nanowires with floral tops and for randomly oriented CeO_2 decorated WO_3 nanowires, respectively. However, from week 19 to week 40, the responses of CeO_2 decorated WO_3 clearly stabilize, which is not the case for pristine WO_3. The sensors were not subjected to any sort of ageing prior to starting the gas sensing measurements. Also, the sensors were exposed towards different gas species for selectivity tests. We perceive that the decrease in the sensor response from week 1 to week 19 is due to

the ageing of the surface and around week 19 the surface is already aged and hence shows stable responses.

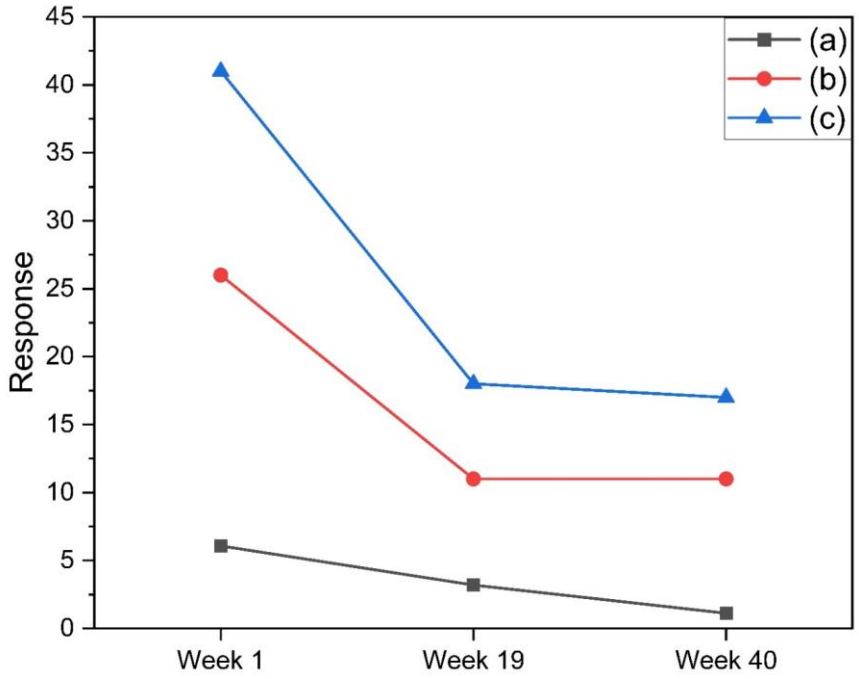

Figure 2.13 Long term stability study for the responses (a) WO_3, (b) CeO_2 decorated WO_3 randomly oriented nanowires, and (c) CeO_2 decorated WO_3 nanowires with floral tops towards 5 ppm ethanol at 250ºC.

2.4. Conclusions

WO_3 nanowires have been successfully deposited onto alumina substrates by a one-step AACVD method. CeO_2 decorated WO_3 makes a desired heterojunction which demonstrates an effective route to bring functionality to WO_3. Pristine and CeO_2 decorated WO_3 nanowires show high purity and crystallinity, as determined by XRD, FESEM and Raman techniques. The gas sensing experiments showed that the optimum working temperature is lower than in most metal oxide-based gas sensors. The sensors produced and studied show highly repeatable results with good long-term stability. These results clearly show the impact of decorating the WO_3 nanowires with CeO_2 for detecting ethanol.

2.5. Acknowledgements

This research is funded in part by MICINN grant no. TED2021-131442B-C31, and by AGAUR grant no. 2021 SGR 147. Shuja Bashir Malik is supported by Martí-Franquès Research grants Programme, Doctoral grants – 2019, (2019PMF-PIPF-14). E. Llobet is supported by the Catalan Institution for Research and Advanced Studies via the 2018 Edition of the ICREA Academia Award.

2.6. References

[1] A. Paleczek, D. Grochala, K. Staszek, S. Gruszczynski, E. Maciak, Z. Opilski, P. Kałużyński, M. Wójcikowski, T.V. Cao, A. Rydosz, An NO2 sensor based on WO3 thin films for automotive applications in the microwave frequency range, Sensors Actuators B Chem. 376 (2023). https://doi.org/10.1016/j.snb.2022.132964.

[2] Y. Zhang, L. Zhu, C. Qin, Y. Wang, J. Cao, Bimetal PtPd functionalized Bi2MoO6 microspheres for conductometric detection of CO: A combined experimental and theoretical study, Sensors Actuators B Chem. 381 (2023). https://doi.org/10.1016/j.snb.2023.133461.

[3] J.J. Rose, L. Wang, Q. Xu, C.F. McTiernan, S. Shiva, J. Tejero, M.T. Gladwin, Carbon monoxide poisoning: Pathogenesis, management, and future directions of therapy, Am. J. Respir. Crit. Care Med. 195 (2017) 596–606. https://doi.org/10.1164/rccm.201606-1275CI.

[4] M.J. Ahemad, T.D. Le, D.S. Kim, Y.T. Yu, Bimetallic AgAualloy@ZnO core-shell nanoparticles for ultra-high detection of ethanol: Potential impact of alloy composition on sensing performance, Sensors Actuators B Chem. 359 (2022) 131595. https://doi.org/10.1016/J.SNB.2022.131595.

[5] V. Postica, A. Vahl, D. Santos-Carballal, T. Dankwort, L. Kienle, M. Hoppe, A. Cadi-Essadek, N.H. De Leeuw, M.I. Terasa, R. Adelung, F. Faupel, O. Lupan, Tuning ZnO Sensors Reactivity toward Volatile Organic Compounds via Ag Doping and Nanoparticle Functionalization, ACS Appl. Mater. Interfaces. 11 (2019) 31452–31466. https://doi.org/10.1021/acsami.9b07275.

[6] S. Liu, W. Zeng, Y. Li, Synthesis of spherical WO3·H2O network for ethanol sensing application, Mater. Lett. 253 (2019) 42–45. https://doi.org/10.1016/J.MATLET.2019.06.037.

[7] C.S. Reddy, G. Murali, A.S. Reddy, S. Park, I. In, GO incorporated SnO2 nanotubes as fast response sensors for ethanol vapor in different atmospheres, J. Alloys Compd. 813 (2020) 152251. https://doi.org/10.1016/J.JALLCOM.2019.152251.

[8] Y. Wang, C. Liu, L. Wang, J. Liu, B. Zhang, Y. Gao, P. Sun, Y. Sun, T. Zhang, G. Lu, Horseshoe-shaped SnO2 with annulus-like mesoporous for ethanol gas sensing application, Sensors Actuators B Chem. 240 (2017) 1321–1329. https://doi.org/10.1016/J.SNB.2016.07.160.

[9] Q. Li, D. Chen, J. Miao, S. Lin, Z. Yu, D. Cui, Z. Yang, X. Chen, Highly sensitive sensor based on ordered porous ZnO nanosheets for ethanol detecting application, Sensors Actuators B Chem. 326 (2021) 128952. https://doi.org/10.1016/J.SNB.2020.128952.

[10] A. Alagh, F.E. Annanouch, K. Al Youssef, C. Bittencourt, F. Güell, P.R. Martínez-Alanis, M. Reguant, E. Llobet, PdO and PtO loaded WS2 boosts NO2 gas sensing characteristics at room temperature, Sensors Actuators B Chem. 364 (2022). https://doi.org/10.1016/j.snb.2022.131905.

[11] G. Neri, First fifty years of chemoresistive gas sensors, Chemosensors. 3 (2015) 1–20. https://doi.org/10.3390/chemosensors3010001.

[12] E. Spagnoli, S. Krik, B. Fabbri, M. Valt, M. Ardit, A. Gaiardo, L. Vanzetti, M. Della Ciana, V. Cristino, G. Vola, S. Caramori, C. Malagù, V. Guidi, Development and characterization of WO3 nanoflakes for selective ethanol sensing, Sensors Actuators B Chem. 347 (2021). https://doi.org/10.1016/j.snb.2021.130593.

[13] X. Wang, Y. Gao, Q. Zhang, X. He, X. Wang, Synthesis of MoO3 (1D) @SnO2 (2D) core-shell heterostructures for enhanced ethanol gas sensing performance, Sensors Actuators B Chem. 382 (2023) 133484. https://doi.org/10.1016/J.SNB.2023.133484.

[14] F. Liu, G. Huang, X. Wang, X. Xie, G. Xu, G. Lu, X. He, J. Tian, H. Cui, High response and selectivity of single crystalline ZnO nanorods modified by In2O3 nanoparticles for n-butanol gas sensing, Sensors Actuators B Chem. 277 (2018) 144–151. https://doi.org/10.1016/J.SNB.2018.08.144.

[15] X. Wang, F. Liu, X. Chen, X. Song, G. Xu, Y. Han, J. Tian, H. Cui, In2O3 Nanoparticles Decorated ZnO Hierarchical Structures for n-Butanol Sensor, ACS Appl. Nano Mater. 3 (2020) 3295–3304. https://doi.org/10.1021/acsanm.0c00025.

[16] K. Wang, W. Wei, Z. Lou, H. Zhang, L. Wang, 1D/2D heterostructure nanofiber flexible sensing device with efficient gas detectivity, Appl. Surf. Sci. 479 (2019) 209–215. https://doi.org/10.1016/J.APSUSC.2019.02.094.

[17] S. Wang, X. Wang, G. Qiao, X. Chen, X. Wang, H. Cui, Core-double shell ZnO@In2O3@ZnO hollow microspheres for superior ethanol gas sensing, Sensors Actuators B Chem. 341 (2021) 130002. https://doi.org/10.1016/J.SNB.2021.130002.

[18] H. Wang, Z. Feng, Y. Zhang, D. Han, J. Ma, X. Chai, S. Sang, Highly sensitive and low detection limit NO2 gas sensor based on In2O3 nanoparticles modified peach kernel-like GaN composites, Sensors Actuators B Chem. 382 (2023) 133452. https://doi.org/10.1016/J.SNB.2023.133452.

[19] Q. Zhang, Q. Ma, X. Wang, Y. Wang, D. Zhao, Surface Double Oxygen Defect Engineering in Button-Shaped Porous Ceo2/Wo2.9 Heterostructures for Excellent N-Butanol Detection at Room Temperature, SSRN Electron. J. 616 (2022). https://doi.org/10.2139/ssrn.4296261.

[20] P. Hu, J. Chen, Q. Ma, J. Yin, D. Zhou, C. Kou, J. Xu, J. Xu, One-step thermal compensation decomposition synthesis of ZnWO4/WO3 composite with synergy of multiple structural effects for efficient trace H2S detection, Sensors Actuators B Chem. 381 (2023) 133388. https://doi.org/10.1016/J.SNB.2023.133388.

[21] J. Zhang, D. Leng, G. Li, J. Liu, H. Wang, Y. Zhu, H. Lu, J. Gao, B. Zhu, Bimetallic–organic framework-derived Co3O4–ZnO heterojunction nanofibers: A new kind of emerging porous nanomaterial for enhanced ethanol sensing, Sensors Actuators B Chem. 349 (2021). https://doi.org/10.1016/j.snb.2021.130732.

[22] G. Li, Y. Zhang, Q. Liang, J. Zhang, J. Liu, Y. Liu, C. Wang, J. Gao, H. Lu, Nanoporous Co3O4–TiO2 Heterojunction Nanosheets for Ethanol Sensing, ACS Appl. Nano Mater. 5 (2022) 4779–4786. https://doi.org/10.1021/acsanm.1c04259.

[23] T.L.H. Doan, J.Y. Kim, J.H. Lee, L.H.T. Nguyen, Y.T. Dang, K.B.T. Bui, A.T.T. Pham, A. Mirzaei, T.B. Phan, S.S. Kim, Preparation of n-ZnO/p-Co3O4 heterojunctions from

zeolitic imidazolate frameworks (ZIF-8/ZIF-67) for sensing low ethanol concentrations, Sensors Actuators B Chem. 348 (2021). https://doi.org/10.1016/j.snb.2021.130684.

[24] J. Fang, X. Chen, R.P. Xiao, J.J. Xue, J.M. Song, High performance ethanol sensor based on Pr-SnO2/In2O3 composite, Ceram. Int. 48 (2022) 9897–9905. https://doi.org/10.1016/j.ceramint.2021.12.193.

[25] H. Cao, Z. Hu, X. Wei, H. Wang, X. Tian, S. Ding, Conductometric ethanol gas sensor based on a bilayer film consisting of SnO2 film and SnO2/ZnSnO3 porous film prepared by magnetron sputtering, Sensors Actuators B Chem. 382 (2023). https://doi.org/10.1016/j.snb.2023.133562.

[26] P. Wang, S.Z. Wang, Y.R. Kang, Z. Sen Sun, X.D. Wang, Y. Meng, M.H. Hong, W.F. Xie, Cauliflower-shaped Bi2O3–ZnO heterojunction with superior sensing performance towards ethanol, J. Alloys Compd. 854 (2021) 157152. https://doi.org/10.1016/J.JALLCOM.2020.157152.

[27] H. Li, Z. Yang, W. Ling, D. Zhu, Y. Pu, UV excited gas sensing SnO2-ZnO aerogels to ppb-level ethanol detection, Sensors Actuators, B Chem. 337 (2021). https://doi.org/10.1016/j.snb.2021.129815.

[28] S. Agarwal, P. Rai, E.N. Gatell, E. Llobet, F. Güell, M. Kumar, K. Awasthi, Gas sensing properties of ZnO nanostructures (flowers/rods)synthesized by hydrothermal method, Sensors Actuators, B Chem. 292 (2019) 24–31. https://doi.org/10.1016/j.snb.2019.04.083.

[29] K. Yuan, C.Y. Wang, L.Y. Zhu, Q. Cao, J.H. Yang, X.X. Li, W. Huang, Y.Y. Wang, H.L. Lu, D.W. Zhang, Fabrication of a Micro-Electromechanical System-Based Acetone Gas Sensor Using CeO2 Nanodot-Decorated WO3 Nanowires, ACS Appl. Mater. Interfaces. 12 (2020) 14095–14104. https://doi.org/10.1021/acsami.9b18863.

[30] F. Pourfayaz, A. Khodadadi, Y. Mortazavi, S.S. Mohajerzadeh, CeO2 doped SnO2 sensor selective to ethanol in presence of CO, LPG and CH4, Sensors Actuators, B Chem. 108 (2005) 172–176. https://doi.org/10.1016/j.snb.2004.12.107.

[31] L. Lei, Y. Wang, Z. Zhang, J. An, F. Wang, Transformations of Biomass, Its Derivatives, and Downstream Chemicals over Ceria Catalysts, ACS Catal. 10 (2020) 8788–8814. https://doi.org/10.1021/acscatal.0c01900.

[32] Z. Dong, Q. Hu, H. Liu, Y. Wu, Z. Ma, Y. Fan, R. Li, J. Xu, X. Wang, 3D flower-like Ni doped CeO2 based gas sensor for H2S detection and its sensitive mechanism, Sensors Actuators B Chem. 357 (2022) 131227. https://doi.org/10.1016/J.SNB.2021.131227.

[33] J. Liu, M. Dai, T. Wang, P. Sun, X. Liang, G. Lu, K. Shimanoe, N. Yamazoe, Enhanced Gas Sensing Properties of SnO2 Hollow Spheres Decorated with CeO2 Nanoparticles Heterostructure Composite Materials, ACS Appl. Mater. Interfaces. 8 (2016) 6669–6677. https://doi.org/10.1021/acsami.6b00169.

[34] È. Navarrete, C. Bittencourt, X. Noirfalise, P. Umek, E. González, F. Güell, E. Llobet, WO3 nanowires loaded with cobalt oxide nanoparticles, deposited by a two-step AACVD for gas sensing applications, Sensors Actuators, B Chem. 298 (2019) 126868. https://doi.org/10.1016/j.snb.2019.126868.

[35] E. Navarrete, C. Bittencourt, P. Umek, E. Llobet, AACVD and gas sensing properties of nickel oxide nanoparticle decorated tungsten oxide nanowires, J. Mater. Chem. C. 6 (2018) 5181–5192. https://doi.org/10.1039/c8tc00571k.

[36] E. Navarrete, C. Bittencourt, P. Umek, D. Cossement, F. Güell, E. Llobet, Tungsten trioxide nanowires decorated with iridium oxide nanoparticles as gas sensing material, J. Alloys Compd. 812 (2020). https://doi.org/10.1016/j.jallcom.2019.152156.

[37] T. Berestok, P. Guardia, J. Blanco, R. Nafria, P. Torruella, L. López-Conesa, S. Estradé, M. Ibáñez, J. De Roo, Z. Luo, D. Cadavid, J.C. Martins, M. V. Kovalenko, F. Peiró, A. Cabot, Tuning Branching in Ceria Nanocrystals, Chem. Mater. 29 (2017) 4418–4424. https://doi.org/10.1021/acs.chemmater.7b00896.

[38] F.E. Annanouch, Z. Haddi, M. Ling, F. Di Maggio, S. Vallejos, T. Vilic, Y. Zhu, T. Shujah, P. Umek, C. Bittencourt, C. Blackman, E. Llobet, Aerosol-Assisted CVD-Grown PdO Nanoparticle-Decorated Tungsten Oxide Nanoneedles Extremely Sensitive and Selective to Hydrogen, ACS Appl. Mater. Interfaces. 8 (2016). https://doi.org/10.1021/acsami.6b00773.

[39] F. Güell, P.R. Martínez-Alanis, S. Roso, C.I. Salas-Pérez, M.F. García-Sánchez, G. Santana, B.M. Monroy, Plasma versus thermal annealing for the Au-catalyst growth of ZnO nanocones and nanowires on Al-doped ZnO buffer layers, Mater. Res. Express. 3 (2016) 1–11. https://doi.org/10.1088/2053-1591/3/6/065013.

[40] M.F. Daniel, B. Desbat, J.C. Lassegues, B. Gerand, M. Figlarz, Infrared and Raman study of WO3 tungsten trioxides and WO3, xH2O tungsten trioxide tydrates, J. Solid State Chem. 67 (1987) 235–247. https://doi.org/10.1016/0022-4596(87)90359-8.

[41] T. Nishide, F. Mizukami, Crystal structures and optical properties of tungsten oxide films prepared by a complexing-agent-assisted sol-gel process, Thin Solid Films. 259 (1995) 212–217. https://doi.org/10.1016/0040-6090(94)06444-X.

[42] L. Pirker, B. Višić, J. Kovač, S.D. Škapin, M. Remškar, Synthesis and characterization of tungsten suboxide wn o3n−1 nanotiles, Nanomaterials. 11 (2021) 1–12. https://doi.org/10.3390/nano11081985.

[43] D. Wei, Z. Huang, L. Wang, X. Chuai, S. Zhang, G. Lu, Hydrothermal synthesis of Ce-doped hierarchical flower-like In2O3 microspheres and their excellent gas-sensing properties, Sensors Actuators B Chem. 255 (2018) 1211–1219. https://doi.org/10.1016/J.SNB.2017.07.162.

[44] D.J. Dwyer, Surface chemistry of gas sensors: H2S on WO3 films, Sensors Actuators B Chem. 5 (1991) 155–159. https://doi.org/10.1016/0925-4005(91)80237-E.

[45] Q. Diao, Y. Yin, W. Jia, X. Xu, Y. Ding, X. Zhang, J. Cao, K. Yang, M. Jiao, Highly sensitive ethanol sensor based on Ce-doped WO3with raspberry-like architecture, Mater. Res. Express. 7 (2020). https://doi.org/10.1088/2053-1591/abcabf.

[46] F.E. Annanouch, Z. Haddi, S. Vallejos, P. Umek, P. Guttmann, C. Bittencourt, E. Llobet, Aerosol-assisted CVD-grown WO3 nanoneedles decorated with copper oxide nanoparticles for the selective and humidity-resilient detection of H2S, ACS Appl. Mater. Interfaces. 7 (2015) 6842–6851. https://doi.org/10.1021/acsami.5b00411.

[47] G. Hui, M. Zhu, X. Yang, J. Liu, G. Pan, Z. Wang, Highly sensitive ethanol gas sensor based on CeO2/ZnO binary heterojunction composite, Mater. Lett. 278 (2020) 128453. https://doi.org/10.1016/J.MATLET.2020.128453.

[48] Y.J. Chen, G. Xiao, T.S. Wang, F. Zhang, Y. Ma, P. Gao, C.L. Zhu, E. Zhang, Z. Xu, Q.H. Li, Synthesis and enhanced gas sensing properties of crystalline CeO2/TiO2 core/shell nanorods, Sensors Actuators B Chem. 156 (2011) 867–874. https://doi.org/10.1016/J.SNB.2011.02.057.

[49] S. Yu, X. Jia, J. Yang, S. Wang, Y. Li, H. Song, Highly sensitive and low detection limit

of ethanol gas sensor based on CeO2 nanodot-decorated ZnSnO3 hollow microspheres, Ceram. Int. 48 (2022) 14865–14875. https://doi.org/10.1016/J.CERAMINT.2022.02.023.

[50] J. Zhang, T. Li, J. Guo, Y. Hu, D. Zhang, Two-step hydrothermal fabrication of CeO2-loaded MoS2 nanoflowers for ethanol gas sensing application, Appl. Surf. Sci. 568 (2021) 150942. https://doi.org/10.1016/J.APSUSC.2021.150942.

[51] G. Hui, M. Zhu, X. Yang, J. Liu, G. Pan, Z. Wang, Highly sensitive ethanol gas sensor based on CeO2/ZnO binary heterojunction composite, Mater. Lett. 278 (2020). https://doi.org/10.1016/j.matlet.2020.128453.

[52] J. Huang, X. Xu, C. Gu, M. Yang, M. Yang, J. Liu, Large-scale synthesis of hydrated tungsten oxide 3D architectures by a simple chemical solution route and their gas-sensing properties, J. Mater. Chem. 21 (2011) 13283–13289. https://doi.org/10.1039/c1jm11292a.

[53] M.F. Al-Kuhaili, S.M.A. Durrani, I.A. Bakhtiari, Carbon monoxide gas-sensing properties of CeO2-WO3 thin films, Mater. Sci. Technol. 26 (2010) 726–731. https://doi.org/10.1179/174328409X443209.

[54] B. Saruhan, R. Lontio Fomekong, S. Nahirniak, Review: Influences of Semiconductor Metal Oxide Properties on Gas Sensing Characteristics, Front. Sensors. 2 (2021) 1–24. https://doi.org/10.3389/fsens.2021.657931.

[55] N. Barsan, U. Weimar, Conduction model of metal oxide gas sensors, J. Electroceramics. 7 (2001) 143–167. https://doi.org/10.1023/A:1014405811371.

[56] S. Agarwal, P. Rai, E. Navarrete, E. Llobet, F. Güell, Sensors and Actuators B : Chemical Gas sensing properties of ZnO nanostructures (fl owers / rods) synthesized by hydrothermal method, 292 (2019) 24–31.

[57] S. Yu, X. Jia, J. Yang, S. Wang, Y. Li, H. Song, Highly sensitive and low detection limit of ethanol gas sensor based on CeO2 nanodot-decorated ZnSnO3 hollow microspheres, Ceram. Int. 48 (2022) 14865–14875. https://doi.org/10.1016/j.ceramint.2022.02.023.

[58] Z. Tang, X. Deng, Y. Zhang, X. Guo, J. Yang, C. Zhu, J. Fan, Y. Shi, B. Qing, F. Fan, MoO3 nanoflakes coupled reduced graphene oxide with enhanced ethanol sensing performance and mechanism, Sensors Actuators B Chem. 297 (2019) 126730.

https://doi.org/10.1016/j.snb.2019.126730.

[59] A.E.-A. A. Said, M.M.M.A. El-Wahab, M.A. El-Aal, The Role of Acid Sites in the Catalytic Performance of Tungsten Oxide during the Dehydration of Isopropyl and Methyl Alcohols, Chem. Mater. Eng. 4 (2016) 17–25. https://doi.org/10.13189/cme.2016.040202.

CHAPTER 3

High-yield synthesis of WS_2 via novel sulfurization method for the selective detection of NH_3 vapors

High-yield synthesis of WS_2 via novel sulfurization method for the selective detection of NH_3 vapors

Shuja Bashir Malik[1,2], Fatima Ezahra Annanouch[1,2], Ransell D´Souza[4], Carla Bittencourt[3], Milica Todorović[4], Eduard Llobet[1,2]

1 Universitat Rovira i Virgili, MINOS, Països Catalans 26, 43007 Tarragona, Catalunya, Spain.
2 IU-RESCAT, Universitat Rovira i Virgili, Joanot Martorell 15, 43480 Vila-seca, Spain.
3 Chimie des Interactions Plasma-Surface (ChIPS), Research Institute for Materials Science and Engineering, University of Mons, 7000 Mons, Belgium
4 Department of Mechanical and Materials Engineering, Faculty of Technology, University of Turku, Vesilinnantie 5, 20500, Turku, Finland
* Correspondence: authors' email: eduard.llobet@urv.cat, fatimaezahra.annanouch@urv.cat

Abstract

Transition metal dichalcogenides (TMDs) have garnered extensive research interest for physical and chemical sensing applications due to their crystal structure and large effective surface area. However, it is quite challenging to synthesize these novel materials with high yield, on different substrates, and in the form of continuous films, which hinders their real-world applications. Herein, we demonstrate, for the first time, the synthesis of two-dimensional (2D) tungsten disulfide (WS_2) sheets, in hundred milligram scale, from a simple sulfurization of tungsten trioxide (WO_3) powder using an atmospheric pressure chemical vapor deposition (APCVD) reactor. The synthesized powders can be employed for developing ink formulations in the solvents of choice to be screen or inkjet printed, spin coated, drop casted or airbrushed onto a broad range of application substrates such as ceramic, silicon-based or flexible polymeric. The structural, morphological, and chemical composition analysis reveals the successful growth of edge-enriched WS_2 sheets. The sensing layers were deposited on alumina substrates to be used as chemoresistive gas sensors. Gas sensing analysis of edge-enriched WS_2 sheets were investigated towards NH_3 at different operating temperatures. The results revealed exceptional gas sensing responses, from WS_2, towards 5 ppm of NH_3. The sensors showed reproducible and stable responses of 100% towards 5 ppm of NH_3 at 150ºC. The sensor detection limit was experimentally verified; it was below 1 ppm of NH_3 at 150ºC. Selectivity test towards NH_3 was performed by using CO, benzene, H_2 and NO_2 as interfering gases. The

results showed that edge-enriched WS_2 films were highly selective to NH_3 at a moderate operating temperature of 150ºC, while they exhibited little or no response towards the interfering species. Furthermore, the edge-enriched growth of the WS_2 imparts the sensors with remarkable resilience against high levels of humidity. The sensor response was slightly decreased (R= 93%) in humid environment compared to dry ambient (R=100%) towards 5 ppm of NH_3 at 150ºC. In atomistic simulations, stable ammonia adsorbates on WS_2 were identified using density functional theory (DFT) and Bayesian optimization —a machine learning-driven approach. DFT studies revealed that the interaction between gas molecules and WS_2 is mainly based on physisorption.

Keywords: WS_2, APCVD, sulfurization, gas sensor, NH_3, 2D materials, TMDs, DFT

3.1. Introduction

The discovery of graphene in 2004 marked the onset of research on two dimensional (2D) materials owing to its distinctive and excellent physical, chemical, and electronic properties [1–3]. However, the zero bandgap of graphene limits its electronic applications [4–6]. The search for a material with desired electronic properties led researchers to transition metal dichalcogenides (TMDs). 2D TMDs have garnered tremendous attention driven by their tunable bandgap, high carrier mobility and environment friendliness [7–9]. TMDs are characterized by their X-M-X (or MX_2) structure, where a transition metal (M) is sandwiched in between two chalcogen atoms (X) with strong interlayer covalent bond and weaker interplanar van der Waals bonds [10]. Moreover, absence of dangling bonds on the TMDs surface helps them in maintaining stability and their pristine quality [11]. Owing to these excellent electronic properties, TMDs materials such as MoS_2, WS_2, SnS_2, GeSe, InSe, and WSe_2 are being extensively studied for gas sensing applications [12].

WS_2 is one of the most important members of the TMDs family which has captured the close attention of the scientific community. It is characterized by layered hexagonal symmetry forming S-W-S [13] structure with an interlayer distance of ~ 0.65-1 nm [10,13]. Interestingly, bulk WS_2 has an indirect band gap of 1.4 eV, which can be tuned to direct band gap of 2 eV in case of monolayer WS_2 [14]. It exhibits ambipolar field modulation behavior [15], excellent thermal conductivity (~ 142 W/mK) [16], outstanding flexibility [17], theoretically predicted high in-plane carrier mobility of (> 1000 cm^2V^{-1}) owing to the reduced effective mass of charge carriers and a high current modulation ratio [18]. The inherent distinctive properties of WS_2

make it a highly sought-after 2D material. There is an imminent requirement for a industrial-scale synthesis method to cater to the burgeoning demand of the electronics market.

Numerous techniques have been developed to grow WS_2 such as microwave irradiation [19,20], solvothermal synthesis [21,22], magnetron sputtering [23,24], molecular beam epitaxy (MBE) [25], micro-mechanical exfoliation [26], and chemical vapor deposition (CVD) [3,9,27–32]. But CVD and metal-organic chemical vapor deposition (MOCVD) emerge as particularly promising cost-effective techniques for achieving scalable, highly crystalline growth in micrometer scale [33] to wafer scale [34]. On one hand, wafer scale synthesis of WS_2 has been achieved using MOCVD, but use of organic compounds and reactive gases leads to a high possibility of carbon contamination [35,36], toxicity [35–38], and longer durations for large area synthesis [35,36] of WS_2. Also, precursor selection for MOCVD is tricky as it requires metal-organic compounds with high-vapor pressure [11]. On the other hand, precursor selection for atmospheric pressure chemical vapor deposition (APCVD) is easier, thus making the technique more desirable. At the same time, the high melting point of commonly used tungsten precursor such as WO_3 (~1473ºC) limits the growth of WS2 via APCVD.

However, several research groups worked on this issue and resolved the problem and reported the synthesis of WS_2 at reduced temperatures using alkali halides [33,39–43]. Li et al. [39] reported successful synthesis of monolayer WSe_2 and WS_2 crystals within temperature range of ~700-850ºC using alkali halides like KCl, NaCl, KI and KBr. The introduction of alkali halides resulted in the decrease in the sublimation temperature of the metal oxide precursor by forming volatile tungsten oxyhalides. Consequently, the growth temperature was found to be dependent upon the melting temperature of the salt used. Shi et al. [33] demonstrated successful synthesis of 460 μm single-crystal monolayer WS_2 at 875ºC via NaCl assisted APCVD. They reported the correlation between the size of the as grown WS_2 crystals and the weight/weight (w/w) ratio of NaCl with respect to WO_3. Lan and co-workers [40] reported single-crystal triangular domain monolayers of WS_2 using sapphire substrates employing NaCl as an additive agent. It was demonstrated that NaCl leads to the supersaturation of tungsten precursors which facilitated the large-area growth of WS_2 monolayer domains (1.7 mm edge length). Yuan et al. [42] proposed an innovative NaCl-assisted CVD method allowing unrestricted substrate positions for synthesizing monolayer WS_2 nanosheets. The maximum grain size of the monolayer WS_2 was reported to be 30 μm. Also, Zhou and co-workers [43] reported NaCl template-assisted in situ CVD for synthesizing 2D WS_2, MoS_2, $MoSe_2$, and WSe_2 on a large scale with single crystalline structure. They reported that the 3D assembly of the cubic NaCl

particles not only provides smooth surfaces to support the lateral growth of the respective TMDs, but also restricts the thickening of the TMDs sheets by creating a 2D confined space. The reaction was carried out at 750ºC for 2 hours under an argon atmosphere. On the one hand, salt assisted CVD process looks promising for a wafer scale synthesis of TMDs, but on the other hand, there are issues related to the synthesis process. Chang et al. [44] reported that WS_2 monolayers grown employing NaCl-assisted CVD undergo degradation process, like oxidation at random positions in the triangular flakes. The study used a photocatalytic reaction to explain the photo-induced degradation mechanism with sulfur vacancies. Also, the specific roles of the alkali metals and halide components are not fully understood in the CVD growth process [45]. Moreover, various research groups demonstrated alkali halide free TMDs growth via hydrogen assisted CVD [46–48]. The introduction of hydrogen in the growth process is not straightforward, as it can be the source of safety issues. Also, the growth of the triangular WS_2 is discontinuous, hindering real-world electronic applications.

For chemoresistive gas sensors, 2D edge-enriched, vertically oriented TMDs exhibit excellent gas sensing properties [49,50]. However, their synthesis in an out-of-plane direction presents a daunting challenge. Indeed, the complex process of growing gas sensitive TMDs materials demands innovative and precision-based synthesis techniques. One of the main obstacles lies in achieving uniform, reproducible and continuous deposition [51–53]. To overcome these challenges, Alagh et al. [54–56] reported hydrogen and alkali halide free direct growth of continuous and vertically oriented WS_2 nanotriangles on standard ceramic transducers. The authors reported a two-step CVD process by combining aerosol assisted CVD (AACVD) and APCVD for the direct growth of WS_2 to be used in chemoresistive sensors. Concurrently, the authors reported the occurrence of WO_3 impurities suggesting an incomplete sulfurization. Also, the direct growth of WS_2 onto transducer substrates at high temperatures (~ 900ºC) makes it impossible to use the material for further applications especially on flexible substrates. The technique is promising for developing gas sensors at the laboratory scale; however, the technique may not be scaled up to industrial level.

Keeping the above-mentioned shortcomings of direct growth of WS_2 into mind, we report, for the first time, a new methodology to synthesize sheet-like edge-enriched WS_2 powder, in hundreds of milligrams scale per run, using a hydrogen and alkali-halide free APCVD technique. The morphology, phase composition, microstructure, and chemical composition were investigated. Moreover, the growth mechanism and morphological evolution of the sheet-like WS_2 are discussed. Besides, the gas-sensing films made out of WS_2 were deposited, onto

alumina transducing substrates, via a home-made airbrush system and they were studied towards low concentrations of NH_3 at various operating temperatures (i.e., RT, 100ºC and 150ºC), under dry and humid atmospheres. To gain insight into the atomistic mechanisms of interaction between NH_3 and the sensing substrate, we employed density functional theory (DFT) simulations. Structure search for the optimal molecular adsorption configuration was accelerated by Bayesian optimization. This allowed us to compute the adsorption energy of NH_3 on WS_2 and examine the electronic structure of the adsorbate to determine the nature of the interaction. Finally, on the basis of the existing literature and in light of the experimental and DFT findings, a gas sensing mechanism is proposed.

3.2. Experimental methods

3.2.1. APCVD synthesis of sheets-like WS_2

Herein, hydrogen-free APCVD technique was employed for synthesizing sheets-like WS_2 with yield in hundred milligrams and possibility of scalability using a novel synthesis strategy. To do this, commercially available tungsten trioxide powder purchased from Sigma Aldrich (CAS: 1314-35-8) was used and sulfurized to obtain sheet-like, edge enriched WS_2 nanostructures in a powder form. The sulfurization reaction was carried out at 900ºC for 60 minutes using metallic sulfur (Sigma Aldrich, CAS: 7704-34-9) in a homemade tube-in-tube setup with temperature gradient. The schematic of the setup is demonstrated in Figure. 3.1. The middle zone of the furnace reaches the set temperature of 900ºC as shown in bright red colored heater coil in the schematic, Figure 3.1 a & b. Zones adjacent to the middle zone of the furnace are at lower temperatures (approximately 400ºC) compared to the middle zone of the reactor. Three corundum boats were positioned within different temperature zones of the furnace; one boat contained 100 mg of WO_3 precursor powder, while the other two boats contained 1 g of sulfur each. The boat containing WO_3 was placed adjacent to a sulfur containing boat inside a semi sealed secondary quartz tube, both situated in the 900ºC temperature zone. The boat outside the secondary quartz tube is placed upstream of argon flow inside the bigger quartz tube. Prior to sulfurization process, the quartz tube was flushed with 100 mL/min of Ar to remove any traces of oxygen present in the reactor. The Ar flow was kept at 30 mL/min during the reaction. The furnace is programmed to heat from room temperature to the set temperature of 900ºC with a ramp of 40ºC/min. As soon as the furnace reaches 900ºC, the external quartz tube is carefully positioned as such that the sulfur boat initially located outside the furnace is in the 400ºC temperature zone of the furnace, Figure 3.1 (b). This strategic placement of the boats

facilitates the creation of a sulfur rich environment ensuring full sulfurization of WO_3. This setup ensures double sulfurization. The argon flow rate, ramp up temperature, time of the reaction, and amount of sulfur are important parameters to be taken into consideration. The furnace was let cool naturally after the reaction is completed.

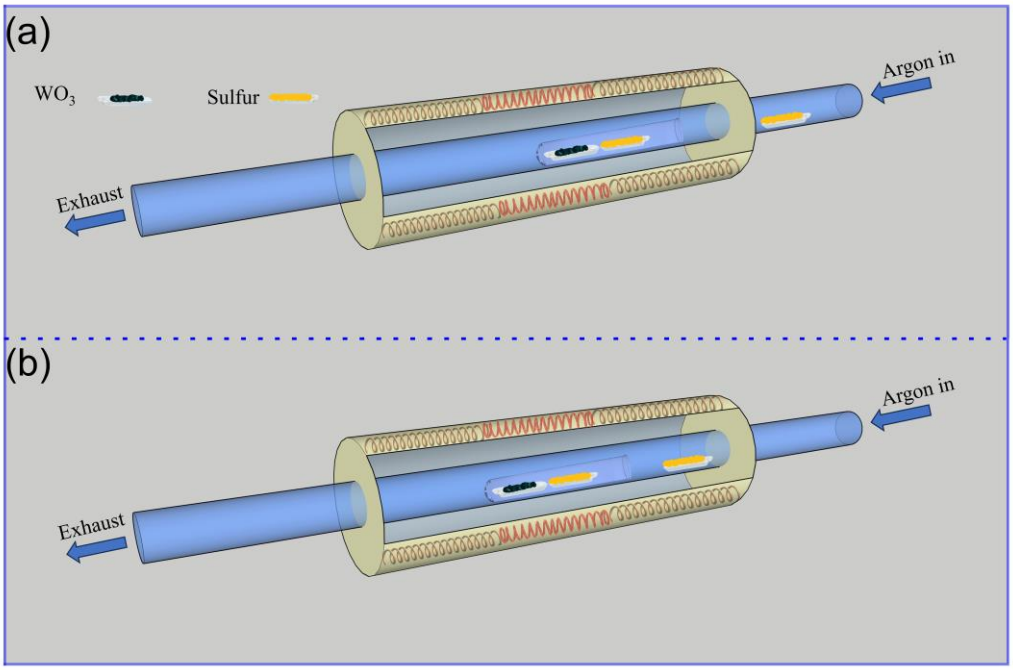

Figure 3.1 Schematic of APCVD furnace used for WS_2 growth.

3.2.2. Gas sensor fabrication

WS_2 sensing films were deposited, via a home-made airbrush system, onto commercial alumina transducer substrates (Ceram Tech GmBH, Germany), which have Pt-interdigitated electrodes with a gap of 300 µm on the front side and Pt-resistive heater meander on the back side. The electrode area was 2.5 mm × 5.1 mm. Prior to their coating with WS_2, substrates were cleaned by sequential sonication in acetone, ethanol, and deionized water followed by blow drying with nitrogen. After that, the cleaned substrates were placed in the hotplate of our home-made airbrushing system, which is composed of a commercial air brush, a hotplate, a multimeter and connectors.

10 mg of WS_2 powder was sonicated in 10 mL of absolute ethanol (Scharlab, CAS: 64-17-5) for 1 hour to yield a brownish suspension. It is worth noting that the airbrushing technique allows us to use the solvent of choice, for this work, absolute ethanol was used to keep the thin film deposition temperature to the minimum possible value, owing to its low boiling point. Next, the obtained solution was transferred to the airbrush container, the electrodes of the substrate transducers were connected to the multimeter, in order to control the resistance of the

deposited films and the hotplate was turned on and set at 55ºC. Finally, the brown solution was airbrushed onto the alumina substrates using N_2 gas as a carrier. It is worth mentioning that this technique allows us to deposit thin films of the functional material over virtually any type of application substrate. Airbrushing deposition was tested over polymethyl methacrylate (PMMA), Kapton, silicon and glass substrates. The adhesion and quality of the deposited films on the substrates was found to be excellent.

3.2.3. Material characterization techniques

The morphology of the sheets-like edge enriched WS_2 nanostructures was examined using a Field Emission Scanning Electron Microscope (Thermo Scientific Scios 2). High Resolution Transmission Electron Microscopy (HRTEM) studies were carried out using a JEOL F200 TEM ColdFEG operated at 200kV. TEM images were acquired with a Gatan OneView camera, a CMOS-based and optical fibre-coupled detector of 4096 by 4096 pixels. X-ray diffraction (XRD) was used to analyze the crystal structure of the synthesized material. The XRD measurements were made using a Bruker-AXS D8-Discover diffractometer equipped with parallel incident beam (Göbel mirror), vertical θ-θ goniometer, XYZ motorized stage and with a GADDS (General Area Diffraction System). The X-ray diffractometer was operated at 40 kV and 40 mA to generate Cukα radiation. The GADDS detector was a VÅNTEC-500 (silicon strip technology) placed at 15 cm from the sample. The Raman spectra were obtained using a Renishaw in Via, laser 514 nm, ion argon – Novatech, 25 mW. For XPS measurements, a Versaprobe PHI 5,000 from Physical Electronics was used to record the spectra. The X-ray source Al Kα was monochromatized, and measurements were taken at a take-off angle 45º from the sample surface. The spot size of 200 µm was utilized, and a pass energy (PE) of 20 eV was employed for the spectra recorded in the core level binding energy regions: W 4f, S 2p, and C 1s. To counter charge build-up on the sample surface during measurements, a dual beam charge neutralization consisting of an electron gun (< 1 eV) and an argon ion gun (< 10 eV) was implemented. The XPS spectra were examined using CASA-XPS software.

3.2.4. Gas sensing measurements

The gas sensing measurements of the as-fabricated WS_2 sensors were performed using a home-made gas detection system employing a Teflon chamber with a volume of 35 mL. The chamber can accommodate four sensors simultaneously. The chamber consists of an inlet and outlet which are connected to the gas delivery system and exhaust respectively. The chamber was connected to a fully automated gas flow measurement set-up with the ability to supply diluted gas mixtures via mass flow controllers (Bronkhorst High-Tech B.V.). Calibrated gas cylinders

balanced in dry synthetic air (Air Premier purity: 99.999%) were used for gas sensing measurements. The operating temperatures of the sensors were controlled by connecting the meander heaters of the sensors to external power supply (Agilent U8002A). Sensor responses were recorded using an Agilent-34972A data acquisition system by monitoring the sensing material resistances upon exposure to different concentrations of target gases such as NH_3, NO_2, H_2, CO and benzene. Sensors were operated at room temperature (RT), 100ºC and 150ºC. To ensure the baseline stabilization, a continuous dry airflow of 100 mL/min was maintained in the chamber for 3 hours prior to initiating gas sensing measurements. The sensors were exposed to gaseous species for 10 minutes followed by an exposure to dry air to recover and stabilize the baseline. The baseline recovery time was adapted according to the sensor operating temperature; 60 minutes for 100ºC and 150ºC and 120 minutes for room temperature operation. Throughout the gas sensing measurements, a 100 mL/min overall flow rate was maintained. For a reducing species like NH_3, the sensor response was calculated using Equation 1, while for oxidizing species like NO_2, the relative response was calculated using Equation 2.

$$R = \frac{R_{gas} - R_{air}}{R_{air}} * 100 \qquad \text{Equation. 1}$$

$$R = \frac{R_{air} - R_{gas}}{R_{air}} * 100 \qquad \text{Equation. 2}$$

R_{air} and R_{gas} are the real time resistances of sensors when exposed to air and to target gas respectively.

3.3. Computational methods

3.3.1. First principles calculations

All simulations were performed with density functional theory (DFT). We utilized the all-electron, numeric atom-centered orbital code FHI-aims [57] , incorporating the Perdew–Burke–Ernzerhof (PBE) exchange–correlation functional [60] and Tkatchenko–Scheffler (TS) vdW corrections [61]. Our DFT calculations employed tier-1 basis sets, light grid settings, and a 4 × 4 × 1 Monkhorst-Pack k-point grid to ensure convergence. The total energy was converged within 10^{-6} eV, and the structures were optimized until all force components were reduced below 10^{-5} eV/Å. To achieve a comprehensive description of the electronic structure and to incorporate the effects of spin-orbit coupling, we utilized relativistic corrections and explicitly included spin-orbit coupling terms in our calculations [62]. A vacuum spacing of 22 Å was employed along the z-direction to mitigate interactions between the substrate layers.

To prevent interactions between adsorbed NH_3 molecules, we adopted a 4 × 4 x-y hexagonal supercell of the WS_2 substrate (lattice constant a=12.7 Å), resulting in a distance of over 10Å between molecule images in neighboring periodic cells.

The combined system comprised a total of 52 atoms, including 4 atoms for the NH_3 molecule and 48 WS_2 substrate atoms. The single-trilayer thick WS_2 substrate was modeled using a hexagonal unit cell characterized by an optimized lattice constant of 3.168 Å, a value that closely aligns with experimental [57] and previous computational findings [58]. The adsorption energy between the substrate and the target molecule (E_{ads}) was evaluated as the difference between the total energy of the adsorbed system E_{tot}) and the sum of the isolated energies of the substrate E_{WS_2}) and the molecule (E_{NH_3})

$$E_{ads} = E_{tot} - (E_{WS_2} + E_{NH_3}) \qquad \text{Equation 3}$$

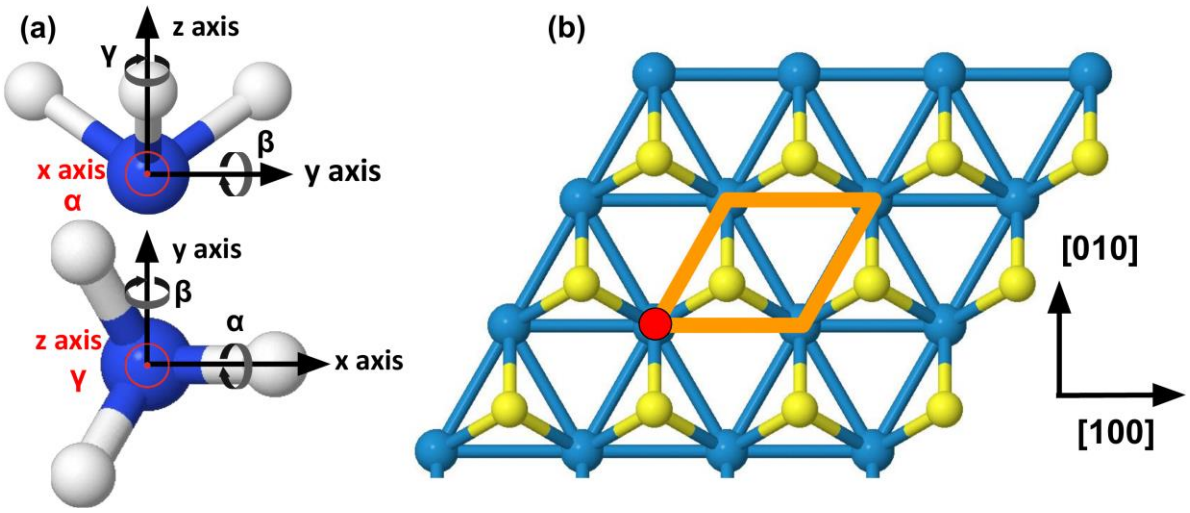

Figure 3.2 Translational and rotational degrees of freedom for the adsorption structure search: a) side view and top view illustration of the NH_3 molecular rotations implemented within the internal molecular frame of reference; (b) illustration of the translational motion of the molecule above the WS_2 substrate. The orange line delineates the periodic search region. Direction [001] is perpendicular to the [100]-[010] plane of the substrate, and the red point denotes the centroid of the NH_3 molecule.

3.3.2. Adsorbate structure identification

The identification of stable ammonia adsorbates on WS_2 was achieved through the application of DFT within the "Bayesian optimization structure search" (BOSS) code [65]. BOSS, a machine learning-driven approach, accelerates the identification of energetically favorable structures by strategically navigating the adsorption energy surface (AES). Given an initial dataset of configurations, BOSS constructs the most probable surrogate model of the AES by

Gaussian process regression. This surrogate model is then iteratively refined through an active learning process, enabling the identification of energetically stable adsorbates within the AES minima, as demonstrated in previous adsorption studies [66].

The structures of the molecule and substrate were optimized independently, then fixed and deployed as 'building blocks' during the structure search. The adsorption energy surface (AES) was explored in a 6D search space, as a function of molecular position and orientation above the substrate. In practice, we applied three translational degrees of freedom (x, y, z) and three rotational degrees of freedom (α, β, γ) to the molecular center of mass (centroid) to perform configurational sampling. The rotational degrees of freedom for α and β were confined within the range of 0° to 360°, whereas that of γ was restricted to the range of 0° to 120°, owing to the rotational symmetry of the NH_3 molecule along the z-axis. The rotational angles (α, β, γ) were implemented around the internal molecular frame of reference, as defined in Figure. 3.2 (a). The translations were applied in directions of crystallographic axes [100], [010] and [001]. Because of the periodic nature of the substrate model, the x-y search was confined to a limited section of the substrate, as depicted in Figure 3.2 (orange lines). Initial tests indicated that the optimal bounds for the molecule height z was between 2 Å and 2.8 Å computed from the highest surface atom. Adsorption energetics was sampled with the exploratory Lower Confidence Bound (eLCB) acquisition function [67], which strikes a balance between exploitation and exploration. To build our 6D kernel, we applied the standard periodic kernel to describe all the periodic degrees of freedom, except from the z coordinate, where we used the radial basis function kernel. The 6D BOSS search was initialized with 200 Sobol space-filling points and continued during 2000 active learning iterations. After we observed convergence of the global minimum of adsorption energy, we identified the atomic configuration behind the inferred global minimum and fully optimized the geometry.

3.3.3. Electronic transport and sensor resistivity

Given the atomic coordinates for the global minimum structure, the Boltzmann transport equations (BTE) were employed to calculate sensor resistivity. Here, the band structure extracted from the FHI-aims calculations provided crucial inputs for calculating transport properties with the Boltztrap2 code [68]. The BTE enables the evaluation of electrical conductivity along two orthogonal principal axes ([100] and [010]) within the x-y plane of the two-dimensional WS_2 layer. The calculated conductivity is averaged over these principal

directions. Within the framework of the Boltzmann transport approximation, the electrical conductivity is expressed as follows:

$$\sigma_{\alpha,\beta}(T,\epsilon) = \frac{1}{V}\int e^2 v_\alpha(\epsilon) v_\beta(\epsilon)\tau(\epsilon)\left[\frac{-\partial f_\mu(T,\epsilon)}{\partial\epsilon}\right]d\epsilon\ ;\ v_a = \frac{1}{\hbar}\frac{\partial\epsilon}{\partial k_\alpha(\epsilon)}\ ;\ f_\mu = (1+e^{\frac{(\epsilon-\mu)}{k_B T}})^{-1}$$

Equation 4

Here, v_α is the energy (ϵ) dependent group velocity of the band electrons along the component, e is the electrical charge, V is the unit cell volume of the WS_2/NH_3 system, $\tau(\epsilon)$ is the energy dependent relaxation time, T is the temperature, μ is the chemical potential, f is the Fermi-dirac distribution, k_B is the Boltzmann constant and $\hbar$ is the Planks constant. The chemical potential associated with the experimentally applied gate voltage [69] was determined by fixing its value as a fitting parameter to the experimental baseline resistivity curve of WS_2 at 0.43 eV in the absence of the target molecule, NH_3.

The resistivity was then defined as the reciprocal of conductivity and the sensor sensitivity was calculated using Equation 1. The calculated sensor response function was obtained by solving the "Step response differential equation",

$$\frac{dR}{dt} + \frac{R}{\tau} = H(t) \qquad \text{Equation 5}$$

Where, 't' is the time, 'R' is the time-dependent resistivity and H(t) is Heaviside step function. The initial conditions for the resistivity during the "gas-in" phase were set as $R_{initial} = R_{WS_2}$ and $R_{final} = R_{WS_2+NH_3}$, respectively. The initial conditions were reversed for the "gas-out" phase. The characteristic time (τ) is a function of the adsorption energy and temperature. τ is also known as the time constant since the differential equation is solved at a constant temperature.

3.4. Results and discussion

3.4.1. Material characterization

3.4.1.1. FESEM

Figure. 3.3 shows FESEM micrographs for the as-synthesized WS_2. The analysis of the FESEM images reveals that WS_2 shows a distinctive zigzag edged triangular sheet architecture with an average thickness of 36 nm. Notably, the majority of the triangle-like nanostructure exhibits an edge-to-edge width of 255 nm as presented in Figure 3.3 (a), while some of the triangles show a higher edge to edge width of 690 nm. Interestingly, these nanostructures can be also self-assembled in the shape of flowers as can be seen in Figure. 3.3 (b). The tendency of WS_2 to grow in triangularly shaped layered structures has been demonstrated earlier as well [59–62].

The reason behind the triangular architecture of the WS_2 grown via CVD technique may be owed to the dependence of crystal growth on two types of crystal face growth rates where the zigzag edge of sulfur and tungsten terminate [4]. This has been confirmed in the growth mechanism of MoS_2 [63].

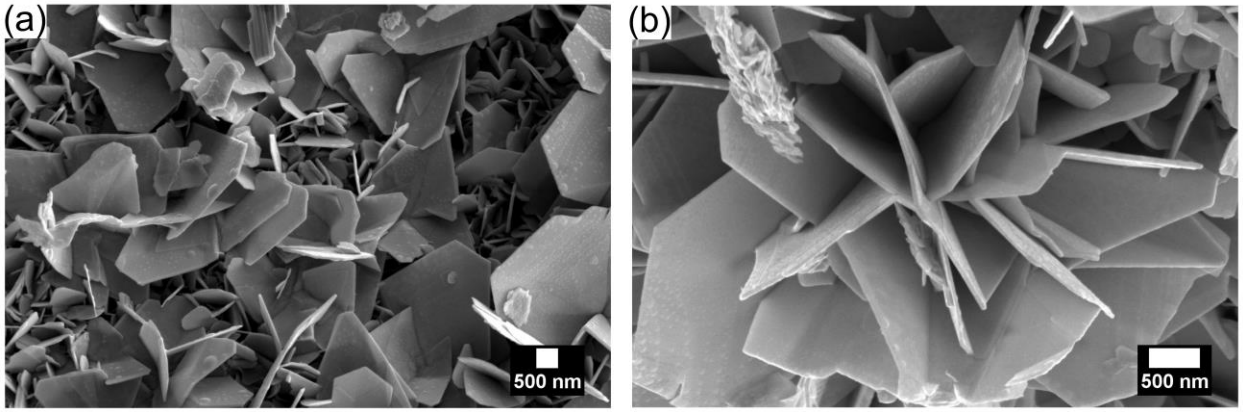

Figure 3.3 FESEM images depicting triangle-like structures of WS_2.

3.4.1.2. XRD

The crystallographic structure and the purity of the synthesized WS_2 powder was evaluated by X-ray diffraction (XRD). Figure3.4 shows the XRD diffractogram recorded on the as-synthesized WS_2 in the range of $2\theta = 5^o$ to 60^o. The diffraction peaks match with rhombohedral phase of WS_2 (ICDD card number: 84-1399) with lattice constants a= 0.3158 nm and c= 1.849 nm belonging to R3m space group. The XRD pattern reveals the presence of intense peaks at 14.35^o, 28.95^o, 33.08^o, 44.04^o and 59.99^o, in agreement with the (003), (006), (101), (009), and (0012) crystal planes of rhombohedral WS_2. Additionally, small peaks were also detected at 23.14^o, 23.64^o, and 24.36^o which were indexed to (002), (020) and (200) crystal planes of triclinic WO_3 traces (ICDD card number: 32-1395) belonging to space group P-1(2) with lattice constants a= 0.7309 nm, b= 0.7522 nm, and c= 0.7678 nm.

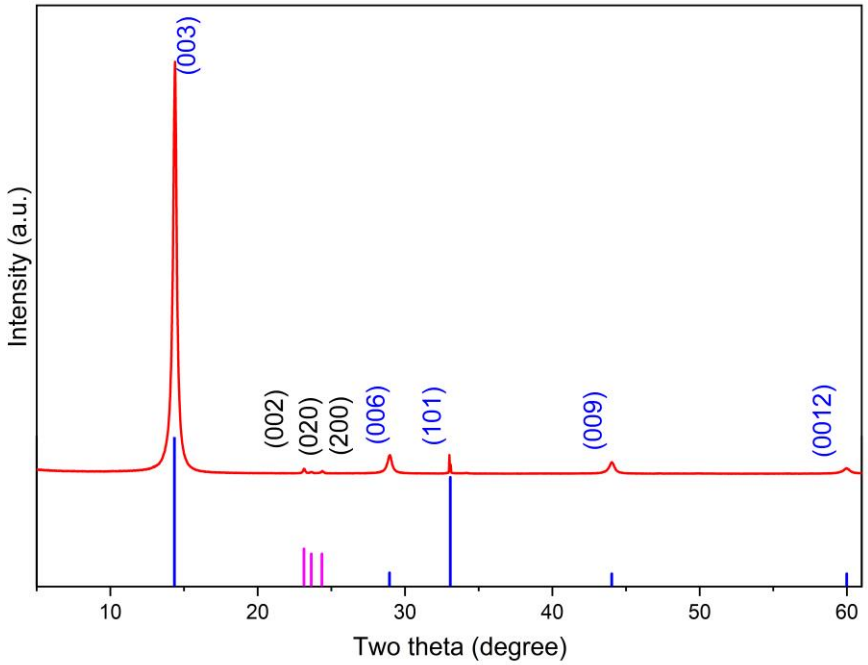

Figure 3.4 XRD diffractogram of as synthesized WS_2 airbrushed on silicon oxide substrate.

3.4.1.3. HRTEM

WS_2 powder was dispersed in absolute ethanol using sonication and drop casted onto carbon-coated copper grids for TEM and HRTEM analysis. Figure 3.5 displays the obtained results. TEM analysis was employed to examine the morphology of the as grown material. From Panel (a), we can observe the presence of large, thin and transparent triangles, which is consistent with the results observed with FESEM. Indeed, tungsten trioxide powder has completely transformed to 2D triangle-like WS_2 structures. The length of the edge sides ranged from 250 nm to 690 nm. This is in agreement with FESEM results. High resolution (HR) TEM image is displayed in panel (b-d) with insets. It allows us to study deeply the composition and the crystallinity of these triangles-like structure. From these images, we can conclude that each triangle is composed of multilayer WS_2 material; the layers were stacked one on top of the other with interplanar spacing (d) of 0.27 nm corresponding to the (101) plane of WS_2 (ICDD card number: 84-1399). This was confirmed by XRD as well.

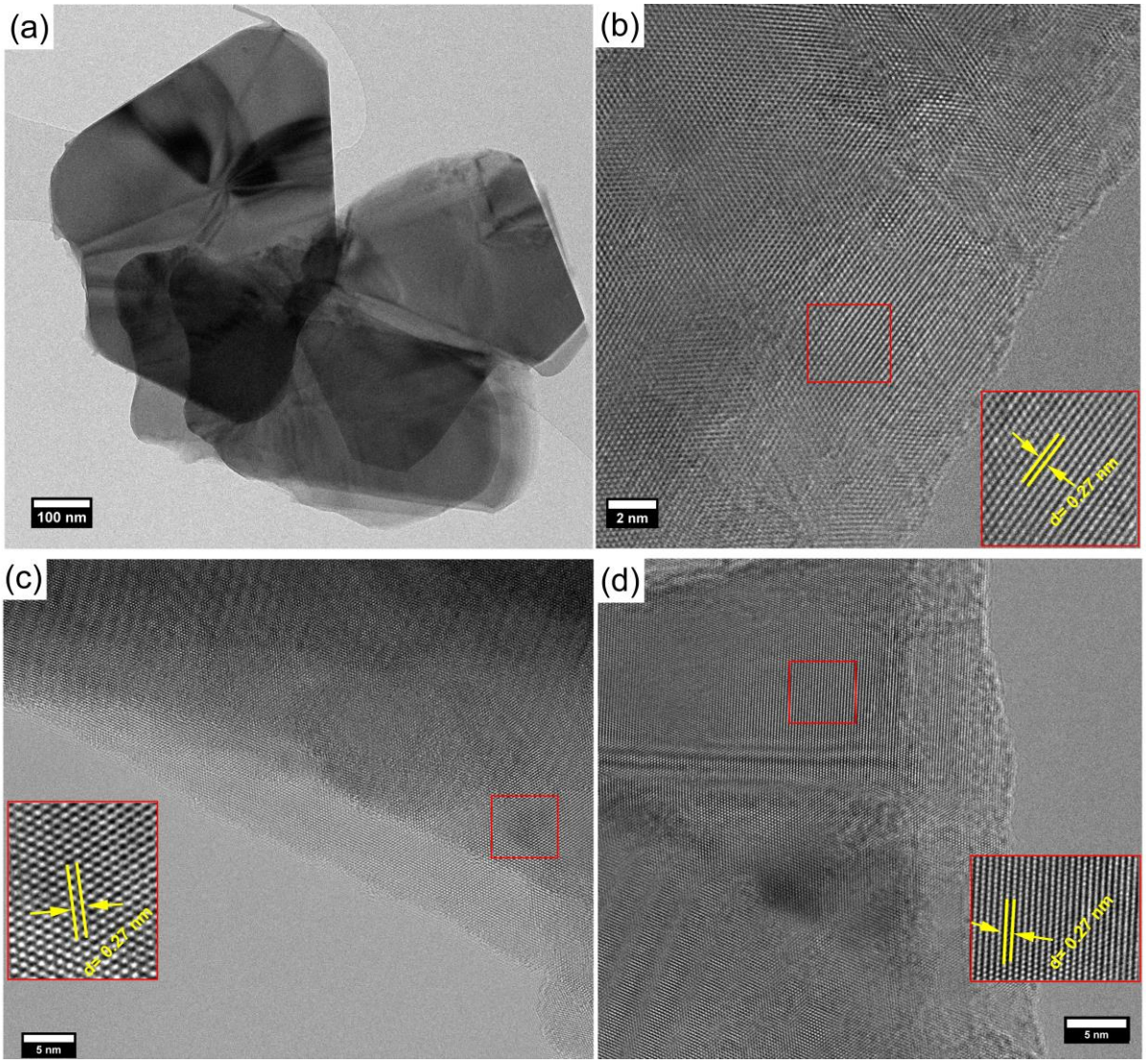

Figure 3.5 (a) TEM image of WS_2, (b-d) HRTEM images of WS_2

3.4.1.4. Raman spectroscopy

Raman spectroscopy is an acknowledged powerful and non-destructive characterization technique to study the purity for layered materials such as transition metal dichalcogenides. In this respect, Raman spectroscopy was used to study the as-synthesized WS_2 using 514 nm wavelength laser. Figure 3.6 displays the recorded Raman spectrum. The results show the two intense peaks at 352 cm^{-1} and 418 cm^{-1} corresponding to in-plane vibrational E^1_{2g} (Γ) and out-of-plane A_{1g}(Γ) modes respectively [64]. The residual peaks found in the spectrum can be identified to longitudinal acoustic phonons $LA(M)$, $A_{1g}(M) - LA(M)$, $2LA(M) - 3E^2_{2g}(M)$, $2LA(M) - 2E^2_{2g}(M)$, $2LA(M) - E^2_{2g}(M)$, $A_{1g} + LA(M)$ and $4LA(M)$ modes of WS_2 [4,64–66]. The longitudinal acoustic phonons are in-plane collective movements of the atoms in lattice. The ratio of peak intensity $I[E^1_{2g}]/I[A_{1g}]$ comes out to be 0.84, indicating the formation of

multilayer WS_2 [27,67], consistent with HRTEM results. No peaks corresponding to WO_3 were found in the Raman spectra, indicating an almost full sulfurization of the WO_3 powders.

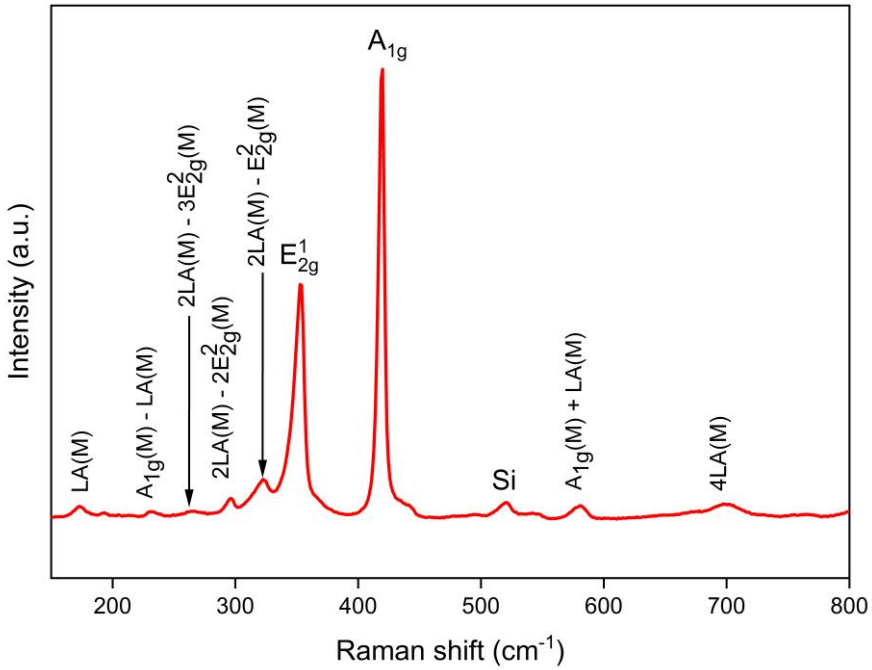

Figure 3.6 Raman spectra of as synthesized WS_2.

3.4.1.5. XPS

X-ray photoelectron spectroscopy was used to explore the chemical composition of the deposited samples. The XPS survey spectrum shows the presence of W, C, S, and O (Figure 3.7. (a). The spectra recorded in the core-level regions allow for determining the oxidation state of the elements. The spectrum recorded in the W4 f binding energy region is well reproduced by one singlet centered at binding energy 38.4 eV corresponding to the $W5p_{3/2}$ core level in WS_2 and two doublets. The doublet with W4 $f_{7/2}$ peak centered at 32.5 eV corresponds to tungsten atoms in the (4 +) valence state in WS_2, while the one at 35.9 eV, to tungsten atoms in the (6 +) valence state in WO_3 (Figure 3.7 (b). A detailed analysis of this spectrum results in 86% of tungsten atoms participating in W-S bonding in WS_2 and 14% in WO_3 [54]. The S 2p spectrum, known by the doublet peaks, S $2p_{1/2}$ and S $2p_{3/2}$ at 163.7 and 162.5 eV, respectively, with a spin–orbit energy separation of 1.2 eV corresponding to WS_2 ($S2-$ oxidation state), can be seen in Figure 3.7 (c). Additionally, the S 2p spectrum of the examined samples does not exhibit any discernible S-O bond component at 168.8 eV [54,68], therefore, the obtained spectra confirm the formation of WS_2 with the presence of small amount of WO_3 impurities.

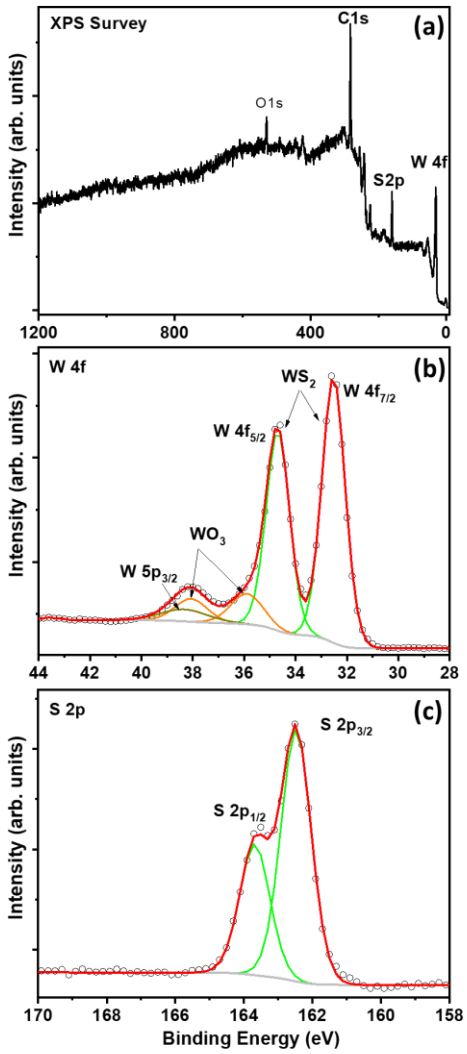

Figure 3.7 XPS spectra of as synthesized WS_2: (a) XPS survey, (b) W 4f core level and (c) S 2p core level.

3.4.2. WS_2 growth mechanism

Sulfurization of WO_3 is an interesting and intriguing process. WO_3 and S powders are the main precursors predominantly used for WS_2 growth by CVD [69]. WO_3 is partially reduced in the sulfur vapor environment to form suboxide species, WO_{3-x}, which is further sulfurized to form WS_2 [70]. The reaction involved is:

$$7S + 2WO_3 \rightarrow 2WS_2 + 3SO_2 \qquad \text{Equation 6}$$

Keeping suboxide species into consideration, the growth stages of WS_2 could be mapped onto two hypothesized reaction stages as proposed by Li et al. [71] and Ji et al. [72]. The reactions proposed are:

$$2WO_3 + xS \rightarrow 2WO_{3-x} + xSO_2 \qquad \text{Equation 7}$$

$$2WO_{3-x} + (7-x)S \rightarrow 2WS_2 + (3-x)SO_2 \qquad \text{Equation 8}$$

This is a complex conversion from monoclinic WO_3 to hexagonal cells of WS_2 since the W atom sites in monoclinic WO_3 cells differ significantly from those of hexagonal unit cells of WS_2. This indicates that the W-W interatomic distances along a and c axes change from 0.73 nm in WO_3 to 0.3158 nm in WS_2 along the a axis and from 0.767 nm in WO_3 to 1.8 nm in WS_2 along c axis [30]. The lattice parameters of the synthesized WS_2 and WO_3 precursor are discussed and demonstrated in XRD characterization section ahead. WO_{3-x} and S react heterogeneously in the gas phase and grow laterally. This process forms randomly distributed flakes rather than a continuous film [73].

In this work, the sulfur powder, placed in the secondary tube, starts to sublimate above 100 ºC, Figure 3.1 (a). The sublimated sulfur is carried by Ar gas flow towards WO_3 precursor powder boat, to maintain the subsequent sulfur-rich environment in the growth zone. Since the sulfurization reaction is carried out in a hydrogen-free environment, the reduction of WO_3 is comparatively slower, hence the second sulfurization reaction is carried out by introducing more sulfur vapors into the reaction chamber, Figure 3.1(b). The growth mechanism schematic of the edge-enriched WS_2 plates is depicted in Figure 3.8.

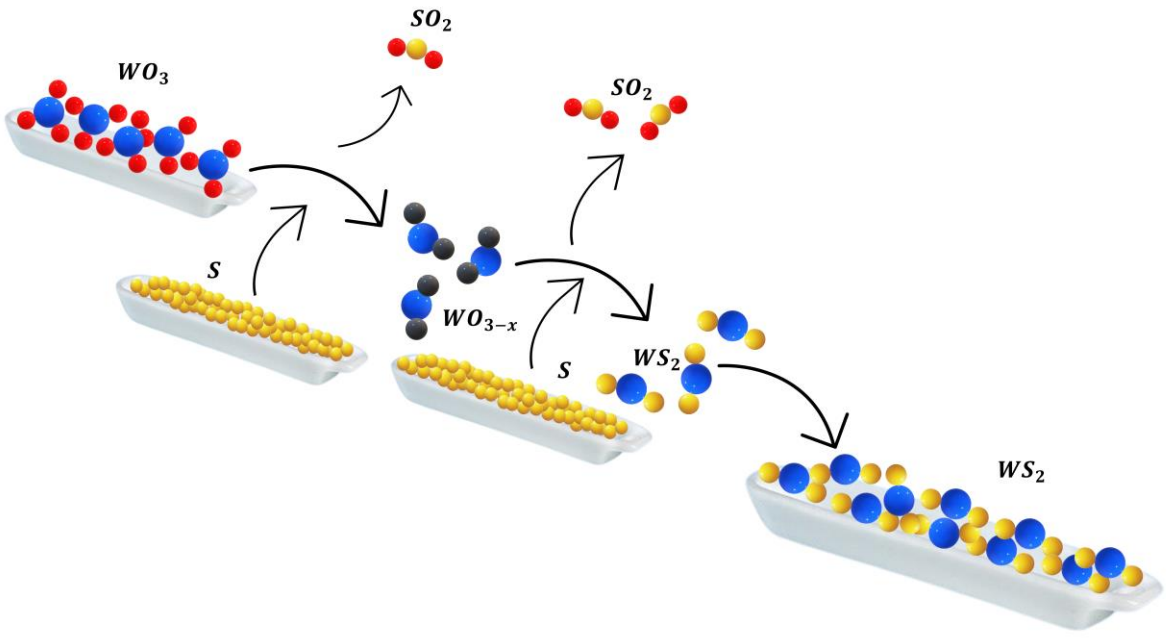

Figure 3.8 Growth mechanism schematic of edge enriched WS_2 plates.

3.4.3. Gas sensing results

3.4.3.1. Ammonia sensing

The gas sensing properties of the as-fabricated WS_2 sensors were tested for ammonia gas and evaluated using a home-made gas monitoring system. To assess the optimal working temperature, the sensors were studied towards 5 ppm of NH_3, at room temperature- RT, 100ºC and 150ºC. Overall, operating temperature is a crucial factor in gauging sensor performance, this is because the sensitivity, selectivity and response/recover dynamics of gas sensing materials heavily depend on operating temperature. A simple procedure to identify the optimum temperature is measuring a single gas concentration of the analyte gas at different operating temperatures. It is worth noting that the maximum operating temperature was set at 150ºC as above 150ºC, the evaporation of the sulfur could potentially deteriorate the sensing material leading to the formation of WO_3/WS_2 complex [54]. Also, operating devices at low temperatures is beneficial for developing low-power devices [52,54].

Figure 3.9(a) shows the sensor responses towards 5 ppm of NH_3 at different operating temperatures ranging from RT (25ºC) to 150ºC. As depicted in the figure, the sensor responses increase with an increase in the operating temperature. The standard deviation of the sensor responses is negligible indicating highly reproducible and stable sensing characteristics. The maximum sensor response at high temperatures could be owed to the enhanced gas molecule adsorption. Indeed, with the increase in the temperature, the activation barrier layer is lowered, enhancing the rate of gas adsorption leading to higher responses [54]. Thus, the operating temperature for all the subsequent studies was established to be at 150ºC, which is quite low as compared to the standard operating temperatures found in metal oxide based gas sensors [74–76].

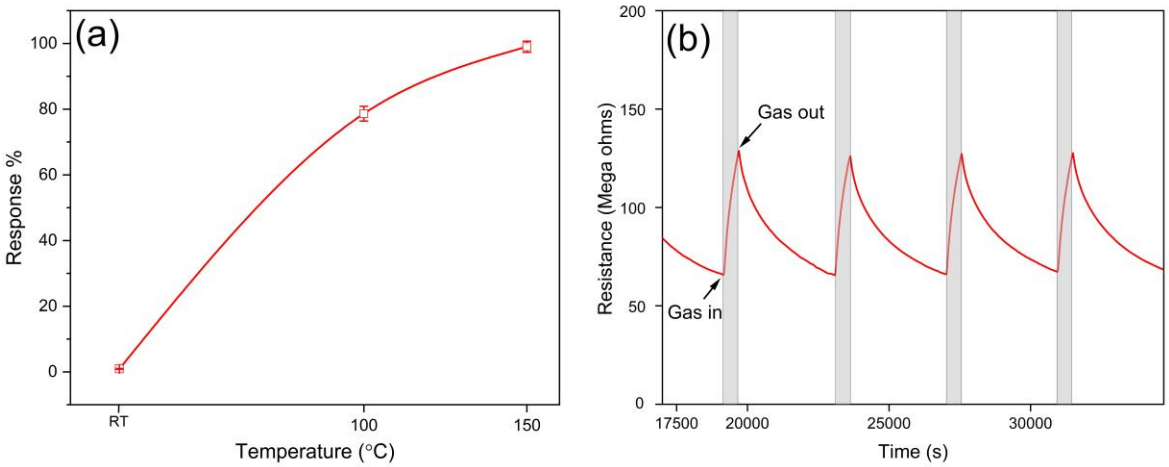

Figure 3.9 (a) Typical sensor response as a function of temperature towards 5 ppm NH_3, (b) sensing film resistance changes as a function of time towards 5 ppm NH_3 at 150ºC.

Furthermore, the sensor responses at room temperature towards 5 ppm of NH_3 were calculated to be 0.89%, rising to 80% at 100ºC and 100% at the optimal working temperature (150ºC). Figure 3.9 (b) shows real film resistance changes as a function of time, towards 5 ppm NH_3 at 150ºC. Upon being exposed to ammonia, a reducing gas species, the WS_2 sensor responds as a p-type semiconductor showing an increase in the resistance. In line with earlier NH_3 studies [77,78] after the adsorption of the NH_3 molecules on to the WS_2 sensing material, a charge transfer takes place where the NH_3 molecules donate electrons to WS_2 leading to an increase in the resistance. The sensors show stable and reproducible responses towards the target gas. The sensor baseline recovers well after each exposure cycle.

Moreover, the sensors were tested towards a wide range of NH_3 gas concentrations ranging from 1, 2.5, 5, 7.5 and 10 ppm at the optimal working temperature. The responses were calculated to be 24.45%, 53.44%, 100%, 135% and 168% respectively. As it is evident from Figure 3.10 (a), there is a linear increase in the response with the increase in the concentration of ammonia. The standard deviation error of the responses is so small that it can hardly be observed in the figure, indicating the stable and reproducible sensing responses of the sensors. As anticipated, increasing the concentration of NH_3 leads to higher resistance changes in the WS_2 sensor resulting in enhanced responses. The linear trend of the sensor responses reveals that the sensors do not saturate by exposure towards ammonia concentrations below 10 ppm. The dynamics of gas sensor film resistance change towards different ammonia concentrations is presented in Figure 3.10 (b). As is evident, the sensors can detect ammonia concentrations as low as 1 ppm. These concentrations are much lower than the legal airborne permissible exposure limit (PEL) of 50 ppm as recommended by the Occupational Safety and Health Administration (OSHA) over an eight-hour work shift [79].

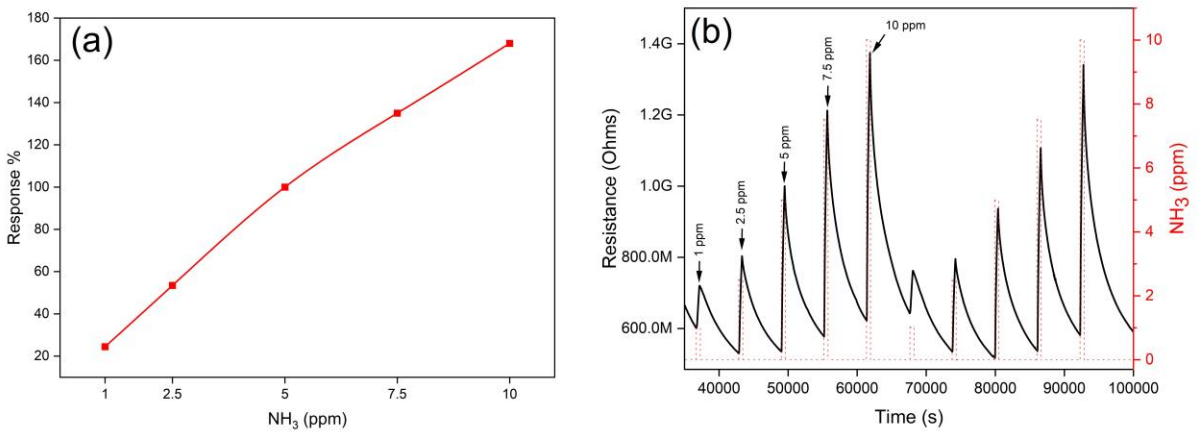

Figure 3.10 (a) WS_2 sensor response as a function of NH_3 concentration at 150ºC, (b) gas sensing film resistance changes as a function of time towards different NH_3 concentrations at 150ºC.

3.4.3.2. Selectivity tests

Selectivity is one of the most important criteria to determine the performance of a sensor. The selectivity of WS_2 sensors was evaluated towards fixed concentrations of various interfering gases such as benzene, carbon monoxide (CO), nitrogen dioxide (NO_2) and hydrogen (H_2) at temperature of 150ºC. These analyte gases as particularly important to test for selectivity owing to their potential health and environmental risks. For example, NO_2 is one of the main contributors of acid rain [80], hydrogen could be potentially dangerous for its highly explosive and flammable properties [81], exposure to 5 ppm of benzene for more than 15 minutes has been linked to the development of cancer [52]. The radar plot depicted in Figure 3.11 shows the responses of the sensors towards tested gases at 150ºC. The results show that among all the gases, the sensors respond towards NH_3 and C_6H_6 only with highest response towards NH_3. These results suggest high selectivity towards NH_3 gas. It is worth mentioning here that all the gas concentrations tested are way below the permitted limits [52,79]. Also, we compared our work with prior research studies employing WS_2 and/or other TMDs or a composite of WS_2, our sensors show better responses with low experimental limit of detection (LoD) as can be seen in Table 3.1. While the research works listed in the table focused on ammonia concentrations beyond the permissible limits, it is worth noting that some studies reported favorable sensor responses. This drawback will limit the real applications of these sensors. In contrast, our sensors excel in detecting ammonia gas at levels below 1 ppm, demonstrating their remarkable sensitivity even in low-concentration environments.

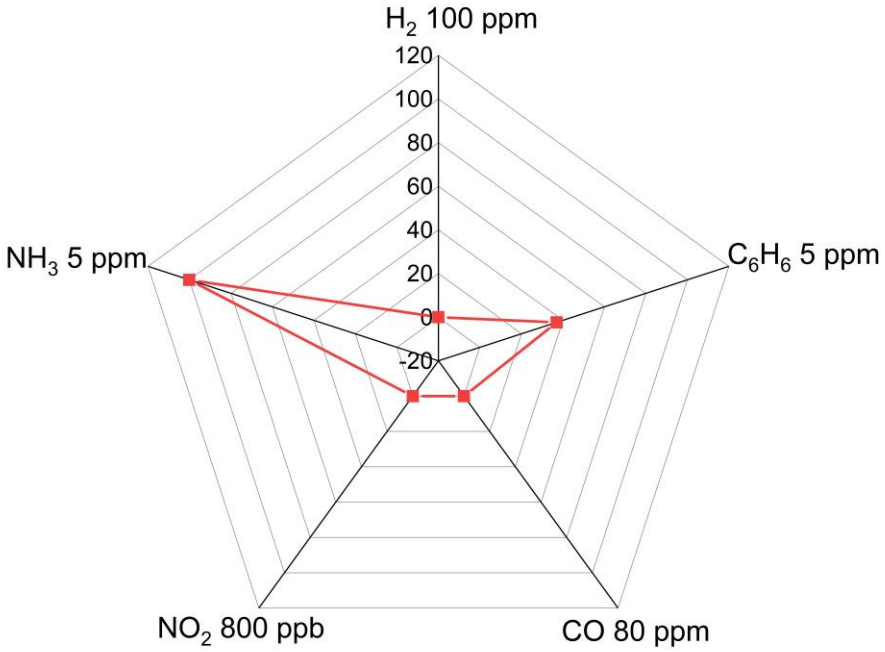

Figure 3.11 Radar plot of response of WS_2 towards NO_2 (800 ppb), H_2 (100 ppm), carbon monoxide (80 ppm), ammonia (5 ppm) and benzene (5 ppm) at 150ºC.

Table 3.1 Ammonia gas sensing characteristics reported in this work are compared with various TMDs Materials

2D material	Conc. Studied (ppm)	Working temp. (°C)	Response	LoD (ppm) experimental	Selectivity	Ref.
WSe_2 NFs	40	150	24.65%	2	NO_2, C_6H_6, CO and H_2	[52]
PPy/WS_2	200	28	30.10%	50	H_2, EtOH, CO, CO_2	[82]
rGO/WS_2	50	33.5	121%	10	NO_2, acetone, EtOH, formaldehyde, methanol, C_6H_6	[83]
MoS_2 nanosheets	10	100	30%	2	CO, H_2, NO_2	[51]
WS_2	100	35	4.61%	50	H_2S, SO_2, acetone, CO	[84]
Pt Qd/WS_2	500	25	14.5%	50	EtOH, acetic acid, CO, H_2, NO_2, ethyl acetate, n-propanol	[85]
WS_2	5	150 100 25	100% 79% 1%	<1	C_6H_6, H_2, NO_2, CO	This work

3.4.3.3. Humidity measurements

The effect of ambient moisture dramatically impacts the gas sensor sensitivity by affecting the electrical properties of the sensing material. This makes it mandatory to evaluate the gas sensor performance under the presence of humidity and verify the sensor capability for real world applications. Figure 3.12 illustrates the WS_2 sensor responses towards 5 ppm of NH_3 under dry and humid (50% relative humidity at 25°C) environments. It is observed that the sensor response decreased slightly from 100% to 93%. The baseline resistance decreased from ~ 60 MΩ in dry environment to ~50 MΩ in humid environment. In general, during the gas sensing measurements in humid environments, there is a competition between hydroxyl groups (water vapors) and ammonia gas molecules. Depending on the relative surface concentration of the hydroxyl groups, the impact of the humidity becomes noticeable [51]. If the concentration of the oxygen species is lower than the surface concentration of the hydroxyl groups, the sensor response decreases. On the contrary, if the sensors demonstrate high moisture resistance, this signifies that most of the active sites are occupied by adsorbed oxygen species. This results in no or little change in the sensor performance. Hence our edge-enriched WS_2 sensors exhibit a high level of immunity against elevated moisture levels. This characteristic feature makes them highly suitable for real world applications.

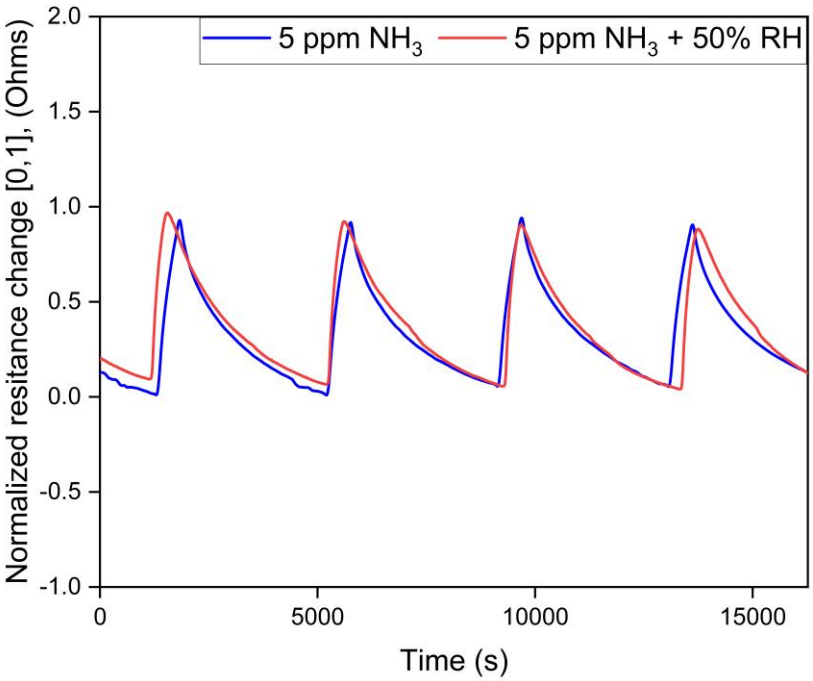

Figure 3.12 Dry and relative humidity cross-sensitivity to 5 ppm NH_3 at 150°C. The sensor resistance changes are normalized to [0,1].

3.4.4. DFT adsorption simulation results

3.4.4.1. Optimal adsorption configuration

After a 6D Bayesian optimization structure search, the global minimum of the adsorption energy landscape was determined to be at coordinates x = 3.19 Å, y = 1.87 Å, z = 2.38 Å, and angles α = 0.0°, β = 179.31°, and γ = 85.15°. During the subsequent structural optimization, the structural and energetic changes were minimal. The global minimum energy of adsorption was 0.21eV. After adsorption, the molecule was positioned at a height of 2.44 Å above the hollow surface site (the gap between adjacent S atoms), illustrated in Figure 3.13(a). The three molecular H atoms were oriented towards the substrate and aligned in the direction of three S atoms in the uppermost layer of the substrate (see Figure 3.13(b)).

3.4.4.2. Electronic structure

The Mulliken analysis of partial atomic charges was employed to compute the charge transfer between the WS_2 structure and the NH_3 target molecule. We observed a very small net charge transfer of 0.024 [e] from the WS_2 lattice towards the NH_3 molecule (e denotes the elementary charge ($|e^-|$). To explore the nature of the chemical bond, we analyzed the partial density of states (DOS) of the WS_2 substrate and NH_3 molecule near the Fermi level and compared them to the electronic states of the isolated gas molecule (not shown here). The results revealed that the electronic states of the molecule remained as narrow as in the gas state, with no evidence of hybridization upon surface adsorption. The calculated bandgap of 1.78 eV for the adsorbed

system was similar to the WS_2 bandgap of 1.61 eV. All the electronic structure observations suggest the absence of covalent bonding between the NH_3 molecule and WS_2 substrate, and point to physisorption as the main mechanism of interaction.

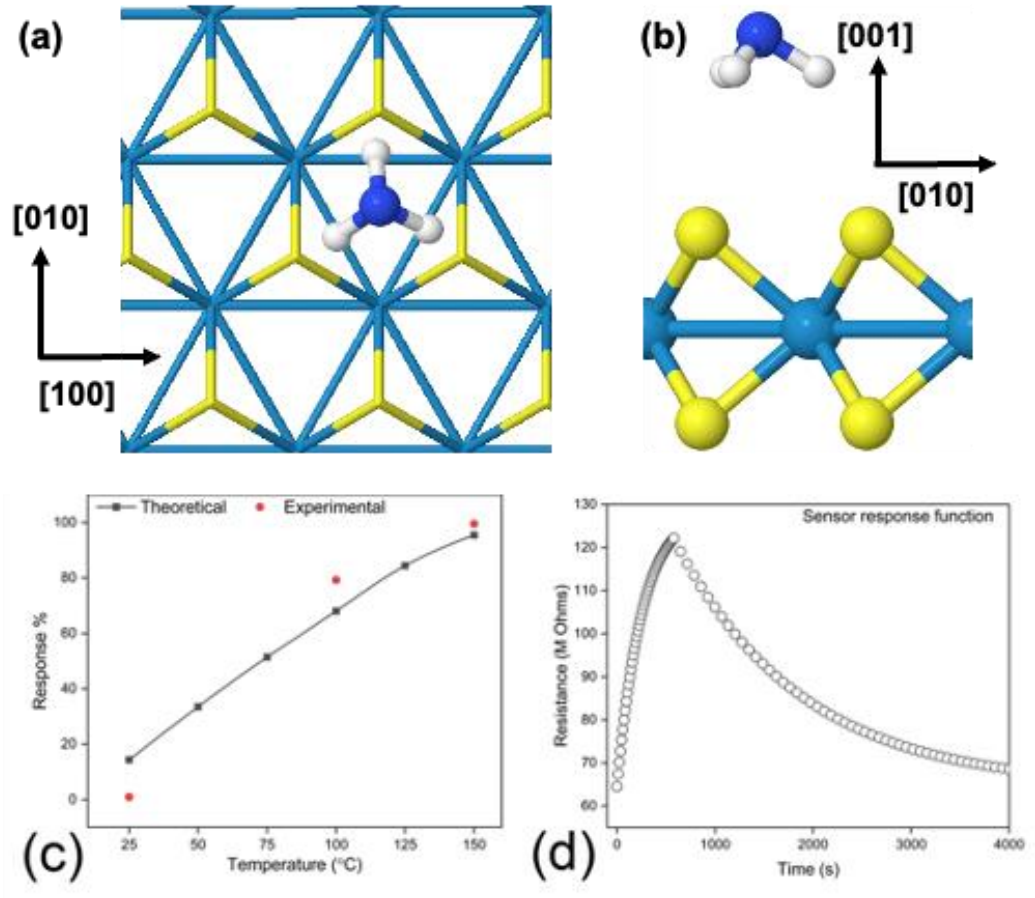

Figure 3.13 Computed adsorption configuration and transport properties. (a) and (b) present the top and side view of the global minimum adsorbate structure of NH_3 on WS_2. (c) temperature-dependent sensor sensitivity from RT to 150ºC. (d) sensor response function computed at 150ºC.

3.4.4.3. Resistivity, Sensitivity, and Sensor response

For the adsorption configuration above, we computed the temperature-dependent resistivity, corresponding sensitivity, and sensor response. Figure 3.13(c) illustrates the rate at which sensor sensitivity increases as operating temperature rises beyond the room temperature conditions. Subsequent computational analysis demonstrated that the increasing trend is a direct result of molecular adsorption. For the bare WS_2 substrate, we recorded a drop in sensitivity with increasing temperature, as expected for a semiconductor. Upon NH_3 adsorption, the shift in the Fermi level was accompanied by a flattening in band curvature, which produced a notable decrease in charge carrier mobility and jump in resistivity. Rising

temperatures made this effect more expressed and resulted in increasing sensor sensitivity. This trend was in very good agreement with experimental data, as observed in Figure 3.13(c). Next, we consider the sensor response function in Figure 3.13 (d). The time evolution of the sensor response was calculated at T = 150ºC to match the experimental conditions. This property is also in good agreement with the experimental observation in Figure 3.12.

3.4.4.4. Gas sensing mechanism

Based in the literature and the obtained results, the gas sensing mechanism of the synthetized edge enriched WS_2 can be described via two different reactions: (i) chemisorption and (ii) physisorption, as shown by Figure 3.14. The first one lies in the adsorption/desorption between the adsorbed oxygen species at the material active sites and the target gas [86–88]. Herein, oxygen species cannot be neglected, as the sensor was flushed with synthetic air to clean the material surface and to reach the steady state. Therefore, when the sensor is exposed to dry synthetic air, the oxygen molecules interact with the WS_2 surface and get adsorbed in the form of O_2^- [89,90], leading to an extraction of electrons from the WS_2 valence band and the formation of a hole accumulation layer (HAL) at the same band [52,91]. It is worth mentioning that the adsorbed oxygen species depend to the sensor working temperature, since they can be adsorbed in the form of O_2^- (<150ºC), O^-(150 to 400ºC), or O^{2-}(>400ºC) [89,90].

The chemical reaction involved can be represented by the following equation:

$$O_2 \rightarrow O_{2(ads)}^- + h^+ \qquad \text{Equation 9}$$

When the sensing layer is exposed to the NH_3 environment, the resistance increases due to the electron donor nature of NH_3 (presence of lone pair of electrons on it), which results in a decrease in the concentration of holes in the HAL region and confirms the p-type semiconductor behavior of WS_2. This reaction can be explained by the following equation [92]:

$$4NH_{3(ads)} + 3O_2^- \rightarrow 2N_2 + 6H_2O + 3e^- \qquad \text{Equation 10}$$

In physisorption reaction, NH_3 molecules have the capability to seep into the layers of WS_2 and get easily adsorbed onto the edge sites of the WS_2, thanks to the strong electronegativity of sulfur layer in WS_2. Hence fore, it injects electrons to the WS_2 layers and itself gets converted into NH_4^+. The electrons released on the WS_2 valence band combine with the existing holes, thereby, decreasing the space charge layer, reducing the concentration of holes and increasing the material resistance [93]. These findings are backed up by our first principles calculations. We found no evidence of any sort of hybridization and a very small charge transfer, suggesting

absence of chemical bonding between NH_3 and WS_2. The close resemblance of the conduction and valence states near the Fermi level in the combined system to their isolated counterparts, coupled with the low adsorption energy and minimal charge transfer, further suggests that the interaction between WS_2 and NH_3 is predominantly attributed to physisorption. Nevertheless, despite the physisorption evidence found in our DFT results, it is essential to acknowledge that the chemisorption process cannot be dismissed, as mentioned earlier in this section.

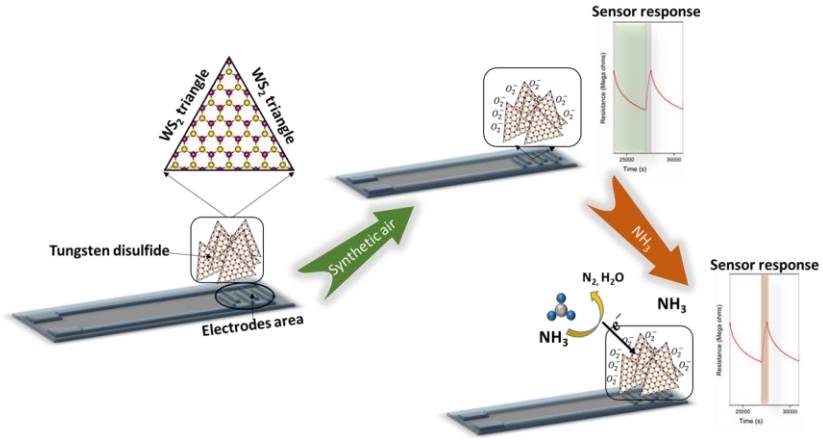

Figure 3.14 Proposed gas sensing mechanism.

3.5. Conclusion

A facile, simple, scalable, and high yield atmospheric pressure CVD technique was used to synthesize plate shaped edge-enriched WS_2 in powder form from commercial WO_3 powders. Thin films of the synthesized WS_2 were deposited on alumina transducer substrates using a simple airbrushing technique to be used as sensing material. WS_2 showed excellent sensitivity towards NH_3 at a substantially low operating temperature of 150ºC. This is for the first time the high-yielding technique has been demonstrated with the resulting material in powder form that can be deposited virtually on any substrate. The cross-sensitivity of the sensors was tested towards H_2, benzene, CO, and NO_2. The sensors showed no or small response towards the interfering species with maximum response towards NH_3. First principles calculations confirmed that the interaction between the WS_2 and NH_3 is physisorption. Moreover, the impact of having a 50% relative humidity background was limited to a slight decrease in sensor response. This confirms the promising gas sensing characteristics for selectively detecting low concentrations of NH_3 by the edge-enriched WS_2 based sensors at moderate operating temperature in real environments.

3.6. Acknowledgements

S. B. M is supported by Martí-Franquès Research grants Programme, Doctoral grants – 2019, (2019PMF-PIPF-14). F. E. A. is a RYC2022-038111-I post-doctoral fellow from the Ramon y Cajal programme. E. L. is supported by the Catalan Institution for Research and Advanced Studies via the 2018 Edition of the ICREA Academia Award. This work is supported by the Agencia Estatal de Investigación (AEI) under grant no. PDC2022-133967-100 and by AGAUR under grant no. 2021 SGR 00147. The HRTEM was partially funded by the operative program FEDER Catalunya 2014-2020 (IU16-015844).

3.7. References

[1] K.S. Novoselov, A.K. Geim, S. V. Morozov, D. Jiang, Y. Zhang, S. V. Dubonos, I. V. Grigorieva, A.A. Firsov, Electric Field Effect in Atomically Thin Carbon Films, Science (80-.). 306 (2004) 666–669. https://doi.org/10.1126/science.1102896.

[2] K.F. Mak, C. Lee, J. Hone, J. Shan, T.F. Heinz, Atomically thin MoS2: A new direct-gap semiconductor, Phys. Rev. Lett. 105 (2010) 2–5. https://doi.org/10.1103/PhysRevLett.105.136805.

[3] M. Okada, J. Pu, Y.C. Lin, T. Endo, N. Okada, W.H. Chang, A.K.A. Lu, T. Nakanishi, T. Shimizu, T. Kubo, Y. Miyata, K. Suenaga, T. Takenobu, T. Yamada, T. Irisawa, Large-Scale 1T′-Phase Tungsten Disulfide Atomic Layers Grown by Gas-Source Chemical Vapor Deposition, ACS Nano. 16 (2022) 13069–13081. https://doi.org/10.1021/acsnano.2c05699.

[4] J. Yan, S. Lian, Z. Cao, Y. Du, P. Wu, H. Sun, Y. An, CVD controlled preparation and growth mechanism of 2H-WS2 nanosheets, Vacuum. 207 (2023) 111564. https://doi.org/10.1016/j.vacuum.2022.111564.

[5] F. Schwierz, Graphene transistors, Nat. Nanotechnol. 5 (2010) 487–496. https://doi.org/10.1038/nnano.2010.89.

[6] N. Joshi, T. Hayasaka, Y. Liu, H. Liu, O.N. Oliveira, L. Lin, A review on chemiresistive room temperature gas sensors based on metal oxide nanostructures, graphene and 2D transition metal dichalcogenides, Microchim. Acta. 185 (2018). https://doi.org/10.1007/s00604-018-2750-5.

[7] H. Wang, H. Yuan, S. Sae Hong, Y. Li, Y. Cui, Physical and chemical tuning of two-

dimensional transition metal dichalcogenides, Chem. Soc. Rev. 44 (2015) 2664–2680. https://doi.org/10.1039/c4cs00287c.

[8] S. Susarla, A. Kutana, J.A. Hachtel, V. Kochat, A. Apte, R. Vajtai, J.C. Idrobo, B.I. Yakobson, C.S. Tiwary, P.M. Ajayan, Quaternary 2D Transition Metal Dichalcogenides (TMDs) with Tunable Bandgap, Adv. Mater. 29 (2017) 1–8. https://doi.org/10.1002/adma.201702457.

[9] L. Zheng, X. Wang, H. Jiang, M. Xu, W. Huang, Z. Liu, Recent progress of flexible electronics by 2D transition metal dichalcogenides, Nano Res. 15 (2022) 2413–2432. https://doi.org/10.1007/s12274-021-3779-z.

[10] M. Chhowalla, H.S. Shin, G. Eda, L.J. Li, K.P. Loh, H. Zhang, The chemistry of two-dimensional layered transition metal dichalcogenide nanosheets, Nat. Chem. 5 (2013) 263–275. https://doi.org/10.1038/nchem.1589.

[11] P. Aggarwal, S. Kaushik, P. Bisht, M. Sharma, A. Singh, B.R. Mehta, R. Singh, Centimeter-Scale Synthesis of Monolayer WS2Using Single-Zone Atmospheric-Pressure Chemical Vapor Deposition: A Detailed Study of Parametric Dependence, Growth Mechanism, and Photodetector Properties, Cryst. Growth Des. 22 (2022) 3206–3217. https://doi.org/10.1021/acs.cgd.2c00049.

[12] S. Aftab, M. Zahir Iqbal, S. Hussain, H.H. Hegazy, F. Kabir, S. Hassan Abbas Jaffery, G. Koyyada, New developments in gas sensing using various two-dimensional architectural designs, Chem. Eng. J. 469 (2023) 144039. https://doi.org/10.1016/j.cej.2023.144039.

[13] C. Lan, C. Li, J.C. Ho, Y. Liu, 2D WS2: From Vapor Phase Synthesis to Device Applications, Adv. Electron. Mater. 7 (2021) 1–36. https://doi.org/10.1002/aelm.202000688.

[14] W.S. Yun, S.W. Han, S.C. Hong, I.G. Kim, J.D. Lee, Thickness and strain effects on electronic structures of transition metal dichalcogenides: 2H-MX 2 semiconductors (M = Mo, W; X = S, Se, Te), Phys. Rev. B - Condens. Matter Mater. Phys. 85 (2012) 1–5. https://doi.org/10.1103/PhysRevB.85.033305.

[15] W. Sik Hwang, M. Remskar, R. Yan, V. Protasenko, K. Tahy, S. Doo Chae, P. Zhao, A. Konar, H. (Grace) Xing, A. Seabaugh, D. Jena, Transistors with chemically synthesized

layered semiconductor WS2 exhibiting 105 room temperature modulation and ambipolar behavior, Appl. Phys. Lett. 101 (2012) 187–188. https://doi.org/10.1063/1.4732522.

[16] X. Gu, R. Yang, Phonon transport in single-layer transition metal dichalcogenides: A first-principles study, Appl. Phys. Lett. 105 (2014). https://doi.org/10.1063/1.4896685.

[17] D. Andrzejewski, R. Oliver, Y. Beckmann, A. Grundmann, M. Heuken, H. Kalisch, A. Vescan, T. Kümmell, G. Bacher, Flexible Large-Area Light-Emitting Devices Based on WS2 Monolayers, Adv. Opt. Mater. 8 (2020) 5–9. https://doi.org/10.1002/adom.202000694.

[18] W. Zhang, Z. Huang, W. Zhang, Y. Li, Two-dimensional semiconductors with possible high room temperature mobility, Nano Res. 7 (2014) 1731–1737. https://doi.org/10.1007/s12274-014-0532-x.

[19] N. Lee, J. Kwak, J.H. Kwak, S.M. Jung, J. Kim, A. Giri, K. Thiyagarajan, Y.T. Kim, S. Jung, J.K. Kim, U. Jeong, Microwave-assisted evolution of WO3and WS2/WO3hierarchical nanotrees, J. Mater. Chem. A. 8 (2020) 9654–9660. https://doi.org/10.1039/d0ta02027c.

[20] P.K. Panigrahi, A. Pathak, Microwave-assisted synthesis of WS2 nanowires through tetrathiotungstate precursors, Sci. Technol. Adv. Mater. 9 (2008). https://doi.org/10.1088/1468-6996/9/4/045008.

[21] M. V. Santhosh, R. Geethu, K.S. Devaky, Solvothermal synthesis of WS2 rectangular nanoplates and their application in photothermal therapy, J. Mater. Sci. Mater. Electron. 34 (2023) 1–10. https://doi.org/10.1007/s10854-022-09788-0.

[22] S. Xu, D. Li, P. Wu, One-pot, facile, and versatile synthesis of monolayer MoS2 /WS2 quantum dots as bioimaging probes and efficient electrocatalysts for hydrogen evolution reaction, Adv. Funct. Mater. 25 (2015) 1127–1136. https://doi.org/10.1002/adfm.201403863.

[23] M.M.S. Villamayor, A. Lindblad, F.O.L. Johansson, T. Tran, N.H. Pham, D. Primetzhofer, N.L.A.N. Sorgenfrei, E. Giangrisotomi, A. Föhlisch, P. Lourenço, R. Bernard, N. Witkowski, G. Prévot, T. Nyberg, Growth of two-dimensional WS2 thin films by reactive sputtering, Vacuum. 188 (2021).

https://doi.org/10.1016/j.vacuum.2021.110205.

[24] L. Zeng, L. Tao, C. Tang, B. Zhou, H. Long, Y. Chai, S.P. Lau, Y.H. Tsang, High-responsivity UV-Vis Photodetector Based on Transferable WS 2 Film Deposited by Magnetron Sputtering, Sci. Rep. 6 (2016) 1–8. https://doi.org/10.1038/srep20343.

[25] D.K. Singh, G. Gupta, van der Waals epitaxy of transition metal dichalcogenides via molecular beam epitaxy: looking back and moving forward, Mater. Adv. 3 (2022) 6142–6156. https://doi.org/10.1039/d2ma00352j.

[26] H. Li, G. Lu, Y. Wang, Z. Yin, C. Cong, Q. He, L. Wang, F. Ding, T. Yu, H. Zhang, Mechanical exfoliation and characterization of single- and few-layer nanosheets of WSe2, TaS2, and TaSe2, Small. 9 (2013) 1974–1981. https://doi.org/10.1002/smll.201202919.

[27] J. Park, W. Lee, T. Choi, S.H. Hwang, J.M. Myoung, J.H. Jung, S.H. Kim, H. Kim, Layer-modulated synthesis of uniform tungsten disulfide nanosheet using gas-phase precursors, Nanoscale. 7 (2015) 1308–1313. https://doi.org/10.1039/c4nr04292a.

[28] J. Hu, F. Zhou, J. Wang, F. Cui, W. Quan, Y. Zhang, Chemical Vapor Deposition Syntheses of Wafer-Scale 2D Transition Metal Dichalcogenide Films toward Next-Generation Integrated Circuits Related Applications, Adv. Funct. Mater. 2303520 (2023) 1–27. https://doi.org/10.1002/adfm.202303520.

[29] M. Okada, T. Sawazaki, K. Watanabe, T. Taniguch, H. Hibino, H. Shinohara, R. Kitaura, Direct chemical vapor deposition growth of WS2 atomic layers on hexagonal boron nitride, ACS Nano. 8 (2014) 8273–8277. https://doi.org/10.1021/nn503093k.

[30] Z. Liu, A.W.A. Murphy, C. Kuppe, D.C. Hooper, V.K. Valev, A. Ilie, WS2 Nanotubes, 2D Nanomeshes, and 2D In-plane films through one single chemical vapor deposition route, ACS Nano. 13 (2019) 3896–3909. https://doi.org/10.1021/acsnano.8b06515.

[31] J. Jelken, M.O. Avilés, F. Lagugné-Labarthet, The Hidden Flower in WS2Flakes: A Combined Nanomechanical and Tip-Enhanced Raman Exploration, ACS Nano. 16 (2022) 12352–12363. https://doi.org/10.1021/acsnano.2c03441.

[32] N. Perea-López, A.L. Elías, A. Berkdemir, A. Castro-Beltran, H.R. Gutiérrez, S. Feng, R. Lv, T. Hayashi, F. López-Urías, S. Ghosh, B. Muchharla, S. Talapatra, H. Terrones, M. Terrones, Photosensor Device Based on Few-Layered WS 2 Films, Adv. Funct.

Mater. 23 (2013) 5511–5517. https://doi.org/10.1002/adfm.201300760.

[33] B. Shi, D. Zhou, R. Qiu, M. Bahri, X. Kong, H. Zhao, C. Tlili, D. Wang, High-efficiency synthesis of large-area monolayer WS2 crystals on SiO2/Si substrate via NaCl-assisted atmospheric pressure chemical vapor deposition, Appl. Surf. Sci. 533 (2020) 147479. https://doi.org/10.1016/j.apsusc.2020.147479.

[34] C. Lan, Z. Zhou, Z. Zhou, C. Li, L. Shu, L. Shen, D. Li, R. Dong, S.P. Yip, J.C. Ho, Wafer-scale synthesis of monolayer WS2 for high-performance flexible photodetectors by enhanced chemical vapor deposition, Nano Res. 11 (2018) 3371–3384. https://doi.org/10.1007/s12274-017-1941-4.

[35] C.M. Schaefer, J.M. Caicedo Roque, G. Sauthier, J. Bousquet, C. Hébert, J.R. Sperling, A. Pérez-Tomás, J. Santiso, E. Del Corro, J.A. Garrido, Carbon Incorporation in MOCVD of MoS2Thin Films Grown from an Organosulfide Precursor, Chem. Mater. 33 (2021) 4474–4487. https://doi.org/10.1021/acs.chemmater.1c00646.

[36] K. Kang, S. Xie, L. Huang, Y. Han, P.Y. Huang, K.F. Mak, C.J. Kim, D. Muller, J. Park, High-mobility three-atom-thick semiconducting films with wafer-scale homogeneity, Nature. 520 (2015) 656–660. https://doi.org/10.1038/nature14417.

[37] M. Seol, M.H. Lee, H. Kim, K.W. Shin, Y. Cho, I. Jeon, M. Jeong, H.I. Lee, J. Park, H.J. Shin, High-Throughput Growth of Wafer-Scale Monolayer Transition Metal Dichalcogenide via Vertical Ostwald Ripening, Adv. Mater. 32 (2020) 1–8. https://doi.org/10.1002/adma.202003542.

[38] S.H. Choi, B. Stephen, J.H. Park, J.S. Lee, S.M. Kim, W. Yang, K.K. Kim, Water-Assisted Synthesis of Molybdenum Disulfide Film with Single Organic Liquid Precursor, Sci. Rep. 7 (2017) 1–8. https://doi.org/10.1038/s41598-017-02228-8.

[39] S. Li, S. Wang, D.M. Tang, W. Zhao, H. Xu, L. Chu, Y. Bando, D. Golberg, G. Eda, Halide-assisted atmospheric pressure growth of large WSe2 and WS2 monolayer crystals, Appl. Mater. Today. 1 (2015) 60–66. https://doi.org/10.1016/j.apmt.2015.09.001.

[40] F. Lan, R. Yang, S. Hao, B. Zhou, K. Sun, H. Cheng, S. Zhang, L. Li, L. Jin, Controllable synthesis of millimeter-size single crystal WS2, Appl. Surf. Sci. 504 (2020) 144378. https://doi.org/10.1016/j.apsusc.2019.144378.

[41] W. Wang, H. Shu, J. Wang, Y. Cheng, P. Liang, X. Chen, Defect Passivation and Photoluminescence Enhancement of Monolayer MoS2 Crystals through Sodium Halide-Assisted Chemical Vapor Deposition Growth, ACS Appl. Mater. Interfaces. 12 (2020) 9563–9571. https://doi.org/10.1021/acsami.9b19224.

[42] J. Yuan, S. Zhou, B. Xiao, L. Bao, Z. Ai, Y. Shen, G. Ran, Q. Cheng, Monolayer WS 2 Nanosheets Passivated with HfO 2 for Enhanced Photodetectors, ACS Appl. Nano Mater. 6 (2023) 4594–4601. https://doi.org/10.1021/acsanm.3c00045.

[43] J. Zhou, J. Qin, L. Guo, N. Zhao, C. Shi, E.Z. Liu, F. He, L. Ma, J. Li, C. He, Scalable synthesis of high-quality transition metal dichalcogenide nanosheets and their application as sodium-ion battery anodes, J. Mater. Chem. A. 4 (2016) 17370–17380. https://doi.org/10.1039/c6ta07425a.

[44] Y.P. Chang, W.B. Li, Y.C. Yang, H.L. Lu, M.F. Lin, P.W. Chiu, K.I. Lin, Oxidation and Degradation of WS2Monolayers Grown by NaCl-Assisted Chemical Vapor Deposition: Mechanism and Prevention, Nanoscale. 13 (2021) 16629–16640. https://doi.org/10.1039/d1nr04809k.

[45] C. Xie, P. Yang, Y. Huan, F. Cui, Y. Zhang, Roles of salts in the chemical vapor deposition synthesis of two-dimensional transition metal chalcogenides, Dalt. Trans. 49 (2020) 10319–10327. https://doi.org/10.1039/d0dt01561j.

[46] Y. Hwang, N. Shin, Hydrogen-assisted step-edge nucleation of MoSe2 monolayers on sapphire substrates, Nanoscale. 11 (2019) 7701–7709. https://doi.org/10.1039/c8nr10315a.

[47] H.G. Ji, Y.C. Lin, K. Nagashio, M. Maruyama, P. Solís-Fernández, A. Sukma Aji, V. Panchal, S. Okada, K. Suenaga, H. Ago, Hydrogen-Assisted Epitaxial Growth of Monolayer Tungsten Disulfide and Seamless Grain Stitching, Chem. Mater. 30 (2018) 403–411. https://doi.org/10.1021/acs.chemmater.7b04149.

[48] T. Chen, Y. Zhou, Y. Sheng, X. Wang, S. Zhou, J.H. Warner, Hydrogen-Assisted Growth of Large-Area Continuous Films of MoS2 on Monolayer Graphene, ACS Appl. Mater. Interfaces. 10 (2018) 7304–7314. https://doi.org/10.1021/acsami.7b14860.

[49] W. Koo, J. Cha, J. Jung, S. Choi, J. Jang, D. Kim, I. Kim, Few-Layered WS 2 Nanoplates Confined in Co, N-Doped Hollow Carbon Nanocages: Abundant WS 2 Edges for Highly

Sensitive Gas Sensors, Adv. Funct. Mater. 28 (2018) 116–130. https://doi.org/10.1002/adfm.201802575.

[50] W. Choi, N. Choudhary, G.H. Han, J. Park, D. Akinwande, Y.H. Lee, Recent development of two-dimensional transition metal dichalcogenides and their applications, Mater. Today. 20 (2017) 116–130. https://doi.org/10.1016/j.mattod.2016.10.002.

[51] F.E. Annanouch, A. Alagh, P. Umek, J. Casanova-Chafer, C. Bittencourt, E. Llobet, Controlled growth of 3D assemblies of edge enriched multilayer MoS2 nanosheets for dually selective NH3 and NO2 gas sensors, J. Mater. Chem. C. 10 (2022) 11027–11039. https://doi.org/10.1039/d2tc00759b.

[52] A. Alagh, F.E. Annanouch, A. Sierra-Castillo, E. Haye, J.-F. Colomer, E. Llobet, Three-Dimensional Assemblies of Edge-Enriched WSe 2 Nanoflowers for Selectively Detecting Ammonia or Nitrogen Dioxide, ACS Appl. Mater. Interfaces. 14 (2022) 54946–54960. https://doi.org/10.1021/acsami.2c16299.

[53] J. Yan, S. Lian, Z. Cao, Y. Du, P. Wu, H. Sun, Y. An, CVD controlled preparation and growth mechanism of 2H-WS2 nanosheets, Vacuum. 207 (2023) 111564. https://doi.org/10.1016/j.vacuum.2022.111564.

[54] A. Alagh, F.E. Annanouch, P. Umek, C. Bittencourt, A. Sierra-Castillo, E. Haye, J.F. Colomer, E. Llobet, CVD growth of self-assembled 2D and 1D WS2 nanomaterials for the ultrasensitive detection of NO2, Sensors Actuators, B Chem. 326 (2021) 128813. https://doi.org/10.1016/j.snb.2020.128813.

[55] A. Alagh, F.E. Annanouch, K. Al Youssef, C. Bittencourt, F. Güell, P.R. Martínez-Alanis, M. Reguant, E. Llobet, PdO and PtO loaded WS2 boosts NO2 gas sensing characteristics at room temperature, Sensors Actuators B Chem. 364 (2022). https://doi.org/10.1016/j.snb.2022.131905.

[56] A. Alagh, F.E. Annanouch, P. Umek, C. Bittencourt, J.F. Colomer, E. Llobet, An Ultrasensitive Room-Temperature HS Gas Sensor Based on 3D Assembly of CuO Decorated WS Nanomaterial, IEEE Sens. J. 21 (2021) 21212–21220. https://doi.org/10.1109/JSEN.2021.3103925.

[57] W.J. Schutte, J.L. De Boer, F. Jellinek, Crystal structures of tungsten disulfide and

diselenide, J. Solid State Chem. 70 (1987) 207–209. https://doi.org/10.1016/0022-4596(87)90057-0.

[58] H. Kahnouji, P. Kratzer, S.J. Hashemifar, Ab initio simulation of the structure and transport properties of zirconium and ferromagnetic cobalt contacts on the two-dimensional semiconductor WS2, Phys. Rev. B. 99 (2019) 035418. https://doi.org/10.1103/PhysRevB.99.035418.

[59] Z. Zeng, X. Sun, D. Zhang, W. Zheng, X. Fan, M. He, T. Xu, L. Sun, X. Wang, A. Pan, Controlled Vapor Growth and Nonlinear Optical Applications of Large-Area 3R Phase WS 2 and WSe 2 Atomic Layers, Adv. Funct. Mater. 29 (2019) 1–8. https://doi.org/10.1002/adfm.201806874.

[60] W.T. Hsu, Z.A. Zhao, L.J. Li, C.H. Chen, M.H. Chiu, P.S. Chang, Y.C. Chou, W.H. Chang, Second harmonic generation from artificially stacked transition metal dichalcogenide twisted bilayers, ACS Nano. 8 (2014) 2951–2958. https://doi.org/10.1021/nn500228r.

[61] Y. Yue, J.C. Chen, Y. Zhang, S.S. Ding, F. Zhao, Y. Wang, D. Zhang, R.J. Li, H. Dong, W. Hu, Y. Feng, W. Feng, Two-Dimensional High-Quality Monolayered Triangular WS2 Flakes for Field-Effect Transistors, ACS Appl. Mater. Interfaces. 10 (2018) 22435–22444. https://doi.org/10.1021/acsami.8b05885.

[62] X.Q. Zhang, C.H. Lin, Y.W. Tseng, K.H. Huang, Y.H. Lee, Synthesis of lateral heterostructures of semiconducting atomic layers, Nano Lett. 15 (2015) 410–415. https://doi.org/10.1021/nl503744f.

[63] J. Cheng, T. Jiang, Q. Ji, Y. Zhang, Z. Li, Y. Shan, Y. Zhang, X. Gong, W. Liu, S. Wu, Kinetic Nature of Grain Boundary Formation in As-Grown MoS2 Monolayers, Adv. Mater. 27 (2015) 4069–4074. https://doi.org/10.1002/adma.201501354.

[64] Q. Fu, W. Wang, L. Yang, J. Huang, J. Zhang, B. Xiang, Controllable synthesis of high quality monolayer WS2 on a SiO2/Si substrate by chemical vapor deposition, RSC Adv. 5 (2015) 15795–15799. https://doi.org/10.1039/c5ra00210a.

[65] A. Berkdemir, H.R. Gutiérrez, A.R. Botello-Méndez, N. Perea-López, A.L. Elías, C.I. Chia, B. Wang, V.H. Crespi, F. López-Urías, J.C. Charlier, H. Terrones, M. Terrones, Identification of individual and few layers of WS2 using Raman Spectroscopy, Sci. Rep.

3 (2013) 1–8. https://doi.org/10.1038/srep01755.

[66] F. Chen, S. Ding, W. Su, A feasible approach to fabricate two-dimensional WS2 flakes: From monolayer to multilayer, Ceram. Int. 44 (2018) 22108–22112. https://doi.org/10.1016/j.ceramint.2018.08.322.

[67] H.R. Gutiérrez, N. Perea-López, A.L. Elías, A. Berkdemir, B. Wang, R. Lv, F. López-Urías, V.H. Crespi, H. Terrones, M. Terrones, Extraordinary room-temperature photoluminescence in triangular WS 2 monolayers, Nano Lett. 13 (2013) 3447–3454. https://doi.org/10.1021/nl3026357.

[68] K.M. McCreary, A.T. Hanbicki, G.G. Jernigan, J.C. Culbertson, B.T. Jonker, Synthesis of Large-Area WS 2 monolayers with Exceptional Photoluminescence, Sci. Rep. 6 (2016) 1–7. https://doi.org/10.1038/srep19159.

[69] Y. Shi, H. Li, L.J. Li, Recent advances in controlled synthesis of two-dimensional transition metal dichalcogenides via vapour deposition techniques, Chem. Soc. Rev. 44 (2015) 2744–2756. https://doi.org/10.1039/c4cs00256c.

[70] Y. Zhang, Y. Zhang, Q. Ji, J. Ju, H. Yuan, J. Shi, T. Gao, D. Ma, M. Liu, Y. Chen, X. Song, H.Y. Hwang, Y. Cui, Z. Liu, Controlled Growth of High-Quality Monolayer WS 2 Layers on Sapphire and Imaging Its Grain Boundary, ACS Nano. 7 (2013) 8963–8971. https://doi.org/10.1021/nn403454e.

[71] X.L. Li, Y.D. Li, Formation of MoS2 inorganic fullerenes (IFs) by the reaction of MoO3 nanobelts and S, Chem. - A Eur. J. 9 (2003) 2726–2731. https://doi.org/10.1002/chem.200204635.

[72] Q. Ji, Y. Zheng, Y. Zhang, Z. Liu, Chemical vapour deposition of group-VIB metal dichalcogenide monolayers: Engineered substrates from amorphous to single crystalline, Chem. Soc. Rev. 44 (2015) 2587–2602. https://doi.org/10.1039/c4cs00258j.

[73] Y. Lee, J.W. Jung, J.S. Lee, Highly electroconductive and uniform WS2film growth by sulfurization of W film using diethyl sulfide, Mater. Chem. Front. 5 (2021) 3692–3698. https://doi.org/10.1039/d1qm00173f.

[74] L.-Y. Zhu, L.-X. Ou, L.-W. Mao, X.-Y. Wu, Y.-P. Liu, H.-L. Lu, Advances in Noble Metal-Decorated Metal Oxide Nanomaterials for Chemiresistive Gas Sensors: Overview, Nano-Micro Lett. 15 (2023) 89. https://doi.org/10.1007/s40820-023-01047-

z.

[75] S.B. Malik, K. V. Mejia-Centeno, P.R. Martínez-Alanis, A. Cabot, F. Güell, F.E. Annanouch, E. Llobet, Synergistic effect of CeO2 nanoparticles and WO3 nanowires in gas sensing applications, Sensors Actuators B Chem. 400 (2024). https://doi.org/10.1016/j.snb.2023.134879.

[76] S.B. Malik, F.E. Annanouch, E. Llobet, Pd-Nanoparticle-Decorated Multilayered MoS2 Sheets for Highly Sensitive Hydrogen Sensing, Chemosensors. 11 (2023) 550. https://doi.org/10.3390/chemosensors11110550.

[77] X. Li, X. Li, Z. Li, J. Wang, J. Zhang, WS2 nanoflakes based selective ammonia sensors at room temperature, Sensors Actuators B Chem. 240 (2017) 273–277. https://doi.org/10.1016/j.snb.2016.08.163.

[78] X. Guo, H. Yang, X. Mo, R. Bai, Y. Wang, Q. Han, S. Han, Q. Sun, D.W. Zhang, S. Hu, L. Ji, Modulated wafer-scale WS 2 films based on atomic-layer-deposition for various device applications, RSC Adv. 13 (2023) 14841–14848. https://doi.org/10.1039/D3RA00933E.

[79] Occupational Safety and Health Administration, Permissible Exposure Limits − Annotated Tables, (n.d.). https://www.osha.gov/annotated-pels/table-z-1.

[80] Y. Wang, Y. Zhou, J. Li, R. Zhang, H. Zhao, Y. Wang, Ag decoration-enabled sensitization enhancement of black phosphorus nanosheets for trace NO2 detection at room temperature, J. Hazard. Mater. 435 (2022) 129086. https://doi.org/10.1016/j.jhazmat.2022.129086.

[81] A. V. Agrawal, R. Kumar, G. Yang, J. Bao, M. Kumar, M. Kumar, Enhanced adsorption sites in monolayer MoS2 pyramid structures for highly sensitive and fast hydrogen sensor, Int. J. Hydrogen Energy. 45 (2020) 9268–9277. https://doi.org/10.1016/j.ijhydene.2020.01.119.

[82] Y. Sood, S.D. Lawaniya, H. Mudila, K. Awasthi, A. Kumar, Polypyrrole-Tungsten disulphide 2D nanocomposites for ammonia sensing, Sensors Actuators B Chem. 394 (2023) 134298. https://doi.org/10.1016/j.snb.2023.134298.

[83] X. Wang, D. Gu, X. Li, S. Lin, S. Zhao, M.N. Rumyantseva, A.M. Gaskov, Reduced graphene oxide hybridized with WS2 nanoflakes based heterojunctions for selective

ammonia sensors at room temperature, Sensors Actuators, B Chem. 282 (2019) 290–299. https://doi.org/10.1016/j.snb.2018.11.080.

[84] Z. Qin, X. Song, J. Wang, X. Li, C. Wu, X. Wang, X. Yin, D. Zeng, Development of flexible paper substrate sensor based on 2D WS2 with S defects for room-temperature NH3 gas sensing, Appl. Surf. Sci. 573 (2022) 151535. https://doi.org/10.1016/j.apsusc.2021.151535.

[85] C. Ouyang, Y. Chen, Z. Qin, D. Zeng, J. Zhang, H. Wang, C. Xie, Two-dimensional WS 2 -based nanosheets modified by Pt quantum dots for enhanced room-temperature NH 3 sensing properties, Appl. Surf. Sci. 455 (2018) 45–52. https://doi.org/10.1016/j.apsusc.2018.05.148.

[86] X. Li, X. Li, Z. Li, J. Wang, J. Zhang, WS2 nanoflakes based selective ammonia sensors at room temperature, Sensors Actuators B Chem. 240 (2017) 273–277. https://doi.org/10.1016/j.snb.2016.08.163.

[87] M. Donarelli, S. Prezioso, F. Perrozzi, F. Bisti, M. Nardone, L. Giancaterini, C. Cantalini, L. Ottaviano, Response to NO2 and other gases of resistive chemically exfoliated MoS2-based gas sensors, Sensors Actuators B Chem. 207 (2015) 602–613. https://doi.org/10.1016/j.snb.2014.10.099.

[88] D. Burman, H. Raha, B. Manna, P. Pramanik, P.K. Guha, Substitutional Doping of MoS 2 for Superior Gas-Sensing Applications: A Proof of Concept, ACS Sensors. 6 (2021) 3398–3408. https://doi.org/10.1021/acssensors.1c01258.

[89] F.E. Annanouch, Z. Haddi, S. Vallejos, P. Umek, P. Guttmann, C. Bittencourt, E. Llobet, Aerosol-assisted CVD-grown WO3 nanoneedles decorated with copper oxide nanoparticles for the selective and humidity-resilient detection of H2S, ACS Appl. Mater. Interfaces. 7 (2015) 6842–6851. https://doi.org/10.1021/acsami.5b00411.

[90] N. Barsan, U. Weimar, Conduction model of metal oxide gas sensors, J. Electroceramics. 7 (2001) 143–167. https://doi.org/10.1023/A:1014405811371.

[91] K. Xu, N. Li, D. Zeng, S. Tian, S. Zhang, D. Hu, C. Xie, Interface bonds determined gas-sensing of SnO2-SnS2 hybrids to ammonia at room temperature, ACS Appl. Mater. Interfaces. 7 (2015) 11359–11368. https://doi.org/10.1021/acsami.5b01856.

[92] A. Moumen, G.C.W. Kumarage, E. Comini, P-Type Metal Oxide Semiconductor Thin

Films: Synthesis and Chemical Sensor Applications, Sensors. 22 (2022) 1359. https://doi.org/10.3390/s22041359.

[93] Z. Qin, D. Zeng, J. Zhang, C. Wu, Y. Wen, B. Shan, C. Xie, Effect of layer number on recovery rate of WS 2 nanosheets for ammonia detection at room temperature, Appl. Surf. Sci. 414 (2017) 244–250. https://doi.org/10.1016/j.apsusc.2017.04.063.

CHAPTER 4

Graphene functionalized WS_2 for detecting ultra-low NO_2 concentrations

Graphene functionalized WS_2 for detecting ultra-low NO_2 concentrations

Shuja Bashir Malik[1,2], Fatima Ezahra Annanouch[1,2], Eduard Llobet[1,2]

1 Universitat Rovira i Virgili, MINOS, Països Catalans 26, 43007 Tarragona, Catalunya, Spain.

2 IU-RESCAT, Universitat Rovira i Virgili, Joanot Martorell 15, 43480 Vila-seca, Spain.

* Correspondence: authors' email: fatimaezahra.annanouch@urv.cat, eduard.llobet@urv.cat

Abstract

Two-dimensional (2D) transition metal dichalcogenides (TMDs) show great promise for low-temperature gas sensing applications, particularly for NO_2 detection. However, several areas require enhancement and optimizations, including low sensitivity at low limits of detection (LoD), selectivity issues, and poor recovery. To address these challenges and improve gas sensor efficiency, researchers have proposed the functionalization of 2D TMDs. This aids in elucidating the synergistic effects, particularly when combined with carbon-based materials. This paper presents a novel approach for fabricating hybrid heterostructures of atmospheric pressure chemical vapor deposition (APCVD) synthesized tungsten disulfide (WS_2) and graphene. Facile airbrushing technique was used to fabricate the sensors with N_2 as carrier gas. The morphological and structural investigation reveal sheet like growth of edge-enriched 2D WS_2 and a homogenous distribution of the sensing materials in the hybrids. The gas sensing properties of the sensing materials was tested towards NO_2 gas at different operating temperatures. The hybrid sensors exhibit excellent responses to ultra-low concentrations of NO_2 (10 ppb) at substantially low temperature of 100°C compared to their graphene and WS_2 counterparts. The gas detecting capabilities for CO, H_2, C_6H_6, and NH_3 were also investigated to better comprehend the selectivity of the sensors. Furthermore, sensor responses nearly double in humid environments (50% RH at 25ºC), suggesting practical applications for selective NO_2 detection.

Keywords: WS_2, APCVD, sulfurization, gas sensor, NO_2, TMDs, 2D materials

4.1. Introduction

A steep increase in industrialization and population has heightened the emission of toxic gases and volatile organic compounds (VOCs) into the atmosphere leading to life threatening situations [1]. The main contributors of severe respiratory issues, including chronic bronchitis, respiratory irritation and asthma are parts per million (ppm) levels of NH_3 and parts per billion (ppb) levels of NO_2 [2,3]. The common sources of these pollutant gases include power plant exhausts, industries, vehicular emission, and fertilizer production [4,5]. Moreover, NO_2 reacts with ambient compounds, contributing to acid rain and ozone formation, exacerbating air pollution concerns [4][6]. The United States Environmental Protection Agency underscores the adverse effects of prolonged exposure to NO_2. Low concentrations of NO_2, as low as several hundred parts per billion (ppb) can induce eye and lung irritation, necessitating its regulation with an exposure limit of 53 ppb [7,8]. Hence, it becomes imperative to identify and quantify the atmospheric concentrations of NH_3 and NO_2 to safeguard chemical processes, monitor human health, and ensure protection against gas leakage and chemical disasters [2]. This makes it imperative to develop gas sensors capable of real-time monitoring of low concentrations of combustible and toxic gases. The sensors need to possess key attributes like high sensitivity, selectivity, accuracy, reliability, and long-term stability, all while being cost-effective and energy-efficient.

Semiconductor gas sensors, particularly metal oxide-based sensors (MOX) have garnered a tremendous attention for their ease of fabrication, miniaturization, simple operation, and possibility of mass production [6]. However, their use is limited by the fact that they operate at particularly high temperatures which compromises their stability and increases energy consumption [6]. While researchers have been successful in exploring the strategies to make hybrids of MOX with MXenes to lower the operating temperature of the sensors [9], still pristine graphene shows promising gas sensing results at lower temperatures than MOX sensors especially at room temperature [10]. Graphene exhibits desired intrinsic properties that even surpass those of MOX and TMDs, particularly in terms of thermal conductivity (5000 W mK^{-1} at 27°C) [11], high room-temperature carrier mobility (20,000 cm^2 V^{-1} s^{-1}) [12], low density (0.77 mg m^{-2}) [13], and exceptional chemical stability and mechanical durability (Young's modulus approximately 1.02 TPa) [14]. These characteristics make graphene highly suitable for the development of miniaturized, flexible gas sensors with superior sensitivity at low

operating temperatures [10]. Nevertheless, graphene-based sensors face challenges in sensitivity and recovery speed, necessitating exploration of alternative materials [15].

Two-dimensional transition-metal dichalcogenides (2D TMDs), such as MoS_2 and WS_2, have attracted attention for their unique electrical, chemical, and optical properties [16]. They represent a promising class of layered van der Waals materials with excellent responses to hazardous gas species, especially NOx [17]. Their large surface-area-to-volume ratios provide suitable adsorption sites for gas molecules, and the sensing mechanism is based on direct charge transfer upon gas adsorption [18,19]. However, limitations include low sensitivity to NO_2 at the ppb level, and surface defects like grain boundaries, vacancies, and edges, leading to incomplete recovery and prolonged recovery times [10]. Prolonged exposure of TMDs to atmospheric oxygen can accelerate oxidation, degrading sensing performance [20]. Therefore, research aims to synthesize TMDs-based sensing materials capable of sensitively and selectively detecting NO_2 at ppb levels with enhanced stability over prolonged use.

Concurrently, efforts are underway to explore the excellent properties of heterojunctions formed from different 2D materials such as reduced graphene oxide (rGO)/metal oxide [21], TMDs/TMDs [22], TMDs/metal oxide [23,24], or rGO/TMDs [25,26]. These heterojunctions exhibit excellent prospects for gas-sensing applications due to their unique properties compared to their pristine counterparts [25]. Considerable amount of research has been focussed on the fabrication of 2D-2D hybrids. Diverse 2D layered nanomaterials are stacked to facilitate the regulation and manipulation of charge carrier generation, confinement, and transport [27]. A rational design of hybrids involves understanding the behavior of individual materials and exploiting their combined effects to enhance sensing behavior. Sardana et al. [2] exploited synergistic effects of WS_2 grown on MXenes to identify, quantify and differentiate lower concentrations of NH_3 and NO_2. Commercial MXene were mixed with WS_2 in water-ethanol mixture and homogenized by probe sonication. The sensors were able to detect 0.1-5 ppm NH_3 and 1- 100 ppb of NO_2 by adjusting the weight proportions of WS_2 to MXene.

Studies by Schedin et al. highlight the gas-sensing behavior of graphene, emphasizing the regulation of local carrier concentration by gas molecules like NO_2, resulting in changes in sensor conductivity [28]. However, the carrier change induced by gas interaction is relatively small compared to the background carriers in metal-like graphene, leading to a minimal change in resistance magnitude [29]. Gas-sensing applications based on graphene and its derivatives often require additional modifications to enhance adsorption and electronic characteristics. Doping with various heteroatoms has been employed for this purpose [30]. Both graphene and

its derivatives, such as reduced graphene oxide (rGO), demonstrate a distinct advantage in NO2 gas detection due to their high carrier mobility and large surface-to-volume ratio [30,31]. Hou and co-workers [25] reported MoS_2/GO nanocomposite for triethylamine (TEA)-sensing applications. The MoS_2/GO hybrid was synthesized using a facile hydrothermal technique. The sensors were able to detect low concentrations of 1 ppm of TEA with high stability. Ma et al. [32] demonstrated self-powered photovoltaic flexible gas sensors through defect engineering controlled by ion irradiation employing a WS_2/graphene heterostructure. The graphene and WS_2 monolayers were grown via chemical vapor deposition which were then transferred to Si substrate employing wet-chemical processes. The sensors were able to detect as low as 50 ppb of NO_2. Graphene offers superior electrical conductivity and mechanical strength compared to reduced graphene oxide, making it more suitable for gas sensing applications, electronic devices, and advanced composites [33,34]. Moumen et al. [22] reported ultra-sensitive NO_2 (300 ppb) sensor working at room temperature employing WS_2-WSe_2 p-p heterostructure. The heterostructure was prepared using atmospheric pressure chemical vapor deposition (APCVD) and liquid phase exfoliation (LPE). The sensors demonstrated long term stability of approximately 2.5 months even in elevated humidity conditions (40-90% RH). However, hydrothermal synthesis can be hindered by long reaction times and high energy consumption, limiting its scalability and efficiency. Also, liquid phase exfoliation suffers from challenges such as limited control over the size and quality of the produced materials, leading to variations in material properties. Moreover, the process often involves the use of hazardous solvents, posing environmental and safety concerns. Also, most of the reported methods for heterojunction fabrication involve drop casting method where the thickness of the deposited film is seldom controlled.

Considering the above-mentioned shortcomings, this work demonstrates an excellent hybrid sensing material for detecting ultra-low concentrations of NO_2. We report a methodology to fabricate a WS_2-graphene hybrid thin films using simple airbrush. WS_2 was grown using APCVD technique. The hybrid films are directly deposited on the transducer substrate with full control over the thickness. The films were characterized for morphology, microstructure, phase, and chemical composition. The gas sensing properties of the films were studied towards ultra-low NO_2 concentrations at various operating temperatures (i.e., RT, 100ºC and 150ºC) in dry and humid environments, and other interfering species like NH_3, CO, H_2 and C_6H_6. The sensors responded excellently towards ultra-low concentrations of NO_2 with an experimental limit of detection (LoD) of 10 ppb.

4.2. Experimental

4.2.1. APCVD synthesis of sheet-like WS_2

Atmospheric pressure chemical vapor deposition (APCVD) technique was used to synthesize sheet-like WS_2 with yield in hundreds of milligrams. The technique holds the potential of being scaled to industrial level. Commercially available tungsten trioxide powder procured from Sigma Aldrich (CAS: 1314-35-8) was employed and sulfurized to obtain sheet-like WS_2 nanostructures in powder form. The sulfurization was carried out for 60 minutes at 900ºC using metallic sulfur (Sigma Aldrich, CAS: 7704-34-9) in a home-made tube in tube furnace with a temperature gradient. The schematic of the furnace is shown in Figure 4.1. The middle zone of the furnace reaches a set temperature of 900ºC while as the zones adjacent to the middle zone reach approximately 400ºC. Three alumina boats were positioned strategically within different temperature zones of the furnace; one boat contained 100 mg of WO_3 precursor powder, while the other two boats contained 1 g of sulfur each. One of the sulfur boats was placed adjacent to the WO_3 containing boat inside a semi sealed secondary quartz tube, both situated in the 900ºC temperature zone. The reaction chamber was flushed with 100 mL/min of argon prior to sulfurization reaction to remove oxygen present in the reactor. The boat outside the secondary quartz tube was placed upstream of argon flow inside the bigger quartz tube, Figure 4.1 (a). The argon flow was kept at 30 mL/min during the reaction. The furnace was programmed to reach the set temperature of 900ºC with a ramp of 40ºC/min. Upon reaching the set temperature (900ºC), the external quartz tube is carefully positioned as such that the sulfur boat located outside the furnace is in the 400ºC temperature zone of the furnace, Figure 4.1 (b). This configuration ensures a sulfur rich environment and double sulfurization. The furnace was let to cool naturally after the completion of the reaction.

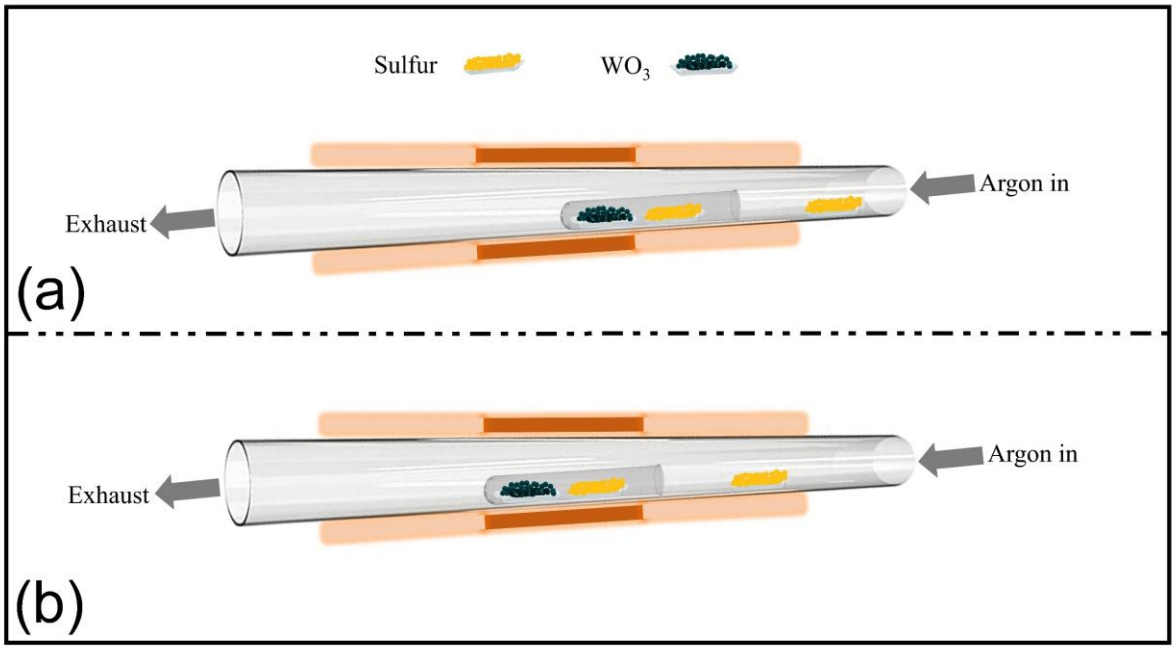

Figure 4.1 Schematic of APCVD reactor.

4.2.2. Graphene-WS_2 hybrid

Commercial graphene (STREM, CAS 1034343-98-0) was mixed with synthesized WS_2 powder to form WS_2-graphene hybrids. Three hybrid combinations, with ratios of 3:1, 1:1 and 1:3 of WS_2 to graphene, were prepared to be deposited as gas sensing films.

4.2.3. Gas sensor fabrication

Pristine graphene and WS_2 and WS_2-graphene hybrid sensing films were deposited on commercial alumina substrates (Ceram Tech GmBH, Germany) using a simple airbrushing technique. The alumina substrates have Pt-interdigitated electrodes with a gap of 300 µm on the front side (2.5 mm x 5.1 mm) and a Pt-resistive heater meander on the back side. The substrates were cleaned with sequential sonication in acetone, ethanol and deionized water followed by nitrogen blow drying. The cleaned substrates were placed in a home-made airbrush system consisting of a hot plate, commercial air brush, a multimeter, and connectors.

To deposit thin films of pristine graphene and pristine WS_2, 10 mg of graphene and WS_2 powder were separately sonicated in 10 mL of absolute ethanol (Scharlab, CAS: 64-17-5) for 1 hour each, resulting in a black and brownish suspension, respectively. In the case of WS_2-graphene hybrids, a constant total weight of 10 mg was maintained for both WS_2 and graphene. For hybrid A, 7.5 mg of WS_2 was mixed with 2.5 mg of graphene; for hybrid B, 5 mg of WS_2 was mixed with 5 mg of graphene, and for hybrid C, 2.5 mg of WS_2 was mixed with 7.5 mg of

graphene. The sensors are named as Sensor A, Sensor B and Sensor C respectively henceforth. The amount of ethanol was kept constant at 10 ml in all the cases like that of pristine graphene and WS_2 solutions. The obtained solutions were transferred to an airbrush system. The alumina substrates were placed on a hot plate kept at 55ºC and electrodes were connected to a multimeter in order to monitor the resistance of the deposited film in real time. This helps in achieving a high reproducibility in the films deposited. The solutions were airbrushed onto the alumina substrates using N_2 as a carrier gas.

4.2.4. Material characterization techniques

The morphology of the materials was analyzed using Field Emission Scanning Electron Microscopy (Thermo Scientific Scios 2). High Resolution Transmission Electron Microscopy (HRTEM) was carried out at using a JEOL F200 TEM ColdFEG operated at 200 kV. Gatan OneView camera was used to acquire the TEM images which is a CMOS-based and optical fiber coupled detector of 4096 by 4096 pixels. X-ray diffraction (XRD) was used to analyze the crystal structure of the synthesized WS_2 and hybrid materials. A Bruker-AXS D8-Discover diffractometer was used for XRD measurements which was equipped with parallel incident beam (Göbel mirror), vertical θ-θ goniometer, XYZ motorized stage and with a GADDS (General Area Diffraction System). The X-ray diffractometer was operated at 40 kV and 40 mA to generate Cukα radiation. The GADDS detector was a VÅNTEC-500 (silicon strip technology) placed at 15 cm from the sample. Renishaw in Via laser 514 nm, ion argon – Novatech, 25 mW was used to acquire Raman spectra.

4.2.5. Gas sensing measurements

The gas sensing measurements were performed using a home-made gas detection system consisting of a Teflon chamber with a net volume of 35 mL. The chamber consists of an inlet and outlet accommodating four sensors simultaneously. The inlet and outlet of the chamber are connected to the gas delivery system and exhaust respectively. Fully automated gas flow measurement system comprising of mass flow controllers (MFCs, Bronkhorst High-Tech B.V.) was employed to supply precise amount of diluted gas mixtures. Calibrated gas cylinders balanced in dry synthetic air (Air Premier purity: 99.999%) were used for gas sensing measurements. The operating temperatures of the sensors were controlled by connecting the meander heaters of the sensors to external power supply (Agilent U8002A). Sensor responses were recorded using an Agilent-34972A data acquisition system by monitoring the sensing material resistances upon exposure to different concentrations of target gases such as NH_3,

NO_2, H_2, CO and benzene. The sensor responses were evaluated at three different temperatures: room temperature (RT), 100ºC, and 150ºC. To ensure the stable baseline, a continuous flow of 100 mL/min of dry air was maintained in the chamber for three hours prior to commencing the gas sensing experiments. The sensors were exposed to a specific gas species for ten minutes, followed by a baseline recovery cycle, which was adjusted based on the sensor operating temperature: 60 minutes for 100ºC and 150ºC, and 120 minutes for RT operation. The overall flow of the dry air remained constant at 100 mL/min throughout the gas sensing measurements. The humidity effect on the sensing performance was evaluated by humidifying (at room temperature) the gas stream through a controller evaporator mixer from Bronkhorst. For oxidizing species like NO_2, the sensor response was calculated using equation 1, while as for reducing species like NH_3, the sensor responses were calculated using equation 2.

$$R = \frac{R_{air} - R_{gas}}{R_{air}} * 100 \quad \text{Equation 1}$$

$$R = \frac{R_{gas} - R_{air}}{R_{air}} * 100 \quad \text{Equation 2}$$

R_{air} and R_{gas} are the real time resistances of sensors when exposed to air and to target gas respectively.

4.3. Results and discussion

4.3.1. Material Characterization

4.3.1.1. FESEM

Field Emission Electron Microscopy (FESEM) was conducted to study the structure and morphology of the materials. Bare graphene illustrated in the FESEM image in Figure 4.2 (a) reveals a highly porous structure which is desired for gas sensing applications as porous structures lead to enhanced sensing performance [35]. Figure 4.2 (b) demonstrates pristine WS_2 with a distinct triangular sheet-like morphology. This peculiar triangular shape of WS_2 has been reported earlier as well [36–39]. The triangular morphology of WS_2 can be attributed to the fact that the crystal growth predominantly relies on the growth rates of two specific types of crystal faces especially where the zigzag edge of tungsten or sulfur atoms terminate [40,41]. Upon in-depth analysis of the WS_2, it was found that the edge-to-edge width of the sheets is ~ 700 nm with the presence of some large sheets measuring around 1.5 µm with an average thickness of ~ 40 nm. Figure 4.2 (c) depicts the WS_2-graphene hybrid (Sensor A). As is evident from the figure, the mixture of the two individual materials is uniform and homogenous.

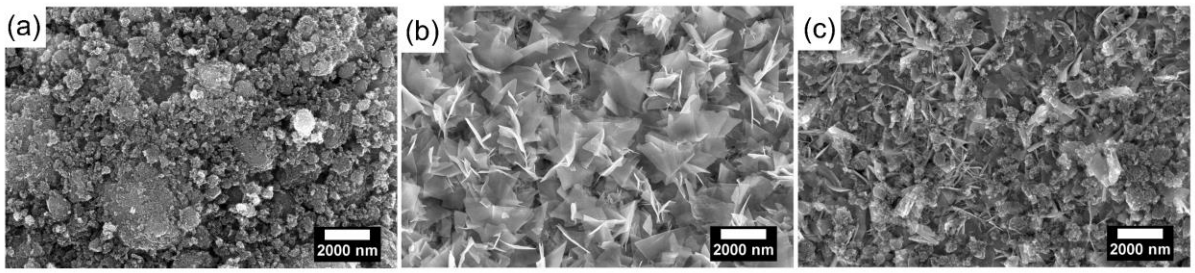

Figure 4.2 FESEM images of (a) graphene, (b) WS_2 and (c) WS_2-graphene hybrid, (Sensor A).

4.3.1.2. XRD

X-ray diffraction (XRD) analysis was carried out to study the crystal structure of graphene, WS_2 and WS_2-graphene hybrid. Figure 4.3 depicts the diffractogram of the materials. All the peaks match well with the standard rhombohedral phase of WS_2 (ICDD card number: 84-1399) with lattice constants a= 0.3158 nm and c= 1.849 nm belonging to R3m space group. The diffractogram reveals the presence of intense peaks at 14.35°, 28.95°, 33.08°, 44.04°, 58.39°, 60.47°, 68.78° and 75.94° corresponding to (003), (006), (101), (009), (110), (113), (021) and (119) crystal planes. As can be seen from the diffractogram, the intense peak at 26.61° can be attributed to (111) lattice phase of carbon corresponding to graphene (ICDD card number: 75-2078), Sensor A. Furthermore, minor peaks at 23.14°, 23.64°, and 24.36° corresponding to (002), (020) and (200) crystal planes of triclinic WO_3 traces (ICDD card number: 32-1395) were identified with lattice parameters a= 7.30 nm, b= 7.522 and c= 7.678 nm.

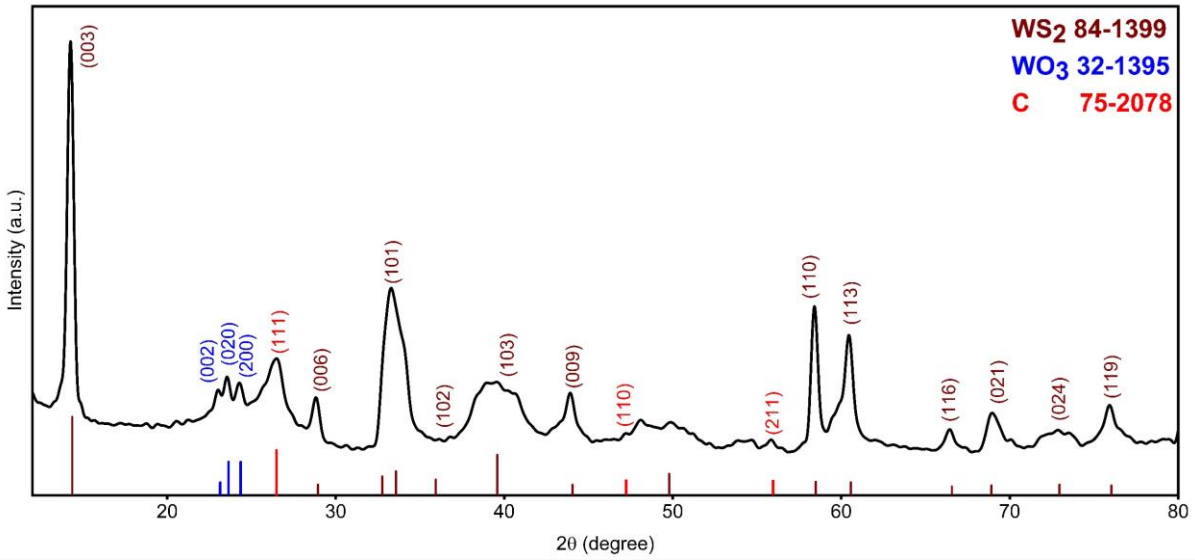

Figure 4.3 X-ray diffractogram of WS_2-graphene hybrid, (Sensor A).

4.3.1.3. HRTEM

Transmission electron microscopy (TEM) and high-resolution electron microscopy (HRTEM) was conducted to better understand the morphology and internal structure of the samples respectively. Figure 4.4 shows the high-resolution transmission electron microscopy images of WS_2-graphene hybrid (hybrid A). We can observe presence of large, thin, and transparent WS_2 sheets stacked on top of each other with presence of graphene as well. The insets in the figure show the interplanar distance of WS_2 and graphene. Upon further examination of the HRTEM images, the interplanar distances were determined to be 0.616 nm and 0.27 nm, corresponding to the (003) and (101) planes of WS_2 (ICDD card number: 84-1399). The inset, displaying the interplanar distance, d = 0.334 nm (111) plane is attributed to graphene (ICDD card number: 75-2078). These results confirm the formation of WS_2-graphene hybrid and are in agreement with the XRD results. In order to study the accurate distribution of elements of the WS_2-graphene hybrid, EDS elemental mapping was conducted as show in Figure 4.5. The analysis confirms the presence of C, W and S elements distributed uniformly over the WS_2 sheets. Also, Figure 4.5 (f) shows the EDX spectra of the hybrid material with respective elements confirming high purity of the material.

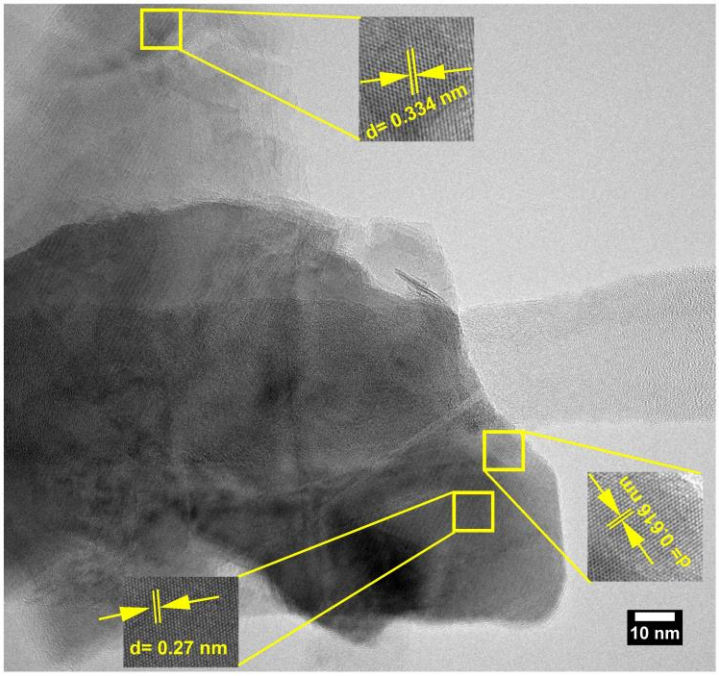

Figure 4.4 HRTEM image WS_2-graphene hybrid (Sensor A).

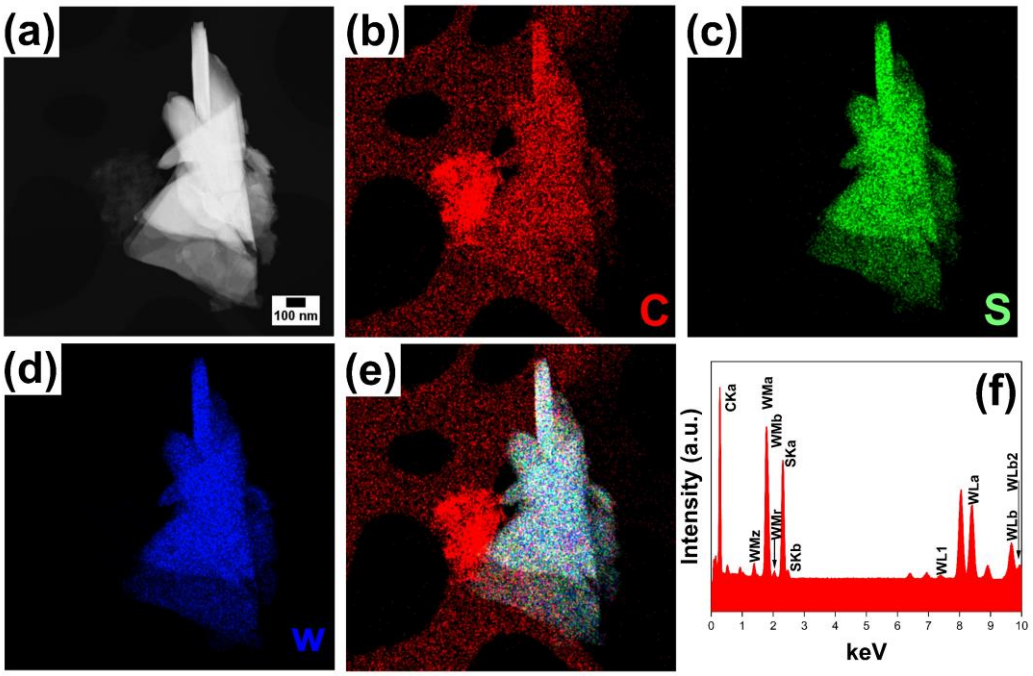

Figure 4.5 Color mapping and EDS of WS_2-graphene hybrid, (Sensor A).

4.3.1.4. Raman Spectroscopy

Raman spectroscopy was conducted to further study the structure of the samples. Raman spectra of Sensor A is shown in Figure 4.6. Intense and sharp peaks appear at 352.7 and 419.8 cm^{-1}, corresponding to E^1_{2g} and A_{1g} vibration modes of WS_2, which are the primary Raman peaks of WS_2. The A_{1g} peak denotes the out-of-plane vibrational mode of S atoms and E^1_{2g} peak indicates vibration modes of W and S atoms. This confirms the formation of 2 H phase-WS_2 [2]. Also, the wavenumber difference between the Raman modes depends on the WS_2 film thickness. The difference between Raman shift of $(A_{1g} - E^1_{2g})$ is 67.1 indicating multiple layered WS_2 film [42]. As can be observed from the spectrum, the characteristic D and G bands of carbon materials were found around 1350 and 1580 cm^{-1} respectively. The D band is referred to the disorder or defect band which originates from a hybridized vibrational mode related to the edges of graphene. While as, the G band is the result of first-order scattering of the E_{2g} mode of sp2 carbon domains. The graphene exhibited an I_D/I_G value of 0.85, indicating a higher number of defects that facilitate gas adsorption [43], which is desired for gas sensing applications.

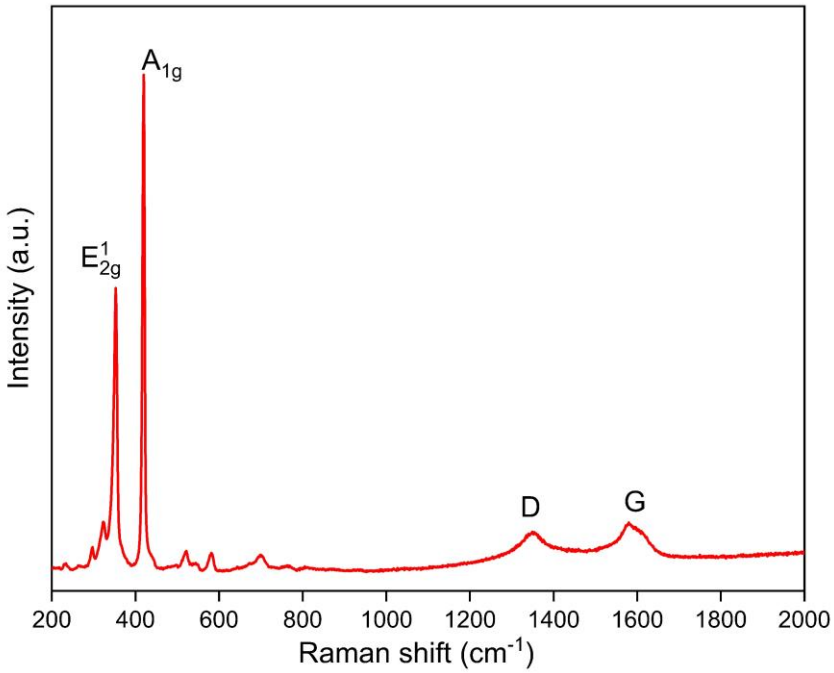

Figure 4.6 Raman spectra of WS_2-graphene hybrid (Sensor A).

4.3.2. Gas sensing results

The gas sensing properties of graphene, WS_2, and WS_2-graphene hybrid sensors were tested for NO_2 at different operating temperatures. To study the optimal working temperature, the sensors were studied towards 50 ppb of NO_2 at room temperature, 100ºC and 150ºC. The maximum tested temperature was 150ºC as the temperatures exceeding 150ºC could lead to evaporation of sulfur, consequently causing deterioration of the sensing layer by forming a WO_3/WS_2 complex [39]. The optimal working temperature is an important parameter to study the overall sensor performance. The sensor sensitivity, selectivity, response, and recovery speeds depend on the optimal working temperature. In this research, the introduction of graphene not only helped in decreasing the optimal working temperature but also enhanced sensitivity. This can be attributed to the enhanced electron mobility between WS_2-graphene and adsorbed analyte species at slightly lower operating temperature, resulting in an enhanced response [25]. Graphene being a promising 2D material has properties of high carrier mobility, large specific surface area and good chemical stability [25,44]. These properties offer the main advantages of fabricating WS_2-graphene hybrid-based sensors to not only increase the contact area for efficient charge transfer across the hybrid interfaces, but also shorten the charge transportation time because the sp^2 carbon orbits of the graphene allow quick and efficient charge transfer [45,46].

Figure 4.7 shows the sensor responses towards 50 ppb of NO_2 at different operating temperatures ranging from RT (25ºC) to 150ºC. As is evident from the figure, the response of the all the sensors increases from room temperature and is highest at 100ºC and then decreases with increase in the temperature to 150ºC. Thus, the operating temperature for all the subsequent studies was established to be at 100ºC. This working temperature is relatively low as compared to metal oxide-based gas sensors [6,47,48]. Figure 4.8 depicts the dynamic resistance changes of the sensors when exposed to 50 ppb of NO_2 while being operated at 100ºC. Upon being exposed to NO_2, an oxidizing gas species, the sensors respond as p-type semiconductor showing a decrease in the resistance. This is in accordance with earlier research [3,39]. The decrease in resistance upon NO_2 exposure can be attributed to the spontaneous adsorption of NO_2 gas molecules on the sensing material surface. In this process, electrons are withdrawn via the valence band, leading to an increase in hole concentration and resulting in an overall decrease in the electrical resistance of the sensing film [39,49,50]. The pure WS_2 sensor and Sensor C demonstrated no or negligible responses and are therefore not discussed. In contrast, pure graphene exhibited a response of 1.28 ± 0.01%, Sensor A displayed highest response of 14.32 ± 0.04%, and Sensor B showed a 2.25 ± 0.02% response. Moreover, pristine WS_2 sensors exhibit no response to NO_2 concentrations below 100 ppb; hence, the corresponding results are not shown. Nevertheless, as the NO_2 concentration rises from 100 ppb and beyond, pristine WS_2 sensors demonstrate a heightened response, surpassing that of all other sensors. The results are summarized in Figure S1. The inset in the figure shows the sensor responses from 10 ppb NO_2 to 100 ppb NO_2. Only the pure graphene sensor displayed a slight drift in the baseline resistance, suggesting the synergistic effect of WS_2 and graphene on the gas sensing properties and stability towards NO_2. Moreover, when the target gas is removed during the recovery cycle, the sensors return completely to the original baseline resistance in a dry air environment. [47,51].

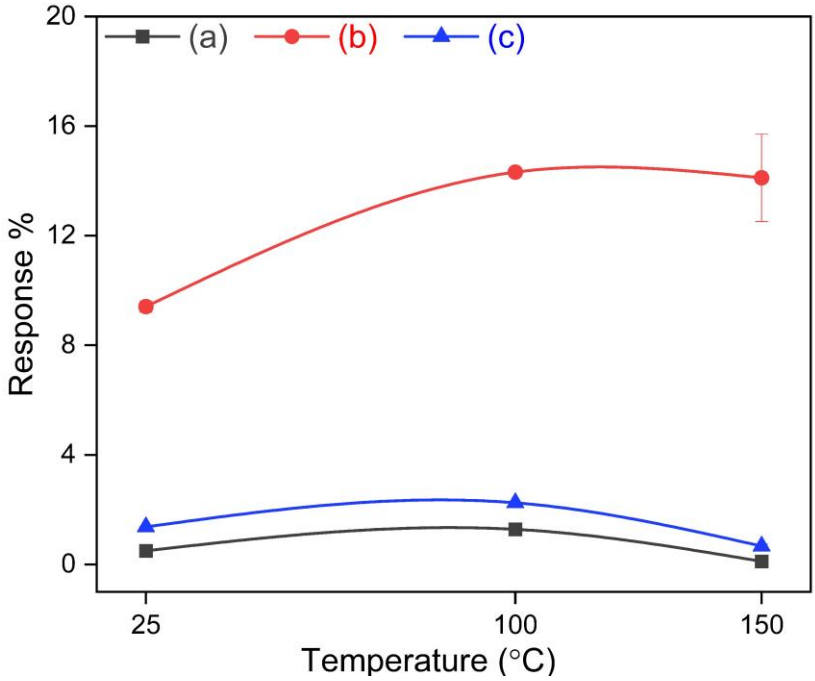

Figure 4.7 Sensor responses as a function of temperature towards 50 ppb of NO_2, (a) graphene, (b) sensor A and (c) sensor B.

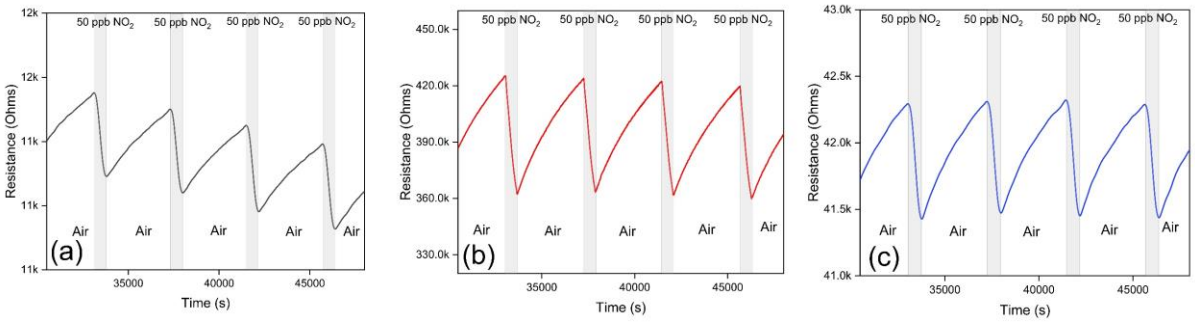

Figure 4.8 Dynamic resistance changes of (a) graphene, (b) Sensor A and (c) Sensor B towards 50 ppb of NO_2 at 100°C.

Moreover, the sensors were tested towards a wide range of NO_2 gas concentrations ranging from 10, 20, 30, 40 and 50 ppb at the optimal working temperature. The calculated responses are demonstrated in Figure 4.9. As is evident from the figure, there is a linear increase in the response with the increase in the NO_2 concentration. This indicates that the sensors do not saturate by exposure towards NO_2 concentrations below 50 ppb. As expected, the resistance changes recorded increase when the NO_2 concentration is also increased. The dynamics of the gas sensor film changes towards different NO_2 concentrations are presented in Figure 4.10. As shown in the figure, Sensor A can efficiently detect as low as 10 ppb of NO_2. These detected concentrations are much lower than the permissible NO_2 concentrations [52]. Moreover, it can be seen from the Figure 4.10 (a) and (c) that there is no response towards 10 ppb of NO_2. The

American Conference of Governmental Industrial Hygienists (ACGIH) has established occupational guidelines for NO_2, suggesting a time-weighted average (TWA) of 3 ppm and short-term exposure limits (STEL) of 5 ppm. Meanwhile, the National Institute for Occupational Safety and Health (NIOSH) recommends a short-term exposure limit of 1 ppm over a 15-minute period [52,53]. Notably, exposure to elevated concentrations of NO_2 gas (> 1 ppm) during both postnatal and prenatal stages may pose significant health risks, including headaches, pneumonia, inflammation, and asthma [54]. Continuous exposure to NO_2 gas levels exceeding 53 ppb could contribute to conditions such as eczema, chronic bronchitis, and acute respiratory illnesses in children [54–57].

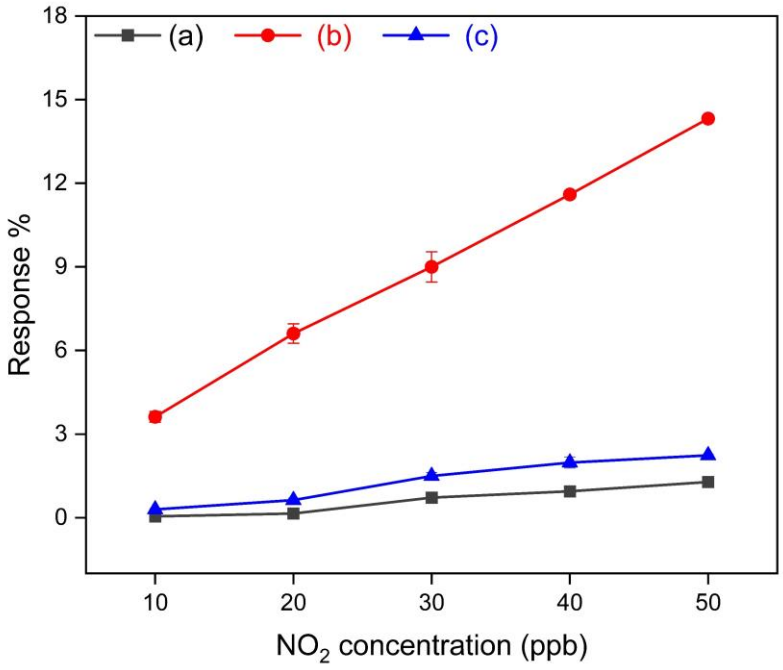

Figure 4.9 Sensor responses as a function of NO_2 concentration at 100°C, (a) graphene, (b) Sensor A and (c) Sensor B.

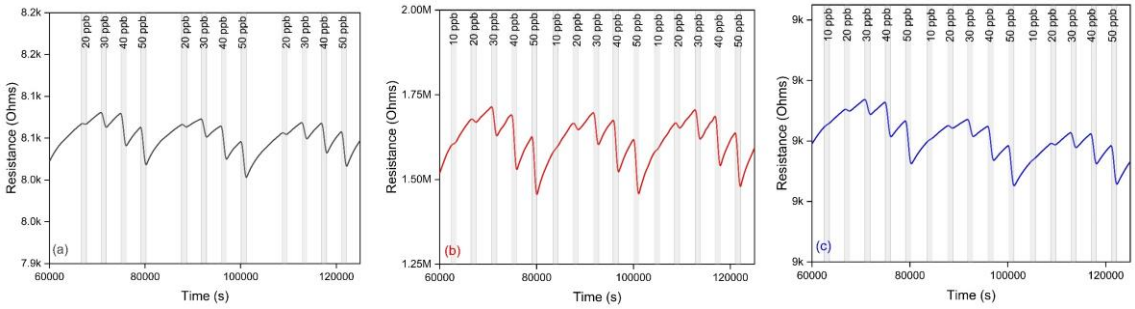

Figure 4.10 Gas sensing film resistance changes as a function of time towards different NO_2 concentrations, (a) graphene, (b) Sensor A and (c) Sensor B.

4.3.3. Selectivity tests

Selectivity is one of the important criteria to determine sensor performance. The selectivity of the sensors was evaluated towards fixed concentrations of various interfering species viz. carbon monoxide (CO), benzene (C_6H_6), ammonia (NH_3), and hydrogen (H_2) at the optimum working temperature of 100ºC. The fixed concentrations of the different gases were selected keeping in view the permissible exposure limits of the respective analytes. Determining the selectivity towards these analyte gases is particularly important owing to their potential health and environment risks. For example, benzene is designated as group 1 carcinogen by the International Agency for Research on Cancer [58]. Exposure to low levels of ammonia in the workplace can result in the development of disorders affecting the breath, skin, blood, and kidneys [59]. Similarly, CO is highly toxic to the human body and seriously endangers the brain, heart, liver, kidney, lung and other tissues [60] and hydrogen leakage detection is of prime importance owing to its highly flammable properties [16]. Figure 4.11 shows the responses of the sensors towards the tested gases at 100ºC. The results show that among all the sensors, Sensor A responds to an extremely low concentration of NO_2 (50 ppb) with highest response of approximately 14%. The results suggest a high selectivity of the Sensor A towards a meagre NO_2 concentration of 50 ppb. All the gas concentrations tested are way below the permissible limits [53]. Notably, there is an exponential decrease in sensitivity from Sensor A to Sensor C. The combination of porous graphene and edge-enriched WS_2 particularly enhances sensitivity towards NO_2 [4].

The gas sensing properties of WS_2-graphene are significantly enhanced by the presence of defects in graphene. The defects in graphene are well demonstrated in Raman spectra (Figure 4.6).The graphene layer plays a crucial role in improving charge transfer between WS_2 and the target gas [30]. Furthermore, the presence of graphene (a layer in which charge carriers can move efficiently) enhances the collection of the generated charge carriers by the sensor device electrodes. Specifically, in the case of NO_2, the oxygen functional groups on WS_2 facilitate the adsorption of nitrogen dioxide molecules [22], leading to the creation of more holes in the material and a subsequent decrease in sensor resistance. Pristine monolayer graphene, characterized by high electron mobility (2×10^5 cm^2 V^{-1} s^{-1}) and a large specific surface area (2630 m^2 g^{-1}) [61,62] exhibits distinct gas sensing properties..

The sensing properties of pristine WS_2 can be interpreted by the statement that WS_2 sensors exhibit a high response when exposed to 5 ppm of NH_3 at the temperature of 100ºC. The results

are demonstrated in Figure S2. Interestingly, even though the concentration of ammonia is 100 times higher than that of NO_2, the WS_2 sensors are particularly effective in detecting NO_2. This suggests that WS_2 sensors display a greater sensitivity and specificity toward NO_2, even when exposed to a much lower concentration of NO_2 compared to ammonia. Consequently, the superior responsiveness of WS_2 to NO_2 at lower concentrations makes it an ideal material for the detection of nitrogen dioxide, highlighting its potential as a robust and selective sensor for NO_2 in various applications. Combining WS_2 with graphene further enhances sensitivity towards various volatile organic compound (VOC) vapors and NO_2 gas, with the degree of enhancement tunable by varying the WS_2-graphene ratios.

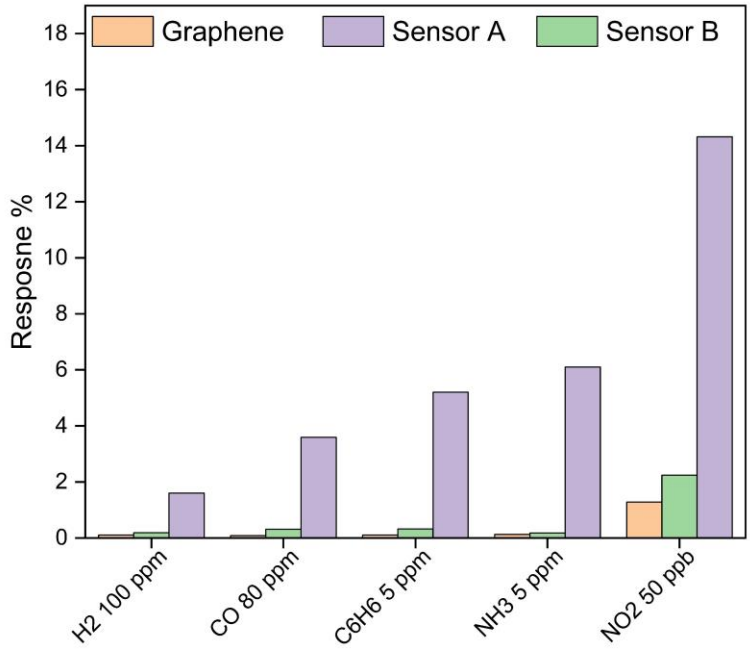

Figure 4.11 Selectivity studies of sensors towards different interfering gas species.

4.3.4. Sensing mechanism

As mentioned in section 1 (introduction), semiconductor hybrids or heterojunction based semiconducting materials are one of the strategies to boost performance in chemoresistive gas sensors. The basic principle of chemoresistive gas sensors is the change in the sensing film resistance while interacting with gas molecules [63]. Depending on the nature of the gas molecules, oxidizing, or reducing, these gas molecules can have donor−acceptor properties. The sensor films react in accordance with their semiconductor characteristics, whether they are of n-type or p-type towards the respective gases. Majority of the charge carriers in case of n-type semiconductors are electrons and holes in p-type semiconductors strongly driving the electrical properties of the respective semiconductors.

In this research work, we aim to use WS_2 as host and first understand the sensing characteristics of the host material. Subsequently, we aim to study the enhancement in the NO_2 gas sensing performance of the hybrid. The sensing mechanism of graphene, WS_2, and WS_2-graphene relies on a charge transfer between the sensing materials and the target gases [64,65]. As an oxidizing gas, NO_2 acts as an electron acceptor. Upon exposure to NO_2, NO_2 molecules get adsorbed on the surface of graphene and attract electrons from it. Consequently, the number of holes increases in p-type graphene, and its resistance decreases. In the case of pure WS_2, the tightly aggregated multilayer structure exposes only a minimal number of active sites to the surroundings. Consequently, gas adsorption can only occur on partially exposed surfaces, resulting in a low response.

In contrast, WS_2-graphene exhibits enhanced gas sensing properties attributed to its increased specific surface area. This hierarchical structure improves the adsorption and diffusion of NO_2 within the space between WS_2 nanosheets. Thus, the abundant WS_2 edges promote the adsorption of NO_2 as well as the reaction kinetics [66]. Additionally, the porous structure of WS_2-graphene significantly increases reaction sites on graphene for NO_2 molecules. Furthermore, electron deficiency in WS_2 can be compensated by electrons donated from graphene, resulting in additional changes in resistance in WS_2-graphene through electron transfer between WS_2 and graphene, leading to excellent sensing properties compared to pure graphene and WS_2 alone. The work function of pristine graphene is 4.2 eV [67,68], and that of WS_2 is 4.5 eV [69]. Due to the difference in work function between graphene and WS_2, electrons in graphene are preferentially transferred to the WS_2 nanosheets, leaving holes in graphene. The obtained gas sensing characteristic curves in Figure 4.8 indicate that both graphene and WS_2-graphene possess a p-type sensing property, with a decrease in resistance towards NO_2, an oxidizing gas. When the sensor is exposed to NO_2, electrons are further transferred to NO_2. Upon exposure to air again, NO_2 desorbs from the surface of the sensing materials and returns electrons to the system. The resistance of the sensing material increases to the baseline values. Furthermore, the remarkable sensitivity demonstrated, and the exceptionally low limit of detection achieved are credited to the porous surface and the increased number of sulfur edges in WS_2 arising from the random three-dimensional assembly of WS_2 nanosheets [70]. Density Functional Theory (DFT) calculations demonstrate that edges on WS_2 enhance gas sensing performance. Additionally, DFT calculations show that adsorption is weakest at the basal planes of WS_2 and highest at the edges. This strong adsorption can

induce a large charge transfer compared to adsorption on the basal planes, thereby leading to remarkable sensitivity of WS_2-graphene.

The capability of the WS_2-graphene hybrid material to detect ultra-low concentrations of NO_2 can thus be maily owed to the following three factors. (i) both the materials used in the hybrid are of high specific surface area and ultimately leading to an increase in the average specific surface area. This in turn leads to an exponential increase in the adsorption sites, which increases the adsorption rate and hence gas response [71]. (ii) the hybrid formed consists of two materials with different Fermi levels. The formation of p-p heterojunction leads to an increase in the charge carrier mobility. (iii) presence of defects especially S vacancies in WS_2 leads to enhanced response towards NO_2 [3]. These factors also help the sensing material to sense the ultra-low concentrations of NO_2 in humid conditions.

4.3.5. Humidity studies

To verify the practicability of the sensors, the impact of relative humidity on the sensor responses towards NO_2 was investigated. The results are summarized in Figure 4.12. The sensors were tested towards 50 ppb of NO_2 at 100ºC in a 50% humidified air background. Figure 4.13 shows the dynamic resistance change in humid and dry environment. We noticed a twofold increase in the sensing responses in humid conditions. in case of Sensor A. It is observed that the sensor baselines increased under humid environment. These results are in agreement with previously published results [72,73]. The increase in the baseline resistance under humid environment could be explained based on electrons mechanism. The adsorbed water molecules are known to behave like electron donors [74,75]. WS_2-graphene material behaves as p-type semiconducting material, the increase in the humidity results in the reduction of holes density, leading to an increase in the baseline resistance. In general, when testing sensors in a humid environment, there is a competition between the target gas molecules and water vapor (hydroxyl group) at the active sites. If the relative surface distribution of the hydroxyl group surpasses that of oxygen species, the sensor's performance declines, and the impact of humidity becomes more pronounced. Conversely, a sensor with strong resistance to moisture shows consistent performance, as the majority of active sites are occupied by absorbed oxygen species. This confirms that the WS_2-graphene sensors are excellent candidates for real life applications.

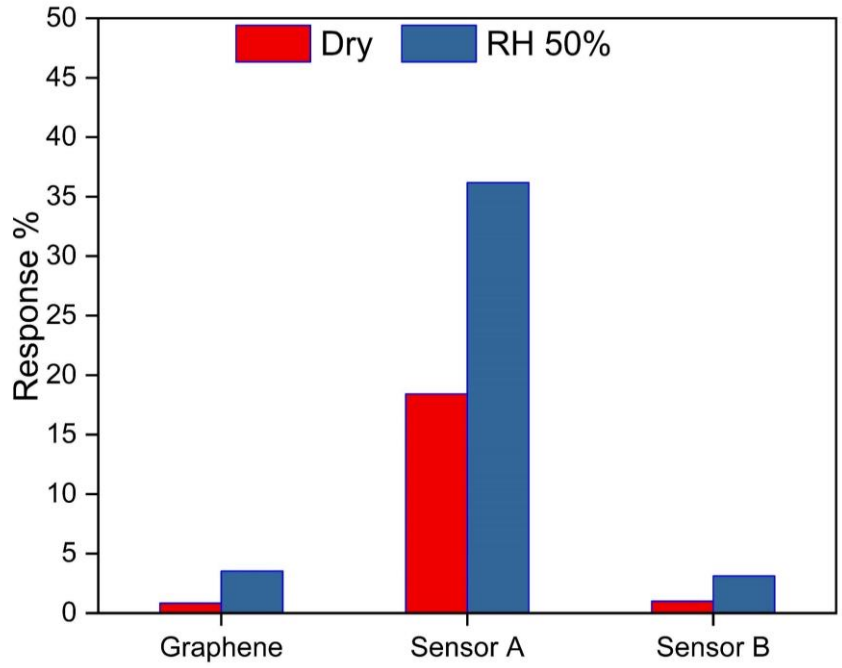

Figure 4.12 Dry and relative humidity cross-sensitivity to 50 ppb NO_2 at 100°C.

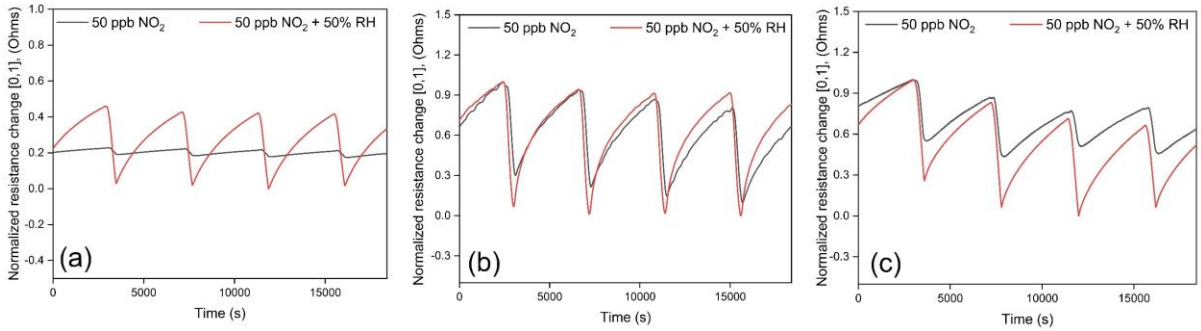

Figure 4.13 Dry and relative humidity cross-sensitivity towards 50 ppb NO_2 at 100°C. The sensor resistance changes are normalized to [0,1], (a) graphene, (b) Sensor A, and (c) Sensor B.

4.4. Conclusion

This research underscores the promising potential of two-dimensional (2D) transition metal dichalcogenides (TMDs) for low-temperature NO_2 sensing. APCVD was used as a high yield synthesis method to synthesize edge enriched WS_2. As synthesized WS_2 was mixed with graphene to form a WS_2-graphene hybrid to be used as a gas sensing material. A facile airbrushing technique with N_2 as the carrier gas was used to fabricate the sensors. The sensors demonstrate exceptional sensitivity to ultra-low concentrations of NO_2 (10 ppb) at a notably low operating temperature of 100°C, surpassing the overall sensor responses of individual graphene and WS_2 sensors. Moreover, the cross-sensitivity tests revealed CO, H_2, C_6H_6, and NH_3 have negligible effect on NO_2 gas detection at the optimum working temperature of 100ºC. Importantly, the sensor responses nearly double in humid environments (50% RH at 25°C),

indicating practical applications for selective NO_2 detection even under varying environmental conditions. This comprehensive approach lays the foundation for the development of highly efficient and selective gas sensors for real-world applications.

4.5. Acknowledgements

S. B. M is supported by Martí-Franquès Research grants Programme, Doctoral grants – 2019, (2019PMF-PIPF-14). F. E. A. is a RYC2022-038111-I post-doctoral fellow from the Ramon y Cajal programme. E. L. is supported by the Catalan Institution for Research and Advanced Studies via the 2018 Edition of the ICREA Academia Award. This work is supported by the Agencia Estatal de Investigación (AEI) under grant no. PDC2022-133967-100 and by AGAUR under grant no. 2021 SGR 00147. The HRTEM was partially funded by the operative program FEDER Catalunya 2014-2020 (IU16-015844).

4.6. References

[1] T.H.P. Doan, Q.T.H. Ta, A. Sreedhar, N.T. Hang, W. Yang, J.-S. Noh, Highly Deformable Fabric Gas Sensors Integrating Multidimensional Functional Nanostructures, ACS Sensors. 5 (2020) 2255–2262. https://doi.org/10.1021/acssensors.0c01083.

[2] S. Sardana, A.K. Debnath, D.K. Aswal, A. Mahajan, WS2 nanosheets decorated multi-layered MXene based chemiresistive sensor for efficient detection and discrimination of NH3 and NO2, Sensors Actuators B Chem. 394 (2023). https://doi.org/10.1016/j.snb.2023.134352.

[3] A. Alagh, F.E. Annanouch, K. Al Youssef, C. Bittencourt, F. Güell, P.R. Martínez-Alanis, M. Reguant, E. Llobet, PdO and PtO loaded WS2 boosts NO2 gas sensing characteristics at room temperature, Sensors Actuators B Chem. 364 (2022). https://doi.org/10.1016/j.snb.2022.131905.

[4] A. Alagh, F.E. Annanouch, A. Sierra-Castillo, E. Haye, J.F. Colomer, E. Llobet, Three-Dimensional Assemblies of Edge-Enriched WSe2Nanoflowers for Selectively Detecting Ammonia or Nitrogen Dioxide, ACS Appl. Mater. Interfaces. 14 (2022) 54946–54960. https://doi.org/10.1021/acsami.2c16299.

[5] B. Izelaar, D. Ripepi, D.D. van Noordenne, P. Jungbacker, R. Kortlever, F.M. Mulder, Identification, Quantification, and Elimination of NO x and NH 3 Impurities for

Aqueous and Li-Mediated Nitrogen Reduction Experiments, ACS Energy Lett. 8 (2023) 3614–3620. https://doi.org/10.1021/acsenergylett.3c01130.

[6] S.B. Malik, K. V. Mejia-Centeno, P.R. Martínez-Alanis, A. Cabot, F. Güell, F.E. Annanouch, E. Llobet, Synergistic effect of CeO2 nanoparticles and WO3 nanowires in gas sensing applications, Sensors Actuators B Chem. 400 (2024). https://doi.org/10.1016/j.snb.2023.134879.

[7] S. Behi, J. Casanova-Chafer, E. González, N. Bohli, E. Llobet, A. Abdelghani, Metal loaded nano-carbon gas sensor array for pollutant detection *, Nanotechnology. 33 (2022) 195501. https://doi.org/10.1088/1361-6528/ac4e43.

[8] L. Cai, X. Zhang, Sodium titanate: A proton conduction material for ppb-level NO2 detection with near-zero power consumption, J. Hazard. Mater. 462 (2024) 1–10. https://doi.org/10.1016/j.jhazmat.2023.132781.

[9] K. Jayaramulu, B. Devi, Hybrid Two-Dimensional Porous Materials, Chem. Mater. 35 (2023) 9473–9492. https://doi.org/10.1021/acs.chemmater.3c00829.

[10] P. Recum, T. Hirsch, Graphene-based chemiresistive gas sensors, Nanoscale Adv. 6 (2024) 11–31. https://doi.org/10.1039/D3NA00423F.

[11] X. Huang, C. Zhi, Y. Lin, H. Bao, G. Wu, P. Jiang, Y.-W. Mai, Thermal conductivity of graphene-based polymer nanocomposites, Mater. Sci. Eng. R Reports. 142 (2020) 100577. https://doi.org/10.1016/j.mser.2020.100577.

[12] K. Thodkar, F. Gramm, Enhanced Mobility in Suspended Chemical Vapor-Deposited Graphene Field-Effect Devices in Ambient Conditions, ACS Appl. Mater. Interfaces. 15 (2023) 37756–37763. https://doi.org/10.1021/acsami.3c04012.

[13] M. Pandey, K. Deshmukh, A. Raman, A. Asok, S. Appukuttan, G.R. Suman, Prospects of MXene and graphene for energy storage and conversion, Renew. Sustain. Energy Rev. 189 (2024) 114030. https://doi.org/10.1016/j.rser.2023.114030.

[14] S. Jin, B. Chung, H.J. Park, B. V. Cunning, J. Lee, A. Yoon, M. Huang, H. Seo, D. Lee, Z. Lee, R.S. Ruoff, S. Ryu, Ultrahigh Strength and Modulus Graphene-Based Hybrid Carbons with AB-Stacked and Turbostratic Structures, Adv. Funct. Mater. 30 (2020) 1–11. https://doi.org/10.1002/adfm.202005381.

[15] H. Chen, F. Zhuo, J. Zhou, Y. Liu, J. Zhang, S. Dong, X. Liu, A. Elmarakbi, H. Duan,

Y. Fu, Advances in graphene-based flexible and wearable strain sensors, Chem. Eng. J. 464 (2023) 142576. https://doi.org/10.1016/j.cej.2023.142576.

[16] S.B. Malik, F.E. Annanouch, E. Llobet, Pd-Nanoparticle-Decorated Multilayered MoS2 Sheets for Highly Sensitive Hydrogen Sensing, Chemosensors. 11 (2023) 550. https://doi.org/10.3390/chemosensors11110550.

[17] R. Kumar, N. Goel, M. Hojamberdiev, M. Kumar, Transition metal dichalcogenides-based flexible gas sensors, Sensors Actuators A Phys. 303 (2020) 111875. https://doi.org/10.1016/j.sna.2020.111875.

[18] S. Manzoor, M. Talib, S.M. Novikov, A. V. Arsenin, V.S. Volkov, P. Mishra, Physisorption-Mediated Charge Transfer in TiS2 Nanodiscs: A Room Temperature Sensor for Highly Sensitive and Reversible Carbon Dioxide Detection, ACS Sensors. 8 (2023) 3435–3447. https://doi.org/10.1021/acssensors.3c00931.

[19] A. Kushwaha, R. Kumar, N. Goel, Chemiresistive gas sensors beyond metal oxides: Using ultrathin two-dimensional nanomaterials, FlatChem. 43 (2023) 100584. https://doi.org/10.1016/j.flatc.2023.100584.

[20] D. Shin, I. Sohn, J. Kim, T. Nakazawa, S. Lee, H. Yoon, J. Yoo, J. Park, S. Chung, H. Kim, Defect-Selective Functionalization of 2D-WS 2 Nanofilms with Pt Nanoparticles for Enhanced Room-Temperature NO 2 Gas Sensing, ACS Appl. Nano Mater. 6 (2023) 19327–19337. https://doi.org/10.1021/acsanm.3c03566.

[21] S.B. Kang, A. Sanger, M.H. Jeong, J.M. Baik, K.J. Choi, Heterogeneous stacking of reduced graphene oxide on ZnO nanowires for NO2 gas sensors with dramatically improved response and high sensitivity, Sensors Actuators B Chem. 379 (2023) 133196. https://doi.org/10.1016/j.snb.2022.133196.

[22] A. Moumen, R. Konar, D. Zappa, E. Teblum, G.D. Nessim, E. Comini, Room-Temperature NO 2 Sensing of CVD-Modified WS 2 –WSe 2 Heterojunctions, ACS Appl. Nano Mater. 6 (2023) 7323–7329. https://doi.org/10.1021/acsanm.3c00435.

[23] I. Sohn, S. Wi, Y. Kim, D. Shin, M. Kim, S. Lee, H. Yoon, J. Yoo, S. Chung, H. Kim, Selective passivation of 2D TMD surface defects by atomic layer deposited Al2O3 to enhance recovery properties of gas sensor, Appl. Surf. Sci. 646 (2024) 158906. https://doi.org/10.1016/j.apsusc.2023.158906.

[24] Y. Kim, I. Sohn, D. Shin, J. Yoo, S. Lee, H. Yoon, J. Park, S. Chung, H. Kim, Recent Advances in Functionalization and Hybridization of Two-Dimensional Transition Metal Dichalcogenide for Gas Sensor, Adv. Eng. Mater. (2023). https://doi.org/10.1002/adem.202301063.

[25] X. Hou, Z. Wang, G. Fan, H. Ji, S. Yi, T. Li, Y. Wang, Z. Zhang, L. Yuan, R. Zhang, J. Sun, D. Chen, Hierarchical three-dimensional MoS2/GO hybrid nanostructures for triethylamine-sensing applications with high sensitivity and selectivity, Sensors Actuators B Chem. 317 (2020) 128236. https://doi.org/10.1016/j.snb.2020.128236.

[26] E. Ghaleghafi, M.B. Rahmani, Characterization and room temperature ammonia sensing application of hydrothermally synthesized MoS2/RGO nanocomposites, Diam. Relat. Mater. 137 (2023) 110174. https://doi.org/10.1016/j.diamond.2023.110174.

[27] H. Yu, M. Dai, J. Zhang, W. Chen, Q. Jin, S. Wang, Z. He, Interface Engineering in 2D/2D Heterogeneous Photocatalysts, Small. 19 (2023) 1–30. https://doi.org/10.1002/smll.202205767.

[28] F. Schedin, A.K. Geim, S. V Morozov, E.W. Hill, P. Blake, M.I. Katsnelson, K.S. Novoselov, Detection of individual gas molecules adsorbed on graphene, Nat. Mater. 6 (2007) 652–655. https://doi.org/10.1038/nmat1967.

[29] N. Tammanoon, A. Wisitsoraat, C. Sriprachuabwong, D. Phokharatkul, A. Tuantranont, S. Phanichphant, C. Liewhiran, Ultrasensitive NO2 Sensor Based on Ohmic Metal-Semiconductor Interfaces of Electrolytically Exfoliated Graphene/Flame-Spray-Made SnO2 Nanoparticles Composite Operating at Low Temperatures, ACS Appl. Mater. Interfaces. 7 (2015) 24338–24352. https://doi.org/10.1021/acsami.5b09067.

[30] Y. Niu, R. Wang, W. Jiao, G. Ding, L. Hao, F. Yang, X. He, MoS2 graphene fiber based gas sensing devices, Carbon N. Y. 95 (2015) 34–41. https://doi.org/10.1016/j.carbon.2015.08.002.

[31] J. Choi, T. Kim, H. Li, H.T. Jung, D. Zhao, Gas Sensors with Two-Dimensional rGO@COF Composite Materials for Fast NO2 Detection under Room Temperature, ACS Appl. Mater. Interfaces. 15 (2023) 44119–44126. https://doi.org/10.1021/acsami.3c10304.

[32] X. Ma, X. Cai, M. Yuan, Y. Qu, Y. Tan, F. Chen, Self-powered and flexible gas sensor

using defect-engineered WS2/G heterostructure, Sensors Actuators B Chem. 371 (2022). https://doi.org/10.1016/j.snb.2022.132523.

[33] S.K. Tiwari, S. Sahoo, N. Wang, A. Huczko, Graphene research and their outputs: Status and prospect, J. Sci. Adv. Mater. Devices. 5 (2020) 10–29. https://doi.org/10.1016/j.jsamd.2020.01.006.

[34] J. Phiri, L.-S. Johansson, P. Gane, T. Maloney, A comparative study of mechanical, thermal and electrical properties of graphene-, graphene oxide- and reduced graphene oxide-doped microfibrillated cellulose nanocomposites, Compos. Part B Eng. 147 (2018) 104–113. https://doi.org/10.1016/j.compositesb.2018.04.018.

[35] J. Casanova-Chafer, P. Umek, S. Acosta, C. Bittencourt, E. Llobet, Graphene Loading with Polypyrrole Nanoparticles for Trace-Level Detection of Ammonia at Room Temperature, ACS Appl. Mater. Interfaces. 13 (2021) 40909–40921. https://doi.org/10.1021/acsami.1c10559.

[36] H.R. Gutiérrez, N. Perea-López, A.L. Elías, A. Berkdemir, B. Wang, R. Lv, F. López-Urías, V.H. Crespi, H. Terrones, M. Terrones, Extraordinary room-temperature photoluminescence in triangular WS 2 monolayers, Nano Lett. 13 (2013) 3447–3454. https://doi.org/10.1021/nl3026357.

[37] Y. Yue, J.C. Chen, Y. Zhang, S.S. Ding, F. Zhao, Y. Wang, D. Zhang, R.J. Li, H. Dong, W. Hu, Y. Feng, W. Feng, Two-Dimensional High-Quality Monolayered Triangular WS2 Flakes for Field-Effect Transistors, ACS Appl. Mater. Interfaces. 10 (2018) 22435–22444. https://doi.org/10.1021/acsami.8b05885.

[38] J. Jelken, M.O. Avilés, F. Lagugné-Labarthet, The Hidden Flower in WS2Flakes: A Combined Nanomechanical and Tip-Enhanced Raman Exploration, ACS Nano. 16 (2022) 12352–12363. https://doi.org/10.1021/acsnano.2c03441.

[39] A. Alagh, F.E. Annanouch, P. Umek, C. Bittencourt, A. Sierra-Castillo, E. Haye, J.F. Colomer, E. Llobet, CVD growth of self-assembled 2D and 1D WS2 nanomaterials for the ultrasensitive detection of NO2, Sensors Actuators, B Chem. 326 (2021). https://doi.org/10.1016/j.snb.2020.128813.

[40] J. Cheng, T. Jiang, Q. Ji, Y. Zhang, Z. Li, Y. Shan, Y. Zhang, X. Gong, W. Liu, S. Wu, Kinetic Nature of Grain Boundary Formation in As-Grown MoS2 Monolayers, Adv.

Mater. 27 (2015) 4069–4074. https://doi.org/10.1002/adma.201501354.

[41] J. Yan, S. Lian, Z. Cao, Y. Du, P. Wu, H. Sun, Y. An, CVD controlled preparation and growth mechanism of 2H-WS2 nanosheets, Vacuum. 207 (2023) 111564. https://doi.org/10.1016/j.vacuum.2022.111564.

[42] M.W. Iqbal, M.Z. Iqbal, M.F. Khan, M.A. Shehzad, Y. Seo, J. Eom, Deep-ultraviolet-light-driven reversible doping of WS2 field-effect transistors, Nanoscale. 7 (2015) 747–757. https://doi.org/10.1039/c4nr05129g.

[43] G. Wang, J. Fan, Y. Xie, M. Yu, K. Li, X. Guo, J. Wu, K. Shi, K. Pan, Monodisperse Y-type CoO hierarchical nanostructure/reduced graphene oxide for improved NO2 detection at room temperature with enhanced moisture resistance, Sensors Actuators B Chem. 394 (2023) 134391. https://doi.org/10.1016/j.snb.2023.134391.

[44] M.S. Choi, A. Nipane, B.S.Y. Kim, M.E. Ziffer, I. Datta, A. Borah, Y. Jung, B. Kim, D. Rhodes, A. Jindal, Z.A. Lamport, M. Lee, A. Zangiabadi, M.N. Nair, T. Taniguchi, K. Watanabe, I. Kymissis, A.N. Pasupathy, M. Lipson, X. Zhu, W.J. Yoo, J. Hone, J.T. Teherani, High carrier mobility in graphene doped using a monolayer of tungsten oxyselenide, Nat. Electron. 4 (2021) 731–739. https://doi.org/10.1038/s41928-021-00657-y.

[45] L. Yuan, T.F. Chung, A. Kuc, Y. Wan, Y. Xu, Y.P. Chen, T. Heine, L. Huang, Photocarrier generation from interlayer charge-transfer transitions in WS2-graphene heterostructures, Sci. Adv. 4 (2018) 1–10. https://doi.org/10.1126/sciadv.1700324.

[46] J. Bradford, M. Shafiei, J. MacLeod, N. Motta, Synthesis and characterization of WS2/graphene/SiC van der Waals heterostructures via WO3−x thin film sulfurization, Sci. Rep. 10 (2020) 1–10. https://doi.org/10.1038/s41598-020-74024-w.

[47] Q. Li, W. Zeng, Y. Li, Metal oxide gas sensors for detecting NO2 in industrial exhaust gas: Recent developments, Sensors Actuators B Chem. 359 (2022) 131579. https://doi.org/10.1016/j.snb.2022.131579.

[48] L.-Y. Zhu, L.-X. Ou, L.-W. Mao, X.-Y. Wu, Y.-P. Liu, H.-L. Lu, Advances in Noble Metal-Decorated Metal Oxide Nanomaterials for Chemiresistive Gas Sensors: Overview, Nano-Micro Lett. 15 (2023) 89. https://doi.org/10.1007/s40820-023-01047-z.

[49] G. Jiménez-Cadena, J. Riu, F.X. Rius, Gas sensors based on nanostructured materials, Analyst. 132 (2007) 1083. https://doi.org/10.1039/b704562j.

[50] H. Fei, G. Wu, W.Y. Cheng, W. Yan, H. Xu, D. Zhang, Y. Zhao, Y. Lv, Y. Chen, L. Zhang, C. Ó Coileáin, C. Heng, C.R. Chang, H.C. Wu, Enhanced NO 2 Sensing at Room Temperature with Graphene via Monodisperse Polystyrene Bead Decoration, ACS Omega. 4 (2019) 3812–3819. https://doi.org/10.1021/acsomega.8b03540.

[51] L.-Y. Zhu, L.-X. Ou, L.-W. Mao, X.-Y. Wu, Y.-P. Liu, H.-L. Lu, Advances in Noble Metal-Decorated Metal Oxide Nanomaterials for Chemiresistive Gas Sensors: Overview, Nano-Micro Lett. 15 (2023) 89. https://doi.org/10.1007/s40820-023-01047-z.

[52] S. Kailasa Ganapathi, M. Kaur, M. Shaheera, A. Pathak, S.C. Gadkari, A.K. Debnath, Highly sensitive NO2 sensor based on ZnO nanostructured thin film prepared by SILAR technique, Sensors Actuators, B Chem. 335 (2021) 129678. https://doi.org/10.1016/j.snb.2021.129678.

[53] California Division of Occupational Safety and Health Webpage. PERMISSIBLE EXPOSURE LIMITS FOR CHEMICAL CONTAMINANTS TABLE AC-1, (n.d.) 1–26. http://www.dir.ca.gov/title8/5155table_ac1.html.

[54] K.S. Pasupuleti, D. Vidyasagar, L.N. Ambadi, N. Bak, S.-G. Kim, M.-D. Kim, UV light activated g-C3N4 nanoribbons coated surface acoustic wave sensor for high performance sub-ppb level NO2 detection at room temperature, Sensors Actuators B Chem. 394 (2023) 134471. https://doi.org/10.1016/j.snb.2023.134471.

[55] M. Ganesan, V. Jayaraman, P. Selvaraj, K.M. Mani, D.-H. Kim, Pyrochlore cerium stannate (Ce2Sn2O7) for highly sensitive NO2 gas sensing at room temperature, Appl. Surf. Sci. 624 (2023) 157135. https://doi.org/10.1016/j.apsusc.2023.157135.

[56] W. Bian, H. Dou, X. Wang, C. Li, Y. Zhang, C. Gong, N. Sun, S. Liu, P. Li, Q. Jing, B. Liu, Fabrication and Computational Study of a Chemiresistive NO 2 Gas Sensor Based on the Carbon Dots-WO 3 Heterostructure for Operating below Room Temperature, ACS Sensors. 8 (2023) 748–756. https://doi.org/10.1021/acssensors.2c02291.

[57] I.S. Saggu, S. Singh, K. Chen, Z. Xuan, M.T. Swihart, S. Sharma, Ultrasensitive Room-Temperature NO 2 Detection Using SnS 2 /MWCNT Composites and Accelerated

Recovery Kinetics by UV Activation, ACS Sensors. 8 (2023) 243–253. https://doi.org/10.1021/acssensors.2c02104.

[58] K.B. Kim, Y.K. Moon, T.H. Kim, B.H. Yu, H.Y. Li, Y.C. Kang, J.W. Yoon, Highly selective and sensitive detection of carcinogenic benzene using a raisin bread-structured film comprising catalytic Pd-Co3O4 and gas-sensing SnO2 hollow spheres, Sensors Actuators B Chem. 386 (2023). https://doi.org/10.1016/j.snb.2023.133750.

[59] Q. Guang, B. Huang, J. Yu, M. Bonyani, M. Moaddeli, M. Kanani, A. Mirzaei, H.W. Kim, S.S. Kim, X. Li, PtS-decorated WS2 microflakes based sensors for selective ammonia detection at room temperature, Sensors Actuators B Chem. 394 (2023) 1–13. https://doi.org/10.1016/j.snb.2023.134399.

[60] M.U. Ali, Y. Yu, B. Yousaf, M.A.M. Munir, S. Ullah, C. Zheng, X. Kuang, M.H. Wong, Health impacts of indoor air pollution from household solid fuel on children and women, J. Hazard. Mater. 416 (2021). https://doi.org/10.1016/j.jhazmat.2021.126127.

[61] J. Guo, B. Ruan, J. Zhu, X. Dai, Y. Xiang, H. Zhang, Low-threshold optical bistability in a metasurface with graphene, J. Phys. D. Appl. Phys. 50 (2017) 434003. https://doi.org/10.1088/1361-6463/aa8ac6.

[62] L. Zhang, K. Khan, J. Zou, H. Zhang, Y. Li, Recent Advances in Emerging 2D Material-Based Gas Sensors: Potential in Disease Diagnosis, Adv. Mater. Interfaces. 6 (2019) 1–27. https://doi.org/10.1002/admi.201901329.

[63] V. Galstyan, A. Moumen, G.W.C. Kumarage, E. Comini, Progress towards chemical gas sensors: Nanowires and 2D semiconductors, Sensors Actuators B Chem. 357 (2022) 131466. https://doi.org/10.1016/j.snb.2022.131466.

[64] J.-H. Cha, S.-J. Choi, S. Yu, I.-D. Kim, 2D WS 2 -edge functionalized multi-channel carbon nanofibers: effect of WS 2 edge-abundant structure on room temperature NO 2 sensing, J. Mater. Chem. A. 5 (2017) 8725–8732. https://doi.org/10.1039/C6TA11019C.

[65] S.-Y. Cho, S.J. Kim, Y. Lee, J.-S. Kim, W.-B. Jung, H.-W. Yoo, J. Kim, H.-T. Jung, Highly Enhanced Gas Adsorption Properties in Vertically Aligned MoS 2 Layers, ACS Nano. 9 (2015) 9314–9321. https://doi.org/10.1021/acsnano.5b04504.

[66] Y. Xu, J. Xie, Y. Zhang, F. Tian, C. Yang, W. Zheng, X. Liu, J. Zhang, N. Pinna, Edge-enriched WS2 nanosheets on carbon nanofibers boosts NO2 detection at room

temperature, J. Hazard. Mater. 411 (2021) 125120. https://doi.org/10.1016/j.jhazmat.2021.125120.

[67] J. Casanova-Chafer, R. Garcia-Aboal, P. Atienzar, M. Feliz, E. Llobet, Octahedral Molybdenum Iodide Clusters Supported on Graphene for Resistive and Optical Gas Sensing, ACS Appl. Mater. Interfaces. 14 (2022) 57122–57132. https://doi.org/10.1021/acsami.2c15716.

[68] P. V. Kumar, M. Bernardi, J.C. Grossman, The Impact of Functionalization on the Stability, Work Function, and Photoluminescence of Reduced Graphene Oxide, ACS Nano. 7 (2013) 1638–1645. https://doi.org/10.1021/nn305507p.

[69] P. Aggarwal, P. Bisht, A. Ghosh, A.K. Gourishetty, E.Y. Chang, B.R. Mehta, R. Singh, γ-Ray-Induced Surface-Charge Redistribution and Change of the Surface Morphology in Monolayer WS 2, ACS Appl. Nano Mater. 6 (2023) 7404–7413. https://doi.org/10.1021/acsanm.3c00516.

[70] A. Alagh, F.E. Annanouch, P. Umek, C. Bittencourt, A. Sierra-Castillo, E. Haye, J.F. Colomer, E. Llobet, CVD growth of self-assembled 2D and 1D WS2 nanomaterials for the ultrasensitive detection of NO2, Sensors Actuators, B Chem. 326 (2021) 128813. https://doi.org/10.1016/j.snb.2020.128813.

[71] J. Hu, X. Xiong, W. Guan, Y. Chen, H. Long, Design and construction of core-shelled Co3O4-CoFe2O4 heterojunction for highly sensitive and selective detection of ammonia, Chem. Eng. J. 452 (2023) 139346. https://doi.org/10.1016/j.cej.2022.139346.

[72] V. Paolucci, S.M. Emamjomeh, L. Ottaviano, C. Cantalini, Near room temperature light-activated ws2-decorated rgo as no2 gas sensor, Sensors (Switzerland). 19 (2019). https://doi.org/10.3390/s19112617.

[73] R. Guo, Y. Han, C. Su, X. Chen, M. Zeng, N. Hu, Y. Su, Z. Zhou, H. Wei, Z. Yang, Ultrasensitive room temperature NO2 sensors based on liquid phase exfoliated WSe2 nanosheets, Sensors Actuators, B Chem. 300 (2019). https://doi.org/10.1016/j.snb.2019.127013.

[74] M. Ikram, L. Liu, H. Lv, Y. Liu, A. Ur Rehman, K. Kan, W.J. Zhang, L. He, Y. Wang, R. Wang, K. Shi, Intercalation of Bi2O3/Bi2S3 nanoparticles into highly expanded MoS2 nanosheets for greatly enhanced gas sensing performance at room temperature, J.

Hazard. Mater. 363 (2019) 335–345. https://doi.org/10.1016/j.jhazmat.2018.09.077.

[75] Y. Li, Z. Song, Y. Li, S. Chen, S. Li, Y. Li, H. Wang, Z. Wang, Hierarchical hollow MoS2 microspheres as materials for conductometric NO2 gas sensors, Sensors Actuators, B Chem. 282 (2019) 259–267. https://doi.org/10.1016/j.snb.2018.11.069.

CHAPTER 5

ZnO/WS_2 hybrid material, for NO_2 detection, via the combination of AACVD and APCVD techniques

ZnO/WS_2 hybrid material, for NO_2 detection, via the combination of AACVD and APCVD techniques

Shuja Bashir Malik [1], Eduard Llobet [1] and Fatima Ezahra Annanouch[1,*]

1 Departament d'Enginyeria Electronica, Universitat Rovira i Virgili, Països Catalans 26, 43007 Tarragona, Spain.

Emails: shujabashir.malik@urv.cat, Eduard.llobet@urv.cat

* Correspondence: fatimaezahra.annanouch@urv.cat ;

† Presented at the Eurosensors XXXIV, Lecce, Italy, 10-13 September 2023.

Abstract

We report for the first time the successful synthesis of ZnO/WS_2 hybrid material, using a combination of aerosol assisted chemical vapor deposition (AA-CVD) and atmospheric pressure CVD techniques. The morphology and the composition of the grown films were investigated, and the results confirm the co-existence of both materials. Moreover, gas sensing results towards 500 ppb of NO_2 revealed the influence of WS_2 material on the ZnO gas sensing performances. The operating temperature has shifted towards lower values from 300°C to 150°C. Besides, the ZnO/WS_2 sensor was able to detect such a small concentration of NO_2 at room temperature.

Keywords: Gas sensors; metal oxides; TMDs; AACVD; APCVD; nanomaterials.

5.1. Introduction

Zinc oxide (ZnO) is an n-type semiconductor with a wide band gap of 3.3 eV and high chemical and thermal stability[1]. It has been extensively studied and employed in gas sensing application, thanks to its low cost, non-toxicity and excellent gas sensing response. However, ZnO-based gas sensors operate at high temperatures (300°C to 500°C) and suffer from lack of selectivity, which are issues that hinder their use in wide real-time applications. In a quest to overcome these shortcomings, researchers have been drawn towards the synthesis of hybrid nanocomposite of metal oxides with two-dimensional (2D) nanomaterial, to create heterojunctions through the nanocomposite and achieve outstanding gas sensing performances. In this context, tungsten disulfide (WS_2) is one of the most studied 2D transition metal-dichalcogenides materials (TMDs). It is characterized by its high sensitivity, stability, and low

operating temperature. The co-deposition of these new materials (TMDs) with metal oxides is very challenging, due to the problems that face their synthesis for instance: low production yield and difficulties to their integration in standard transducing substrates. Hence fore, we report for the first time, the successful synthesis of ZnO/WS_2 nanocomposite for NO_2 detection, using the combination of AACVD and APCVD.

5.2. Materials and Methods

WS_2 synthesis: WS_2 synthesis was performed by using two steps depositions: the first one is the AACVD of tungsten hexacarbonyl ($W(CO)_6$; 50 mg) dissolved in a mixture of acetone and methanol (20 ml) to form tungsten oxide nanoneedles. In the second step, the obtained nanoneedles were subjected to an ambient-pressure CVD sulfurization using a sulfur powder and argon as a carrier gas, which resulted in a homogenous film composed of WS_2 nanotriangles, directly grown on alumina sensor transducer (Pt interdigitated electrode from one side and a resistive Pt heater at the back side). More details can be found in our previous reports [2]. ZnO/WS_2 synthesis: herein, ZnO nanorods were directly grown on the top of WS_2 based alumina substrate using AACVD of $Zn(Cl)_2$ dissolved in ethanol at 400ºC. Nitrogen was used as carrier gas and the deposition time was about 30 min.

5.3. Discussion

Figure 5.1 (a) and (b) illustrate the morphology of bare ZnO nanorods and WS_2 nanotriangles, respectively. Figure 5.1 (c and d) show the morphology of the obtained ZnO/WS_2 nanocomposite. As we can observe ZnO nanorods were successfully grown on top of WS_2 nanotriangles, using a simple combination of AACVD and APCVD techniques. To confirm the structure and the composition, we analyzed our samples (ZnO and ZnO/WS_2) with Raman (Figure 5.1 (e and f) and energy dispersive spectroscopy (EDX) techniques (Figure 5.1 (g). The results confirm the simultaneous presence of multilayers WS_2 and ZnO materials.

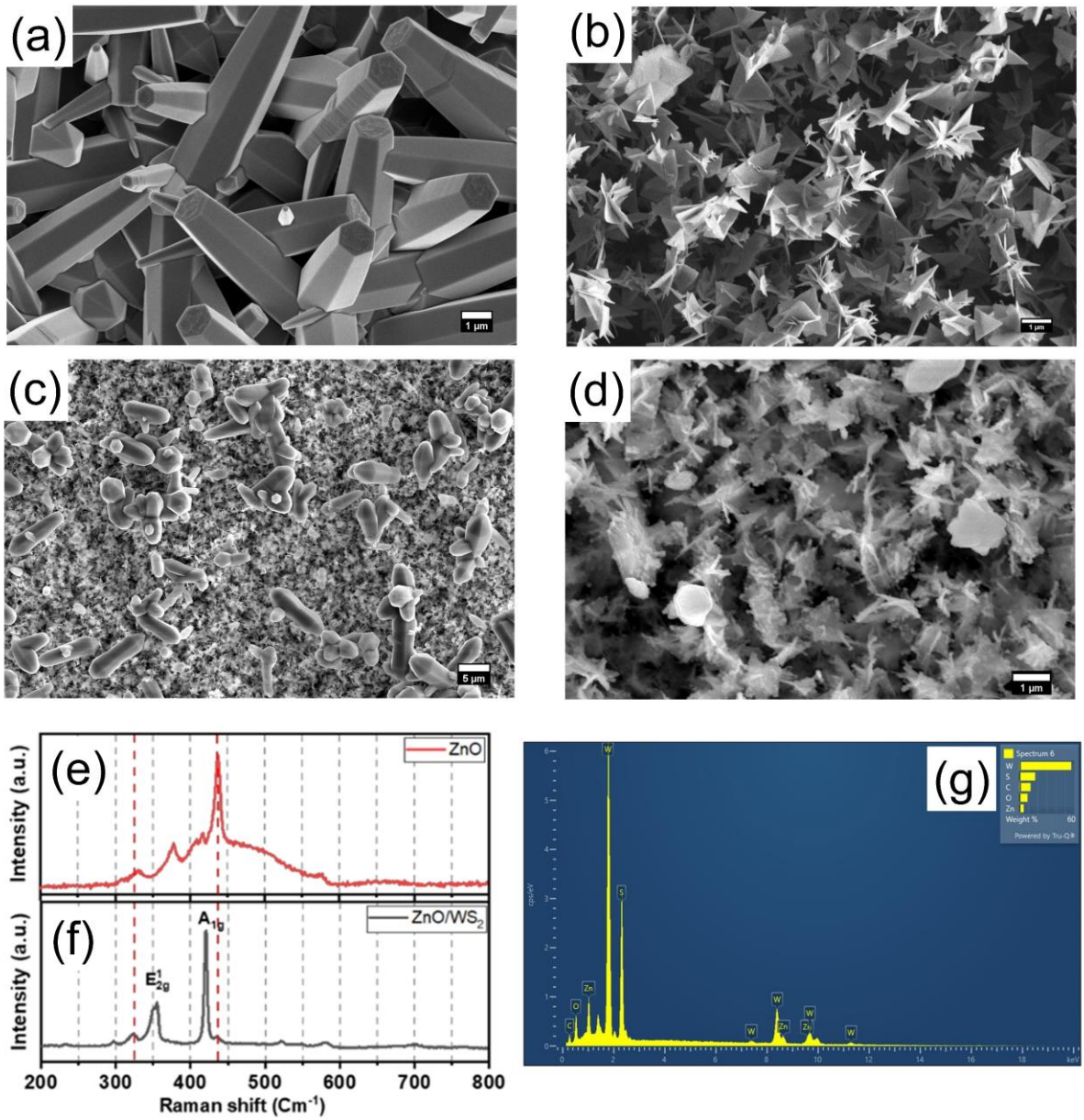

Figure 5.1 FESEM images of (a) ZnO, (b) WS_2, (c,d) ZnO/WS_2, (e,f) Raman spectra and (g) EDX analysis of ZnO/WS_2.

Furthermore, we have tested bare ZnO and ZnO/WS_2 gas sensors towards 500 ppb of NO_2 at different working temperatures. According to the results (Figure 5.2 (a and b), bare ZnO showed no response below 200°C and its optimal working temperature was considered at 300°C. In contrast, hybrid ZnO/WS_2 sensor was quite responsive at very low temperature, especially at 150°C where it shows stable and reproducible responses with good sensitivity (Figure 5.2 (c). Hence fore, this shift in the optimal working temperature demonstrates the effect of the addition of TMDs nanomaterials to the ZnO host matrix.

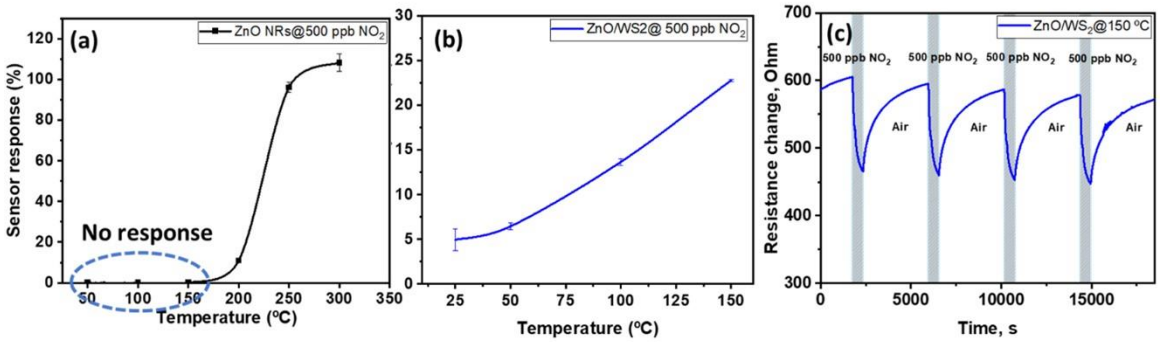

Figure 5.2 Sensor response as a function of temperature (a) ZnO, (b) ZnO/WS_2 and (c) example of ZnO/WS_2 resistance change towards 500 ppb of NO_2.

5.4. References

1. Vallejos, S.; Pizúrová, N.; Gràcia, I.; Sotelo-Vazquez, C.; Čechal, J.; Blackman, C.; Parkin, I.; Cané, C. ZnO Rods with Exposed {100} Facets Grown via a Self-Catalyzed Vapor–Solid Mechanism and Their Photocatalytic and Gas Sensing Properties. ACS Appl Mater Interfaces 2016, 8, 33335–33342.

2. Alagh, A.; Annanouch, F.E.; Colomer, J.F.; Llobet, E. 3D Assembly of WS 2 Nanomaterial for H 2 S Gas Sensing Application. 6, 2–5

CHAPTER 6

Pd-Nanoparticle-Decorated Multilayered MoS_2 Sheets for Highly Sensitive Hydrogen Sensing

Pd-Nanoparticle-Decorated Multilayered MoS_2 Sheets for Highly Sensitive Hydrogen Sensing

Shuja Bashir Malik [1,2], Fatima Ezahra Annanouch [1,2,*] and Eduard Llobet [1,2]

1. Universitat Rovira i Virgili, MINOS, Països Catalans 26, 43007 Tarragona, , Spain; shujabashir.malik@urv.cat (S.B.M.); eduard.llobet@urv.cat (E.L.)
2. IU-RESCAT, Universitat Rovira i Virgili, Joanot Martorell 15, 43480 Vila-seca, Spain

*Correspondence: fatimaezahra.annanouch@urv.cat

Abstract

In this work, efficient hydrogen gas sensors based on multilayered p-type bare MoS_2 and Pd-decorated MoS_2 were fabricated. MoS_2 was deposited onto alumina transducers using an airbrushing technique to be used as a sensing material. Aerosol-assisted chemical vapor deposition (AACVD) was used to decorate layered MoS_2 with Pd nanoparticles at 250°C. The bare and Pd-decorated MoS_2 was characterized using field emission scanning electron microscopy (FESEM), high-resolution transmission electron microscopy (HR-TEM), X-ray diffraction (XRD), and Raman spectroscopy. The characterization results reveal the multilayered crystalline structure of MoS_2 with successful Pd decoration. The size of the Pd nanoparticles ranges from 15 nm to 23 nm. Gas sensing studies reveal that a maximum response of 55% is achieved for Pd-decorated MoS_2 operated at 150°C to 100 ppm of H_2, which is clearly below the explosive limit (4%) in air. The higher sensitivity due to Pd nanoparticle decoration was owed to a spillover effect. This study reveals that the sensitivity of the sensors is highly dependent on the amount of Pd decoration. Moreover, sensor responses increase slightly when exposed to 50% relative humidity (RH at 25°C).

Keywords: gas sensor; spillover; nanoparticles; TMDs; AACVD; decoration

6.1. Introduction

The ever-increasing demand for sustainable and clean energy sources has put hydrogen (H_2) at the forefront as one of the most promising candidates for the next generation of energy. Due to the abundance of hydrogen in nature, it offers the potential in the future to replace fossil fuels as its combustion yields water; thus, it will [1] significantly reduce greenhouse gas emissions [2]. However, hydrogen is highly explosive and flammable (air mixtures at H_2 concentrations

above 4%), which demands the utmost caution in its storage and Even a small leakage of hydrogen can pose a grave threat to safety. Therefore, the development handling [3]. of highly sensitive and selective hydrogen gas sensors with fast detection and recovery are of paramount importance to detect and mitigate potential hazards associated with hydrogen storage, transport, and leakage.

Metal oxide gas sensors (MOX) have been widely used for hydrogen sensing [4], but they suffer from several limitations like poor selectivity and a high working temperature (200–400°C) [5–7]. This leads to an increase in the power consumption and, at the same time, reduces a sensor's lifetime by inducing changes in the material morphology [8]. Moreover, with hydrogen being extremely flammable, sensors working at high temperatures could be potentially dangerous [9], requiring necessary remedies to mitigate damage. Recently, the scientific community has turned its attention towards two-dimensional materials (2D) to overcome the shortcomings of MOX sensors. Indeed, 2D materials have garnered tremendous attention due to their unique electronic and remarkable sensing properties [10,11]. Among 2D materials, on the one hand, graphene has demonstrated outstanding sensing capabilities for toxic gases like NO_2, ammonia, and CO [12,13]. Decorating graphene with metal nanoparticles (NP) like Au, Pt, Pd, or Ag has been found to enhance the sensitivity to gas molecules due to the catalytic effect of the nanoparticles [14,15].

On the other hand, transition metal dichalcogenides (TMDs) have emerged as an exciting class of 2D materials for gas sensing applications[16–19]. Among the TMDs, molybdenum disulfide (MoS_2) has garnered significant interest and attention due to its exceptional sensing, electronic, optical, and catalytic properties [3,20,21]. MoS_2 is a layered structure, with each layer consisting of covalently bonded Mo-S atoms, and neighboring layers are stacked to each other via van der Waals forces[22]. Bulk MoS_2 has an indirect band gap of 1.2 eV, while, as for the atomically thin MoS_2 sheets, there is a transition to a direct bandgap of 1.8 eV, leading to enhanced charge transport, high specific surface areas due to their sheet-like structures with large basal planes and highly reactive edges, and increased electron concentration at the surface [23]. These properties of MoS_2 make it highly desirable for the development of next-generation memory devices [24], photodetectors [25], solar cells [26], and gas sensors [3,11,27].

Several research works have demonstrated the potential of MoS_2-based gas sensors for detecting gases like nitrogen dioxide (NO_2) [28], ammonia (NH_3) [29], nitric oxide (NO) [30], and hydrogen [11,18,27]. Duesberg et al. demonstrated the synthesis of MoS_2 patterns and recorded high-sensitivity detection of ammonia with a limit of detection at the ppm level [31]. Zhou et al. reported Schottky-contact MoS_2-based sensors which are sensitive to 20 ppb and 1

ppm of NO_2 and NH_3, respectively [32]. Zhang and co-workers presented the influence of the thickness on the performance of MoS_2 gas sensors to NO [33]. Zhou et al. demonstrated a MoS_2-based sensor with a 92.6% response to 500 ppm of CO at 230°C [34]. Moreover, Agarwal et al. presented a highly sensitive and fast hydrogen sensor based on monolayer MoS_2 pyramid structures with a 69.1% response to 1% of hydrogen [3].

However, sensors based on bare MoS_2 suffer from sluggish response–recovery speeds and low sensitivity, especially when it comes to the detection of hydrogen gas [3,35]. We have seen that functionalizing the host matrix with a determined noble metal enhances the sensitivity and the selectivity of the sensor to a specific gas. Based on our previous works, we found that CuO nanoparticles are very suitable for the detection of H_2S [36]. Additionally, we showed that Pd/PdO nanoparticles have highly enhanced the sensitivity and selectivity of WO3 to H_2 [37]. Additionally, it was reported that the incorporation of noble metal nanoparticles onto MoS_2 has shown promise in detecting hydrogen with low power consumption and high sensitivity [9,27,35,38–40] . The improved sensing response attributed to the incorporation of noble metals is a result of electronic sensitization (ES) and chemical sensitization (CS) [41,42]. Electronic sensitization involves the oxidized form of the noble metal creating electron-depletion layers (EDLs) at the interface between the noble metal and the sensing layer [41,43], while chemical sensitization arises from a catalytic surface reaction in which noble metals offer low energy sites for the gas adsorption, leading to enhanced sensor sensitivity via a spillover process [41],[44]. Noble metal decoration not only enhances sensitivity and helps in decreasing the optimal sensing temperature but helps in enhancing the long-term stability of the sensors as well [41]. Irrespective of the functionalization process employed, two crucial factors governing noble metal decoration are the amount and the size of the nanoparticles. The optimization of nanoparticle decoration amounts on the sensing layer is important as it directly influences the dissociation of gas molecules. If the decoration is insufficient, the sensitization effect will be diminished. Conversely, excessive decoration would lead to the formation of a continuous film, leading to reduced sensitivity [45].

MoS_2 offers functional groups on both the basal plane and edge sites, which allows for easy incorporation of adatoms on the surface [46,47][33]. The most common method to deposit nanosized metal nanoparticles on MoS_2 using a vacuum is with an e-beam evaporator, as explored by Park et al. to decorate MoS_2 with Pt nanoparticles for NH_3 and H_2S detection [48]. Suh et al. also utilized an e-beam evaporator to decorate Pd and Au on MoS_2 to demonstrate the selectivity of the composite to C_2H_5OH, H_2, NH_3, and NO_2 [49]. Nonetheless, vacuum-based processes pose drawbacks such as high costs and power consumption, limiting gas sensor

development. Burman et al. employed a solution process using glucose as a reducing agent for Au doping on MoS_2 for detecting ammonia with high sensitivity [50]. Huang et al. took advantage of various capping and reducing agents for the epitaxial growth of Pd, Pt, and Ag metal nanostructures on MoS_2 [51]. The use of reducing agents for nanostructure decorations indeed facilitates the reduction of metal precursors into controllable shapes of metal nanoparticles but may act as a barrier for gas sensing [52]. Kim et al. addressed this issue by using a solution process reaction without reducing agents to decorate 2D MoS_2 nanoflakes with Au, Pt, and Pd for selective ammonia, hydrogen, and ethanol sensing [52]. Lee and co-workers deposited Pt using atomic layer deposition (ALD) on MoS_2 for H_2 sensing [53].

Herein, we report the development of bare and Pd-NP-decorated multilayer MoS_2 for hydrogen sensing. Our method is a simple two-step procedure: (i) airbrushing MoS_2 onto alumina substrates, followed by (ii) low-temperature AACVD decoration of Pd nanoparticles onto MoS_2 sensing layers. To the best of our knowledge, none of the reported works have combined airbrushing and low-temperature AACVD methods to functionalize TMD materials. The sensing materials were characterized with FESEM, HRTEM, XRD, and Raman spectroscopy to study the morphology, crystal structure, and decoration characteristics. We investigated the chemiresistive sensing mechanism of bare and Pd-decorated MoS_2 and studied the impact of Pd decoration on the sensing properties of MoS_2 to hydrogen gas. The sensors display a response of 55% to 100 ppm of hydrogen gas at 150°C and show a clear impact of Pd decoration on hydrogen sensitivity.

6.2. Experimental Section

6.2.1. Materials, Chemicals, and Sensor Fabrication

6.2.1.1. Materials and Sensor Fabrication

MoS_2 powder (CAS:1317-33-5) was purchased from SigmaAldrich, Spain and used without further modifications. A total of 20 mg of MoS_2 powders was sonicated in 10 mL of ethanol (Scharlab, Spain CAS: 64-17-5) for 45 min to obtain a homogenous suspension. The suspension was immediately airbrushed onto alumina transducers (Ceram Tech GmBH, Germany) to achieve MoS_2 thin films coating the interdigitated electrode area. Nitrogen was used as a carrier gas during the airbrushing. In order to achieve thin films of reproducible thickness, the resistance of the films was monitored during deposition by connecting the alumina transducer to a multimeter. As soon as the desired resistance of the material was reached, the deposition process was stopped. Samples were fabricated in four sets for each type

of material. The average resistance of a pristine set of sensors was 400 MΩ ± 12 MΩ, while, as for sensors with 1 mg of Pd precursor (MoS_2−Pd_1), the average resistance was 72 MΩ ± 4 MΩ. Also, for the sample with 2 mg of Pd precursor (MoS_2−Pd_2), the average resistance was 55 MΩ ± 6 MΩ. All these resistance values were calculated at room temperature. Moreover, the average thickness of the deposited layers was calculated to be around 582 nm using focus ion beam (FIB). The FESEM images of the thickness analysis of the sensing layer are presented in Figure S1.

6.2.1.2. Pd-Nanoparticle-Decorated MoS_2 Nanosheets using AACVD Method

Palladium nanoparticles were incorporated onto the fabricated MoS_2 sensors using aerosol-assisted chemical vapor deposition (AACVD). The reaction was performed at comparatively low temperature of 250°C. To study the effect of Pd concentration on the sensor responses, two amounts of the palladium precursor were used to decorate MoS_2 sensors. In a typical synthesis procedure, 1 mg and 2 mg of Palladium (II) acetylacetonate (Sigma Aldrich, Spain CAS: 14024-61-4) were dissolved in 5 mL methanol (CAS: 67-56-1). The solution was ultrasonicated to ensure full solubilization. The solution was placed in an ultrasonic humidifier to generate aerosol. N_2 gas with a flow of 0.5 L/min was used as a carrier gas to transport the aerosol to the MoS_2 sensors preheated at 250°C in a hot wall reactor. The AACVD method is similar to our previous reported works [54,55]. The deposition time was about 5 min; after that, the chamber was left to cool down naturally. The sensors were named according to the Pd decoration concentration, viz., MoS_2−Pd_1 and MoS_2−Pd_2 for 1 mg and 2 mg precursor amounts, respectively.

6.2.1.3. Material Characterization Techniques

The morphology of the prepared samples was analyzed using a field emission scanning electron microscope (FESEM-Thermo Scientific Scios 2). The FESEM microscope used in this study is equipped with EDX as well to calculate the wt.% of palladium nanoparticles. Moreover, the FESEM equipment is also equipped with the focus ion beam (FIB) tool used here to calculate the thickness of the sensing layer. The crystal structure was analyzed via X-ray diffraction using a Bruker AXS D8 diffractometer equipped with parallel incident beam (Gobel mirror) vertical θ-θ goniometer, XYZ motorized stage, and with a GADDS (General Area Diffraction System). A JEOL F200 TEM ColdFEG operated at 200 kV was used for the high-resolution transmission electron microscopy (HRTEM) characterization. EDX spectra and elemental analysis was performed using the same HRTEM equipment. The Raman spectra were recorded using a Renishaw in Via, laser 514 nm, ion argon-Novatech, 25 mW.

6.2.1.4. Gas Sensing Measurements

The gas sensing measurements were conducted using a homemade detection system in a Teflon® chamber with a volume of 35 mL. The chamber is designed to accommodate four sensors simultaneously. The chamber consists of an inlet connected to the gas delivery system and an outlet which is connected to the exhaust. Commercial alumina substrates with interdigitated platinum electrodes (300 µm electrode gap) on the front side and a platinum resistive meander on the back side were used to deposit the sensing material. The sensor responses were recorded by monitoring the sensing material resistance using an Agilent-34972A data acquisition system. Calibrated cylinders of NO_2 (total concentration, 1 ppm), H_2 (total concentration, 1000 ppm), NH_3 (total concentration, 100 ppm), CO (total concentration, 100 ppm), and benzene (total concentration, 10 ppm) were mixed with pure synthetic air using Bronkhorst mass-flow controllers. A constant flow rate of 100 mL min^{-1} was maintained during all the experiments. The sensors were exposed to the analyte gas for 10 min and subsequently cleaned in dry air for 60 min. The cleaning time to recover the baseline was adapted according to the sensor operating temperature; 60 min for 50°C, 100°C, and 150°C and 120 min for room temperature operation. Prior to gas sensing measurements, sensors were kept under a constant flow of dry air for a minimum of 5 h to completely stabilize their initial baseline resistance. The sensor responses were calculated using Equation (1) for reducing gas species and Equation (2) for oxidizing gas species.

$$\left(\frac{R_{gas}-R_{air}}{R_{air}} * 100\right) \% \qquad \text{Equation 1}$$

$$\left(\frac{R_{air}-R_{gas}}{R_{air}} * 100\right) \% \qquad \text{Equation 2}$$

where R_{air} and R_{gas} are the real-time resistances of the sensor exposed to air and to analyte, respectively.

6.3. Results and Discussions

6.3.1. Material Characterization

6.3.1.1. FESEM Analysis

Figure 6.1 depicts the FESEM images of the sensing materials. Upon analysis, it is evident that the deposited MoS_2 exhibits a multilayered structure, as shown in Figure 6.1 (a). The size of the MoS_2 structures varies from 200 nm to 1.5 µm (edge to edge), displaying clear and distinct

ridges. In the case of MoS_2−Pd_1, most of the decorated Pd nanoparticles are spherical with an average size of 15 nm, as shown in Figure 6.1 (b). In the case of MoS_2−Pd_2, the decorated nanoparticles are a mix of spherical and rice-grain shaped with an average size slightly larger (23 nm) than that observed in MoS_2−Pd_1, as illustrated in Figure 6.1 (c). Decorating with a higher concentration of palladium leads to higher coverage, which can be seen in the FESEM images. Different Pd decoration amounts were used to check the impact of the decoration amount on the gas sensing properties of the material. The decoration of the sensors was kept at low concentrations to avoid hindering the transport of dissociated hydrogen atoms to the MoS_2 channel. This could be owed to the hampering of the catalytic effect due to the increased concentration of Pd [53]. Moreover, it is clear that the deposition of metal nanoparticles has no visible influence on the morphology of the MoS_2. Also, an Energy Dispersive X-ray Analysis (EDX) of the samples was conducted to determine the average weight percentage (wt.%) of Palladium (Pd) in the respective samples. The EDX analysis was carried out at various spots on the samples; the resulting data were analyzed to calculate the average wt.% of palladium. Based on the calculations, the average wt.% of Pd in the MoS_2−Pd_1 sample was 7.27 wt.%, while, as in the MoS_2−Pd_2 sample, the wt.% of palladium was 11.69 wt.%.

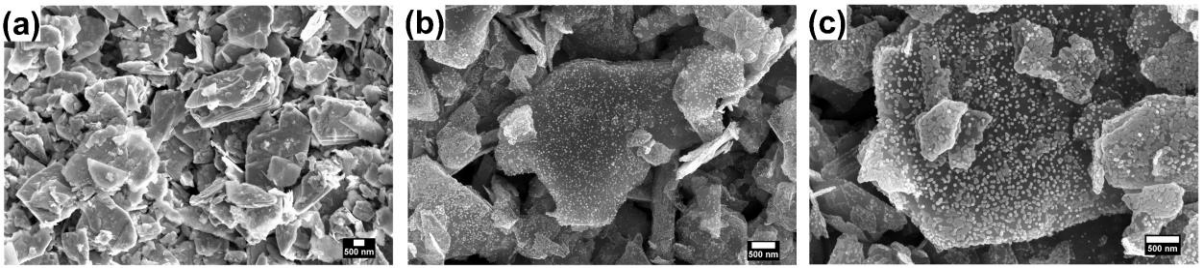

Figure 6.1 FESEM images of (**a**) MoS_2, (**b**) MoS_2−Pd_1, and (**c**) MoS_2−Pd_2.

6.3.1.2. HRTEM Analysis

Supplementing the FESEM morphological data, an HRTEM analysis of one of the sensing materials, MoS_2−Pd_2, was performed combined with EDX spectroscopy. Pd-decorated MoS_2 films were scraped off the alumina substrate and drop-casted over carbon-coated copper grids. Analysis of the HRTEM results reveals the crystalline layered structure of the MoS_2 with successful Pd decoration, as shown in Figure 6.2 (a,b). At some places, the layers are randomly oriented, while at other places the layers are stacked one on other. EDX spectra and HRTEM images of the sensing material are presented in Figure 6.2 (c–e), respectively. EDX analysis revealed the presence of Pd nanoparticles on MoS_2 sheets. Upon further analysis, we verified the interlayer distance, with d equal to 0.215 nm corresponding to the

(103) plane of MoS_2 (ICDD card number: 65-1951) as shown in Figure 6.2 (d). The d-spacing calculated for Pd nanoparticles is 0.232 nm, which corresponds to the (111) plane of Pd (ICDD card number 88-2335). The interlayer distance results of both MoS_2 and palladium were confirmed with XRD analysis.

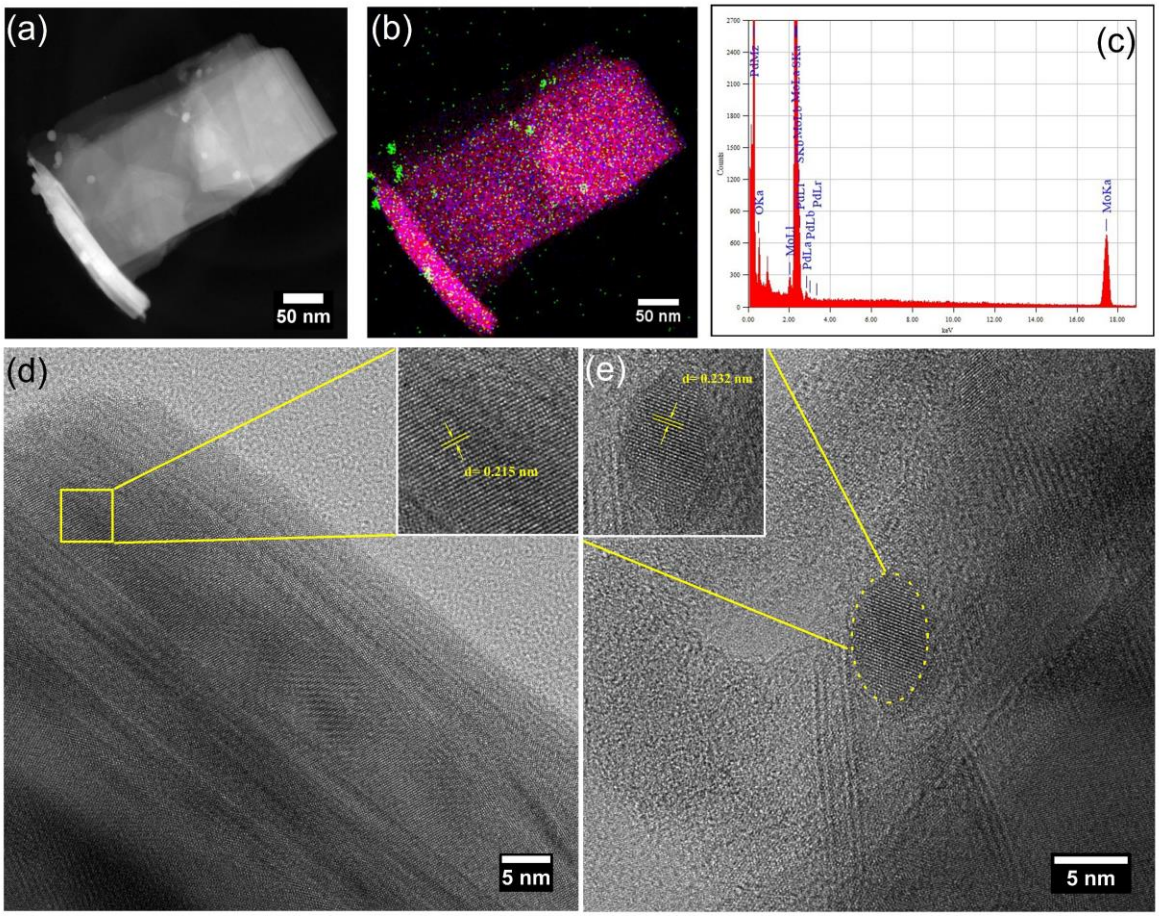

Figure 6.2 (**a**) TEM image of multilayer MoS_2_Pd, (**b**) color mapping of MoS_2_Pd, (**c**) EDX pattern of MoS_2_Pd, (**d**) HRTEM image of multilayer pristine MoS_2 with d-spacing of 0.215 nm, (**e**) close-up of Pd nanoparticle with d-spacing 0.232 nm.

6.3.1.3. XRD

The crystal structure of the sensing films was analyzed using an X-ray diffraction (XRD) method. Figure 6.3 shows the XRD diffractogram recorded from pristine MoS_2 and Pd-decorated MoS_2 in the range of $2\theta = 5°$ to 80°. The observed diffraction peaks match with the hexagonal phase of MoS_2 (ICDD card number: 65-1951) with lattice constants a = 0.316 nm and c = 1.2294 nm belonging to the P63/mmc space group. The major diffraction peaks can be indexed to the (002) at 14.42°, (102) at 35.88°, (103) at 39.56°, and (105) at 49.81° lattice planes. Some additional peaks are observed in Figure 6.3 (b,c). These peaks can be indexed to palladium (ICDD card number: 88-2335). The diffraction peaks of palladium match the cubic phase with lattice constant a = 0.39 nm (Fm-3m space group). At $2\theta = 40.01$, 46.53, and 67.92,

the peaks of MoS_2 and Al_2O_3 almost coincide with the peaks of Pd. Hence, in Figure 6.3 (b,c), the peaks are more intense than those in Figure 6.3 (a), which corresponds to pristine MoS_2. This confirms the presence of Pd decorating the surface of MoS_2.

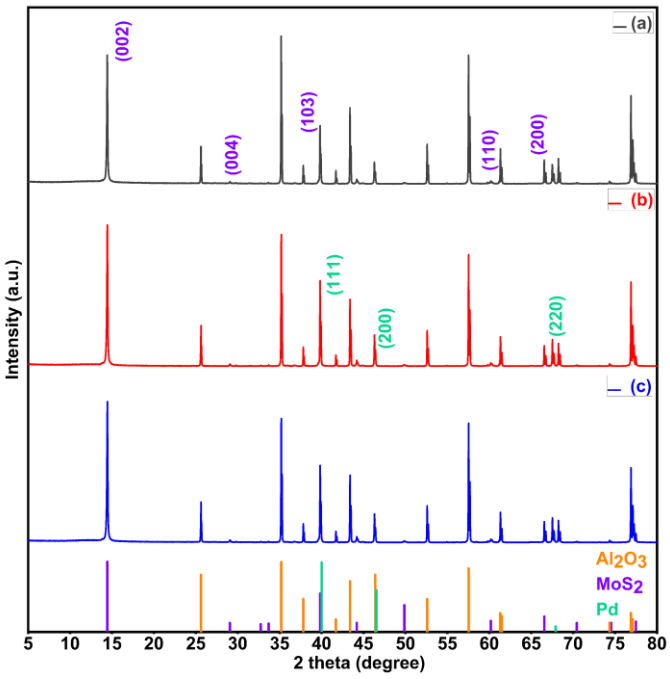

Figure 6.3 XRD diffractogram of (**a**) MoS_2, (**b**) MoS_2–Pd_1, and (**c**) MoS_2–Pd_2.

6.3.1.4. Raman Spectroscopy

Figure 6.4 shows the typical Raman spectra of pristine and Pd-decorated MoS_2. The Raman spectra of all the samples show peaks near 400 cm^{-1}, which confirms the 2H phase of MoS_2. The two characteristic peaks signify the vibration modes for MoS_2: E^1_{2g} , which corresponds to in-plane vibration of the molybdenum atom and is opposite to two sulfur atoms, and A_{1g}, mode which corresponds to the out-of-plane vibration of sulfur atoms (Mo atom being immobile) [56]. In addition to the main characteristic peaks, the small peak at ~283 cm^{-1} can be assigned to the MoO_2 phase [57,58]. Table 6.1 summarizes the Raman peak positions of all the samples. The values of Δ provide the information about the number of layers in the MoS_2. As can be seen from the table, $\Delta \geq 25$, indicating the multilayered structure of MoS_2 [59,60]. This is in agreement with the FESEM and HRTEM results.

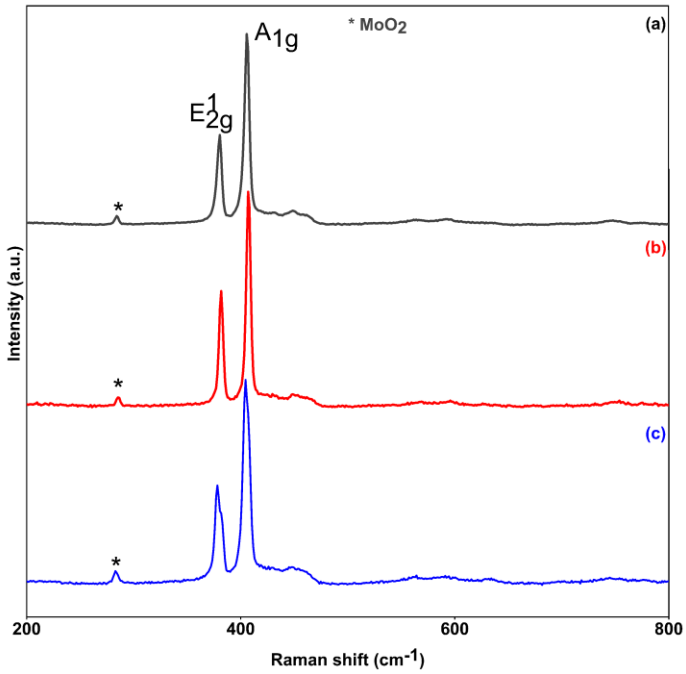

Figure 6.4 Raman spectra of (**a**) MoS_2, (**b**) MoS_2–Pd_1, and (**c**) MoS_2–Pd_2.

Table 6.1 Summary of Raman data.

Sample	E^1_{2g}	A_{1g}	$\Delta = (A_{1g} - E^1_{2g})$
MoS_2	381	406	25
MoS_2–Pd_1	381	407	26
MoS_2–Pd_2	378	405	27

6.3.2. Gas Sensing Results

6.3.2.1. Hydrogen Gas Sensing

The gas sensing characteristics of pristine and Pd-decorated MoS_2 thin films were analyzed to hydrogen gas. The sensor responses were checked at different operating temperatures (room temperature, 50°C, 100°C, and 150°C) to study the optimal working temperature. Optimal temperature is an important parameter to define thermally active interactions between the target gas molecules and the adsorbed oxygen ionic species. Operating temperature plays an important role in determining the gas sensing performance of the sensors as it directly affects the selectivity, sensitivity, and response/recovery time. The desorption rate of the reacted by-products surpasses the adsorption rate of the target gas as temperature increases, reaching the peak efficiency at the optimal working temperature [61]. Figure 6.5 shows the sensor responses to 100 ppm H_2 with respect to increases in temperature. The sensor responses increase with

increases in the temperature, showing maximum response at 150°C. Thus, the optimal working temperature of the sensors is 150°C. The sensors were not operated beyond 150°C to avoid the risk of oxidizing MoS_2 to MoO_x [62].

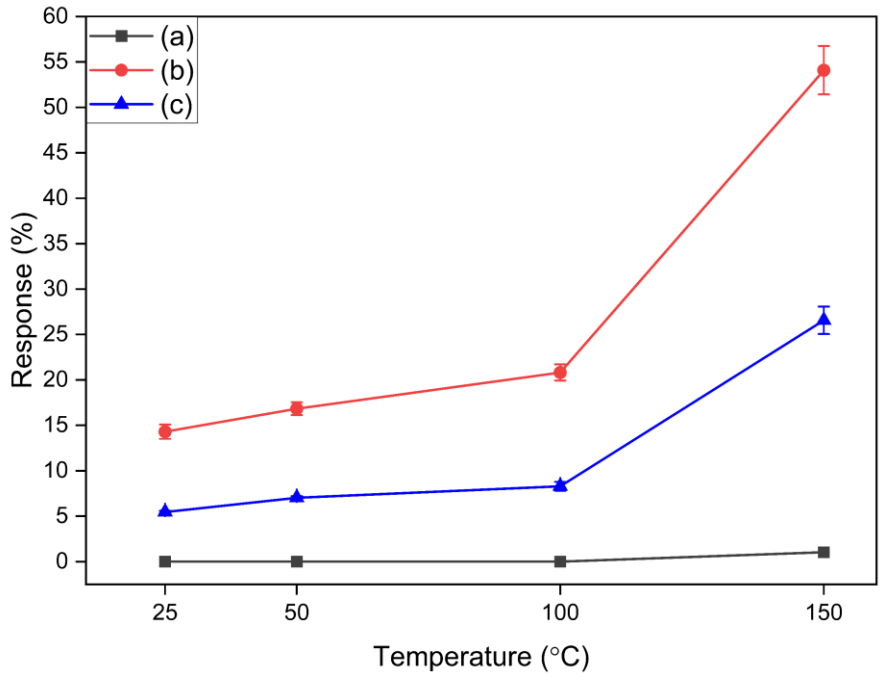

Figure 6.5 Sensor responses as a function of temperature to 100 ppm H_2, (**a**) MoS_2, (**b**) MoS_2−Pd_1, and (**c**) MoS_2−Pd_2.

Indeed, based on our previous studies regarding the long-term stability of TMD-based gas sensors operated at temperatures equal to or below 150°C, there were no remarkable changes in the material characteristics or the gas sensing performances. It is clear from the figure that there is a significant increase in the sensor response from pristine MoS_2 to Pd-decorated MoS_2, specifically in the case of MoS_2−Pd_1. All three sensors showed reproducible responses. The sensor responses were calculated to be 55% at 150°C to 100 ppm of H_2 for MoS_2−Pd_1, which is 1471% higher than the responses recorded in the case of pristine MoS_2. Also, in the case of MoS_2−Pd_2, the response is 300% higher than that for the pristine MoS_2 sensor. As is evident from Figure 6.5, the minimum response recorded in the case of MoS_2−Pd_1 is 14.3% at room temperature, which is 2760% higher than that of the pristine MoS_2 under the same conditions. We can clearly observe the impact of Pd decoration on the sensitivity of the sensors to H_2 gas. The main reason behind this increase in the sensitivity is the reaction between Pd and H_2 atoms generating palladium hydride (PdH_x) at room temperature [63,64] and also the affinity of MoS_2 for H atoms [65]. Moreover, Pd nanoparticles have one of the highest sticking and diffusion coefficients [66]. Therefore, the results confirm the synergistic contribution of Pd and MoS_2

for H_2 sensing. The dynamics of resistance change and baseline recovery for all the sensors in a hydrogen environment as well as in synthetic air are shown in Figure 6.6.

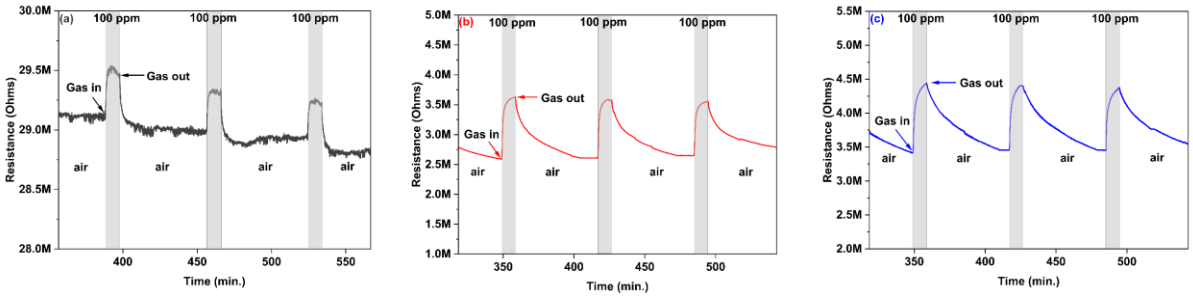

Figure 6.6 Sensor resistance dynamics (**a**) MoS_2, (**b**) MoS_2−Pd_1, and (**c**) MoS_2−Pd_2 to 100 ppm H_2 at 150°C.

The amount of Pd decoration has a clear impact on the response of the sensors to hydrogen. Higher Pd coverage leads to the formation of more Schottky barriers, which, in turn, increases the resistance. In our case, we found the baseline resistance of the sensors with higher Pd decoration approximately 1 MΩ higher than the sensors with low Pd decoration (Figure 6.6 (b,c). When exposed to air, Pd tends to oxidize and form PdO nanoparticles, a p-type semiconductor. The decrease in the baseline resistance indicates that PdO nanoparticles inject holes in the MoS_2 films. Moreover, excessive decoration of Pd on MoS_2 impedes the transport efficiency of dissociated hydrogen atoms to the MoS_2 channel, consequently hindering the catalytic effect. Furthermore, abundant Pd decoration leads to a reduction in the available surface area of MoS_2 for interactions with hydrogen gas species owing to increased coverage by Pd nanoparticles. This results in lower sensing characteristics of the MoS_2, suggesting lower Pd decoration amounts [41]. We compared our sensor responses with the highest-performing sensors in the literature based on noble metals and MoS_2. Our sensors outperform the sensors in every aspect. Table 6.2 shows the comparison of our sensors with some highly responsive MoS_2-based sensors for hydrogen sensing.

Table 6.2 Hydrogen gas sensing comparison of various noble metal-doped/decorated MoS_2 sensors.

Gas Sensing Material	Conc.	Response Calculation Formula	Response %	Operating Temperature	Ref.
ALD Pt-decorated MoS_2 nanosheets	1000 ppm	$\frac{R_{air}}{R_{H_2}}$	440	250°C	[53]
Pd nanoclusters–MoS_2 heterostructure	140 ppm	$\frac{R_{H_2} - R_{air}}{R_{air}} * 100$	17	RT (with light activation)	[9]
Pd-functionalized MoS_2 nanosheet	10,000 ppm	$\frac{R_{H_2}-R_{air}}{R_{air}}*100$	35.3	RT	[38]
Pt-decorated MoS_2 hollow structures	40,000 ppm	$\frac{R_{H_2}-R_{air}}{R_{air}}*100$	11.2	RT	[63]
Pd-functionalized edge-enriched MoS_2	500 ppm	$\frac{R_{H_2-R_{air}}}{R_{air}} * 100$	33.7	RT	[67]
Pd-decorated MoS_2	100 ppm	$\frac{R_{H_2} - R_{air}}{R_{air}} * 100$	55	150°C	This work
			14.9	RT	

The increase in the electrical resistance values of the sensors upon exposure to hydrogen molecules (reducing gas) indicates the p-type nature of both the pristine and Pd-decorated sensors. Also, the sensors were exposed to increasing concentrations of H_2 ranging from 50 ppm to 500 ppm in a background of dry air. Figure 6.7 show the resistance change dynamics of the sensors to increasing H_2 pulses while being operated at 150°C. As can be seen in the figure, the sensors responded well to the respective hydrogen concentrations with almost complete baseline recovery except in the case of pristine MoS_2, which shows a slight drift. The sensors were able to detect a very low concentration of 50 ppm of H_2 with excellent sensitivity. Rapid changes in the sensing signals exceeding final steady-state values can be seen in Figure 6.7 (b,c). This can be owed to the competition between reaction speed and gas diffusion [68–70]. The phenomenon is prominent when H_2 concentration is high or Pd decoration is in excess. That is why this is much more prominent in the sensor with higher Pd content, as depicted in Figure 6.7 (c). To suppress this issue, when sensing higher concentrations of H_2, thinner materials with high porosity can be helpful [63].

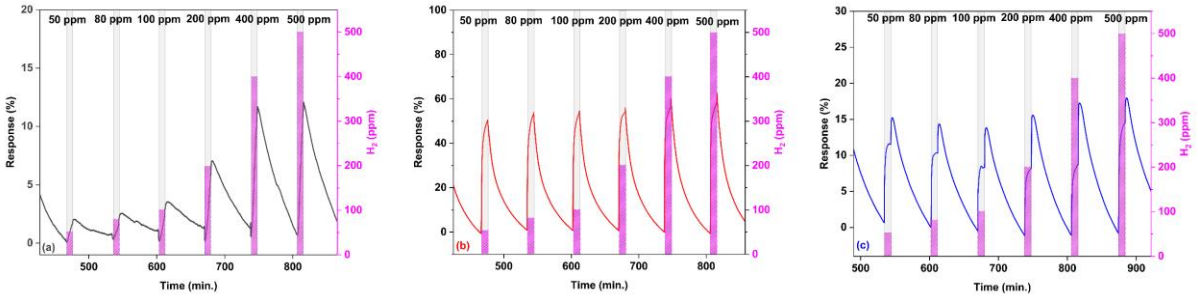

Figure 6.7 Sensor responses to increasing concentration of H_2 at 150°C (**a**) MoS_2, (**b**) MoS_2−Pd_1, and (**c**) MoS_2−Pd_2.

Figure 6.8 shows the sensor response as a function of the hydrogen concentration. The Pd-decorated sensor response values saturate above 100 ppm, and up to 100 ppm, the relationship between the sensor responses and the H_2 concentration is quite linear. Also, the sensor responses with respect to H_2 concentration in the case of pristine MoS_2 are linear. It is worth mentioning that 100 ppm is much below the permissible limit for H_2 gas for safety purposes. Palladium facilitates the dissociation of hydrogen molecules into chemisorbed hydrogen atoms (H) on its surface under ambient conditions without encountering any significant barriers. After their formation, these atoms quickly saturate the surface and migrate into interstitial lattice sites in the subsurface region before finally diffusing into the bulk. The diffusion of H atoms is impeded by an energy landscape characterized by subsurface sites that are energetically more favorable compared with bulk interstitials. Therefore, it is safe to assume that subsurface sites are occupied irrespective of the hydrogen concentration in the bulk. Additionally, it has been demonstrated that the presence of hydrogen in the subsurface layer can lead to the generation of lattice strain, which can impact the thermodynamics of the sorption process in nanoscale systems like nanoparticles [71].

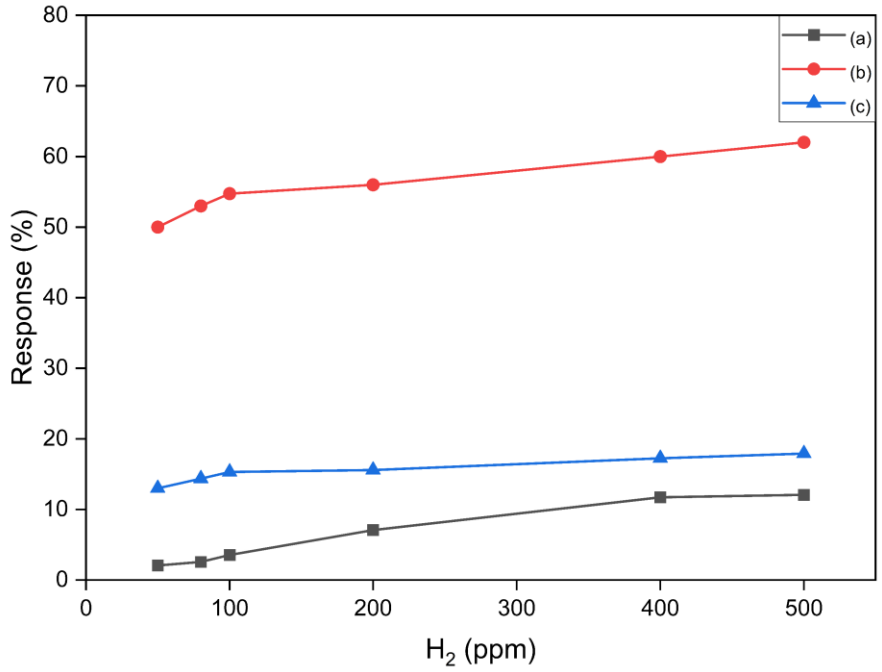

Figure 6.8 Calibration curves to H_2 for the different types of sensors tested. Sensors operated at 150°C, (**a**) MoS_2, (**b**) MoS_2−Pd_1, and (**c**) MoS_2−Pd_2

6.3.2.2. Selectivity Test

In addition to H_2 gas, the gas sensing performance of MoS_2 and Pd-decorated MoS_2 was investigated to reducing gases such as CO, NH_3, ethanol, and benzene. Also, the sensor responses were investigated against an oxidizing gas: NO_2. The typical resistance response dynamics for 5 ppm benzene, 80 ppm CO, 10 ppm ethanol, and 5 ppm NH_3 are shown in Figures S2, S3, S4, and S5, respectively (supporting information). The histogram in Figure 6.9 summarizes the sensing results analyzed for each gas. Decorating MoS_2 with Pd clearly enhances the response to H_2 and diminishes cross-sensitivity to carbon monoxide, ammonia, benzene, and ethanol. However, all the sensors respond to NO_2 with a significant response. It is worth mentioning and stressing that 800 ppb of NO_2 is a very high concentration. The United States Environmental Protection Agency (U.S. EPA) has regulated the limit of exposure of NO_2 at less than 100 ppb, keeping in view its negative effects both on the environment and human life [72]. For NO_2 concentrations of 100 ppb, the sensor response is 18%. The pristine MoS_2 demonstrates a robust response to NO_2, while it lacks sensitivity to H_2. By combining these two distinct sensors, we anticipate that the composite system can effectively mitigate the issue of cross-sensitivity displayed by Pd-decorated MoS_2 to NO_2. The complementary nature of the individual sensors, with pristine MoS_2 being selective to NO_2 and Pd-decorated MoS_2 being responsive to H_2, allows for a synergistic response that can enhance the discrimination

capabilities of the composite sensor. This combination holds promise in suppressing the undesired cross-sensitivity exhibited by the Pd-decorated MoS_2 sensor to NO_2, enabling more accurate and reliable gas sensing applications. All the interfering species were tested at significantly higher concentrations; hence, it can be derived that Pd decoration improved selectivity to H_2.

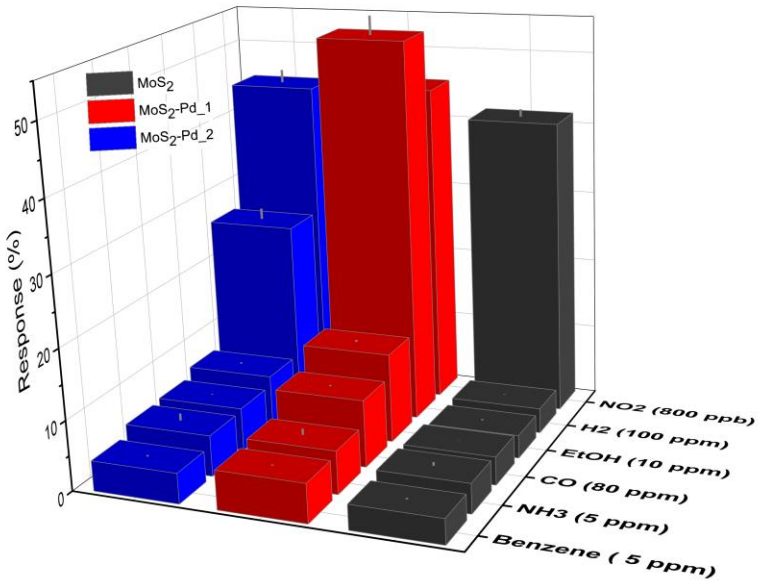

Figure 6.9 Response histogram of MoS_2, MoS_2−Pd_1, and MoS_2−Pd_2 to NO_2 (800 ppb), H_2 (100 ppm), ethanol (10 ppm), carbon monoxide (80 ppm), ammonia (5 ppm), and benzene (5 ppm) at 150°C.

Ambient moisture affects the electrical properties of gas sensors dramatically and ultimately impacts the sensitivity heavily. This makes it mandatory to evaluate the behavior of the gas sensors in humid environments. Figure 6.10 depicts the sensor responses to 5 ppm of benzene (a reducing gas) under dry air and at 50% relative humidity (at 25°C). Also, Figure S6 illustrates the normalized sensor resistance changes as a function of time. Analysis of the results reveals an overall decrease in the baseline resistance of the sensing layer when exposed to a humid environment. This has been reported in metal oxide semi-conducting materials as well [73]. We noticed a slight increase in the sensor responses, except in the MoS_2−Pd_2 sensor. Generally, in humid environments, the water vapors (hydroxyl group) and the target gas molecules enter a competition at the active sites. The impact of the humidity is much more prominent when the relative surface distribution of the hydroxyl groups is much higher than

the oxygen species [60]. The obtained results indicate that the sensors exhibit strong resilience to high levels of moisture.

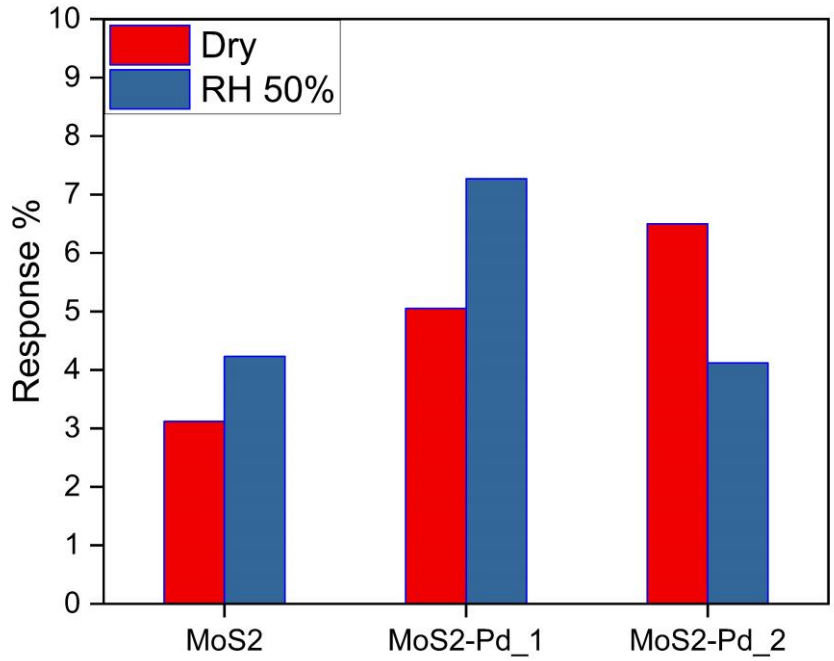

Figure 6.10 Sensor responses to 5 ppm benzene at 150°C.

6.3.2.3. Hydrogen Gas Sensing Mechanism

The sensing mechanism of chemoresistive gas sensors is based on electrical resistance modulation, which can be attributed to the interactions occurring on the sensor substrate because of the chemical reactions between the sensor surface and target gas [74]. When a sensor surface interacts with hydrogen, a reducing gas, it donates electrons upon adsorption. Depending on the type of the material (n-type or p-type), the transferred electrons lead to an increase or decrease in the electrical resistance of the material [39,40,75,76]. In this work, the resistance of MoS_2 increased upon exposure to H_2, indicating the p-type behavior of the material.

When the sensors are exposed to air, the oxygen molecules dissociate on the MoS_2 surface, resulting in the formation of adsorbed oxygen species like (O_2^- *and* O^-) at elevated temperatures [39], as is shown in Equations (3) and (4).

$$O_2\,(g) \rightarrow O_2(ads) \qquad \text{Equation 3}$$

$$O_{2\,(ads)} + e^- \rightarrow O_{2\,(ads)}^- \qquad \leq 100℃ \qquad \text{Equation 4}$$

Pd nanoparticle addition promotes the gas sensing ability of MoS_2 by acting as an electronic sensitizer while sensing H_2. Pd enhances the sensor responses by increasing the rate of chemical processes. One of the main roles of the Pd is to make catalytic oxidation easy on the MoS_2 active layer [39]. When the sensors are exposed to hydrogen, the Pd nanoparticles provide adsorption sites for hydrogen molecules, as seen in Equation (5). Pd decoration enables barrierless dissociation of hydrogen molecules (H_2) into chemisorbed hydrogen atoms (H) on its surface. The dissociation of the adsorbed hydrogen molecules takes place to form hydrogen atoms (Equation (6)). This process is known as the spillover effect of Pd catalysts with respect to H_2 sensing [63]. For Pd particles larger than 5 to 10 nm (as in our case), the diffusion lengths for H atoms to reach the core are shorter [77]. The hydrogen atoms react with the O^- oxygen species (Equation (7)), facilitating the electrons to the sensor. These electrons combine with holes and reduce the charge carrier concentration, eventually leading to the increase in the sensor resistance. This increase is proportional to the concentration of hydrogen gas. These reactions are facilitated by the presence of Pd nanoparticles in the matrix owing to their strong affinity for the mitigation of chemisorbed gaseous species.

$$H_{2\,(gas)} \rightarrow 2H_{(ads)} \qquad \text{Equation 5}$$

$$H_{2\,(ads)} \rightarrow 2H_{(ads)} \qquad \text{Equation 6}$$

$$2H_{(ads)} + O^-_{(ads)} \rightarrow H_2O + e^- \qquad \text{Equation 7}$$

6.4. Conclusions

In this paper, layered MoS_2 was successfully deposited onto alumina substrates. AACVD at 250°C was employed for the Pd decoration of MoS_2. The sensing material was well characterized using FESEM, XRD, HRTEM, and Raman spectroscopy. Multilayered crystalline MoS_2 sheets were observed with homogenous Pd nanoparticle decoration. The size of the Pd nanoparticles was between 15 nm and 23 nm. The gas sensing results of bare and Pd-decorated MoS_2 to H_2 were analyzed. The Pd-nanoparticle-decorated MoS_2 sensing layer acts as an active hydrogen-sensing layer with a maximum response of 55% at 150°C to 100 ppm of H_2. The sensors show high resilience to humidity, as the sensor responses increase slightly when exposed to 50% relative humidity. The effect of Pd decoration is evident with the sensitivity of the sensors depending on the amount of Pd decoration. A combined bare and Pd-

decorated MoS_2 sensor system holds promise for achieving a highly sensitive and selective H_2 detection.

Supplementary Materials: The following supporting information can be downloaded at: www.mdpi.com/xxx/s1, Figure S1 depicts the thickness of the sensing layer, Figure S2, S3, S4 and S5 show resistance dynamics towards interfering gases and Figure S6 shows normalized resistance dynamics in humid environment.

Author Contributions: Conceptualization, S.B.M.; Methodology, S.B.M. and F.E.A.; Validation, E.L.; Formal analysis, S.B.M.; Investigation, S.B.M. and F.E.A.; Writing – original draft, S.B.M.; Writing – review & editing, F.E.A.; Visualization, F.E.A.; Supervision, F.E.A. and E.L.; Funding acquisition, E.L. All authors have read and agreed to the published version of the manuscript.

Funding: This research was funded by Martí-Franquès Research grants Programme (Grant Number: 2019PMF-PIPF-14), Agencia Estatal de Investigación (Grant Number: TED2021-131442B-C31), and AGAUR (Grant Number: 2021 SGR 00147).

Institutional Review Board Statement: Not applicable.

Informed Consent Statement: Not applicable.

Data Availability Statement: Raw data is available from the authors upon request.

6.5. Acknowledgments

S.B.M is supported by the Martí-Franquès Research grant Programme, Doctoral grants—2019, (2019PMF-PIPF-14). F.E.A. is a Juan de la Cierva incorporacion Post-Doctoral Fellow. E.L. is supported by the Catalan Institution for Research and Advanced Studies via the 2018 Edition of the ICREA Academia Award. This work is supported by the Agencia Estatal de Investigación (AEI) under grant no. TED2021-131442B-C31 and by AGAUR under grant no. 2021 SGR 00147. The HRTEM was partially funded by the operative program FEDER Catalunya 2014-2020 (IU16-015844).

Conflicts of Interest: The authors declare no conflict of interest.

6.6. References

[1] M.Z. Jacobson, W.G. Colella, D.M. Golden, Atmospheric science: Cleaning the air and improving health with hydrogen fuel-cell vehicles, Science (80-.). 308 (2005) 1901–1905. https://doi.org/10.1126/science.1109157.

[2] S. van Renssen, The hydrogen solution?, Nat. Clim. Chang. 10 (2020) 799–801. https://doi.org/10.1038/s41558-020-0891-0.

[3] A. V. Agrawal, R. Kumar, G. Yang, J. Bao, M. Kumar, M. Kumar, Enhanced adsorption sites in monolayer MoS2 pyramid structures for highly sensitive and fast hydrogen sensor, Int. J. Hydrogen Energy. 45 (2020) 9268–9277. https://doi.org/10.1016/j.ijhydene.2020.01.119.

[4] A. V. Almaev, V.I. Nikolaev, N.N. Yakovlev, P.N. Butenko, S.I. Stepanov, A.I. Pechnikov, M.P. Scheglov, E. V. Chernikov, Hydrogen sensors based on Pt/α-Ga2O3:Sn/Pt structures, Sensors Actuators B Chem. 364 (2022) 131904. https://doi.org/10.1016/j.snb.2022.131904.

[5] A. Gurlo, Nanosensors: Towards morphological control of gas sensing activity. SnO2, In2O3, ZnO and WO3 case studies, Nanoscale. 3 (2011) 154–165. https://doi.org/10.1039/c0nr00560f.

[6] X. Liu, T. Ma, N. Pinna, J. Zhang, Two-Dimensional Nanostructured Materials for Gas Sensing, Adv. Funct. Mater. 27 (2017). https://doi.org/10.1002/adfm.201702168.

[7] M.H. Raza, K. Movlaee, S.G. Leonardi, N. Barsan, G. Neri, N. Pinna, Gas Sensing of NiO-SCCNT Core–Shell Heterostructures: Optimization by Radial Modulation of the Hole-Accumulation Layer, Adv. Funct. Mater. 30 (2020). https://doi.org/10.1002/adfm.201906874.

[8] J. Zhang, X. Liu, G. Neri, N. Pinna, Nanostructured Materials for Room-Temperature Gas Sensors, Adv. Mater. 28 (2016) 795–831. https://doi.org/10.1002/adma.201503825.

[9] H.D. Mai, S. Jeong, T.K. Nguyen, J.S. Youn, S. Ahn, C.M. Park, K.J. Jeon, Pd Nanocluster/Monolayer MoS2Heterojunctions for Light-Induced Room-Temperature Hydrogen Sensing, ACS Appl. Mater. Interfaces. 13 (2021) 14644–14652. https://doi.org/10.1021/acsami.0c20475.

[10] H.S.S. Ramakrishna Matte, A. Gomathi, A.K. Manna, D.J. Late, R. Datta, S.K. Pati,

C.N.R. Rao, MoS2 and WS2 analogues of graphene, Angew. Chemie - Int. Ed. 49 (2010) 4059–4062. https://doi.org/10.1002/anie.201000009.

[11] Y.-H. Lee, X.-Q. Zhang, W. Zhang, M.-T. Chang, C.-T. Lin, K.-D. Chang, Y.-C. Yu, J.T.-W. Wang, C.-S. Chang, L.-J. Li, T.-W. Lin, Synthesis of Large-Area MoS 2 Atomic Layers with Chemical Vapor Deposition, Adv. Mater. 24 (2012) 2320–2325. https://doi.org/10.1002/adma.201104798.

[12] W. Li, X. Geng, Y. Guo, J. Rong, Y. Gong, L. Wu, X. Zhang, P. Li, J. Xu, G. Cheng, M. Sun, L. Liu, Reduced graphene oxide electrically contacted graphene sensor for highly sensitive nitric oxide detection, ACS Nano. 5 (2011) 6955–6961. https://doi.org/10.1021/nn201433r.

[13] G. Lu, L.E. Ocola, J. Chen, Reduced graphene oxide for room-temperature gas sensors, Nanotechnology. 20 (2009) 445502. https://doi.org/10.1088/0957-4484/20/44/445502.

[14] A. Gutés, B. Hsia, A. Sussman, W. Mickelson, A. Zettl, C. Carraro, R. Maboudian, Graphene decoration with metal nanoparticles: Towards easy integration for sensing applications, Nanoscale. 4 (2012) 438–440. https://doi.org/10.1039/C1NR11537E.

[15] H. Hashtroudi, A. Yu, S. Juodkazis, M. Shafiei, Two-Dimensional Dy2O3-Pd-PDA/rGO Heterojunction Nanocomposite: Synergistic Effects of Hybridisation, UV Illumination and Relative Humidity on Hydrogen Gas Sensing, Chemosensors. 10 (2022). https://doi.org/10.3390/chemosensors10020078.

[16] A.K. Geim, K.S. Novoselov, The rise of graphene, Nat. Mater. 6 (2007) 183–191. https://doi.org/10.1038/nmat1849.

[17] B. Radisavljevic, A. Radenovic, J. Brivio, V. Giacometti, A. Kis, Single-layer MoS2 transistors, Nat. Nanotechnol. 6 (2011) 147–150. https://doi.org/10.1038/nnano.2010.279.

[18] D. Sarkar, X. Xie, J. Kang, H. Zhang, W. Liu, J. Navarrete, M. Moskovits, K. Banerjee, Functionalization of transition metal dichalcogenides with metallic nanoparticles: Implications for doping and gas-sensing, Nano Lett. 15 (2015) 2852–2862. https://doi.org/10.1021/nl504454u.

[19] X. Xie, D. Sarkar, W. Liu, J. Kang, O. Marinov, J. Deen, K. Banerjee, C. Engineering, S. Barbara, U. States, Low-Frequency Noise in Bilayer MoS 2, (2014) 5633–5640.

[20] M.D. Siao, W.C. Shen, R.S. Chen, Z.W. Chang, M.C. Shih, Y.P. Chiu, C.M. Cheng, Two-

dimensional electronic transport and surface electron accumulation in MoS2, Nat. Commun. 9 (2018). https://doi.org/10.1038/s41467-018-03824-6.

[21] L. Mennel, M.M. Furchi, S. Wachter, M. Paur, D.K. Polyushkin, T. Mueller, Optical imaging of strain in two-dimensional crystals, Nat. Commun. 9 (2018). https://doi.org/10.1038/s41467-018-02830-y.

[22] G. Eda, H. Yamaguchi, D. Voiry, T. Fujita, M. Chen, M. Chhowalla, Photoluminescence from chemically exfoliated MoS 2, Nano Lett. 11 (2011) 5111–5116. https://doi.org/10.1021/nl201874w.

[23] C. Winkler, S.S. Harivyasi, E. Zojer, Controlling the electronic properties of van der Waals heterostructures by applying electrostatic design, 2D Mater. 5 (2018). https://doi.org/10.1088/2053-1583/aabea6.

[24] F. Liao, Z. Guo, Y. Wang, Y. Xie, S. Zhang, Y. Sheng, H. Tang, Z. Xu, A. Riaud, P. Zhou, J. Wan, M.S. Fuhrer, X. Jiang, D.W. Zhang, Y. Chai, W. Bao, High-performance logic and memory devices based on a dual-gated MoS2 architecture, ACS Appl. Electron. Mater. 2 (2020) 111–119. https://doi.org/10.1021/acsaelm.9b00628.

[25] S.H. Yu, Y. Lee, S.K. Jang, J. Kang, J. Jeon, C. Lee, J.Y. Lee, H. Kim, E. Hwang, S. Lee, J.H. Cho, Dye-sensitized MoS2 photodetector with enhanced spectral photoresponse, ACS Nano. 8 (2014) 8285–8291. https://doi.org/10.1021/nn502715h.

[26] L.Y. Gan, Q. Zhang, Y. Cheng, U. Schwingenschlögl, Photovoltaic heterojunctions of fullerenes with MoS2 and WS 2 monolayers, J. Phys. Chem. Lett. 5 (2014) 1445–1449. https://doi.org/10.1021/jz500344s.

[27] C. Kuru, C. Choi, A. Kargar, D. Choi, Y.J. Kim, C.H. Liu, S. Yavuz, S. Jin, MoS2 Nanosheet–Pd Nanoparticle Composite for Highly Sensitive Room Temperature Detection of Hydrogen, Adv. Sci. 2 (2015) 1–5. https://doi.org/10.1002/advs.201500004.

[28] H. Tabata, H. Matsuyama, T. Goto, O. Kubo, M. Katayama, Visible-Light-Activated Response Originating from Carrier-Mobility Modulation of NO2Gas Sensors Based on MoS2Monolayers, ACS Nano. 15 (2021) 2542–2553. https://doi.org/10.1021/acsnano.0c06996.

[29] J. Bai, Y. Shen, S. Zhao, Y. Chen, G. Li, C. Han, D. Wei, Z. Yuan, F. Meng, Flower-like MoS2 hierarchical architectures assembled by 2D nanosheets sensitized with SnO2

quantum dots for high-performance NH3 sensing at room temperature, Sensors Actuators B Chem. 353 (2022) 131191. https://doi.org/10.1016/J.SNB.2021.131191.

[30] S. Hou, R. Pang, S. Chang, L. Ye, J. Xu, X. Wang, Y. Zhang, Y. Shang, A. Cao, Synergistic CNFs/CoS2/MoS2Flexible Films with Unprecedented Selectivity for NO Gas at Room Temperature, ACS Appl. Mater. Interfaces. 12 (2020) 29778–29786. https://doi.org/10.1021/acsami.0c05953.

[31] K. Lee, R. Gatensby, N. McEvoy, T. Hallam, G.S. Duesberg, High-Performance Sensors Based on Molybdenum Disulfide Thin Films, Adv. Mater. 25 (2013) 6699–6702. https://doi.org/10.1002/adma.201303230.

[32] B. Liu, L. Chen, G. Liu, A.N. Abbas, M. Fathi, C. Zhou, High-performance chemical sensing using Schottky-contacted chemical vapor deposition grown monolayer MoS2 transistors, ACS Nano. 8 (2014) 5304–5314. https://doi.org/10.1021/nn5015215.

[33] H. Li, Z. Yin, Q. He, H. Li, X. Huang, G. Lu, D.W.H. Fam, A.I.Y. Tok, Q. Zhang, H. Zhang, Fabrication of Single- and Multilayer MoS2 Film-Based Field-Effect Transistors for Sensing NO at Room Temperature, Small. 8 (2012) 63–67. https://doi.org/10.1002/smll.201101016.

[34] Q. Zhou, C. Hong, Y. Yao, S. Hussain, L. Xu, Q. Zhang, Y. Gui, M. Wang, Hierarchically MoS2 nanospheres assembled from nanosheets for superior CO gas-sensing properties, Mater. Res. Bull. 101 (2018) 132–139. https://doi.org/10.1016/j.materresbull.2018.01.030.

[35] F. Ozaki, S. Tanaka, W. Osada, K. Mukai, M. Horio, T. Koitaya, S. Yamamoto, I. Matsuda, J. Yoshinobu, Functionalization of the MoS2 basal plane for activation of molecular hydrogen by Pd deposition, Appl. Surf. Sci. 593 (2022) 153313. https://doi.org/10.1016/j.apsusc.2022.153313.

[36] A. Alagh, F.E. Annanouch, P. Umek, C. Bittencourt, J.F. Colomer, E. Llobet, An Ultrasensitive Room-Temperature HS Gas Sensor Based on 3D Assembly of CuO Decorated WS Nanomaterial, IEEE Sens. J. 21 (2021) 21212–21220. https://doi.org/10.1109/JSEN.2021.3103925.

[37] F.E. Annanouch, Z. Haddi, M. Ling, F. Di Maggio, S. Vallejos, T. Vilic, Y. Zhu, T. Shujah, P. Umek, C. Bittencourt, C. Blackman, E. Llobet, Aerosol-Assisted CVD-Grown PdO Nanoparticle-Decorated Tungsten Oxide Nanoneedles Extremely Sensitive

and Selective to Hydrogen, ACS Appl. Mater. Interfaces. 8 (2016). https://doi.org/10.1021/acsami.6b00773.

[38] D.-H. Baek, J. Kim, MoS 2 gas sensor functionalized by Pd for the detection of hydrogen, Sensors Actuators B Chem. 250 (2017) 686–691. https://doi.org/10.1016/j.snb.2017.05.028.

[39] S.R. Gottam, C.T. Tsai, L.W. Wang, C.T. Wang, C.C. Lin, S.Y. Chu, Highly sensitive hydrogen gas sensor based on a MoS2-Pt nanoparticle composite, Appl. Surf. Sci. 506 (2020). https://doi.org/10.1016/j.apsusc.2019.144981.

[40] K.M.B. Urs, N.K. Katiyar, R. Kumar, K. Biswas, A.K. Singh, C.S. Tiwary, V. Kamble, Multi-component (Ag-Au-Cu-Pd-Pt) alloy nanoparticle-decorated p-type 2D-molybdenum disulfide (MoS2) for enhanced hydrogen sensing, Nanoscale. 12 (2020) 11830–11841. https://doi.org/10.1039/d0nr02177f.

[41] J.H. Lee, A. Mirzaei, J.Y. Kim, J.H. Kim, H.W. Kim, S.S. Kim, Optimization of the surface coverage of metal nanoparticles on nanowires gas sensors to achieve the optimal sensing performance, Sensors Actuators, B Chem. 302 (2020). https://doi.org/10.1016/j.snb.2019.127196.

[42] J.S. Lee, A. Katoch, J.H. Kim, S.S. Kim, Effect of Au nanoparticle size on the gas-sensing performance of p-CuO nanowires, Sensors Actuators, B Chem. 222 (2016) 307–314. https://doi.org/10.1016/j.snb.2015.08.037.

[43] S.S. Kim, J.Y. Park, S.W. Choi, H.S. Kim, H.G. Na, J.C. Yang, C. Lee, H.W. Kim, Room temperature sensing properties of networked GaN nanowire sensors to hydrogen enhanced by the Ga2Pd5 nanodot functionalization, Int. J. Hydrogen Energy. 36 (2011) 2313–2319. https://doi.org/10.1016/J.IJHYDENE.2010.11.050.

[44] M. Stolze, D. Gogova, L.-K. Thomas, Analogy for the maximum obtainable colouration between electrochromic, gasochromic, and electrocolouration in DC-sputtered thin WO3−y films, Thin Solid Films. 476 (2005) 185–189. https://doi.org/10.1016/j.tsf.2004.09.034.

[45] I.S. Hwang, J.K. Choi, H.S. Woo, S.J. Kim, S.Y. Jung, T.Y. Seong, I.D. Kim, J.H. Lee, Facile control of C2H5OH sensing characteristics by decorating discrete Ag nanoclusters on SnO2 nanowire networks, ACS Appl. Mater. Interfaces. 3 (2011) 3140–3145. https://doi.org/10.1021/am200647f.

[46] D.J. Late, Y.K. Huang, B. Liu, J. Acharya, S.N. Shirodkar, J. Luo, A. Yan, D. Charles, U. V. Waghmare, V.P. Dravid, C.N.R. Rao, Sensing behavior of atomically thin-layered MoS2 transistors, ACS Nano. 7 (2013) 4879–4891. https://doi.org/10.1021/nn400026u.

[47] T.H. Eom, S.H. Cho, J.M. Suh, T. Kim, T.H. Lee, S.E. Jun, J.W. Yang, J. Lee, S.H. Hong, H.W. Jang, Substantially improved room temperature NO2sensing in 2-dimensional SnS2nanoflowers enabled by visible light illumination, J. Mater. Chem. A. 9 (2021) 11168–11178. https://doi.org/10.1039/d1ta00953b.

[48] J. Park, J. Mun, J.S. Shin, S.W. Kang, Highly sensitive two dimensional MoS2 gas sensor decorated with Pt nanoparticles, R. Soc. Open Sci. 5 (2018) 1–9. https://doi.org/10.1098/rsos.181462.

[49] J.M. Suh, Y.S. Shim, K.C. Kwon, J.M. Jeon, T.H. Lee, M. Shokouhimehr, H.W. Jang, Pd- and Au-Decorated MoS2 Gas Sensors for Enhanced Selectivity, Electron. Mater. Lett. 15 (2019) 368–376. https://doi.org/10.1007/s13391-019-00128-9.

[50] D. Burman, H. Raha, B. Manna, P. Pramanik, P.K. Guha, Substitutional Doping of MoS 2 for Superior Gas-Sensing Applications: A Proof of Concept, ACS Sensors. 6 (2021) 3398–3408. https://doi.org/10.1021/acssensors.1c01258.

[51] X. Huang, Z. Zeng, S. Bao, M. Wang, X. Qi, Z. Fan, H. Zhang, Solution-phase epitaxial growth of noble metal nanostructures on dispersible single-layer molybdenum disulfide nanosheets, Nat. Commun. 4 (2013) 1444–1448. https://doi.org/10.1038/ncomms2472.

[52] T. Kim, T.H. Lee, S.Y. Park, T.H. Eom, I. Cho, Y. Kim, C. Kim, S.A. Lee, M.J. Choi, J.M. Suh, I.S. Hwang, D. Lee, I. Park, H.W. Jang, Drastic Gas Sensing Selectivity in 2-Dimensional MoS2 Nanoflakes by Noble Metal Decoration, ACS Nano. 17 (2023) 4404–4413. https://doi.org/10.1021/acsnano.2c09733.

[53] S. Lee, Y. Kang, J. Lee, J. Kim, J.W. Shin, S. Sim, D. Go, E. Jo, S. Kye, J. Kim, J. An, Atomic layer deposited Pt nanoparticles on functionalized MoS2 as highly sensitive H2 sensor, Appl. Surf. Sci. 571 (2022). https://doi.org/10.1016/j.apsusc.2021.151256.

[54] A. Alagh, F.E. Annanouch, K. Al Youssef, C. Bittencourt, F. Güell, P.R. Martínez-Alanis, M. Reguant, E. Llobet, PdO and PtO loaded WS2 boosts NO2 gas sensing characteristics at room temperature, Sensors Actuators B Chem. 364 (2022). https://doi.org/10.1016/j.snb.2022.131905.

[55] A. Alagh, F.E. Annanouch, P. Umek, C. Bittencourt, A. Sierra-Castillo, E. Haye, J.F.

Colomer, E. Llobet, CVD growth of self-assembled 2D and 1D WS2 nanomaterials for the ultrasensitive detection of NO2, Sensors Actuators, B Chem. 326 (2021) 128813. https://doi.org/10.1016/j.snb.2020.128813.

[56] S. Li, S. Wang, M.M. Salamone, A.W. Robertson, S. Nayak, H. Kim, S.C.E. Tsang, M. Pasta, J.H. Warner, Edge-Enriched 2D MoS2 Thin Films Grown by Chemical Vapor Deposition for Enhanced Catalytic Performance, ACS Catal. 7 (2017) 877–886. https://doi.org/10.1021/acscatal.6b02663.

[57] K. Shomalian, M.M. Bagheri-Mohagheghi, M. Ardyanian, Characterization and study of reduction and sulfurization processing in phase transition from molybdenum oxide (MoO2) to molybdenum disulfide (MoS2) chalcogenide semiconductor nanoparticles prepared by one-stage chemical reduction method, Appl. Phys. A Mater. Sci. Process. 123 (2017) 1–9. https://doi.org/10.1007/s00339-016-0719-y.

[58] V. Ramakrishnan, C. Alex, A.N. Nair, N.S. John, Designing Metallic MoO2 Nanostructures on Rigid Substrates for Electrochemical Water Activation, Chem. - A Eur. J. 24 (2018) 18003–18011. https://doi.org/10.1002/chem.201803570.

[59] C. Lee, H. Yan, L.E. Brus, T.F. Heinz, J. Hone, S. Ryu, Anomalous lattice vibrations of single- and few-layer MoS2, ACS Nano. 4 (2010) 2695–2700. https://doi.org/10.1021/nn1003937.

[60] F.E. Annanouch, A. Alagh, P. Umek, J. Casanova-Chafer, C. Bittencourt, E. Llobet, Controlled growth of 3D assemblies of edge enriched multilayer MoS2 nanosheets for dually selective NH3 and NO2 gas sensors, J. Mater. Chem. C. 10 (2022) 11027–11039. https://doi.org/10.1039/d2tc00759b.

[61] M. Bendahan, J. Guérin, R. Boulmani, K. Aguir, WO3 sensor response according to operating temperature: Experiment and modeling, Sensors Actuators B Chem. 124 (2007) 24–29. https://doi.org/10.1016/J.SNB.2006.11.036.

[62] S. Park, A.T. Garcia-Esparza, H. Abroshan, B. Abraham, J. Vinson, A. Gallo, D. Nordlund, J. Park, T.R. Kim, L. Vallez, R. Alonso-Mori, D. Sokaras, X. Zheng, Operando Study of Thermal Oxidation of Monolayer MoS2, Adv. Sci. 8 (2021) 1–8. https://doi.org/10.1002/advs.202002768.

[63] C.H. Park, W.T. Koo, Y.J. Lee, Y.H. Kim, J. Lee, J.S. Jang, H. Yun, I.D. Kim, B.J. Kim, Hydrogen Sensors Based on MoS2Hollow Architectures Assembled by Pickering

Emulsion, ACS Nano. 14 (2020) 9652–9661. https://doi.org/10.1021/acsnano.0c00821.

[64] E. Kowalska, E. Czerwosz, R. Diduszko, A. Kaminska, M. Danila, Influence of PdHx formation ability on hydrogen sensing properties of palladium-carbonaceous films, Sensors Actuators, A Phys. 203 (2013) 434–440. https://doi.org/10.1016/j.sna.2013.06.026.

[65] Z. Huang, W. Luo, L. Ma, M. Yu, X. Ren, M. He, S. Polen, K. Click, B. Garrett, J. Lu, K. Amine, C. Hadad, W. Chen, A. Asthagiri, Y. Wu, Dimeric [Mo2S12]2- Cluster: A Molecular Analogue of MoS2 Edges for Superior Hydrogen-Evolution Electrocatalysis, Angew. Chemie - Int. Ed. 54 (2015) 15181–15185. https://doi.org/10.1002/anie.201507529.

[66] X. Tang, P.A. Haddad, N. Mager, X. Geng, N. Reckinger, S. Hermans, M. Debliquy, J.P. Raskin, Chemically deposited palladium nanoparticles on graphene for hydrogen sensor applications, Sci. Rep. 9 (2019) 1–11. https://doi.org/10.1038/s41598-019-40257-7.

[67] J. Jaiswal, P. Tiwari, P. Singh, R. Chandra, Fabrication of highly responsive room temperature H2 sensor based on vertically aligned edge-oriented MoS2 nanostructured thin film functionalized by Pd nanoparticles, Sensors Actuators B Chem. 325 (2020) 128800. https://doi.org/10.1016/J.SNB.2020.128800.

[68] N. Matsunaga, G. Sakai, K. Shimanoe, N. Yamazoe, Diffusion equation-based study of thin film semiconductor gas sensor-response transient, Sensors Actuators, B Chem. 83 (2002) 216–221. https://doi.org/10.1016/S0925-4005(01)01043-7.

[69] N. Matsunaga, G. Sakai, K. Shimanoe, N. Yamazoe, Formulation of gas diffusion dynamics for thin film semiconductor gas sensor based on simple reaction-diffusion equation, Sensors Actuators, B Chem. 96 (2003) 226–233. https://doi.org/10.1016/S0925-4005(03)00529-X.

[70] S. Suresh, K.M.B. Urs, A.T. Vasudevan, S. Sriram, V.B. Kamble, Analysis of Unusual and Instantaneous Overshoot of Response Transients in Gas Sensors, Phys. Status Solidi - Rapid Res. Lett. 13 (2019) 1–7. https://doi.org/10.1002/pssr.201800683.

[71] I. Darmadi, F.A.A. Nugroho, C. Langhammer, High-Performance Nanostructured Palladium-Based Hydrogen Sensors - Current Limitations and Strategies for Their Mitigation, ACS Sensors. 5 (2020) 3306–3327. https://doi.org/10.1021/acssensors.0c02019.

[72] J. Wang, Y. Yang, Y. Xia, Mesoporous MXene/ZnO nanorod hybrids of high surface area for UV-activated NO2 gas sensing in ppb-level, Sensors Actuators B Chem. 353 (2022) 131087. https://doi.org/10.1016/J.SNB.2021.131087.

[73] N. Barsan, U. Weimar, Understanding the fundamental principles of metal oxide based gas sensors; the example of CO sensing with SnO 2 sensors in the presence of humidity, J. Phys. Condens. Matter. 15 (2003) R813–R839. https://doi.org/10.1088/0953-8984/15/20/201.

[74] H. Hashtroudi, P. Atkin, I.D.R. Mackinnon, M. Shafiei, Low-operating temperature resistive nanostructured hydrogen sensors, Int. J. Hydrogen Energy. 44 (2019) 26646–26664. https://doi.org/10.1016/J.IJHYDENE.2019.08.128.

[75] A. Mirzaei, H.R. Yousefi, F. Falsafi, M. Bonyani, J.H. Lee, J.H. Kim, H.W. Kim, S.S. Kim, An overview on how Pd on resistive-based nanomaterial gas sensors can enhance response toward hydrogen gas, Int. J. Hydrogen Energy. 44 (2019) 20552–20571. https://doi.org/10.1016/j.ijhydene.2019.05.180.

[76] L. Chacko, E. Massera, P.M. Aneesh, Enhancement in the Selectivity and Sensitivity of Ni and Pd Functionalized MoS 2 Toxic Gas Sensors , J. Electrochem. Soc. 167 (2020) 106506. https://doi.org/10.1149/1945-7111/ab992c.

[77] Y. Asakuma, S. Miyauchi, T. Yamamoto, H. Aoki, T. Miura, Numerical analysis of absorbing and desorbing mechanism for the metal hydride by homogenization method, Int. J. Hydrogen Energy. 28 (2003) 529–536. https://doi.org/10.1016/S0360-3199(02)00136-2.

CHAPTER 7

Fabrication of plate shaped ZnO-based piezoelectric nanogenerators on flexible substrates

Fabrication of plate shaped ZnO-based piezoelectric nanogenerators on flexible substrates

Shuja Bashir Malik[1], Carolina Silva[2], Mariana Rocha[2], Ana Pires[2], André Pereira[3], Eduard Llobet[1]

1 Universitat Rovira i Virgili, MINOS, Països Catalans 26, 43007 Tarragona, Catalunya, Spain.

2 IFIMUP—Instituto de Física de Materiais Avançados, Nanotecnologia e Fotónica, Departamento de Física e Astronomia, Faculdade de Ciências, Universidade do Porto, Rua do Campo Alegre s/n, 4169-007 Porto, Portugal.

Abstract

With the internet of things (IoTs) at its peak, wearable electronics and sensors all around us, there is a need of a sustainable, renewable, and green energy. Piezoelectric nanogenerators (PENGs) are booming as a solution for providing an efficient source for green energy. In this work, ZnO was synthesized via a facile coprecipitation method with high yield (~1.7 g). Two reaction conditions were used: one with 12 ml NaOH and other with 30 ml NaOH. PENGs were fabricated on commercial PET substrates by screenprinting ZnO-H_3PO_4:PVA ink composite as a working piezoelectric active layer and commercial silver ink for electrodes. The curing temperature for ZnO inks and silver electrode inks was low (50ºC), which makes it possible to use low-cost polymer substrates for PENG fabrication. The maximum output voltage obtained was 760 mV and 1500 mV for 12 ml NaOH and 30 ml NaOH reaction conditions respectively. The maximum power output recorded was 450µW/m^2 in PENG fabricated using ZnO synthesized using 30 ml NaOH. It was also found that because of the presence of H_3PO_4 in the polymer, around 50% of the ZnO reacts to form hopeite ($Zn_3(PO_4)_2.4H_2O$).

7.1. Introduction

Depletion of fossil fuel reserves and increase in the levels of greenhouse gases has led to an eager search for alternate sources of energy. Now a days a tremendous focus is on the sustainable harvesting of renewable sources of energy like solar energy, wind energy, bioenergy, kinetic energy, and tidal energy. However, these sources of renewable energies are greatly affected by environmental factors and not always financially viable to harvest.

Advancement in the field of nanotechnology led to harvesting mechanical energy with the help piezoelectric nanogenerators (PENGs). One of the main sources of these mechanical energies into consideration is human body movements among others like pulsation, airflow. This paves a way for wearable and flexible electronics [1]. Polymers and polymer composites are a popular choice for wearable electronics owing to their flexibility, cost effectiveness and relatively large piezoelectric coefficient [1]. Piezoelectric materials when deformed by external force develop piezoelectric potentials [2]. When connected to an external load, electrical current will flow in the circuit and continues to flow till the mechanical energy is sustained. Piezoelectric effect is found in some natural substances like topaz, quartz, and Rochelle salt. Some piezoelectric materials have been synthesized like lead zirconate titanate; PZT ($Pb(Zr_xTi_{1-x})O_3$) [3,4], barium titanate [5], aluminum nitride (AIN) [6], polyvinylidene fluoride (PVDF) [7] and zinc oxide (ZnO) [8–10]. The main drawback associated with PZT is the toxicity of the lead, thus limiting its usage and demanding lead free, non-toxic, cheap and environment friendly piezoelectric materials such as zinc oxide (ZnO).

Owing to the wide band gap and Schottky barrier height (SBH) of ZnO; a wurtzite semiconductor with non-centrosymmetric crystal structure, it exhibits piezotronics effect [11]. The working principle of piezotronics is governed by the change in SBH in response to external force [12]. Low piezoelectric coefficient (d_{33} = 12.4 pm/V) [13] of ZnO as compared to poly (1,1 difluoroethylene) with d_{33} = 33 pm/V) [11] limits ZnO piezotronics. Piezoelectricity of a material is dependent on its structure [14]. On application of external mechanical force on ZnO, its surface gets polarized due to its non-centrosymmetric structure. Zn^{2+} gets accumulated on one side and O^{2-} on other side of the surface, generating a potential difference causing flow of current [14,15]. However, a complex process is required to fabricate ZnO based nanogenerators which at the end exhibit low output power [16]. To overcome these challenges, one of the strategies devised is to combine ZnO nanomaterials with piezoelectric polymer forming piezoelectric composite [1,16–18]. Piezoelectric phase is increased in the polymer by the introduction of the ZnO nanomaterial forming a composite. The use of piezoelectric composite improves the energy conversion performance of the nanogenerators remarkably. An alternate current is produced by the nanogenerators based on ZnO/piezoelectric polymer because of the production of opposite charges on the surface of the polymer during deformation and recovery process [19]. In order to achieve DC output, fabrication of ZnO-metal Schottky contact is essential [1]. The key to achieve a high-performance DC piezoelectric nanogenerator is to prepare ZnO nanowire/nanorod arrays with controllable c-axis orientation and Schottky contact

[16]. The remarkable piezoelectric properties of ZnO and other synthesized piezoelectric materials has led to an insatiable quest for improving the overall piezoelectric properties of the materials and piezoelectric devices.

As on end of 2021, using Boolean keyword search like piezoelectric, nanogenerators and ZnO yields a result of total 2087 research items since 2006 on Web of Science, of which, 586 pertain to use of ZnO as piezoelectric material. The trend clearly shows a significant interest towards the self-powered nanogenerators by the scientific community. With the report of first nanogenerator in 2006, there has been a boom in the research in the field with a considerable progress in the piezoelectric output. This led to a wide range of applications of PENGs from powering LEDs [9,20], self-power mechanical sensors [21], FET [22], wearable electronics [9], piezoelectric biosensors [23], and sensors [24]. Figure 7.1 depicts the trend of the progress in the research of overall piezoelectric nanogenerators and ZnO as piezoelectric material for nanogenerators.

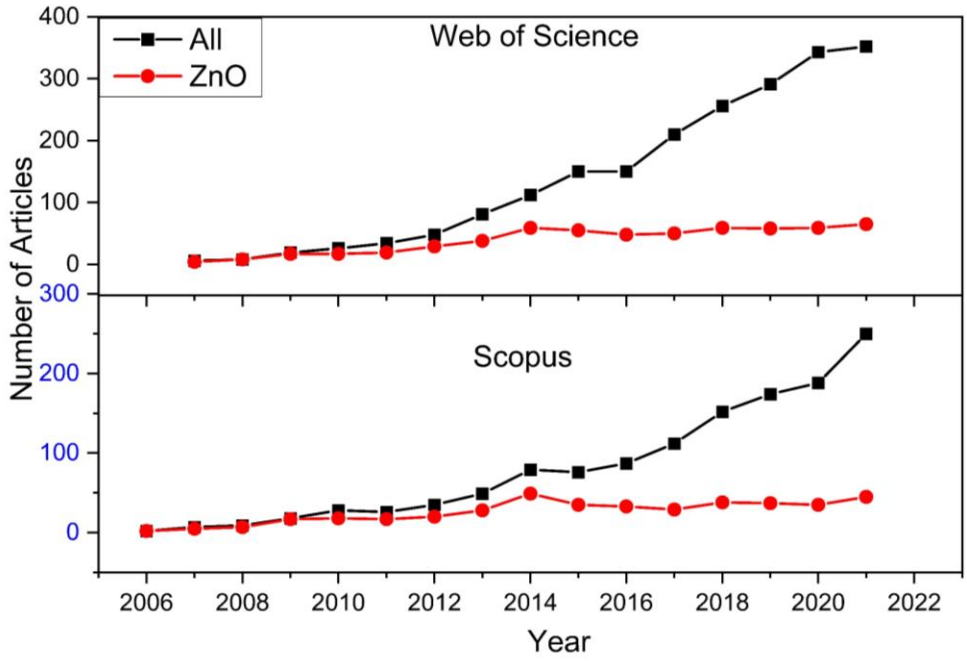

Figure 7.1 Trend showing the number of research articles related to piezoelectric nanogenerators (PENGs) published since 2006. Source: Scopus and Web of Science

In this research, we fabricated ZnO-PVA composite on flexible PET substrates via screenprinting to evaluate the piezoelectric characteristics of ZnO. The aim of the research work was to devise a facile ZnO synthesis method and cost-effective PENG device fabrication method for energy harvesting and sensor applications. The results mentioned in the research work pertain to the optimized PENGs with highest output. PENGs with a maximum output

voltage of 760 mV in case of 12 ml NaOH reaction conditions and 1500 mV in case of 30 ml NaOH reaction conditions were fabricated with a maximum output current of 25 nA in both the cases. The maximum power output of 450 $\mu W/m^2$ was recorded in case of 30 ml NaOH reaction conditions.

7.1.1. Motivation

Increase in the energy demand has led to search of alternative sources of energy over the conventional ones. One of the hot topics which is being explored in the energy harvesting field is scavenging the mechanical energy. Advancement in the internet of things (IoT) and sensors technology pushed this research further. Now a days, there is a high demand for integration of electronic technology into flexible and wearable devices. Human bodies consist of various energies like chemical, thermal and mechanical energy. Among these, the most plentiful is the mechanical energy. To power the wearable electronics and flexible sensors for long-term, continuous, and individual monitoring, the harvesting of the mechanical energy of our bodies is proving prosperous and fruitful. The idea behind this concept is to convert the mechanical energy of the body into electrical energy. Traditional energy harvesters are bulky and inefficient to convert small mechanical energy into considerable electrical energy outputs. The solution thus is smart, light weighted and intelligent energy harvesters. Nanogenerators (NG) are a solution to this. The first nanogenerator was designed in 2006 and has made a significant progress since in terms of output and overall quality. Nanogenerators are typically of two types; a) Piezoelectric nanogenerators (PENGs) and Triboelectric nanogenerators (TENGs)[25].

This research work was designed to fabricate a cost effective, efficient, and biocompatible flexible nanogenerators to harvest mechanical energies for various applications including sensors.

7.2. Experimental

7.2.1. Materials

Zinc acetate dihydrate ($Zn(CH_3COO).2H_2O$) from Panreac, Spain (99.5%) was used as a precursor. Sodium hydroxide (NaOH) pellets from Labchem, Portugal (98.6%) were used in this work. The organic polymer, PVA was purchased from Sigma Aldrich and orthophosphoric acid was purchased from Fisher Chemicals. Sylgard^{TM} Silicone Elastomer kit was purchased from DOW. All the chemicals used in this work were directly used without any purification.

7.2.2. Synthesis of ZnO

Coprecipitation method was used to prepare zinc oxide nanomaterials previously reported by M.M. Maia [26]. A 0.27 M solution of $Zn(CH_3COO).2H_2O$ was prepared in deionized water. A specific volume; 30 ml and 12 ml of 1.2 M solution of NaOH (pH=14) was added drop wise into the zinc acetate solution under vigorous stirring. As soon as the NaOH solution is dropped, white precipitate starts to form. In both the reaction setups, everything except the volume of the NaOH was kept same. The solution was washed with deionized water till pH reaches 7. The washing was done by centrifugation at 10,000 RPM of 5-minute cycles. Finally, the product was dried at 80ºC overnight to obtain ZnO powder. The dried powder was ground gently into fine powder using a ceramic mortar-pistil. Possible chemical reactions involved are [26,27]:

$$Zn(CH_3COO)_2.2H_2O_{(aq)} + 2NaOH_{(aq)} \rightarrow Zn(OH)_{2\,(s)} + 2CH_3COONa_{(s)} + 2H_2O_{(l)}$$

Equation 1

$$Zn(OH)_2 + 2H_2O = Zn^{2+} + 2OH^- + 2H_2O = [Zn(OH)_4]^2 \qquad \text{Equation 2}$$

$$[Zn(OH)_4]^2 \leftrightarrow ZnO_2^{2-} + 2H_2O \qquad \text{Equation 3}$$

$$ZnO_2^{2-} + 2H_2O \leftrightarrow ZnO + 2OH^- \qquad \text{Equation 4}$$

7.2.3. ZnO inks

ZnO inks were formulated by trying different ratios of ZnO and polymer. The polymer is a mixture of Polyvinyl alcohol (PVA) and phosphoric acid (H_3PO_4). The PVA solution was solubilized in H_3PO_4 aqueous solution in a 1:1 weight ratio. The mixture was incubated at 90ºC for 12 hours under continuous stirring. Different ratios of ZnO-PVA were tried, however, the optimum ratio of ZnO-PVA was found to be 45:55, best suited for fabricating ZnO thin films by screen printing.

7.2.4. ZnO Thin films deposition

ZnO thin films were fabricated using screen printing technique. A known amount of ZnO-PVA (ZnO:PVA::45:55) was mixed and spread onto the screen for printing. The squeegee was passed once to form a very thin layer of ZnO-PVA onto the PET substrate. The film was dried at 50ºC, mesh cleaned with DI water and dried with a hot blow drier. A second layer of the ZnO-PVA was printed same as in step one and dried in oven again at 50ºC. The thin films were dried at low temperature to make sure there are no cracks in the final film as in Figure 7.2 (b).

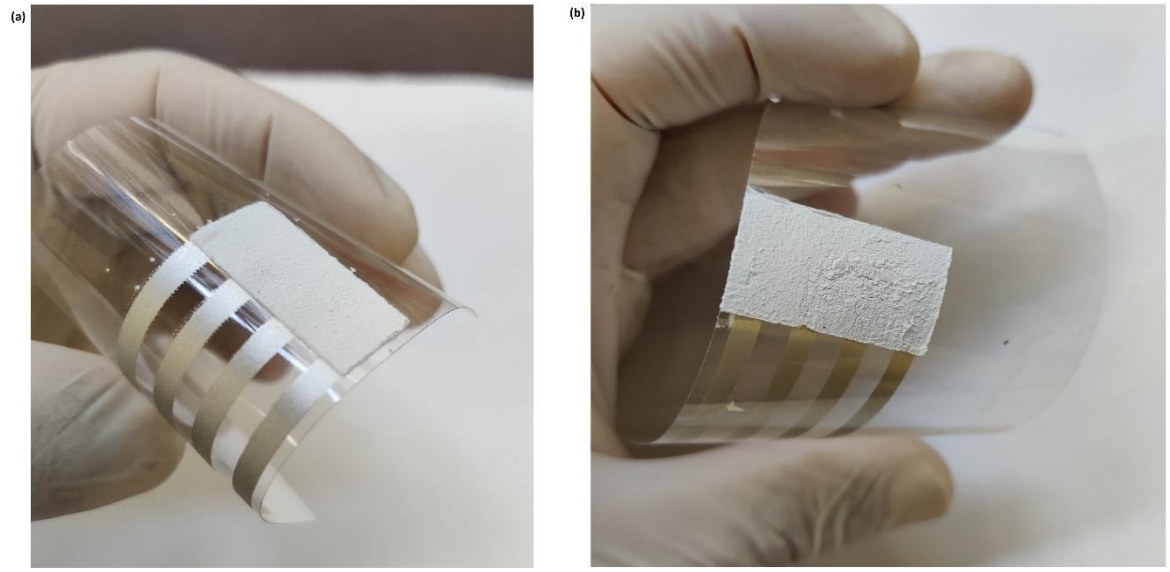

Figure 7.2 Comparison of curing ZnO-PVA ink at, (a) 50ºC and (b) 130ºC. At temperatures higher than 50ºC, ZnO-PVA thin films develop cracks

In case of fabricating pristine PVA films, stencil printing technique was used as it was found that the PVA films fabricated by screen printing were not continuous as in Figure 7.3. Within the yellow rectangle is the magnified silver-ink screen printed electrode. The other part of the picture in red rectangle shows the screen printed PVA. It was found that the film is not continuous but screen mesh shaped structures.

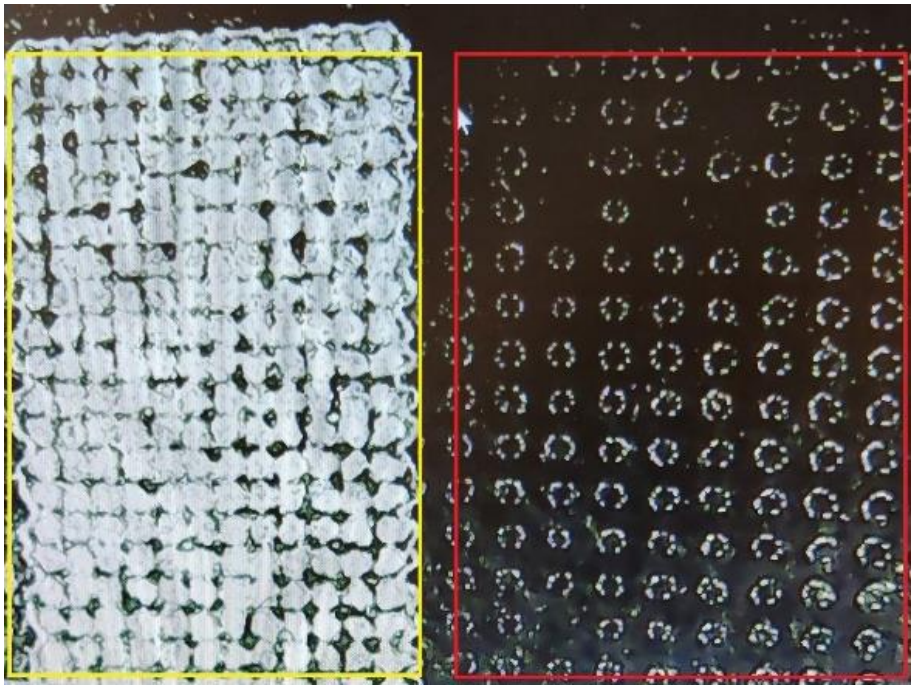

Figure 7.3 Magnified view of screen printed PVA, red rectangle: PVA and yellow rectangle: silver electrode.

7.2.5. PENG Fabrication

The PENG devices were fabricated on commercial PET (polyethylene terephthalate) substrates. A typical schematic and an image of a fabricated PENG is shown in Figure 7.4 (a). Bottom electrodes were screen printed onto the PET substrates using commercial silver ink. The electrodes were cured in an oven at 130ºC. After curing the electrodes, ZnO-PVA thin films were screen printed on to the electrodes as shown in Figure 7.4 (b). The ZnO-PVA thin film was cured at 50ºC. Top electrodes were screen printed on to the ZnO-PVA thin film to complete the PENG. The top electrodes were cured at 50ºC, not at 130ºC to avoid cracks in ZnO-PVA film as in Figure 7.2 (b). Figure 7.5 depicts a fabricated PENG with copper tape to connect the electrodes, wires were soldered to the device to connect to the measurement instrument.

Figure 7.4 (a): Schematic of ZnO PENG, (b): ZnO-PVA screen printed thin film with commercial silver ink busbar electrodes on PET substrate

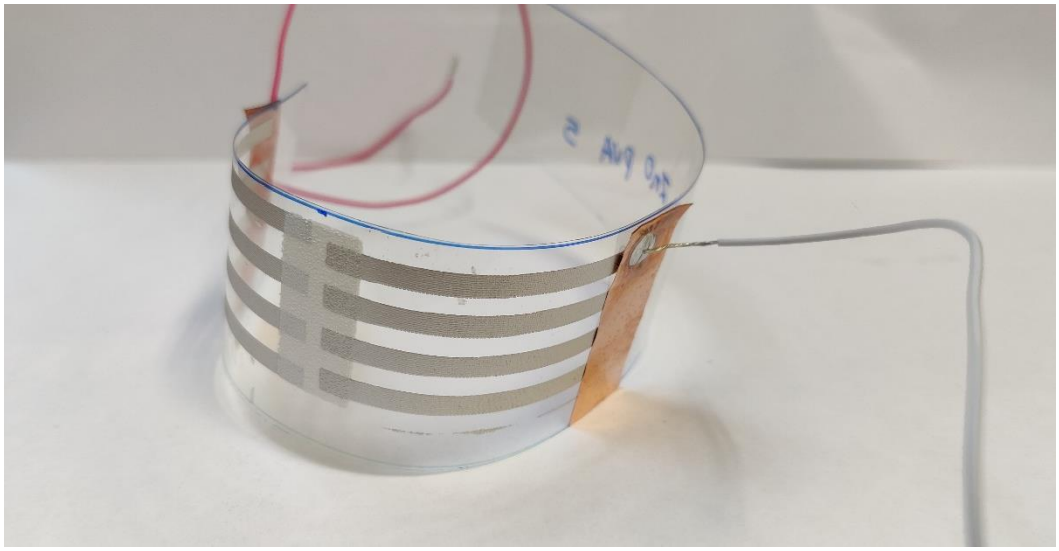

Figure 7.5 Image of a fabricated PENG.

7.2.6. Characterization

Microstructure of the materials was characterized using Field Emission Scanning Electron Microscope (FESEM) (Thermo Fisher Scios 2). Crystallographic and phase studies were done using X-ray diffraction of SmartLab Rigaku diffractometer at room temperature over a range

of 5º to 90º for samples containing polymers and 20º to 90º for zinc oxide samples using Cu K-alpha radiation with wavelength 1.540593 angstroms (current of 200mA and a voltage of 45KV). The thickness measurements were carried out using manual instrument from Mitutoyo. The resistance measurements were calculated using Keithley 487 Picoammeter/voltage source. DLS and Zeta potential measurements were carried out using Zetasizer. The resistance measurements were calculated using Keithley 487 Picoammeter/voltage source. The ZnO-PVA layer with an average thickness of 131 µm has a resistance of 0.1 tera ohms. Impedance and capacitance measurements were carried out using Wayne Kerr Precision Component Analyzer 6440B. The capacitance and impedance measurements were taken as a function of frequency.

7.3. Results and discussion

Figure 7.4 (a) shows a schematic diagram of the piezoelectric nanogenerator (PENG) based on ZnO-PVA. A compression force at one cycle per second was applied to the device. When the force is applied to the device, the mechanical energy is converted into electrical energy. The piezoelectric layer in this research work is ZnO-PVA film. Screen printed silver busbars act as top and bottom electrode of the device.

Figure 7.6 (a and b) demonstrate the microstructure of the ZnO nanoparticles synthesized by coprecipitation method. FESEM images reveal the structure of the ZnO structures to be nano plates. The microstructures have approximately uniform morphologies and dimensions consisting of several plates aggregated together. The thickness of the plates varies from 6 nm to 30 nm in both the cases of 12 ml NaOH and 30 ml NaOH reaction conditions. This type of growth is called coalescence [26] of the grains which results in the formation of plate like structures. The EDX spectrum in Figure 7.7 (a) and (b) of the nanostructures reveals that the nanostructures consist of a majority elements of Zn and O. Peaks pertaining to carbon are from the carbon tape used to study the FESEM and EDX of the samples. No other peaks pertaining to any other elements are found, depicting that the sample is pure and free of any impurities.

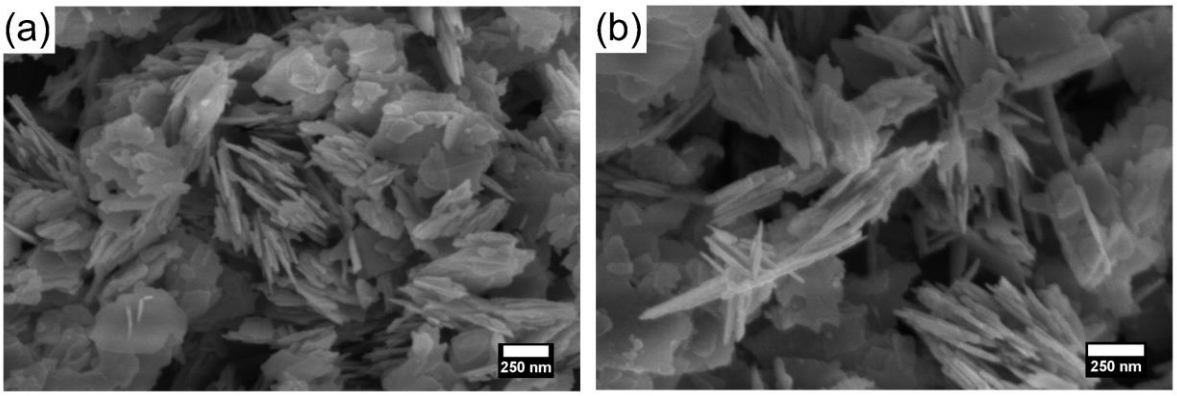

Figure 7.6 FESEM images of ZnO synthesized using (a) 12ml and (b) 30ml NaOH

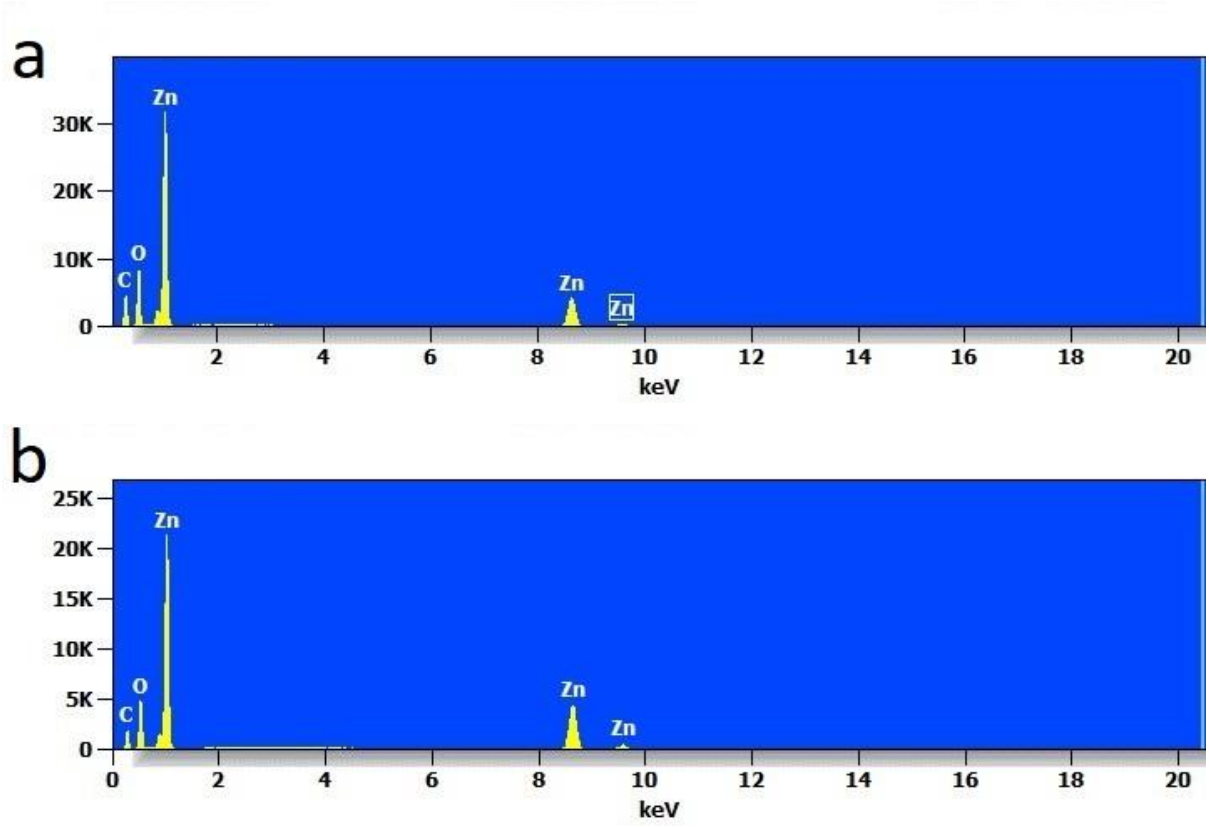

Figure 7.7 EDX spectrum of ZnO. (a) ZnO synthesized using 12ml NaOH (b) ZnO synthesized using 30ml NaOH

The crystal structure of the ZnO nanostructures were analyzed by XRD diffraction. The XRD pattern of ZnO nanostructures is shown is Figure 7.8 (a). The diffraction patterns are indexed to hexagonal wurtzite ZnO phase in accordance with ICSD collection code 086254. The hexagonal crystal structure matches the space group of P63mc with lattice constants a= 3.25300 Å and c= 5.21300 Å. The sharp peaks show a good crystallinity, and no other peak was found, thus indicating no other phases or impurities are present. The average crystallite sizes were calculated using Scherer's formula and were found to be 24 nm for both 12 ml NaOH and 30 ml NaOH volume ZnO. When ZnO was mixed with H_3PO_4 doped PVA, some of the ZnO reacts

with H_3PO_4 and converts to zinc phosphate (Hopeite) as demonstrated by XRD pattern in Figure 7.8 (b). The highest intensity peak is indexed to PVA. Peaks indexed to silver are from the screen-printed silver electrodes.

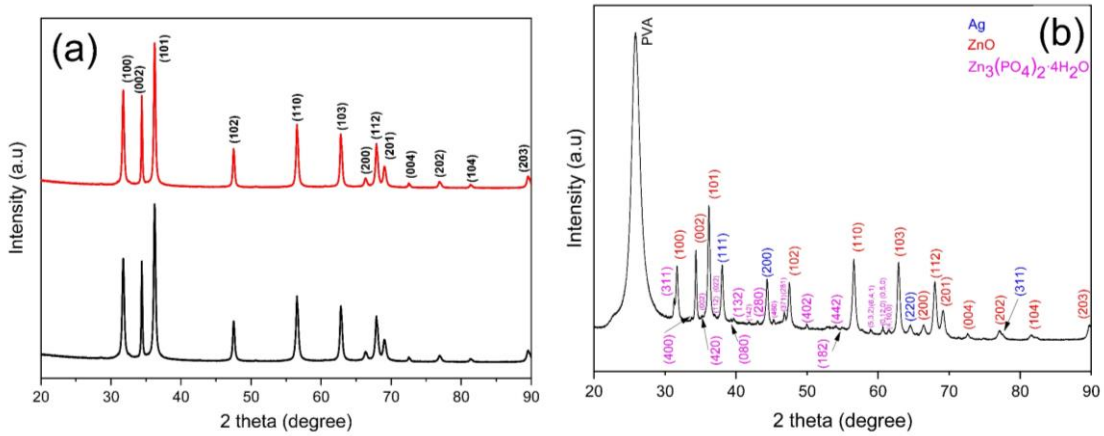

Figure 7.8 (a) XRD patterns of pristine ZnO, (b) XRD pattern of ZnO with H_3PO_4:ZnO

The average thickness of the films was measured by taking a minimum of five values. Control over the thickness of the screen-printed thin films is not much. Hence, each time a film of different thickness was printed over the commercial PET substrates.

Dynamic light scattering (DLS) is a particle size distribution curve. The data from DLS analysis and FESEM images does not match exactly because of the following reasons, (i) the DLS is based on the Brownian motion theory [28] and assumes the particles to be spherical [28,29], however, in FESEM we see clusters of plates. Also, in the DLS technique, the samples are dispersed in water, the effect of the hydration layer (H_2O size) may also be reported [30]. Moreover, the FESEM images are taken at a very small portion, hence for a detailed and exact results, a minimum of 50-100 images are required [30]. As per the results obtained in this study, the average particle ZnO particle size obtained by DLS in case of 12 ml and 30 ml NaOH reaction is 771 nm and 1080 nm respectively. Also, zeta potential of 12 ml and 30 ml NaOH reactions is 16 mV and 4.49 mV respectively.

To investigate the piezoelectric properties of the ZnO nanomaterials, PENG devices were fabricated and tested with compression force of one cycle per second. The PENG devices were mounted onto a stub of the measurement device. The PENG was connected to different load resistances ranging from 100 Ohms to 5 Giga Ohms. Voltage and current measurements were taken in sweep by employing an Arduino. In order to make sure that there is no piezoelectric output from H_3PO_4:PVA, device with PVA without ZnO were fabricated and checked for piezoelectric output. No output was recorded from the pristine PVA devices fabricated by

stencil printing. As a typical characteristic of the PENG device, the voltage output increases with the increase in the load resistance while as the output current decrease with the increase in the load resistance. A nanogenerator output voltage behavior with load resistance can be understood with the help of model proposed by various research groups [31–34]. It can be assumed that a nanogenerator device is equivalent to a voltage source and load resistance (R_L) connected parallel to the device to measure voltage. The voltage drop across load resistance (R_L) increases until the optimum load resistance (R_L) and saturates at theoretically infinite load resistance (R_L) similar to open-circuit voltage [35]. Figure 7.9 shows variation of output voltage under different load resistances. Voltage increases with an increase in the load resistance (R_L) and saturates eventually. The output voltage at higher resistance (>100 MΩ) is close to the open circuit voltage. The load resistance (R_L) dependance of output voltage shows a similar trend on reported in literature of piezoelectric nanogenerator as reported by different researchers [35–39]

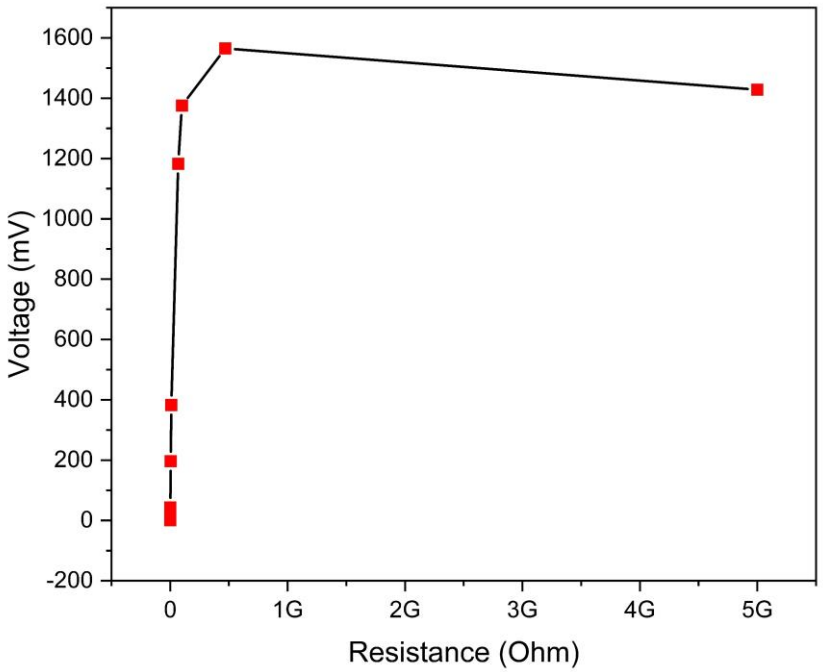

Figure 7.9 Variation of output voltage under load resistances connected in parallel.

shows the typical output of a PENG. The voltage and current curves can be categorized as [40]; (a) constant-current output characteristic region (CC-OCR), (b) maximum-power output characteristic region (MP-OCR) and (c) constant-voltage output characteristic region (CV-OCR). In the first region, CC-OCR, the output current remains constant, but the output voltage tends to increase linearly with the increase in the load resistance. MP-OCR is the middle region. In this region, with the increase in the load resistance, the current drops rapidly and the voltage

increase quickly. The output voltage and current intersect in this region. At the point of the intersection, the output power of the device peaks since the power is the product of output current and voltage. The last region is CV-OCR, where the output voltage remains constant with the increase in the load resistance, while as the current decreases slowly. This typical electrical behavior of the fabricated PENG with load resistance (R_L) is showed in Figure 7.11. Also, the output voltage and current signal are shown in Figure 7.14.

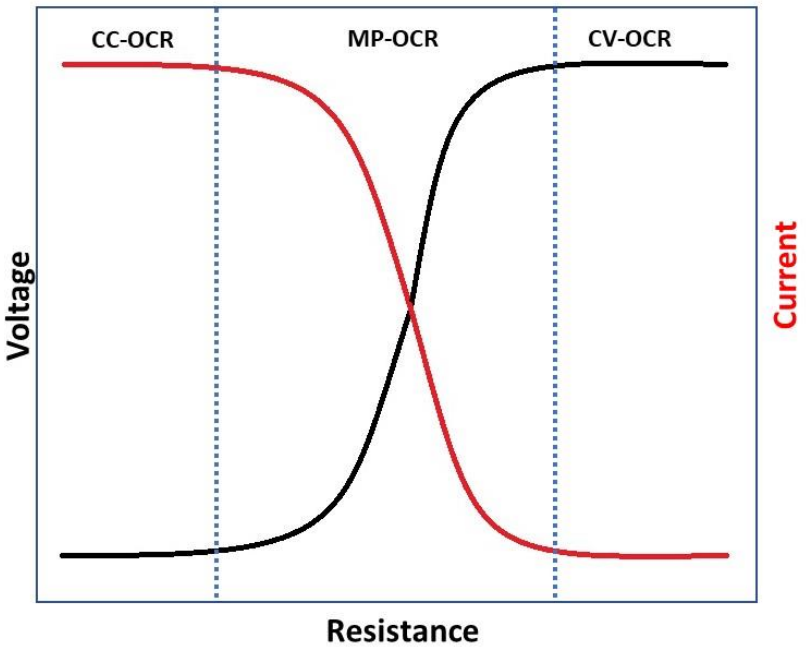

Figure 7.10 Typical output characteristics of PENG

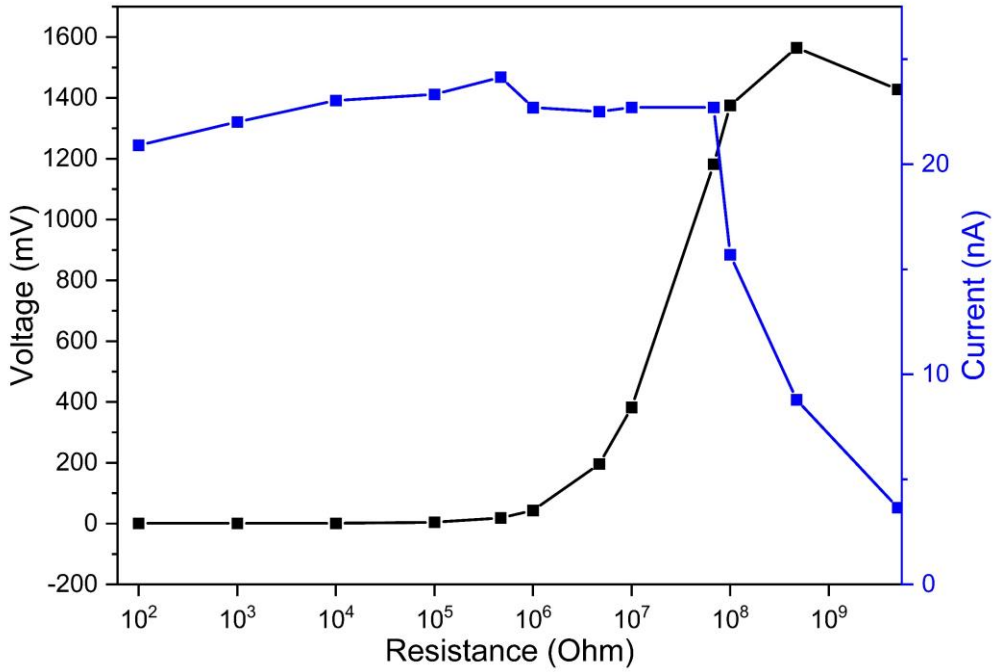

Figure 7.11 Output current and voltage characteristics of ZnO-PVA PENG

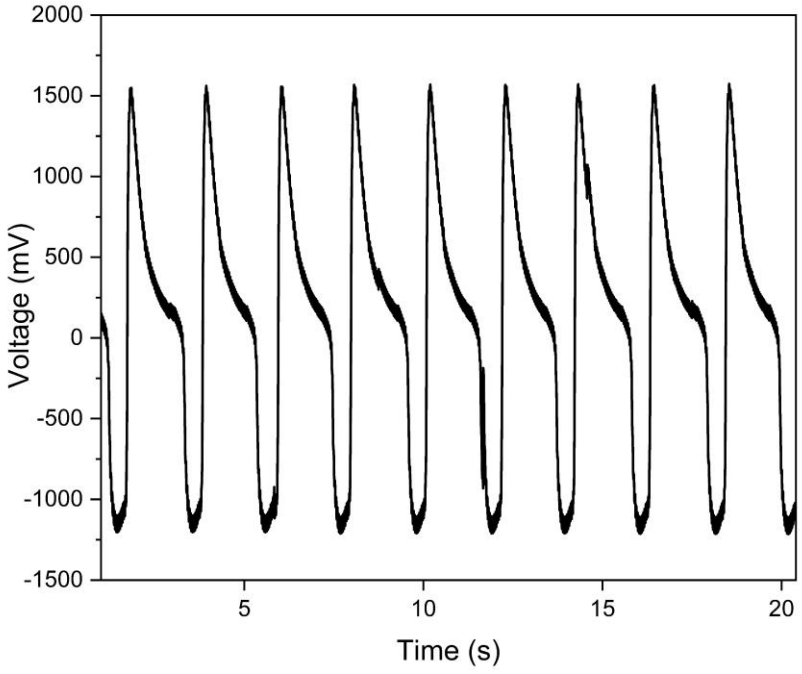

Figure 7.12 Output voltage of ZnO-PENG showing Zn termination.

Figure 7.12 shows a typical output voltage of the fabricated PENG. The cycles show a negative output during compression and positive output during release. This is because of an effect called Zn termination. A negative piezo potential is generated at the top surface in response to the compressive force.

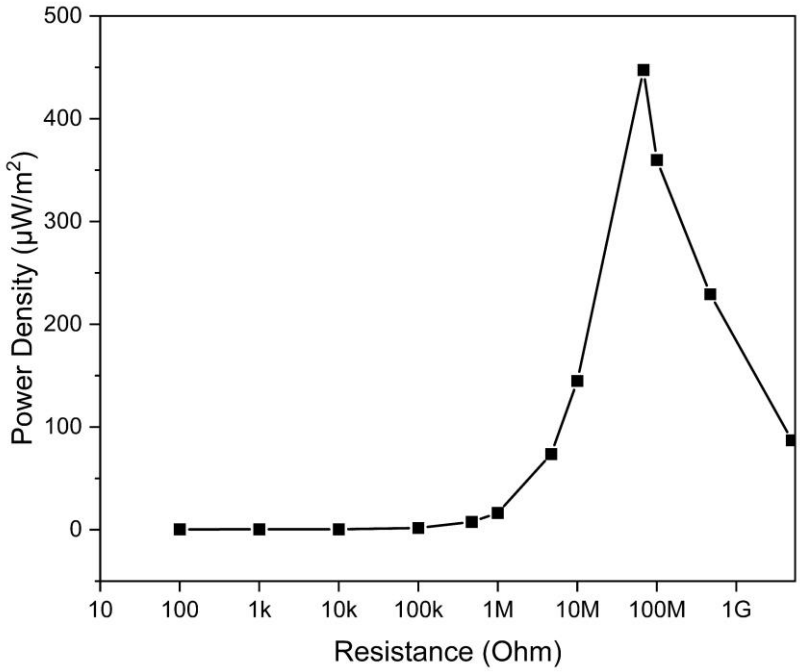

Figure 7.13 Maximum power density of ZnO-PVA PENG

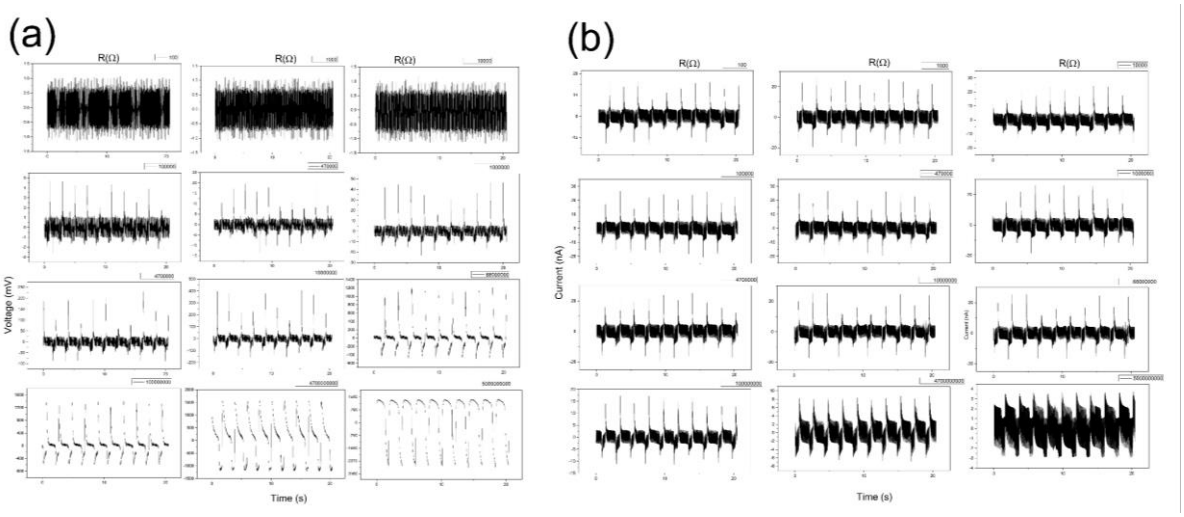

Figure 7.14 (a) Voltage and (b) current output from ZnO-PVA PENG

The maximum voltage output of the PENG devices employing ZnO and PVA mixture as piezoelectric material was found to be 760 mV and 1500 mV for 12 ml and 30 ml NaOH reaction conditions respectively. Also, the maximum current output recorded in the fabricated

PENG devices was approximately 25 nA in both the reaction types. The working area of the PENG device is calculated by measuring the area of the eight busbar overlaps with ZNO-PVA working material. Figure 7.13 shows the maximum power density as 450 μW/m^2 in case of 30 ml NaOH reaction conditions at ~100MΩ load resistance, which is close to the internal resistance of the ZnO-PVA PENG [41,42]. The formula used to calculate the power of the devices is $P = V * I$. This formula was used to give the exact power output by omitting the connector and device resistances. The power density of the device was calculated from the area of the eight contact points of the fabricated PENG as shown in Figure 7.15 in red rectangles. The output power characteristics of the fabricated nanogenerators can be understood from the maximum power transmission theorem [43]. The theorem states that the maximum power transmission occurs when the load resistance values equal the source internal resistance. The dependance of output power with load resistance shows a similar trend as reported in literature of piezoelectric nanogenerators made of different materials [44–46].

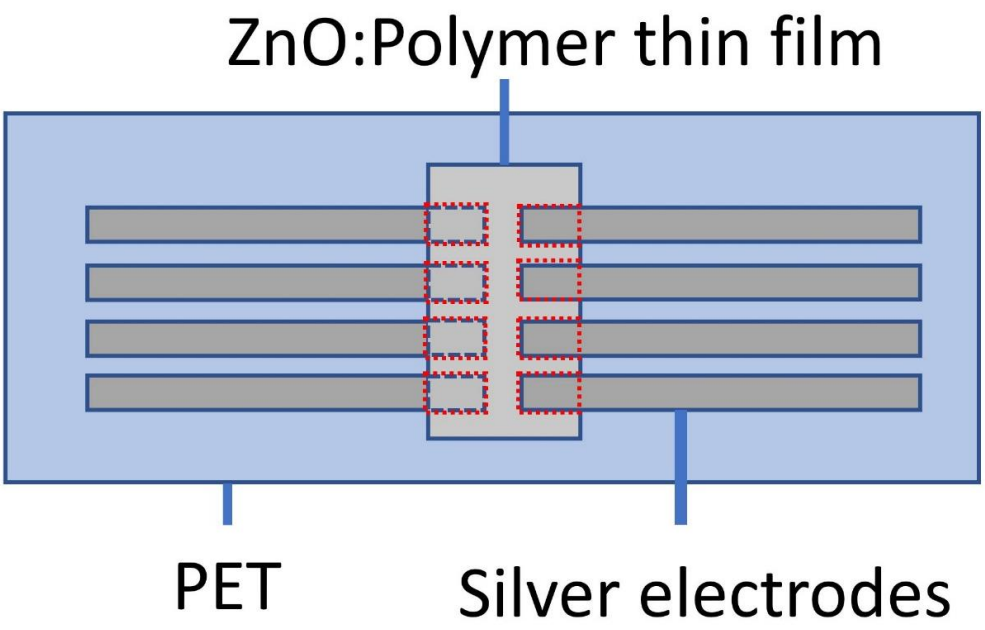

Figure 7.15 Schematic of PENG showing the area calculated for power density calculation (in red rectangles)

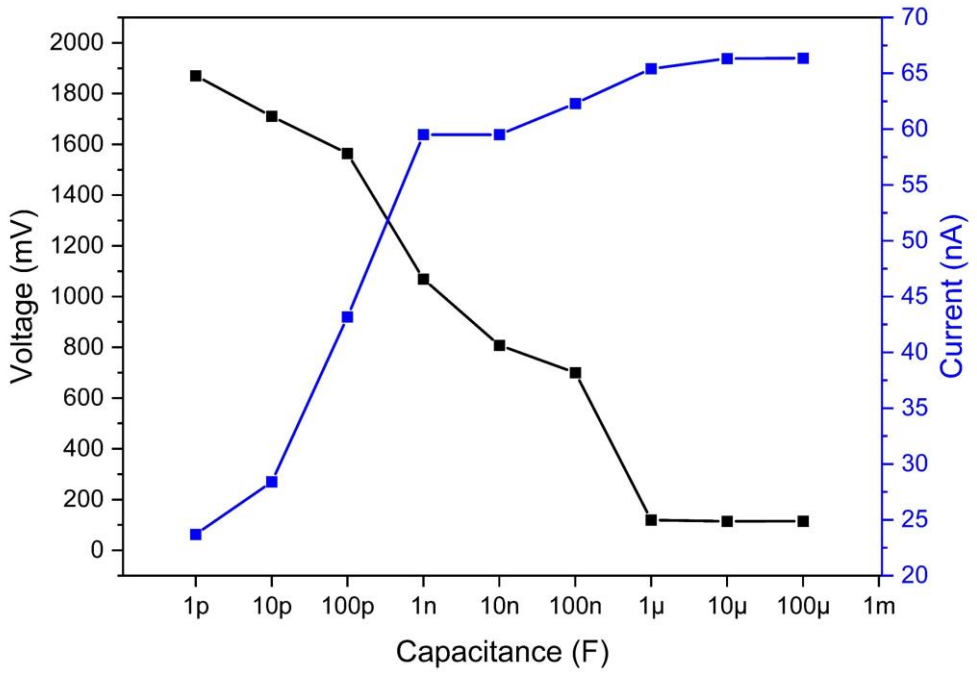

Figure 7.16 Behavior of output voltage and current against load capacitance

Figure 7.16 shows the charging characteristics of the load capacitors (C_L) for the PENGs using one compression cycle per second. The PENGs were used to charge capacitors with the capacitance of 100 µF, 10 µF, 1 µF, 100 nF, 10 nF, 1 nF, 100 pF, 10 pF and 1 pF. The output voltage and current characteristics were analyzed as a function of load capacitance. There is an inverse relation between output voltage and current against the corresponding load capacitor. The trend of capacitive loading is opposite to that of resistive loading. The trend shows that under different load resistances, with an increase in the resistance load, voltage increases and load current decreases. Whereas, with increasing capacitance, load voltage decreases and load current increases. It takes less time to reach saturation in case of smaller load capacitors as can be seen in Figure 7.17.

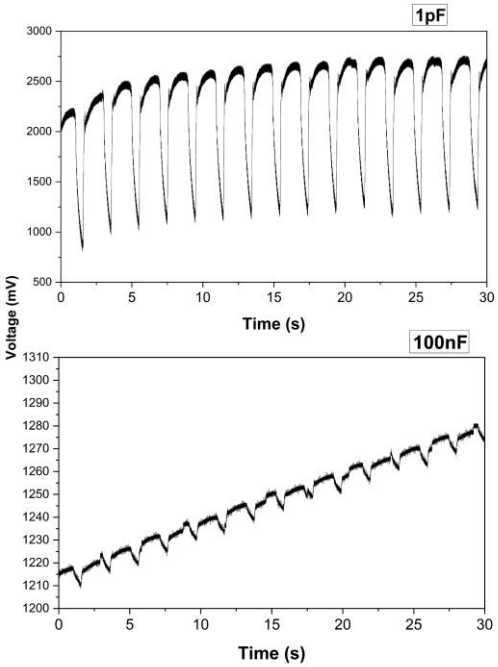

Figure 7.17 Comparison between the charging time of capacitors 1pF and 100nF using ZnO-PVA PENG.

7.4. Conclusions

In this work, coprecipitation ZnO synthesis method with high yield was used. XRD, FESEM studies confirm the crystallinity and purity of ZnO sheets. Nanogenerators were fabricated by screenprinting electrodes of silver and working material (ZnO-PVA) onto commercial PET substrates. Piezoelectric output was successfully recorded from the PENGs fabricated onto commercial PET substrates. The output recorded is comparable to most of the sophisticated reported PENGs. The PENGs when optimized would be efficient energy harvesters and robust sensors.

7.5. Future perspectives

The most significant parameter to be taken into consideration to carry forward this work is to optimize the PENG structure related to ohmic and Schottky contacts. Choice of polymer matrix would be the second most important aspects to be taken into consideration. In this work, because of the presence of H_3PO_4 in the PVA, approximately 50% of the ZnO reacts and converts to zinc phosphate. PDMS is one of the best alternatives to replace PVA. Also, calculation of the amount of force applied during the piezo measurements is a must. This work was carried out at a frequency of one force cycle per minute, the effect of the frequency would be one more parameter to be explored. Also, in this study, ZnO nanomaterials were prepared

by coprecipitation method. Other synthesis methods like hydrothermal methods could be explored with different morphologies.

7.6. References

[1] Y. Sun, Y. Liu, Y. Zheng, Z. Li, J. Fan, L. Wang, X. Liu, J. Liu, W. Shou, Enhanced Energy Harvesting Ability of ZnO/PAN Hybrid Piezoelectric Nanogenerators, ACS Appl. Mater. Interfaces. 12 (2020) 54936–54945. https://doi.org/10.1021/acsami.0c14490.

[2] X. Yan, G. Li, Z. Wang, Z. Yu, K. Wang, Y. Wu, Recent progress on piezoelectric materials for renewable energy conversion, Nano Energy. 77 (2020). https://doi.org/10.1016/j.nanoen.2020.105180.

[3] D. Zou, S. Liu, C. Zhang, Y. Hong, G. Zhang, Z. Yang, Flexible and translucent PZT films enhanced by the compositionally graded heterostructure for human body monitoring, Nano Energy. 85 (2021) 1–10. https://doi.org/10.1016/j.nanoen.2021.105984.

[4] J.-X. Chen, J.-W. Li, C.-C. Cheng, C.-W. Chiu, Piezoelectric Property Enhancement of PZT/Poly(vinylidenefluoride- co -trifluoroethylene) Hybrid Films for Flexible Piezoelectric Energy Harvesters , ACS Omega. (2021). https://doi.org/10.1021/acsomega.1c05451.

[5] M. Habib, M. Javid, M. Hwan, D. Jeong, F. Akram, M. Gul, A. Zeb, I. Ur, M. Kim, T. Kwon, Piezoelectric performance of Zr-modified lead-free BiFeO 3 -BaTiO 3 ceramics, 146 (2022).

[6] M. Mariello, L. Fachechi, F. Guido, M. De Vittorio, Multifunctional sub-100 μm thickness flexible piezo/triboelectric hybrid water energy harvester based on biocompatible AlN and soft parylene C-PDMS-Ecoflex™, Nano Energy. 83 (2021). https://doi.org/10.1016/j.nanoen.2021.105811.

[7] D. Bhattacharya, S. Bayan, R.K. Mitra, S.K. Ray, 2D WS2embedded PVDF nanocomposites for photosensitive piezoelectric nanogenerators with a colossal energy conversion efficiency of ~25.6%, Nanoscale. 13 (2021) 15819–15829. https://doi.org/10.1039/d1nr03808g.

[8] R.K. Pandey, J. Dutta, S. Brahma, B. Rao, C.P. Liu, Review on ZnO-based piezotronics

and piezoelectric nanogenerators: Aspects of piezopotential and screening effect, JPhys Mater. 4 (2021). https://doi.org/10.1088/2515-7639/ac130a.

[9] A.T. Le, M. Ahmadipour, S.Y. Pung, A review on ZnO-based piezoelectric nanogenerators: Synthesis, characterization techniques, performance enhancement and applications, J. Alloys Compd. 844 (2020). https://doi.org/10.1016/j.jallcom.2020.156172.

[10] A. Sam, V. Natraj, G. Marappan, Y. Sivalingam, V.J. Surya, Design and development of novel piezoelectric nanogenerator based on pH dependent ZnO nanostructures, Mater. Lett. 294 (2021). https://doi.org/10.1016/j.matlet.2021.129798.

[11] P.C. Lee, Y.L. Hsiao, J. Dutta, R.C. Wang, S.W. Tseng, C.P. Liu, Development of porous ZnO thin films for enhancing piezoelectric nanogenerators and force sensors, Nano Energy. 82 (2021) 1–10. https://doi.org/10.1016/j.nanoen.2020.105702.

[12] Y. Zhang, Y. Liu, Z.L. Wang, Fundamental theory of piezotronics, Adv. Mater. 23 (2011) 3004–3013. https://doi.org/10.1002/adma.201100906.

[13] J.A. Christman, H. Maiwa, S.H. Kim, A.I. Kingon, R.J. Nemanich, Piezoelectric measurements with atomic force microscopy, Mater. Res. Soc. Symp. - Proc. 541 (1999) 617–622. https://doi.org/10.1557/proc-541-617.

[14] J. Kaur, H. Singh, Fabrication and analysis of piezoelectricity in 0D, 1D and 2D Zinc Oxide nanostructures, Ceram. Int. 46 (2020) 19401–19407. https://doi.org/10.1016/j.ceramint.2020.04.283.

[15] J. Kaur, H. Singh, Synthesis and fabrication of zinc oxide nanostrands based piezoelectric nanogenerator, J. Mater. Sci. Mater. Electron. 30 (2019) 4437–4445. https://doi.org/10.1007/s10854-019-00732-3.

[16] Y. Sun, Y. Zheng, R. Wang, J. Fan, Y. Liu, Direct-current piezoelectric nanogenerator based on two-layer zinc oxide nanorod arrays with equal c-axis orientation for energy harvesting, Chem. Eng. J. 426 (2021) 131262. https://doi.org/10.1016/j.cej.2021.131262.

[17] Z. Li, X. Zhang, G. Li, In situ ZnO nanowire growth to promote the PVDF piezo phase and the ZnO-PVDF hybrid self-rectified nanogenerator as a touch sensor, Phys. Chem. Chem. Phys. 16 (2014) 5475–5479. https://doi.org/10.1039/c3cp54083a.

[18] W. Deng, T. Yang, L. Jin, C. Yan, H. Huang, X. Chu, Z. Wang, Nano Energy Cowpea-structured PVDF / ZnO nano fi bers based fl exible self-powered piezoelectric bending motion sensor towards remote control of gestures, 55 (2019) 516–525.

[19] T. Huang, C. Wang, H. Yu, H. Wang, Human walking-driven wearable all- fi ber triboelectric nanogenerator containing electrospun polyvinylidene fl uoride piezoelectric nano fi bers, (2015) 226–235.

[20] Y. Hu, Y. Zhang, C. Xu, L. Lin, R.L. Snyder, Z.L. Wang, Self-powered system with wireless data transmission, Nano Lett. 11 (2011) 2572–2577. https://doi.org/10.1021/nl201505c.

[21] S. Ying, J.-H. ZHANG, K. Yan, M. Xin, J. Zhang, S. Li, J.-G. Liang, Y. Shi, L. Pan, Self-Powered Direct-current Type Pressure Sensor by Polypyrrole/Metal Schottky Junction, J. Phys. D. Appl. Phys. (2021). https://doi.org/10.1088/1361-6463/ac196c.

[22] C.T. Lee, Y.S. Chiu, Piezoelectric ZnO-nanorod-structured pressure sensors using GaN-based field-effect-transistor, Appl. Phys. Lett. 106 (2015) 1–3. https://doi.org/10.1063/1.4910879.

[23] U. Laraib, S. Sargazi, A. Rahdar, M. Khatami, S. Pandey, Nanotechnology-based approaches for effective detection of tumor markers: A comprehensive state-of-the-art review, Int. J. Biol. Macromol. 195 (2021) 356–383. https://doi.org/10.1016/j.ijbiomac.2021.12.052.

[24] Z. Wu, T. Cheng, Z.L. Wang, Self-powered sensors and systems based on nanogenerators, Sensors (Switzerland). 20 (2020). https://doi.org/10.3390/s20102925.

[25] L. Liu, X. Guo, W. Liu, C. Lee, Recent Progress in the Energy Harvesting Technology — From Self-Powered Sensors to Self-Sustained IoT , and New Applications, (2021).

[26] M.M. Maia, A.L. Pires, A.M.L. Lopes, A.M. Pereira, On manipulating the thermoelectric potential of p-type ZnO by nanostructuring, Mater. Today Energy. 21 (2021) 100752. https://doi.org/10.1016/j.mtener.2021.100752.

[27] D.A.M.O. Osman, M.A. Mustafa, Synthesis and Characterization of Zinc Oxide Nanoparticles using Zinc Acetate Dihydrate and Sodium Hydroxide, J. Nanosci. Nanoeng. 1 (2015) 248–251. http://www.aiscience.org/journal/jnnhttp://creativecommons.org/licenses/by-nc/4.0/.

[28] R. Ebrahimi, K. Hossienzadeh, A. Maleki, R. Ghanbari, R. Rezaee, M. Safari, B. Shahmoradi, H. Daraei, A. Jafari, K. Yetilmezsoy, S.H. Puttaiah, Effects of doping zinc oxide nanoparticles with transition metals (Ag, Cu, Mn) on photocatalytic degradation of Direct Blue 15 dye under UV and visible light irradiation, J. Environ. Heal. Sci. Eng. 17 (2019) 479–492. https://doi.org/10.1007/s40201-019-00366-x.

[29] S. Shahbazkhany, M. Salehi, M. Mousavi-Kamazani, Z. Salarvand, Zn0.94Mn0.06O for adsorption and photo-degradation of methyl orange dye under visible irradiation: Kinetics and isotherms study, Environ. Res. 203 (2022) 111833. https://doi.org/10.1016/j.envres.2021.111833.

[30] S. Shahbazkhany, M. Salehi, M. Mousavi-Kamazani, Z. Salarvand, Zn0.94Mn0.06O for adsorption and photo-degradation of methyl orange dye under visible irradiation: Kinetics and isotherms study, Environ. Res. 203 (2022) 111833. https://doi.org/10.1016/j.envres.2021.111833.

[31] H.J. Lee, S. Sherrit, L.P. Tosi, P. Walkemeyer, T. Colonius, Piezoelectric energy harvesting in internal fluid flow, Sensors (Switzerland). 15 (2015) 26039–26062. https://doi.org/10.3390/s151026039.

[32] Y. Zhou, W. Liu, X. Huang, A. Zhang, Y. Zhang, Z.L. Wang, Theoretical study on two-dimensional MoS2 piezoelectric nanogenerators, Nano Res. 9 (2016) 800–807. https://doi.org/10.1007/s12274-015-0959-8.

[33] Q. Xu, Y. Qin, Theoretical study of enhancing the piezoelectric nanogenerator's output power by optimizing the external force's shape, APL Mater. 5 (2017). https://doi.org/10.1063/1.4975772.

[34] K. Nadaud, F. Morini, A.S. Dahiya, C. Justeau, S. Boubenia, K.P. Rajeev, D. Alquier, G. Poulin-Vittrant, Double buffer circuit for the characterization of piezoelectric nanogenerators based on ZnO nanowires, Appl. Phys. Lett. 112 (2018) 1–6. https://doi.org/10.1063/1.5018145.

[35] A. Sultana, M.M. Alam, S. Garain, T.K. Sinha, T.R. Middya, D. Mandal, An Effective Electrical Throughput from PANI Supplement ZnS Nanorods and PDMS-Based Flexible Piezoelectric Nanogenerator for Power up Portable Electronic Devices: An Alternative of MWCNT Filler, ACS Appl. Mater. Interfaces. 7 (2015) 19091–19097. https://doi.org/10.1021/acsami.5b04669.

[36] X. Li, Z.H. Lin, G. Cheng, X. Wen, Y. Liu, S. Niu, Z.L. Wang, 3D fiber-based hybrid nanogenerator for energy harvesting and as a self-powered pressure sensor, ACS Nano. 8 (2014) 10674–10681. https://doi.org/10.1021/nn504243j.

[37] S. Rafique, A.K. Kasi, J.K. Kasi, Aminullah, M. Bokhari, Z. Shakoor, Fabrication of silver-doped zinc oxide nanorods piezoelectric nanogenerator on cotton fabric to utilize and optimize the charging system, Nanomater. Nanotechnol. 10 (2020) 1–12. https://doi.org/10.1177/1847980419895741.

[38] S. Stassi, V. Cauda, C. Ottone, A. Chiodoni, C.F. Pirri, G. Canavese, Flexible piezoelectric energy nanogenerator based on ZnO nanotubes hosted in a polycarbonate membrane, Nano Energy. 13 (2015) 474–481. https://doi.org/10.1016/j.nanoen.2015.03.024.

[39] S. Ye, C. Cheng, X. Chen, X. Chen, J. Shao, J. Zhang, H. Hu, H. Tian, X. Li, L. Ma, W. Jia, High-performance piezoelectric nanogenerator based on microstructured P(VDF-TrFE)/BNNTs composite for energy harvesting and radiation protection in space, Nano Energy. 60 (2019) 701–714. https://doi.org/10.1016/j.nanoen.2019.03.096.

[40] D. Zhao, X. Yu, Z. Wang, J. Wang, X. Li, Z.L. Wang, T. Cheng, Universal equivalent circuit model and verification of current source for triboelectric nanogenerator, Nano Energy. 89 (2021). https://doi.org/10.1016/j.nanoen.2021.106335.

[41] J. Briscoe, N. Jalali, P. Woolliams, M. Stewart, P.M. Weaver, M. Cain, S. Dunn, Measurement techniques for piezoelectric nanogenerators, Energy Environ. Sci. 6 (2013) 3035–3045. https://doi.org/10.1039/c3ee41889h.

[42] Y. Sun, Y. Zheng, R. Wang, J. Fan, Y. Liu, Direct-current piezoelectric nanogenerator based on two-layer zinc oxide nanorod arrays with equal c-axis orientation for energy harvesting, Chem. Eng. J. 426 (2021). https://doi.org/10.1016/j.cej.2021.131262.

[43] E.C. Theory, Electrical circuit theory and technology, 2001. https://doi.org/10.5860/choice.39-0957.

[44] K. Il Park, J.H. Son, G.T. Hwang, C.K. Jeong, J. Ryu, M. Koo, I. Choi, S.H. Lee, M. Byun, Z.L. Wang, K.J. Lee, Highly-efficient, flexible piezoelectric PZT thin film nanogenerator on plastic substrates, Adv. Mater. 26 (2014) 2514–2520. https://doi.org/10.1002/adma.201305659.

[45] C. Luo, S. Hu, M. Xia, P. Li, J. Hu, G. Li, H. Jiang, W. Zhang, A Flexible Lead-Free BaTiO3/PDMS/C Composite Nanogenerator as a Piezoelectric Energy Harvester, Energy Technol. 6 (2018) 922–927. https://doi.org/10.1002/ente.201700756.

[46] S. Garain, S. Jana, T.K. Sinha, D. Mandal, Design of in Situ Poled Ce3+-Doped Electrospun PVDF/Graphene Composite Nanofibers for Fabrication of Nanopressure Sensor and Ultrasensitive Acoustic Nanogenerator, ACS Appl. Mater. Interfaces. 8 (2016) 4532–4540. https://doi.org/10.1021/acsami.5b11356.

CHAPTER 8

Conclusions and Future perspectives

8.1. Conclusions

This chapter provides an overview of the significant accomplishments of this research, emphasizing both the benefits of the growth process and the improvements in gas sensing capabilities achieved through the integration of various nanomaterial functionalities.

In this research work, a facile aerosol assisted CVD method was developed to control the morphology of the WO_3 nanowires. This is an efficient route to synthesize WO_3 nanowires of different morphologies directly on the transducer substrates. We achieved a great success in synthesizing randomly oriented nanowires and nanowires with floral tops. The nanowires were decorated with CeO_2 nanoparticles with a simple drop casting technique. The decorated nanowires were capable of efficiently detecting low concentrations of ethanol at comparatively low temperatures.

In this study we achieved a significant milestone by synthesizing of two-dimensional (2D) tungsten disulfide (WS_2) sheets on a hundred milligram scale for the first time. This achievement was realized through a simple sulfurization process of tungsten trioxide (WO_3) powder utilizing an atmospheric pressure chemical vapor deposition (APCVD) reactor. The synthesized powders exhibit immense potential for various applications, including the development of ink formulations for screen or inkjet printing, spin coating, drop casting, or airbrushing onto diverse substrates such as ceramics, silicon-based materials, or flexible polymers. Gas sensing experiments towards NH_3 at different temperatures showed exceptional responses from the WS_2-based sensors, with reproducible and stable responses at 150°C, with a detection limit below 1 ppm of NH_3. Selectivity tests demonstrated that the sensors are highly specific to NH_3 while showing minimal response to interfering gases such as CO, benzene, H_2, and NO_2. Furthermore, the edge-enriched growth of WS_2 enhanced the responses of the sensors with remarkable resilience against high humidity levels, with only a slight decrease in response observed in humid environments compared to dry conditions. Atomistic simulations employing density functional theory (DFT) and Bayesian optimization revealed the physisorption-based interaction between ammonia molecules and WS_2, providing valuable insights into the gas sensing mechanism. This study highlights the promising prospects of WS_2-based materials in advancing the development of highly sensitive and selective gas sensors for practical applications.

Furthermore, a simple solution method was used to mix TMDs and graphene for NO_2 sensing applications. The method is efficient for making hybrid heterostructures comprising of tungsten

disulfide (WS_2) and graphene. The sensing films were fabricated using a facile airbrushing technique with N_2 as the carrier gas. Morphological and structural analyses reveal the growth of edge-enriched 2D WS_2 sheets and a uniform distribution of sensing materials within the hybrids. Gas sensing results were performed on the hybrid sensors towards NO_2 gas at various temperatures which demonstrate remarkable responses to ultra-low concentrations (10 ppb) of NO_2, achieved at a notably low operating temperature of 100°C compared to individual graphene and WS_2 counterparts. The sensors show minimum responses towards interfering gases, including CO, H_2, C_6H_6, and NH_3, demonstrating their versatile selective sensing capabilities. Moreover, the sensor responses nearly double in humid conditions (50% RH at 25°C), indicating potential practical applications for selective NO_2 detection in real-world environments.

Moreover, this thesis reports successful development of an aerosol-assisted CVD method for decorating thin films of various TMD materials with different metal and metal oxide nanoparticles. This method proves to be effective for enhancing the properties of such materials with metals and metal oxide nanoparticles, particularly in scenarios where material degradation at elevated temperatures poses a risk. Notably, we achieved successful decoration of MoS_2 with Pd nanoparticles at various ratios, demonstrating excellent detection capabilities for H_2.

In an effort to harness the potential of ZnO nanomaterials for self-powering device applications, piezoelectric nanogenerators (PENGs) were successfully fabricated using a facile screenprinting technique on flexible substrates. These PENGs exhibit promising power output, making them suitable for powering wearable electronics and sensors.

8.2. Future perspectives

This thesis lays the foundation for several key advancements in gas sensing technology: (1) the direct synthesis of metal oxides with diverse morphologies on commercial transducer substrates, eliminating the need for transfer steps; (2) the development of a facile hydrogen-free APCVD technique capable of producing gram-scale TMD powders, offering significant potential for industrial-scale applications; (3) a cost-effective method for enhancing the functionality of TMD host matrices at low temperatures using AACVD; (4) the design of chemoresistive sensors tailored for gas sensing applications; and (5) a simple and affordable approach to designing and fabricating self-powering devices using metal oxide nanomaterials. Despite the promising prospects of TMD materials in gas sensing applications, there exist certain limitations that must be addressed for their commercialization in real-world scenarios. Additionally, the gas sensing mechanism remains inadequately understood and requires further investigation.

However, there still remain some challenges which could be overcome by delving into the synthesis methodologies and understating gas sensing mechanism. Looking ahead, future research endeavors could focus on several areas to advance the field of gas sensing using TMD materials. First and foremost, there is a need to optimize the synthesis conditions of TMDs to enhance their properties and tailor them for specific gas detection. Additionally, efforts could be directed towards lowering the operating temperature of gas sensors to improve energy efficiency and extend their lifespan. Exploring the potential of different nanomaterials for hybridization and decoration holds promise for achieving selective and low-temperature gas sensing capabilities. Moreover, diversifying the types of TMDs beyond MoS_2 and WS_2 could uncover new materials with unique properties and applications in gas sensing. By addressing these challenges and pursuing these avenues of research, the future holds immense potential for advancing the field of gas sensing using TMD materials. Also, a significant amount of research could be dedicated to assessing the biosafety of TMD materials to ensure a sustainable future.

Annex I

Supporting Information

Supporting information for

Synergistic effect of CeO_2 nanoparticles and WO_3 nanowires in gas sensing applications

Shuja Bashir Malik[1], Karol V. Mejia-Centeno[2], Paulina R. Martínez-Alanis[2], Andreu Cabot[2,3], Frank Güell[*1,4,] Fatima Ezahra Annanouch[1] and Eduard Llobet[*1]

[1] Departament d′Enginyeria Electrònica, Universitat Rovira i Virgili, Països Catalans 26, 43007 Tarragona, Catalunya, Spain.

[2] Catalonia Energy Research Institute – IREC, Jardins de les Dones de Negre 1, Sant Adrià de Besós, 08930, Barcelona, Catalunya, Spain.

[3] ICREA, Pg. Lluis Companys, 08010, Barcelona, Catalunya, Spain.

[4] ENFOCAT, Universitat de Barcelona, Martí i Franquès 1, 08028 Barcelona, Catalunya, Spain.

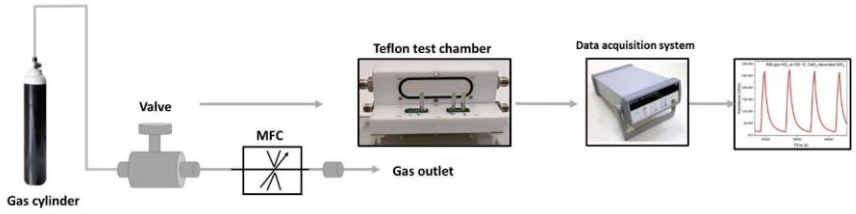

Figure S1: Gas sensing measurement setup

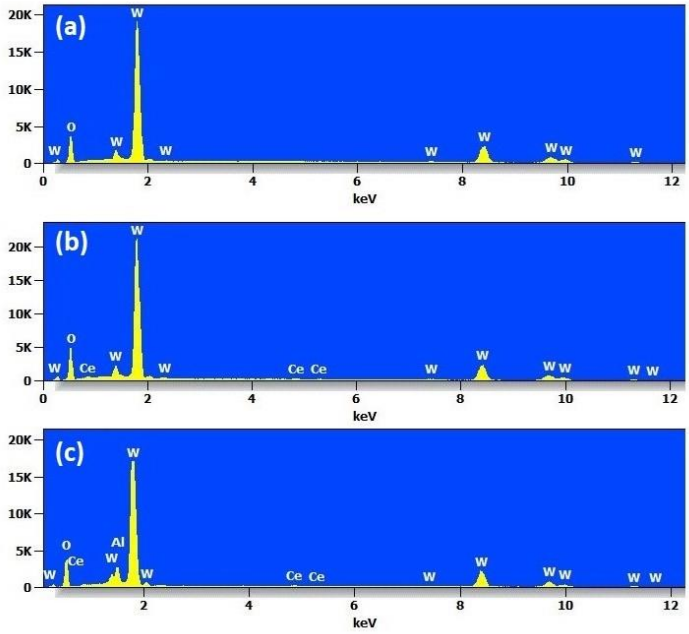

Figure S2 EDX spectra of (a) WO_3, (b) randomly oriented CeO_2 decorated WO_3 nanowires and (c) CeO_2 decorated WO_3 nanowires with floral tops. The elements corresponding to various peaks are indicated.

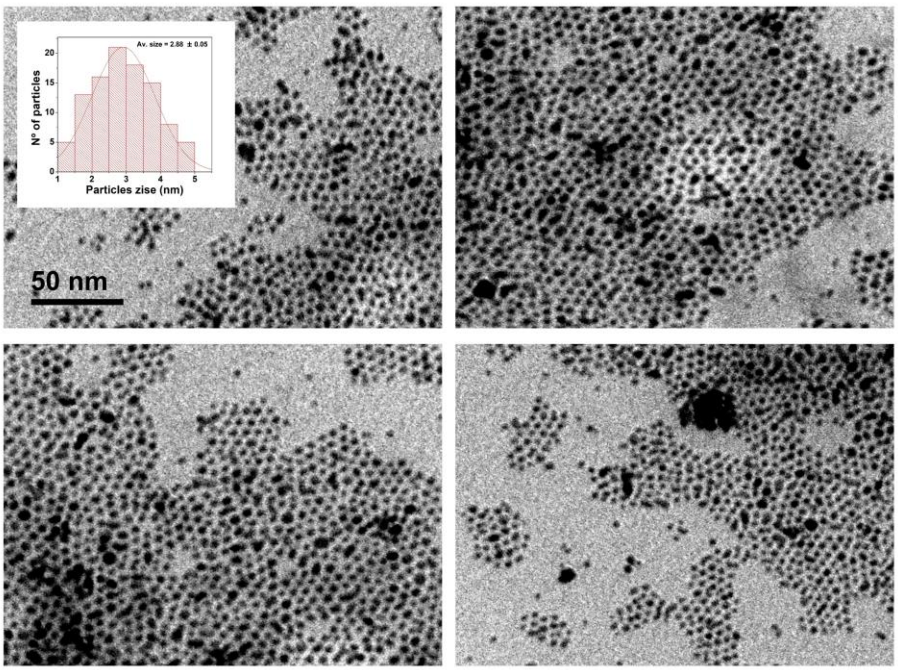

Figure S3 TEM images and size distribution details of CeO_2 nanoparticles.

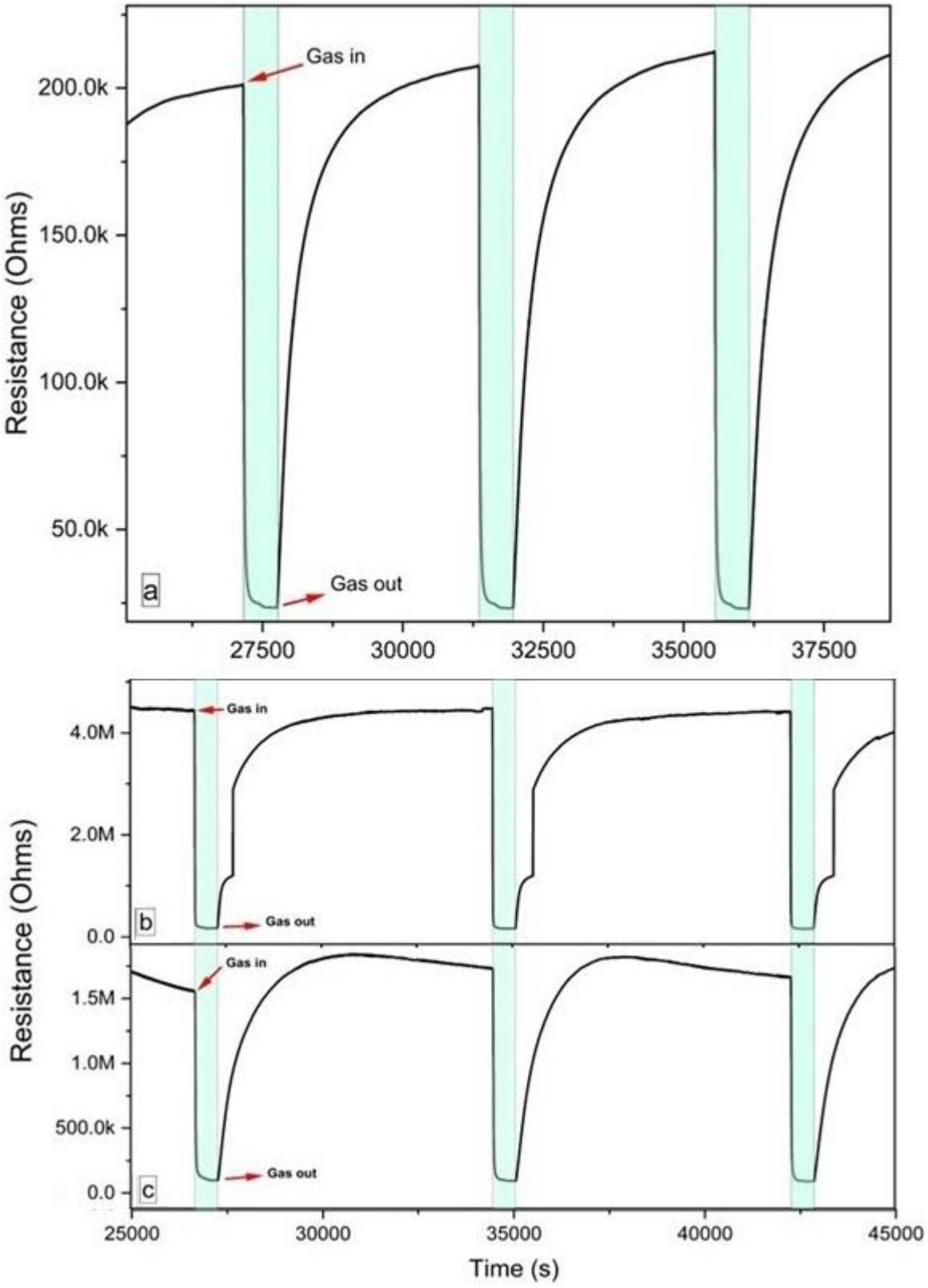

Figure S4 Resistance change of (a) WO_3, (b) randomly oriented CeO_2 decorated WO_3 nanowires and (c) CeO_2 decorated WO_3 nanowires with floral tops towards 5 ppm ethanol at 250ºC

The theory of power law which can be formulated as [1]–[3]:

$$R = AC^{\eta}$$

Applying natural logarithmic on both sides

$$\ln R = \eta \ln C + \ln A$$

Where C is the concentration, R is the response and A is a constant. Using the above relation, the ln R vs ln C is plotted are shown below. CeO_2 decorated WO_3 samples show a very good linear fit with the equation A and equation B for CeO_2 decorated WO_3 randomly oriented nanowires, and CeO_2 decorated WO_3 nanowires with floral tops respectively:

$$\ln R = 0.46 \ln C + 1.66 \qquad A$$

$$\ln R = 0.63 \ln C + 2.75 \qquad B$$

Having $R^2 = 0.98$, $R^2 = 0.93$ values for CeO_2 decorated WO_3 randomly oriented nanowires, and CeO_2 decorated WO_3 nanowires with floral tops respectively.

According to results achieved using 'in operando' spectroscopies, the initial reaction of gases with surface oxygen vacancies in WO_3 is responsible for the sensing response [4]. The annealing process conducted results in pristine tungsten oxide wires that are nearly stoichiometric with a low number of surface defects (as supported by PL and XPS results). The low concentration of surface oxygen vacancies and the low mobility of bulk oxygen vacancies in WO_3 explains the low response observed towards ethanol in pristine tungsten oxide wire films. In contrast, CeO_2 nanoparticles are characterized by having a high number of oxygen vacancies and by the high mobility of bulk oxygen vacancies. This results in a high number of ionosorbed oxygen surface species in CeO_2 NP loaded WO_3 films, and thus, in a high number of adsorption and reaction sites for ethanol molecules. CeO_2 NP loaded WO_3 films show the typical power law response ($G \sim [EtOH]^r$) found in metal oxides (Figure S5), where r is close to 0.5. This is indicative that O^- may be the dominant oxygen surface species in the reaction with ethanol [5].

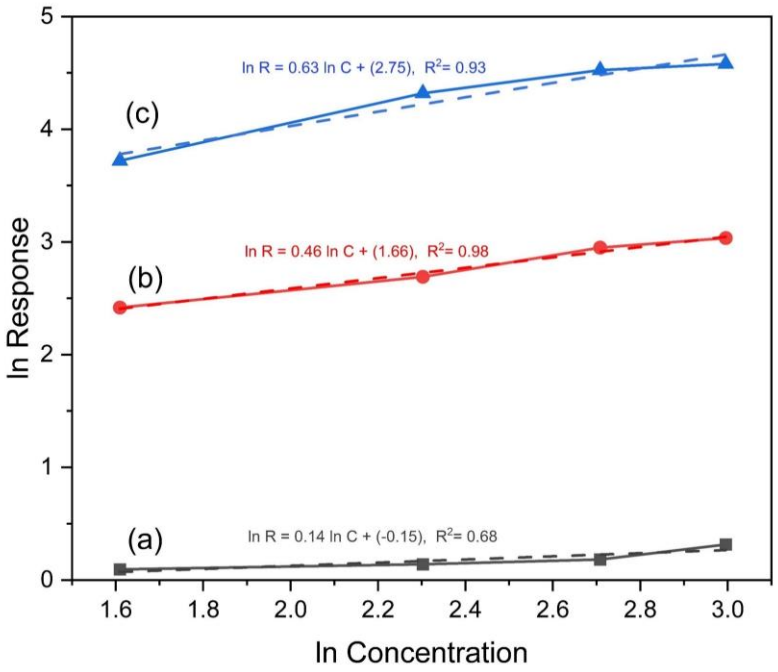

Figure S5 ln response vs ln concentration plot showing sensitivity towards ethanol.

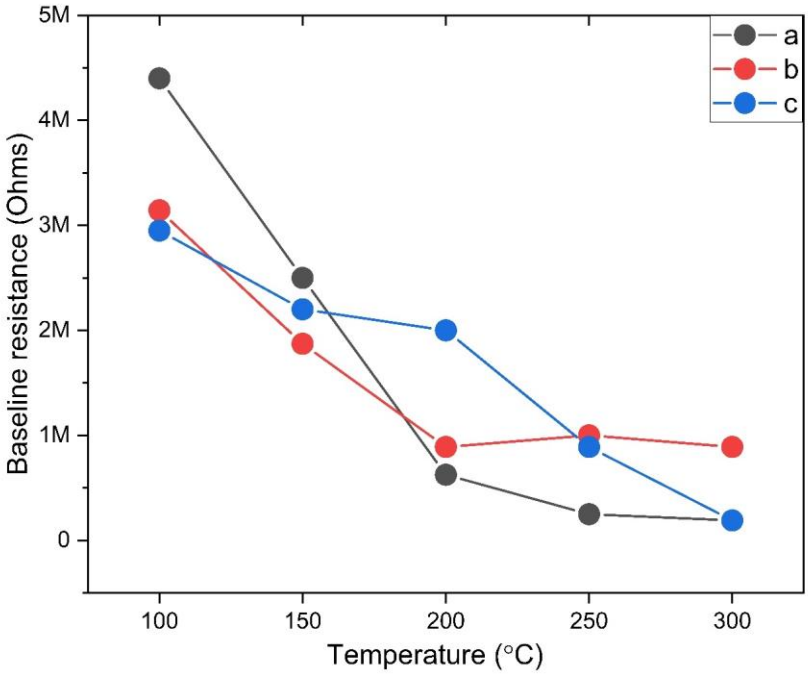

Figure S6 Baseline resistance change with increase in temperature; (a) WO_3, (b) randomly oriented CeO_2 decorated WO_3 nanowires and (c) CeO_2 decorated WO_3 nanowires with floral tops

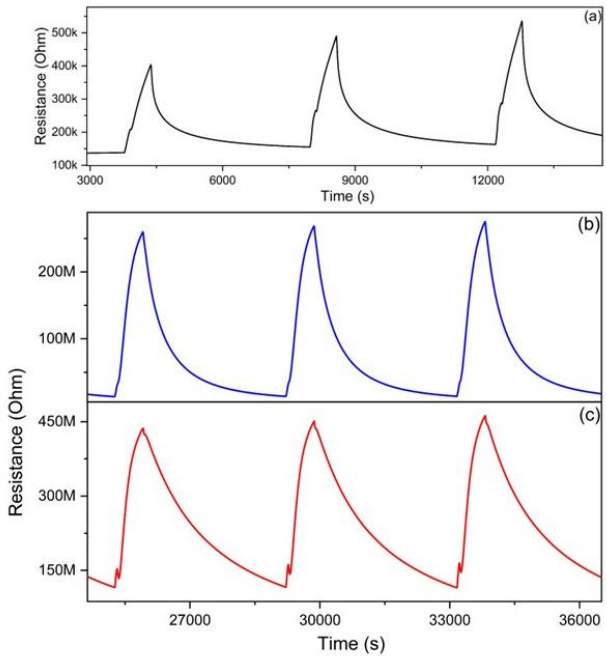

Figure S7 Resistance change of (a) pristine WO_3 at 150ºC, (b) randomly oriented CeO_2 decorated WO_3 nanowires and (c) CeO_2 decorated WO_3 nanowires with floral tops towards 500 ppb NO_2 at 200ºC.

Carbon monoxide (CO)

Carbon monoxide gas responses were studied at concentrations ranging from 1 to 20 ppm. As can be seen from Figure S8, the maximum response towards CO is recorded at 200ºC in case of CeO_2 decorated WO_3 nanowires. In case of pristine WO_3, the maximum response is recorded at 100ºC. However, the pristine WO_3 nanowires show significantly low response as compared to CeO_2 decorated WO_3 nanowires. CeO_2 decorated WO_3 nanowires do not show any response below 150ºC. The signal to noise ratio is too high to be shown here. The typical resistance changes dynamics of the sensors towards 10 ppm of CO at 100ºC and 200ºC for pristine and CeO_2 decorated WO_3 nanowires respectively is shown in Figure S9.

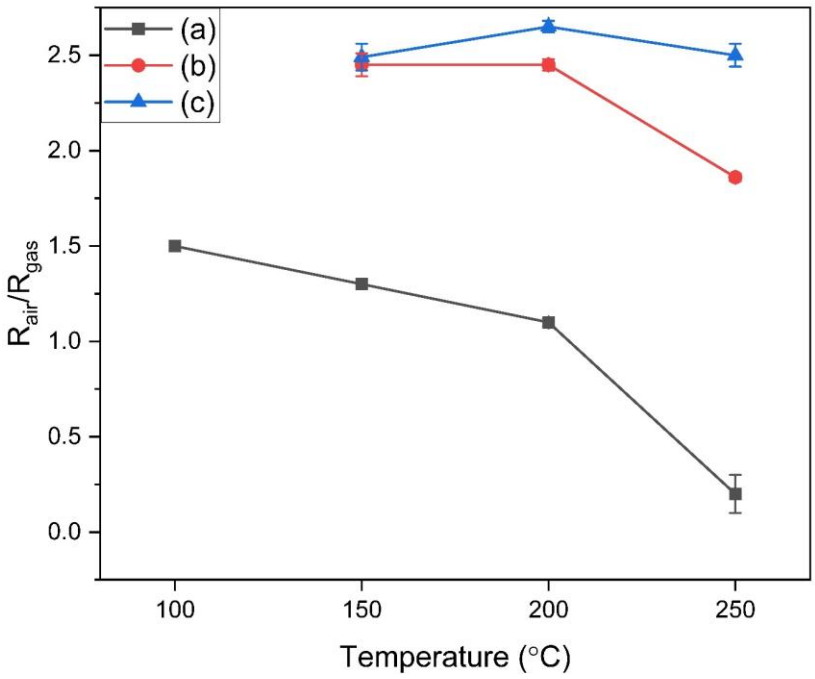

Figure S8 CO sensing results for 20 ppm (a) WO_3, (b) CeO_2 decorated WO_3 randomly oriented nanowires, and (c) CeO_2 decorated WO_3 nanowires with floral tops.

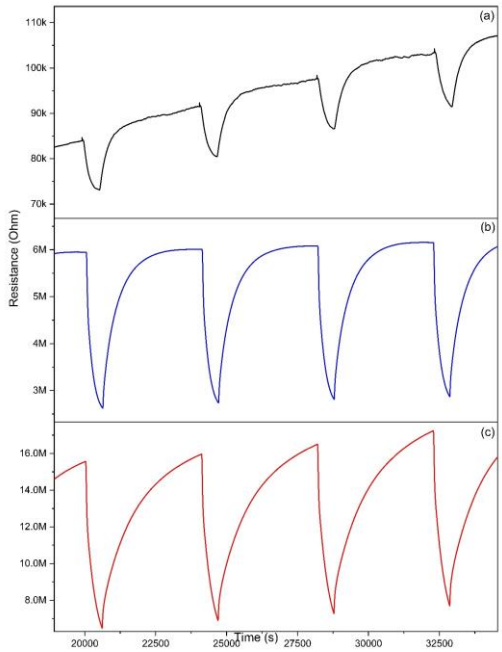

Figure S9 Resistance change of (a) pristine WO_3 at 100°C, (b) randomly oriented CeO_2 decorated WO_3 nanowires and (c) CeO_2 decorated WO_3 nanowires with floral tops towards 10 ppm CO at 200°C.

Hydrogen (H_2)

The sensors were exposed to 50 and 100 ppm of hydrogen to investigate the sensor responses at different temperatures ranging from 150ºC to 250ºC. Below 150ºC and above 250ºC, the sensor responses towards hydrogen are not significant and reproducible. Decorating WO_3 nanowires with CeO_2 enhances the response of the sensors towards hydrogen as can be seen in Figure S10. At 250ºC, the response of CeO_2 decorated floral top WO_3 nanowires is twice as that of the pristine WO_3. 250ºC is the optimum temperature in case of all the sensors and above 250ºC, the response towards hydrogen drops suddenly and is not reproducible hence not shown here. The dynamics of the sensor response is shown in Figure S11. The sensors showed an n-type behaviour, i.e, the electrical resistance decreases when exposed to H_2, a reducing gas.

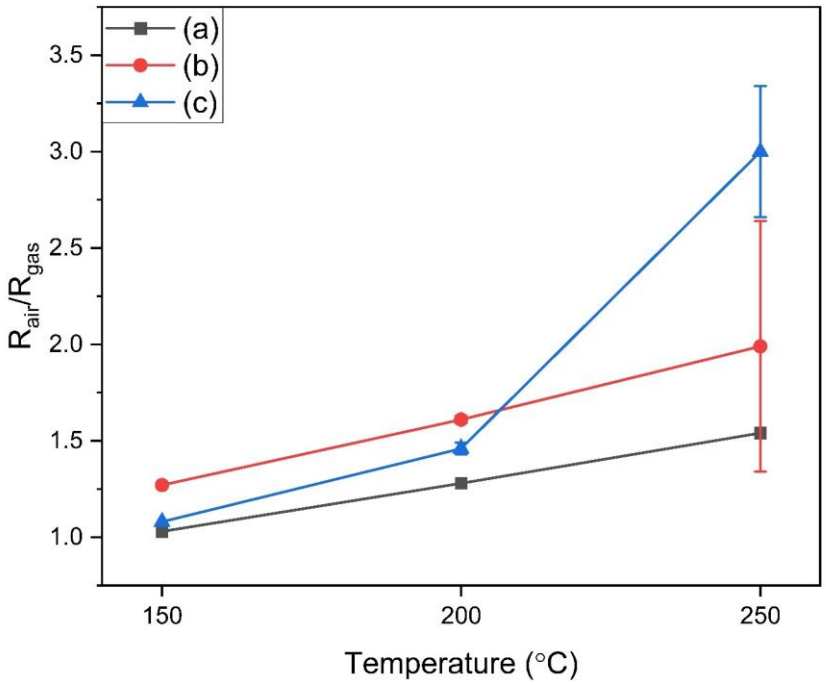

Figure S10 H_2 sensing results for 50 ppm (a) WO_3, (b) CeO_2 decorated WO_3 randomly oriented nanowires, and (c) CeO_2 decorated WO_3 nanowires with floral tops.

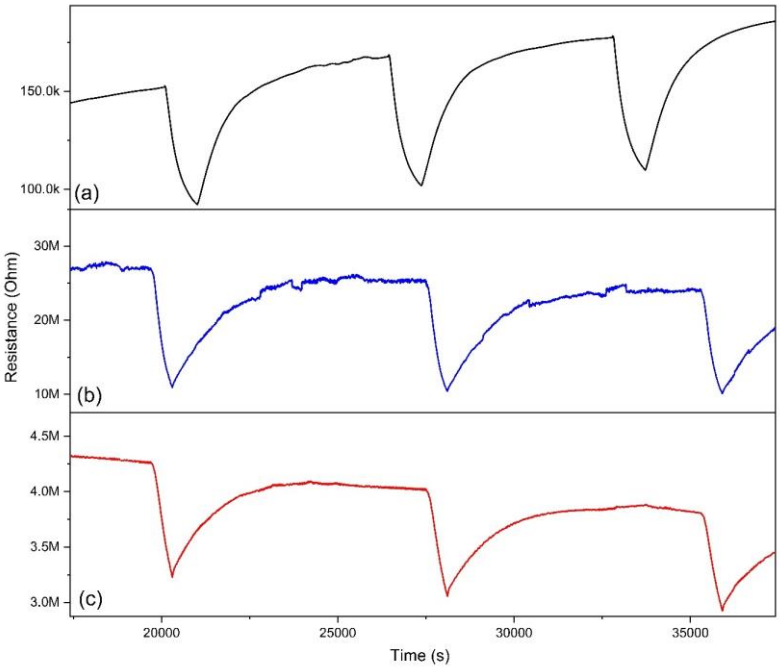

Figure S11 Resistance change of (a) pristine WO_3, (b) randomly oriented CeO_2 decorated WO_3 nanowires and (c) CeO_2 decorated WO_3 nanowires with floral tops towards 50 ppm H_2 at 250ºC

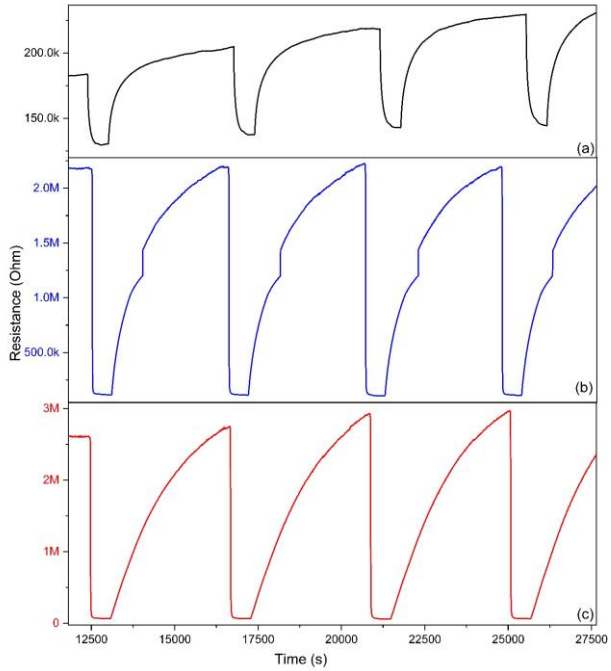

Figure S12 Resistance change (a) pristine WO_3, (b) randomly oriented CeO_2 decorated WO_3 nanowires and (c) CeO_2 decorated WO_3 nanowires with floral tops towards 20 ppm of ethanol in humid environment (50% R.H) at 250ºC.

Table S1 Average diameter details of pristine WO_3 and CeO_2 decorated WO_3 nanowires.

Sample	**Average diameter (nm)**
WO_3	167.61
CeO_2 decorated WO_3 randomly oriented	178.23
CeO_2 decorated WO_3 with floral tops Floral top average diameter	419.89 798

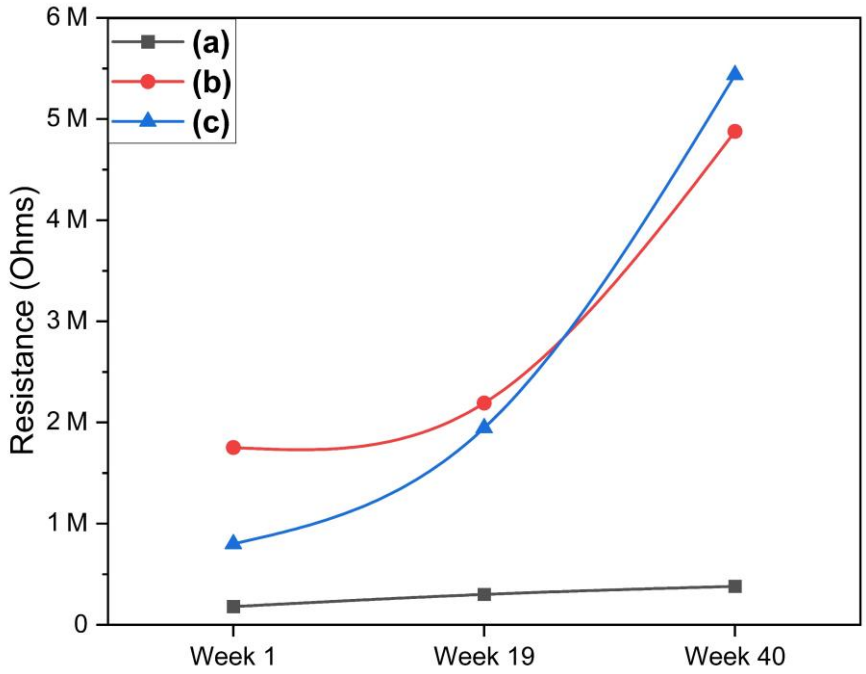

Figure S13 Baseline resistance drift with respect to time of sensor operation. (a) pristine WO_3 nanowires, (b) CeO_2 decorated WO_3 nanowires, and (c) CeO_2 decorated WO_3 floral tops nanowires.

References

[1] N. Yamazoe and K. Shimanoe, “Theory of power laws for semiconductor gas sensors,” *Sensors Actuators B Chem.*, vol. 128, no. 2, pp. 566–573, Jan. 2008, doi: 10.1016/j.snb.2007.07.036.

[2] S. Acharyya and P. K. Guha, “Hierarchical Zinc Stannate Nanoneedle-Based Sensitive Detection of Formaldehyde,” *ACS Appl. Electron. Mater.*, vol. 5, no. 6, pp. 3446–3453, 2023, doi: 10.1021/acsaelm.3c00436.

[3] S. Acharyya, S. Nag, S. Kimbahune, A. Ghose, A. Pal, and P. K. Guha, “Selective Discrimination of VOCs Applying Gas Sensing Kinetic Analysis over a Metal Oxide-Based Chemiresistive Gas Sensor,” *ACS Sensors*, vol. 6, no. 6, pp. 2218–2224, 2021, doi: 10.1021/acssensors.1c00115.

[4] A. Staerz, S. Somacescu, M. Epifani, T. Kida, U. Weimar, and N. Barsan, “WO3-Based Gas Sensors: Identifying Inherent Qualities and Understanding the Sensing Mechanism,” *ACS Sensors*, vol. 5, no. 6, pp. 1624–1633, 2020, doi: 10.1021/acssensors.0c00113.

[5] N. Barsan and U. Weimar, “Conduction model of metal oxide gas sensors,” *J. Electroceramics*, vol. 7, no. 3, pp. 143–167, 2001, doi: 10.1023/A:1014405811371.

Supporting information for

Graphene functionalized WS_2 for detecting ultra-low NO_2 concentrations

Shuja Bashir Malik[1,2], Fatima Ezahra Annanouch[1,2], Eduard Llobet[1,2]

1 Universitat Rovira i Virgili, MINOS, Països Catalans 26, 43007 Tarragona, Catalunya, Spain.

2 IU-RESCAT, Universitat Rovira i Virgili, Joanot Martorell 15, 43480 Vila-seca, Spain.

* Correspondence: authors' email: fatimaezahra.annanouch@urv.cat, eduard.llobet@urv.cat

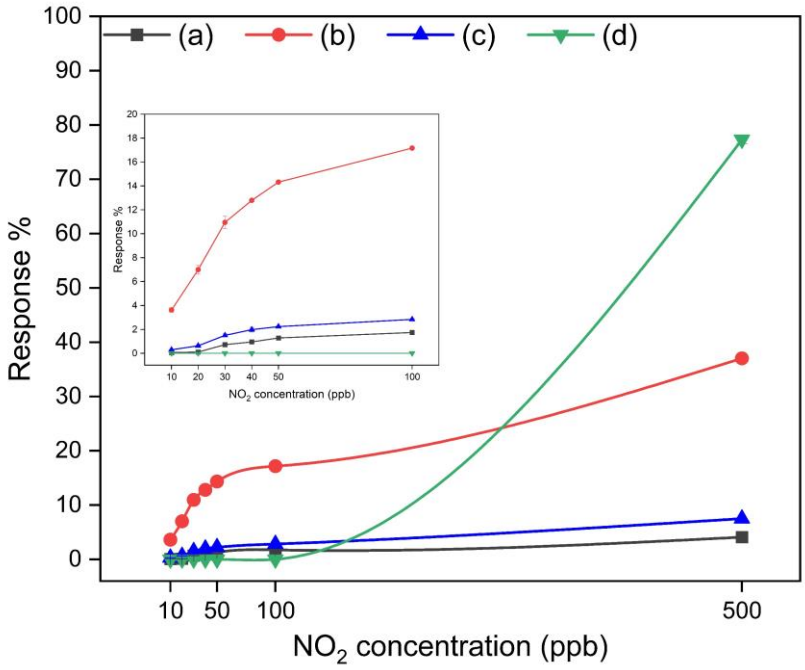

Figure S1 Sensor responses as a function of NO_2 concentration at 100ºC, (a) graphene, (b) Sensor A and (c) Sensor B and (d) pristine WS_2.

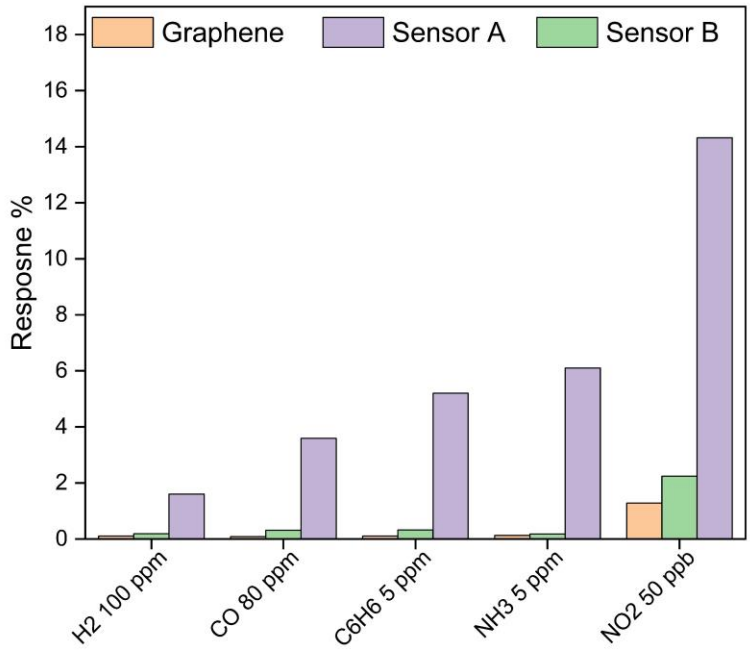

Figure S2 Selectivity studies of sensors towards different interfering gas species.

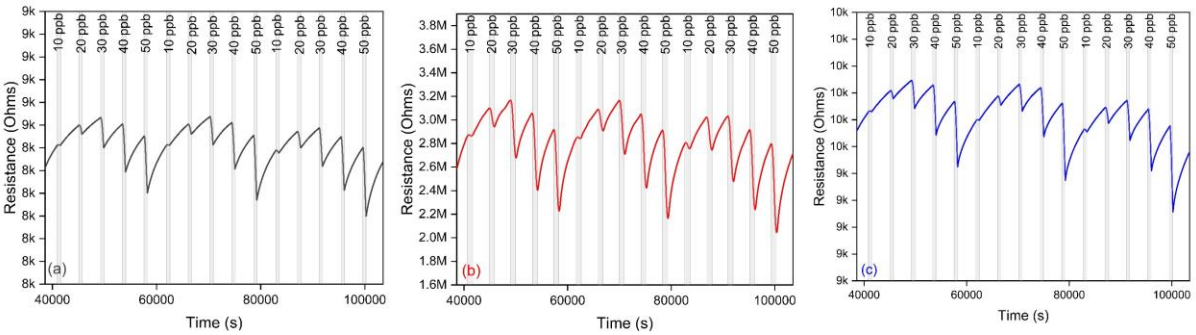

Figure S3 Resistance dynamics of sensors towards 10, 20, 30, 40 and 50 ppb NO_2 under humid environment (RH 50%) at 100ºC, (a) graphene, (b) Sensor A and (c) Sensor B.

Supporting information for

Pd nanoparticle decorated multilayered MoS_2 sheets for highly sensitive hydrogen sensing

Shuja Bashir Malik[1,2], Fatima Ezahra Annanouch[1,2]* and Eduard Llobet[1,2]

[1]Universitat Rovira i Virgili, MINOS, Països Catalans 26, 43007 Tarragona, Catalunya, Spain.
[2]IU-RESCAT, Universitat Rovira i Virgili, Joanot Martorell 15, 43480 Vila-Seca, Spain.
Universitat Rovira i Virgili, MINOS, Països Catalans 26, 43007 Tarragona, Catalunya, Spain.
*Corresponding authors: fatimaezahra.annanouch@urv.cat

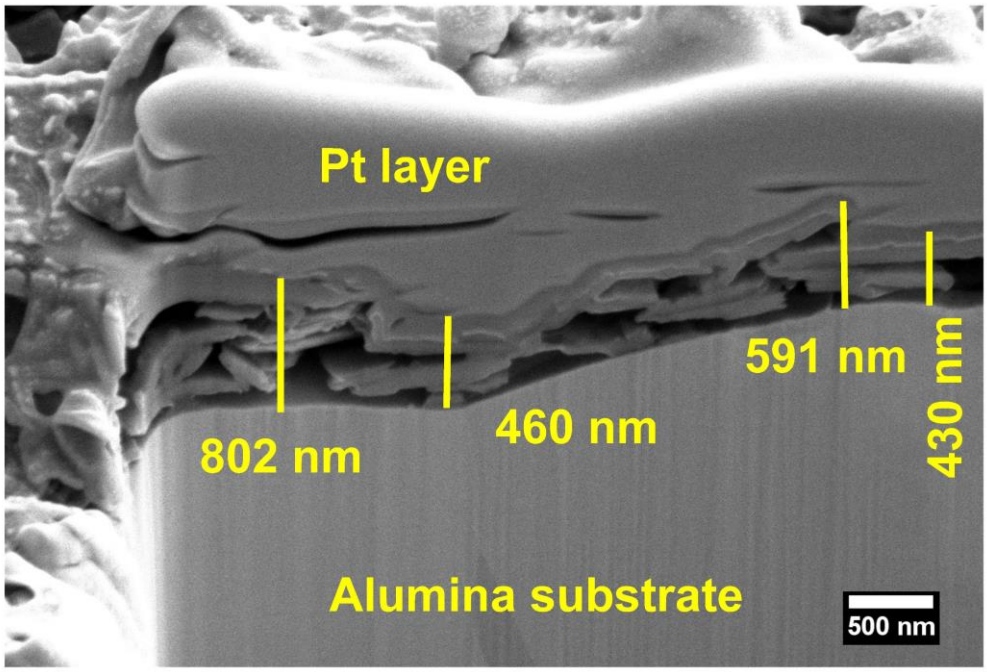

Figure S1 Thickness analysis of MoS_2 layer deposited by airbrushing.

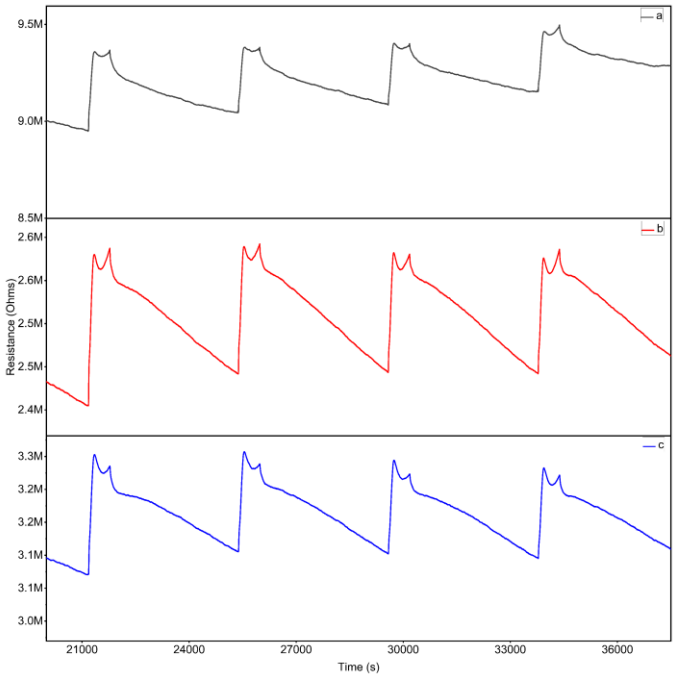

Figure S2 Sensor responses towards 5 ppm benzene at 150ºC, (a) MoS_2, (b) MoS_2-Pd_1 and (c) MoS_2-Pd_2.

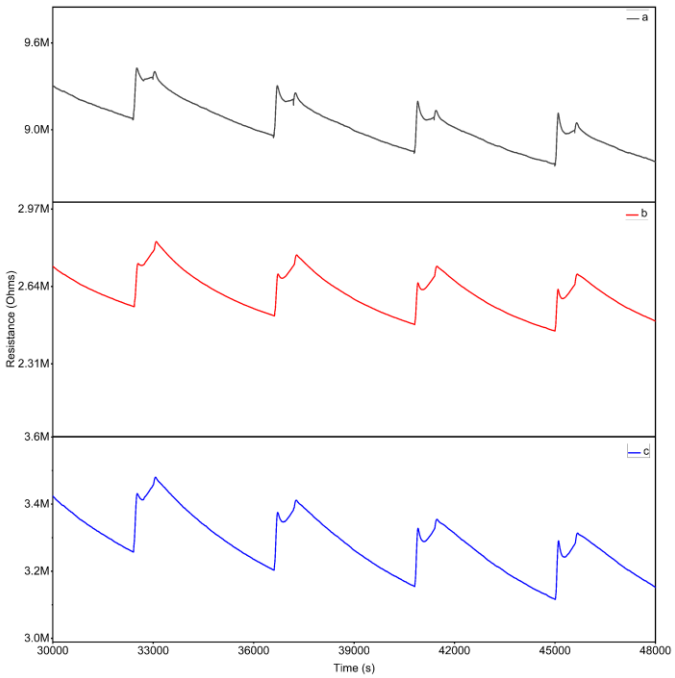

Figure S3 Sensor responses towards 80 ppm CO at 150ºC, (a) MoS_2, (b) MoS_2-Pd_1 and (c) MoS_2-Pd_2.

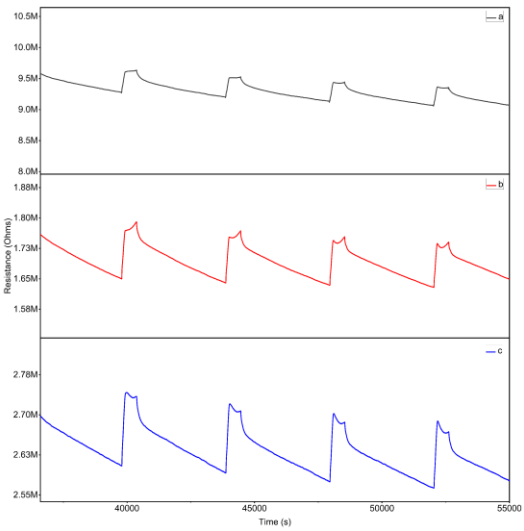

Figure S4 Sensor responses towards 10 ppm ethanol at 150ºC, (a) MoS_2, (b) MoS_2-Pd_1 and (c) MoS_2-Pd_2.

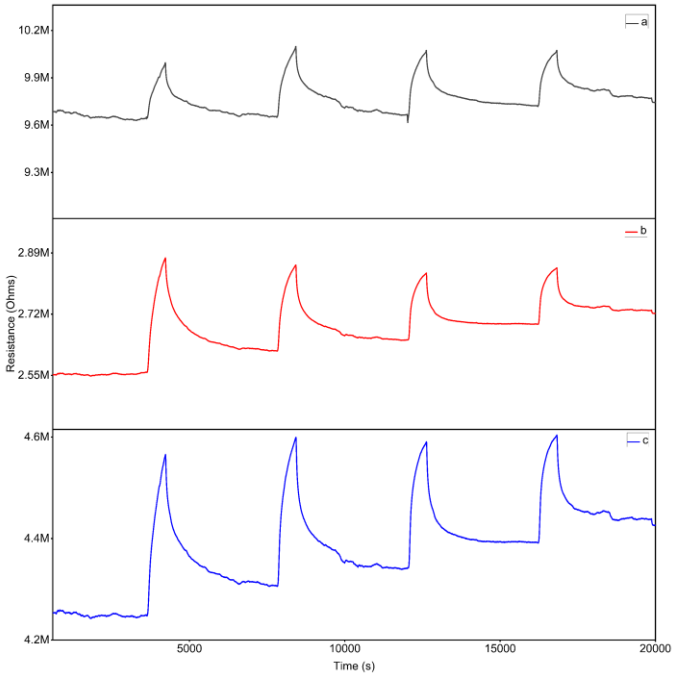

Figure S5 Sensor responses towards 5 ppm NH_3 at 150ºC, (a) MoS_2, (b) MoS_2-Pd_1 and (c) MoS_2-Pd_2.

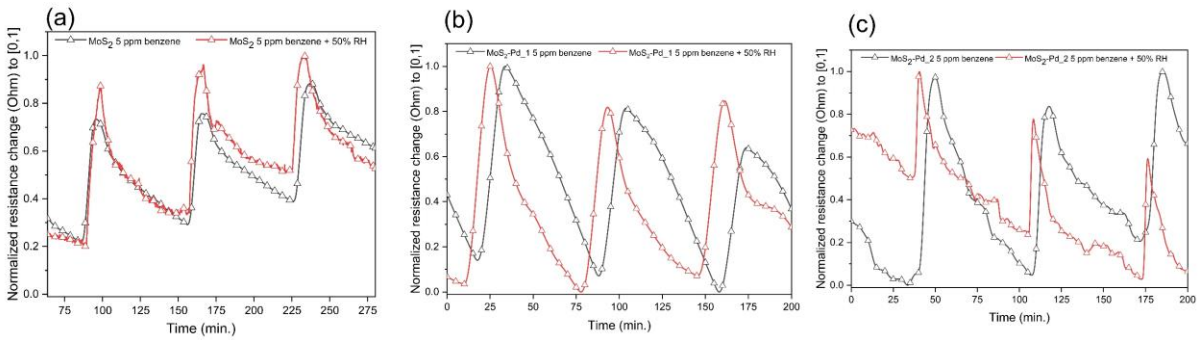

Figure S6 Normalized sensor resistance change as a function of time in dry (black) and 50% relative humidity (red) atmosphere at 150ºC towards 5 ppm benzene, (a) MoS_2, (b) MoS_2-Pd_1 and (c) MoS_2-Pd_2.

Annex II

List of Publications

1. Synergistic effect of CeO_2 nanoparticles and WO_3 nanowires in gas sensing applications, **Shuja Bashir Malik**, Karol V Mejia-Centeno, Paulina R Martínez-Alanis, Andreu Cabot, Frank Güell, Fatima Ezahra Annanouch, Eduard Llobet. **DOI: https://doi.org/10.1016/j.snb.2023.134879**

2. Pd-Nanoparticle-Decorated Multilayered MoS_2 Sheets for Highly Sensitive Hydrogen Sensing, **Shuja Bashir Malik**, F. E. Annanouch and Eduard Llobet. **DOI: https://doi.org/10.3390/chemosensors11110550**

Publications not directly related with the thesis

1. High-performance UV photodetector based on nickel oxide loaded with low amount of nitrogen and boron co-doped reduced graphene oxide for bias-switchable photoconductance, Chiheb Walleni, Nejeh Hamdaoui, **Shuja Bashir Malik**, Mohamed Faouzi Nsib, Eduard Llobet. DOI: https://doi.org/10.1016/j.jallcom.2023.173248

Book Chapter

1. Nanowires for Gas Sensors, Fatima Ezahra Annanouch, **Shuja Bashir Malik**, Eduard Llobet, Frank Guell, Gupta, R.K. (Ed.). (2023). Nanowires: Applications, Chemistry, Materials, and Technologies (1st ed.). CRC Press. DOI: https://doi.org/10.1201/9781003296621

Publications submitted for publication or in preparation

1. High-yield synthesis of WS_2 via novel sulfurization method for the selective detection of NH_3 vapors, **Shuja Bashir Malik**, Fatima Ezahra Annanouch, Ransell D´Souza, Carla Bittencourt, Milica Todorović, Eduard Llobet
2. Graphene functionalized WS_2 for detecting ultra-low NO_2 concentrations, **Shuja Bashir Malik**, Fatima Ezahra Annanouch, Eduard Llobet
3. ZnO decorated Graphene-based NFC tag for personal NO2 exposure monitoring during a workday, Alejandro Santos Betancourt, José C. Santos-Ceballos, Mohamed Ayoub Alouani, **Shuja Bashir Malik**, Alfonso J. Romero, José L. Ramírez, Xavier Vilanova and Eduard Llobet
4. Electronic excitation induced improved gas sensing behavior in $Cd_xZn_{1-x}O$ (x=0.4) nanocomposite as active layer, Arkapava Das, **Shuja Bashir Malik**, Fatima Ezahra Annanouch, Eduard Llobet, Carla Bittencourt
5. Selective NO_2 gas sensors employing nitrogen or boron doped and co-doped reduced graphene oxide, Chiheb Walleni, **Shuja Bashir Malik**, Ghada Missaoui, Mohamed Ayoub Alouani, Mohamed Faouzi Nsib, Eduard Llobet.
6. Role of Substrate Temperature on the Morphological, Structural and Visible Light-Assisted Gas Sensing Properties of WO_3 Nanorods Grown via Aerosol-assisted CVD, Luís F. da Silva, Francesc Gispert-Guirado, Ariadne C. Catto, **Shuja B. Malik**, Xavier B. Martínez, Renan A.P. Ribeiro, Marisa C. de Oliveira, Waldir Avansi Jr, Frank Güell and Eduard Llobet

Annex III

Contribution to conferences

1. **Poster presentation** on High-Performance DMMP Gas Sensor using PtO/WS_2 hybrid Nanosheets, Fatima Ezahra Annanouch, **Shuja Bashir Malik**, Aanchal Alagh, Eduard Llobet, at TecnaTox 2024.

2. **Poster presentation** on Operando studies of gas sensors using Near Ambient Pressure (NAP) XPS: correlation between morphology and electronic structure with the sensing property of ZnO during exposure to O_2 and CO gases at operating temperature, Valmor Roberto Mastelaro, Eduard Llobet, **Shuja Bashir Malik**, Frank Güell Vilà, Luís Fernando da Silva, Ariadne Cristina Catto, Ignacio Villar Garcia, Virginia Pérez Dieste, at 33rd RAU 2023.

3. **Oral Presentation** on Tungsten disulfide (WS_2) flakes synthesized via APCVD for ppb level NO_2 detection, **Shuja Bashir Malik**, F. E. Annanouch and Eduard Llobet, IBERNAM 2023.

4. **Poster presentation** on Highly sensitive 2D TMDs based NO_2 gas sensors via AACVD and APCVD combination, F. E. Annanouch, A. Alagh, **S. B. Malik**, J. F. Colomer, and E. Llobet, at 14th Spanish Conference on Electronic Devices (CDE 2023)

5. **Poster presentation** on High-Performance DMMP Gas Sensor using PtO/WS_2 hybrid Nanosheets, Fatima Ezahra Annanouch, **Shuja Bashir Malik**, Aanchal Alagh, Eduard Llobet, at IEEE Sensors 2023.

6. **Oral Presentation** on Room temperature detection of ppb level NO_2 by WS_2 sensors, **Shuja Bashir Malik**, Fatima Ezahra Annanouch, Eduard Llobet, at IEEE Sensors 2023.

7. **Oral Presentation** on ZnO/WS_2 hybrid material for NO_2 detection via the combination of AACVD and APCVD techniques, **Shuja Bashir Malik**, Eduard Llobet, Fatima Ezahra Annanouch, at EuroSensors 2023.

UNIVERSITAT
ROVIRA i VIRGILI